An exploration of renewable resources for biobased chemicals and materials

Natthamon Inthalaeng

Doctor of Philosophy

University of York

Chemistry

December 2025

Abstract

Valorisation of unavoidable food supply chain (UFSC) waste through circular, zero-waste principles is an important driver in the transition from petroleum-based to biobased refineries for chemicals, materials, and bioenergy. This work explores the valorisation of UFSC wastes, namely, blackcurrant pomace (BC), ginger pomace (GP), aeroponically grown coriander (CR) and Thai basil (ThB) roots, into biobased chemicals and materials.

Microwave hydrothermal (MHT) and acid-assisted treatment of BC yielded low methoxy pectin (Degree of esterification up to 21.1%). Low-temperature MHT (100 °C) produced the highest anthocyanin-rich fraction among all aqueous conditions. Subsequent MHT at 160 °C, followed by alkali bleaching, enabled the production of hydrogel-forming defibrillated celluloses (DFC). Incorporation of BC-derived fractions into sodium alginate (NaAlg) films enhanced antioxidant activity. NaAlg–BCP films were able to detect ammonia, with NaAlg–BCP50 showing the most distinct colour change. Differential scanning calorimetry showed that the films are suitable for high-temperature applications (up to 187 °C), with antifogging properties and high-water vapour permeability, supporting their use in packaging for highly perishable foods and spoilage indicators.

Supercritical CO_2 extraction of GP, CR, and ThB recovered essential oil- and lipid-rich extracts. CR and ThB extracts were rich in fatty acids, while GP extracts contained high phenolics. Microwave-assisted extraction produced soluble proteins at temperatures below 100 °C, whereas temperatures ≥ 80 °C yielded soluble starch from GP with yields up to 37% and high amylose content (41-46%). Further MHT of residues produced DFC with high thermal stability and water-holding capacity. However, only GP-derived DFC formed stable hydrogels, while CR- and ThB-derived DFC were unable to gel due to the presence of highly crystalline calcium oxalate and lignin.

Overall, this work demonstrates an integrated biorefinery approach for converting diverse agro-industrial and agricultural wastes into functional biobased products, contributing to waste reduction, resource efficiency, and sustainable material development.

Author's Declaration

I declare that this thesis is a presentation of original work and I am the sole author. This work has not previously been presented for a degree or other qualification at this University or elsewhere. All sources are acknowledged as references.

Part of this work has been published in the following peer-reviewed journals:

1. Inthalaeng, N.; Gao, Y.; Remón, J.; Dugmore, T. I. J.; Ozel, M. Z.; Sulaeman, A.; Matharu, A. S. Ginger Waste as a Potential Feedstock for a Zero-Waste Ginger Biorefinery: A Review. RSC Sustainability 2023, 1 (2), 213–223. https://doi.org/10.1039/d2su00099g. (**Impact factor, 4.9**).
2. Inthalaeng, N.; Barker, R. E.; Dugmore, T. I. J.; Matharu, A. S. Microwave-Assisted Production of Defibrillated Lignocelluloses from Blackcurrant Pomace via Citric Acid and Acid-Free Conditions. Molecules 2024, 29 (23). https://doi.org/10.3390/molecules29235665. (**Impact factor, 5.3**).
3. Inthalaeng, N.; Dugmore, T. I. J.; Matharu, A. S. Production of Hydrogels from Microwave-Assisted Hydrothermal Fractionation of Blackcurrant Pomace. Gels 2023, 9 (9). https://doi.org/10.3390/gels9090674. (**Impact factor, 4.6**).
4. Inthalaeng, N.; Dugmore, T. I. J.; Matharu, A. S. Repurposing of Blackcurrant Pomace via Microwave-Assisted Hydrothermal Fractionation into pH-Sensitive Films. ACS Sustain Chem Eng 2025, 13 (34), 13988–14002. https://doi.org/10.1021/acssuschemeng.5c05240. (**Impact factor, 7.3**).

This work has also been presented at the following conferences:

1. The 20th International Conference on Renewable Resources and Biorefineries (Poster), organised by Ghent University, Brussels, Belgium (6/6/2024).
2. The AP de Silva symposium (Oral presentation), The University of York, York, UK (24/1/2024).
3. The 16th Eurasia Conference on Chemical Sciences (Poster), organised by Chulalongkorn University, Bangkok, Thailand (15/12/2023).
4. The 5th RSC-CRSI Joint Symposium in Chemical Sciences (Poster winner prize), The University of York, York, UK (12/9/2023).
5. 'Feeding the Future' International Summer School (Oral presentation), The University of York, York, UK (27/7/2023).
6. Chem@York Research Conference (Poster), The University of York, York, UK (6/7/2023)

Table of Contents

List of Figures

List of Tables

List of Appendices

Abbreviations

ACN	Anthocyanin
ANOVA	A one-way analysis of variance
Ara	Arabinose
ATR-IR	Attenuated total reflectance infrared spectroscopy
BC	Blackcurrant pomace
BCP	Blackcurrant pectin
C3G	Cyanidin-3-glucoside
C3R	Cyanidin-3-rutinoside
CA	Citric acid
CCP	Commercial citrus pectin
CMC	Commercial microcrystalline cellulose
CR	Extruded aeroponically grown coriander roots
CrI	Crystallinity index
D3G	Delphinidin-3-glucoside
D3R	Delphinidin-3-rutinoside
DAD	Diode array detector
DE	Degree of esterification
DFC	Defibrillated cellulose
DPPH	2,2-Diphenyl-1-picrylhydrazyl
DSC	Differential scanning calorimetry
EAE	Enzyme-assisted extraction
FAOSTAT	Food and Agriculture Organization Corporate Statistical Database
GA	Gallic acid
GalA	Galacturonic acid
GC	Gas chromatography
GI	Glycaemic index
Glu	Glucose
GP	Extruded ginger pomace
HG	Homogalacturonan
HM pectin	High methoxyl pectin
HPE	High pressure-assisted extraction
HPLC	High performance liquid chromatography
HTC	Hydrothermal carbonisation
HTG	Hydrothermal gasification
HTL	Hydrothermal liquefaction
IEA	International Energy Agency
LC	Liquid chromatography
LM pectin	Low methoxyl pectin
LVR	Linear viscoelastic region
MW	Microwave
MAE	Microwave-assisted extraction
MAN	Mannose, xylose and fructose
MFE	Microfibrillated cellulose

MHDP	Meta-hydroxyldiphenyl
MHT	Microwave hydrothermal treatment
MS	Mass spectrometry
NaAlg	Sodium alginate
NMR	Nuclear magnetic resonance
NREL	National Renewable Energy Laboratory
PFE	Pulsed electric field assisted extraction
PTFE	Polytetrafluoroethylene (Teflon)
pXRD	Powder X-ray diffraction
QT	Quercetin
RG	Rhamnogalacturonan
RID	Refractive index detector
Rham	Rhamnose
SEM	Scanning electron microscopy
SWE	Subcritical water extraction
TAC	Total anthocyanin content
TFC	Total flavonoid content
TGA	Thermogravimetric analysis
TPC	Total phenolic content
ThB	Extruded aeroponically grown Thai basil roots
WHC	Water holding capacity
WVP	Water vapour permeability
WVTR	Water vapour transmission rate
UA	Uronic acid
UAE	Ultrasound-assisted extraction
UFSC	Unavoidable food supply chain
UHT	Ultra-high temperature

Acknowledgement

First and foremost, I would like to express my sincere gratitude to my supervisor, Professor Avtar Matharu, for his unwavering support, assistance, and patience, which enabled the successful completion of my doctoral research. My PhD journey was marked by many challenges and achievements. As an international student, moving more than 6,000 miles away from my family and friends and living abroad for five years was not easy. Throughout this time, I am deeply thankful to my supervisor for his understanding and support, not only academically but also personally. I greatly appreciate his step-by-step guidance and constant encouragement, both inside and outside the laboratory, which provided me with the confidence and motivation to complete this work.

I am also grateful to Dr. Tom Dugmore, my co-supervisor, for his valuable suggestions, critical discussions, and support at various stages of my PhD. I would further like to acknowledge those who provided instrumental analysis and training: Assistant Professor Vincenzo Di Bari (University of Nottingham) for rheology analysis; Paul Guning, Karen Hodgkinson, and Dr. Ewan Ward for SEM analysis; Dr. Ryan Barker and Jolyon Glynn for solid-state NMR analysis; Ed Bergstrom for LC-MS training; and Adrian Whitwood for pXRD training. Special thanks are also extended to Dr. Richard Gammons and Dr. Suranjana Bose for their support and assistance with various instruments within GCCE.

I am thankful to my colleagues in GCCE for their collaboration and support. I gratefully acknowledge the financial support provided by the Royal Thai Government under the DPST scholarship, without which my Master and PhD studies at the University of York and this research would not have been possible.

Finally, I would like to express my deepest gratitude to my family and friends for their unwavering support, patience, and encouragement throughout this journey. Their belief in me provided constant motivation and strength during both challenging and fulfilling moments of my doctoral studies.

Chapter 1: Introduction

1.1. Contextualisation

Climate change and its adverse impact on planetary health is the biggest challenge facing humanity. Seven of the nine Planetary Boundaries for sustainability have already crossed their safe operating space, including climate change (see **Figure 1.1**).[1,2] From 1995-2015, adverse weather patterns leading to intensified storms, floods, droughts, heat waves, have affected more than 4.1 billion people worldwide.[3] The continued rise in global average temperature, *i.e.*, global warming, is linked to increasing levels of atmospheric carbon dioxide (CO_2), a greenhouse gas, which has risen rapidly with respect to pre-industrial period (1850-1900) baseline.[4,5] In 2024, the average global temperature temporarily exceeded the 1.5°C threshold set by the Paris Agreement of 2015.[6] In 2025, CO_2 levels recently reached 423 ppm which was approximately 34% higher than its level in the pre-industrial period.[4,5] The rising trend and the emission of not only carbon dioxide but other greenhouse gases such as, methane (CH_4) and nitrous oxide (N_2O) are largely driven by human-induced or anthropogenic activities associated with processes reliant mainly on fossil fuels as chemical feedstocks and energy carriers.[7,8]

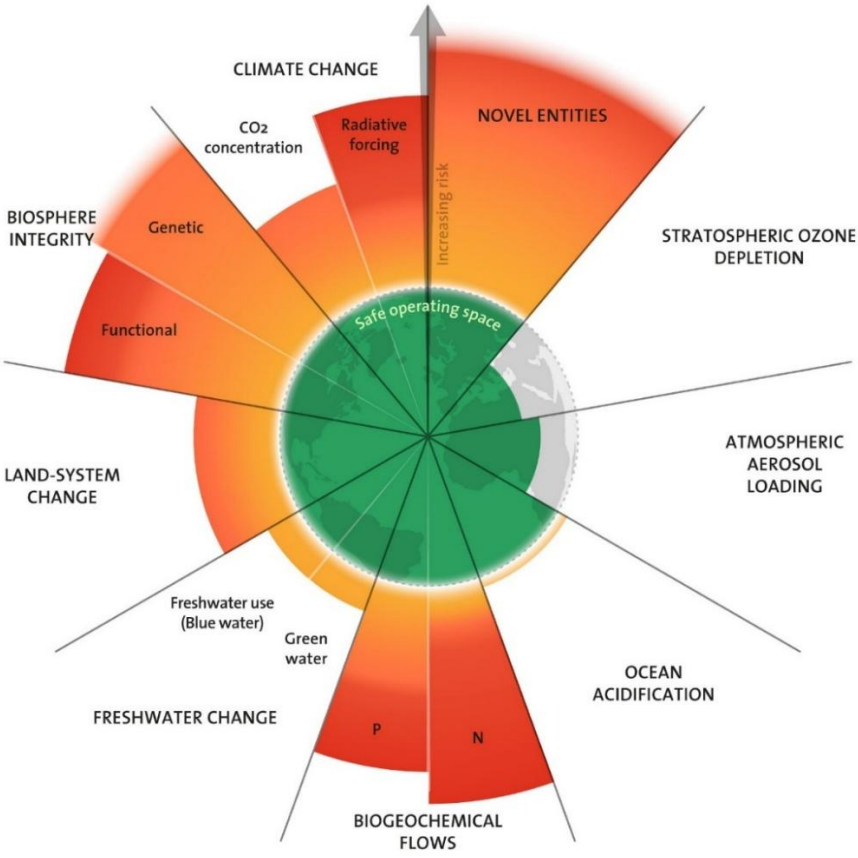

Figure 1.1. Current status of all nine planetary boundaries updated in 2025.[1]

Impending global megatrends such as, increased industrialisation, manufacturing, and urbanisation are associated with an increasing global population of 8.2 billion (2025) to an estimated 10 billion (2070), has led to an increasing demand for petrochemical feedstocks. According to the International Energy Agency (IEA), global oil demand is expected to grow by about 2.5 million barrels per day from 2024 to 2030. The petrochemicals sector is expected to become the dominant source of global oil demand from 2026 onwards, reaching 18.4 million barrels per day by 2030 for the production of polymers and synthetic fibres.[9] Given the unsustainable environmental impact connected with use of fossil fuels for our chemical, material and energy needs, the development of alternative, readily renewable feedstocks is paramount for a sustainable 21st century.

Biomass is both a renewable source of organic carbon plus a plethora of other elements unlike crude oil, is an interesting alternative feedstock to produce chemicals and fuels in biorefineries. Biorefineries adopt the concept from petroleum refineries, where feedstocks are processed to produce fuels, materials and chemicals. However, they differ in the raw materials used, the processing technologies applied, and the types of products derived (**Figure 1.2**).[10] In fact, biorefineries can utilise a wider range of raw materials and potentially produce a more diverse array of products with less processing steps compared to petroleum refineries which are reliant on building chemical complexity into a hydrocarbon feedstock.[8]

Biorefineries can be generally categorised into four classes based on input feedstock(s) and output products.[8] First generation of biorefineries are based on edible, starch, sugar-rich or triglyceride-rich food supply chain-competing feedstocks such as corn (maize), sugar beet, sugar cane, and edible seeds, for conversion into singular biofuels and biochemicals. First generation biorefineries have been tarnished with unethical practices, *i.e.,* food versus fuel debate.[8,11] Second generation of biorefineries use non-edible-lignocellulosic biomass residues such as forestry clippings, sawdust, agricultural and agro-industrial primary and secondary processing residues to produce multiple products, *i.e.*, chemicals, materials and bioenergy. [8,11] Third generation of biorefineries employ aquatic biomass such as microalgae and macroalgae, which have rapid growth rates, do not impact land use for food production, and are also rich in lipids and high value chemicals, making them suitable for biofuel production and speciality chemicals.[8,11] Fourth generation of biorefineries are the least developed and use genetically modified feedstocks/strains that can give bespoke products.[11]

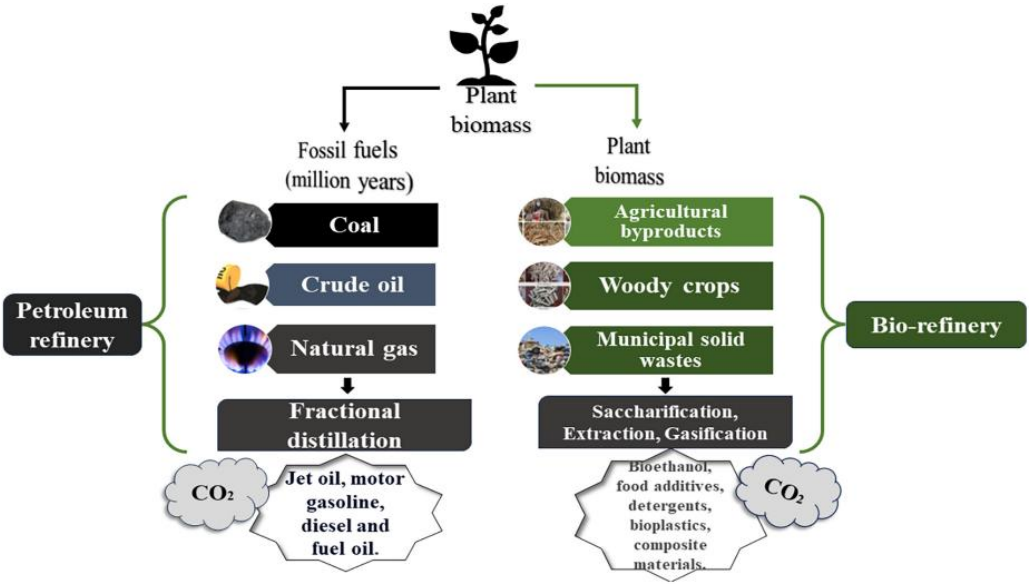

Figure 1.2. Concept of petroleum refinery and biorefinery.[10]

1.2. Typical composition of biomass: a renewable resource

Lignocellulosic biomass typically comprises an array of biopolymers and functional molecules: carbohydrates (cellulose, hemicellulose, starch, pectin), lignin, (poly)phenolics, proteins, lipids, waxes, oils, etc. The chemical composition of these compounds varies depending on the biomass source and the growing environment.[12] **Figure 1.3** illustrates the structure of the plant cell wall and the location of biopolymers within the cell wall.[12] In addition to the major organic constituents, lignocellulosic biomass also contains inorganic components such as ash and minerals.

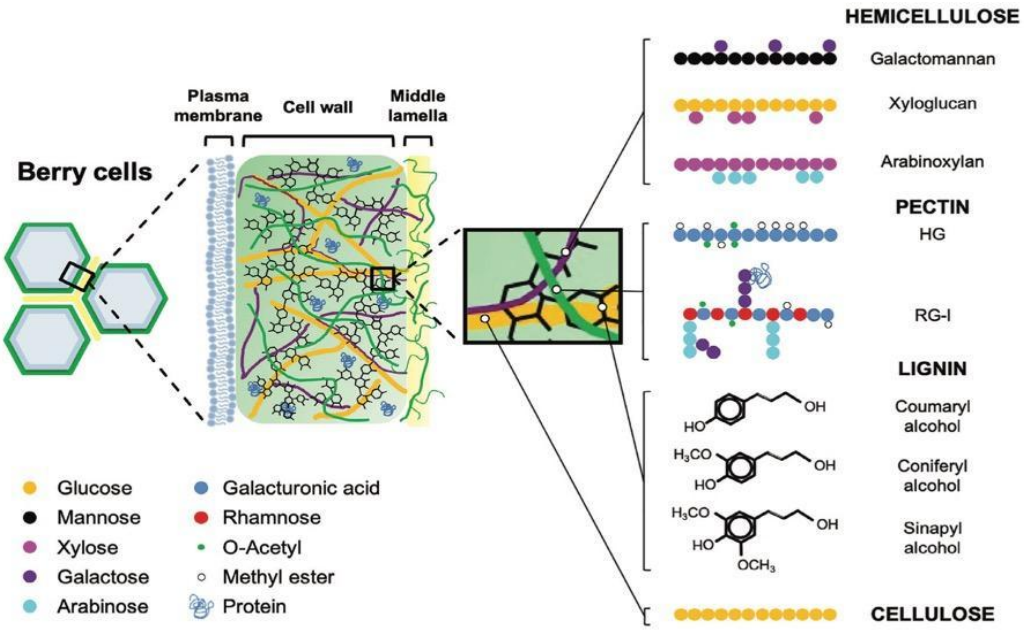

Figure 1.3. Structural composition of biomass biopolymers, illustrated by berry cell walls.[12]

1.2.1. Polysaccharides

Polysaccharides are biopolymers comprising carbon, hydrogen and oxygen. They exhibit considerable diversity, determined by the monosaccharide composition, linkage configuration, side chain, and chain length.

1.2.1.1. Cellulose

Cellulose is a main component in the plant cell walls, typically consisting of linear D-glucose units connected repeatedly in chains by β-(1 → 4) glycosidic linkages. Cellulose is a homopolymer linked together by inter- and intra-molecular hydrogen bonding, allowing the aggregation of polymer chains into highly ordered microfibrils. Thus, native cellulose is insoluble in water (**Figure 1.4**).[13] Structural cellulose occurs in two main forms depending on the degree of chain organisation, in which highly ordered chains normally form crystalline regions, while disordered chains form amorphous regions. Thus, the crystallinity index (CrI%) of cellulose varies based on its organisation.

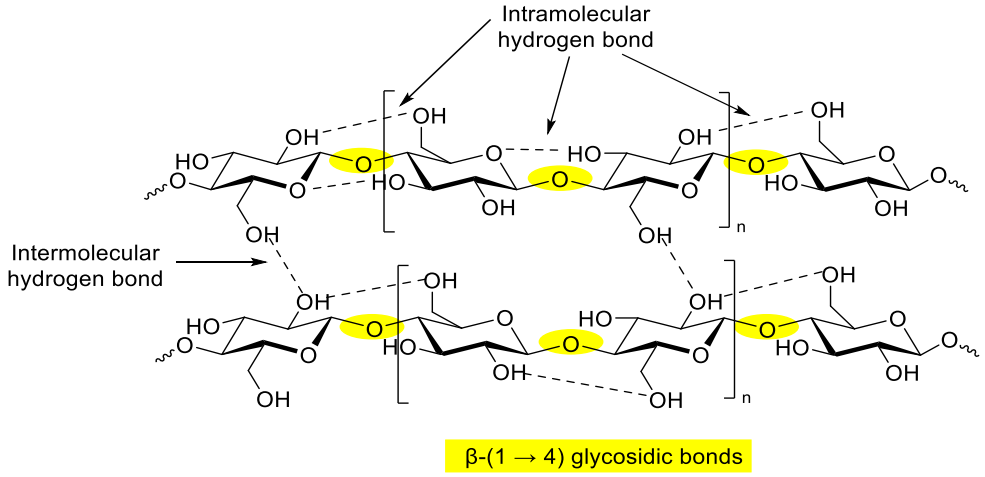

Figure 1.4. Chemical structure of cellulose, adapted from Deshavath et al.[13]

Cellulose crystalline structures can form in several polymorphs due to variation in their hydrogen bonding network. The cellulose repeating unit (see **Figure 1.4**) contains one glycosidic, two ring oxygen and six hydroxyl groups (-OH), providing nine potential hydrogen bond acceptors and six hydrogen bond donors.[14] Four main cellulose polymorphs are categorised as cellulose I, II, III, and IV, respectively, based on differences in chain arrangement (**Figure 1.5**).[14]

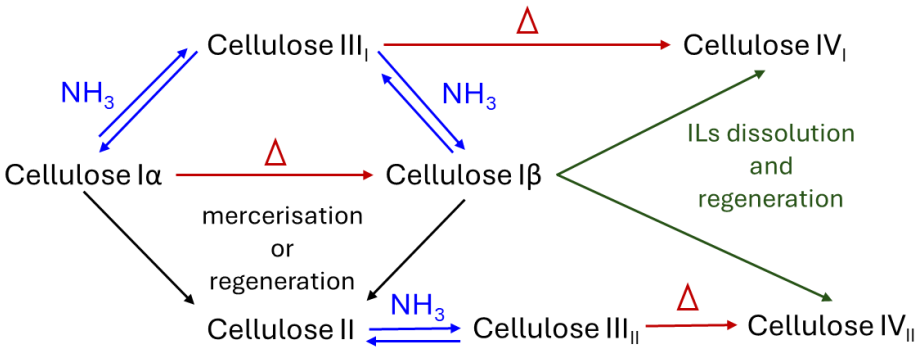

Figure 1.5. Cellulose polymorph conversions, adapted from Neto and Tokumasu et al.[14,15]

Cellulose I is the native crystalline form of cellulose, found in almost all plants, algae, and bacteria. It exists in two forms, namely, cellulose Iα and Iβ. Both subclasses exhibit a parallel arrangement of cellulose chains; however, they differ in their layer packing along the c-axis. As a result, cellulose Iα packs in a triclinic unit cell, while cellulose Iβ reveals a monoclinic unit cell (**Figure 1.6**).[16] Cellulose II also exhibits a monoclinic crystal structure, like cellulose Iβ, but with chains aligned in an antiparallel arrangement. It can be obtained from native cellulose (cellulose I) through alkali treatment, known as mercerisation, or by regeneration via dissolution followed by recrystallisation.[14,17] Cellulose III can be derived from cellulose I and cellulose II through the ammonia-mercerisation, denoted as cellulose III$_I$ for parallel chains and cellulose III$_{II}$ for antiparallel chains, in which ammonia treatment modifies the hydrogen bonding in cellulose packing chains.[18,19] Cellulose IV is generally obtained from cellulose III by heating, existing in parallel (cellulose IV$_I$) and antiparallel forms (cellulose IV$_{II}$). Cellulose IV is often considered not entirely distinct from cellulose I and may represent a partially disordered form of cellulose I.[15] In recent years, cellulose IV has also been prepared directly from cellulose I via dissolution in ionic liquids followed by regeneration.[15,20]

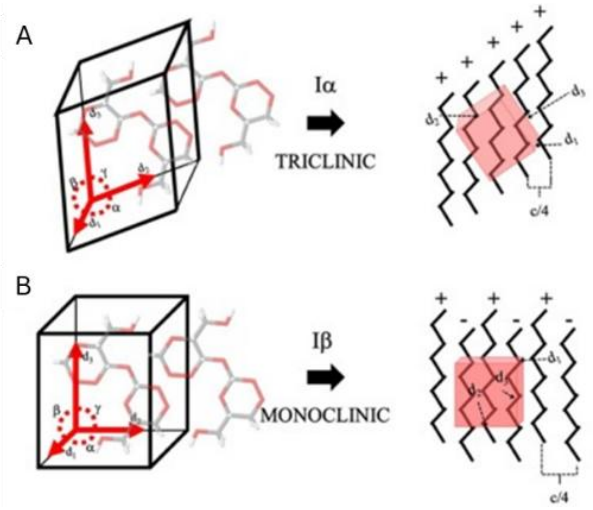

Figure 1.6. Cellulose I polymorph and its packing systems.[16]

1.2.1.2. Hemicellulose

Hemicellulose is one of the most abundant heteropolymeric carbohydrates in biomass. Unlike cellulose, which is linear homopolymeric carbohydrates, hemicellulose composed of various monosaccharides, including pentoses such as xylose, arabinose, and rhamnose; hexoses such as glucose, mannose, and galactose; acid sugars or uronic acids such as D-galacturonic acids, and D-glucuronic acids.[13] The backbone of hemicellulose can be homopolymeric comprising of only, for example, xylan, glucan, and galactan, or heteropolymeric such as glucomannan, and is typically connected by β-(1 → 4) linkages (**Figure 1.7**).[13,21] In addition, the structure of hemicellulose is largely amorphous. Various sugars or uronic acids are linked with the backbones, forming branching structures that hinder the forming of crystalline regions.[22] Among the hemicelluloses present in biomass, particularly in lignocellulosic feedstocks, the most abundant are xylans and glucomannans. Xylans are typically found in hardwoods and herbaceous plants, accounting for approximately 20-30% of their composition, and up to about 50% in grasses. Moreover, large quantities of xylans are produced as by-products of the paper and agro-industries.[13] In softwood plants, glucomannans and galactoglucomannans are the predominant forms of hemicellulose.[22] The structure and composition of hemicellulose vary depending on plant origin and class. For instance, galactomannans, xyloglucans, and glucomannans are commonly found in berry plants (**Figure 1.3**), whereas arabinoxylans and galactomannans are abundant in monocot plants.[12]

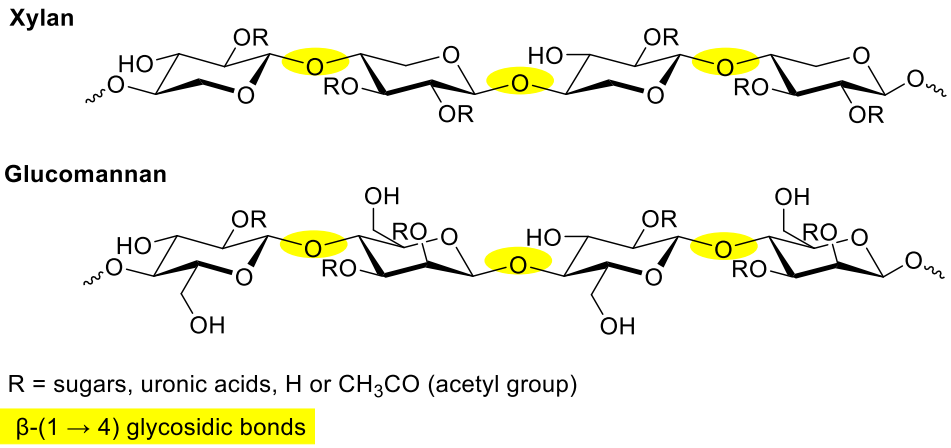

Figure 1.7. Chemical structure of hemicellulose, adapted from Gundekari et al.[21]

1.2.1.3. Starch

Starch is a homopolymeric carbohydrate, composed of D-glucose monomers joined by α-(1 → 4) glycosidic linkages, giving it a helical conformation. Starch typically occurs in two main forms, comprising about 10-20% amylose and 80-90% amylopectin.[21] Amylose, the water soluble fraction of starch, is a mostly linear polymer composed of α-(1 → 4) glycosidic bonds, whereas amylopectin has a branched structure with α-(1 → 4) bonds forming the backbone and additional branches connected through α-(1 → 6) glycosidic bonds (**Figure 1.8**).[21] In addition, the molecular weight of amylose is approximately 10^6, while amylopectin is higher than that of amylose, with about 10^8.[23] The difference in molecular structure of starch significantly impacts macroscopic properties, including its colours, solubility and gel-forming properties.[23]

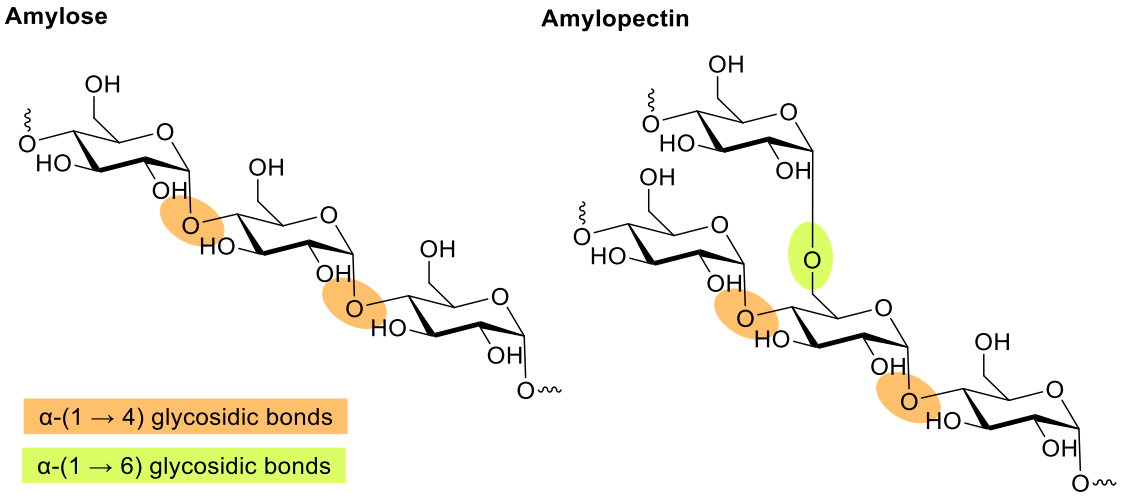

Figure 1.8. Chemical structure of starch, adapted from Gundekari et al.[21]

1.2.1.4. Pectin

Pectin is a polysaccharide mainly consisting of D-galacturonic acid (GalA) units. Its structure is generally divided into smooth and hairy regions (**Figure 1.3**). The smooth region corresponds to homogalacturonan (HG), a linear polymer of GalA units connected through α-(1 → 4) glycosidic linkage, which typically accounts for about 65% of total pectin (**Figure 1.3**).[24] HG chains may be partially acetylated at the C2 or C3 positions, depending on the origin of feedstocks (**Figure 1.9**).[24] The hairy regions consist mainly of rhamnogalacturonans (RGs). Rhamnogalacturonan-I (RG-I) constitutes about 20-35% of pectin. Its backbone is composed of alternating GalA and rhamnose units linked by α-(1 → 4) and α-(1 → 2) glycosidic linkages. The side chains of RG-I may either be linear or branched, depending on the sugars or uronic acids attached on the C4 positions of rhamnosyl moieties (**Figure 1.9**).[24,25]

Rhamnogalacturonan-II (RG-II) is one of substituted galacturonans. Unlike RG-I, RG-II backbone is mainly a HG chain, with lateral chains made up from different oligosaccharides bound on C2 or C3 positions of Gal A main chain.[24] In addition, pectins are classified based on the degree of esterification (DE) of the GalA carboxyl groups at the C6 position. When DE is below 50%, the pectin is defined as low methoxyl pectin (LM), while DE above 50% corresponds to high methoxyl pectin (HM).[26] The DE is influenced by the origin of raw materials and extraction conditions and plays a critical role in determining the gelling properties of pectin.[26]

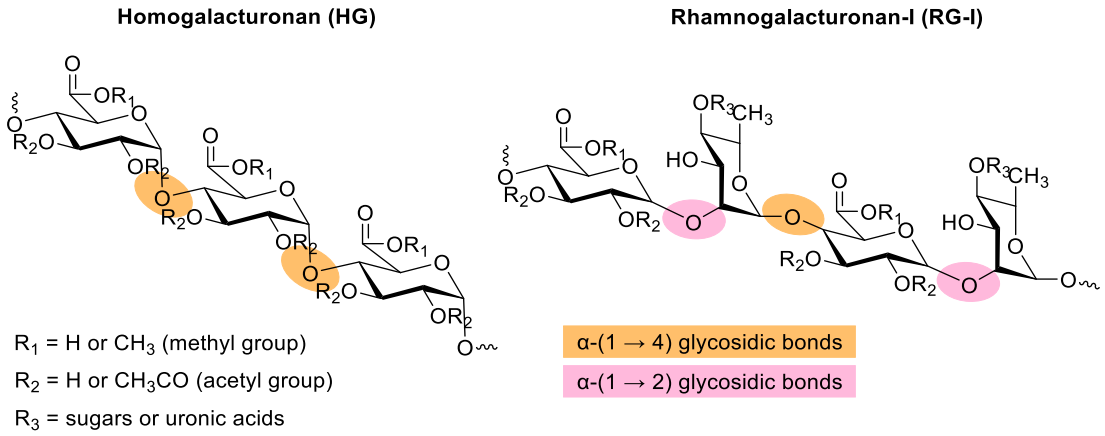

Figure 1.9. Chemical structure of pectin, adapted from Leclere et al and Amos et al.[24,25]

1.2.2. Lignin

Lignin is one of the most abundant biopolymers in biomass, particularly in lignocellulosic materials. It is a complex three-dimensional biopolymer that surrounds

cellulose and hemicellulose in plant cell walls, providing structural rigidity to the biomass.[13] Unlike carbohydrate polymers, lignin is not composed of sugars.[13] Instead, it is primarily built from three monolignols, which are *p*-coumaryl, coniferyl, and sinapyl alcohol, linked through ether or carbon-carbon bonds (**Figure 1.10**).[13,21] Lignin can be classified into four types based on the extraction process, namely Kraft lignin, lignosulfonates, organosolv lignin, and soda lignin.[27] Moreover, the structure, molecular weight, purity, and solubility of lignin are strongly influenced by the delignification process.[27]

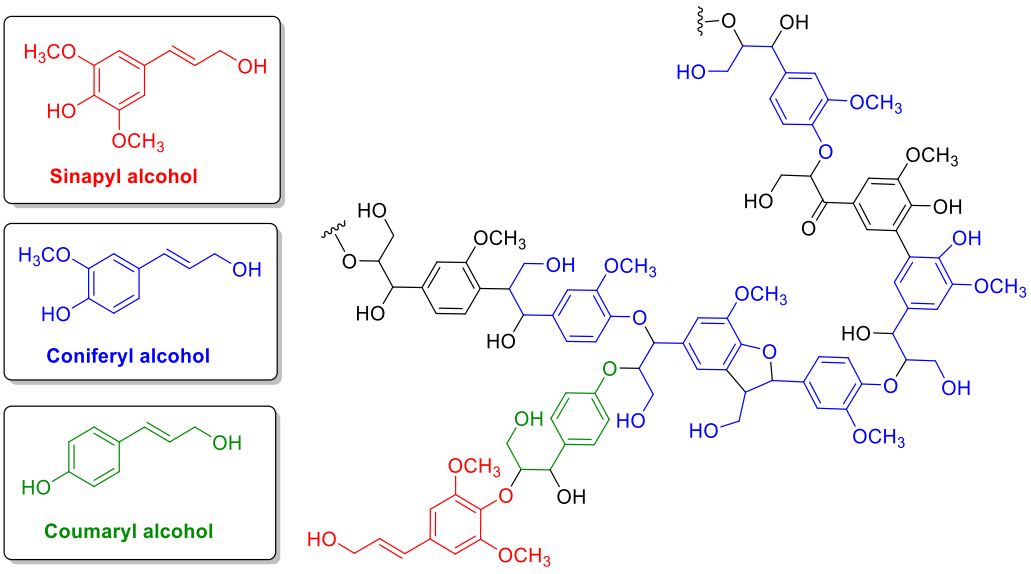

Figure 1.10. Chemical structure of lignin and their monomers.

1.2.3. Polyphenols

Polyphenols are a diverse group of plant-derived chemical compounds with the presence of one or more aromatic rings connected to hydroxyl groups (-OH). They are abundant in edible plants and can be divided into 5 different classes, including phenolic acids, flavonoids, stilbenes, lignans, and tannins (**Figure 1.11**).[28] Phenolic acids are the simplest type of polyphenols, containing a single aromatic ring bearing both carboxylic acids (-COOH) and hydroxyl groups (-OH). Due to their phenolic structure, phenolic acids exhibit antioxidant activity through radical scavenger mechanism and resonance stabilisation by hydrogen atom transfer, electron donation, or singlet oxygen quenching.[28] Flavonoids are a major class of polyphenol phytonutrients, characterised by three-ring core structure (C6-C3-C6), composed of ring A, B, and C (**Figure 1.11**). Because of the structural differences, flavonoids are commonly classified into Flavanols, Flavonols, Flavanones, Isoflavones, Flavones, Chalcones, and Anthocyanins, based on the oxidation degree and substitution pattern of the C ring.[29] Stilbenes represent another kind of

polyphenols, consisting of two phenolic rings connected via a 1,2-diphenylethylene core structure. Lignans, on the other hand, are formed through polymerisation of monolignols or phenylpropanoid derivatives, providing a wide diversity of complex structures.[28,30] Tannins are polymerised form of polyphenols with a molecular weight of 500 to 30,000 kDa, and generally divided into two categories, which are hydrolysed tannins and condensed tannins (polymers of flavan-3-ol units or procyanidins).[28]

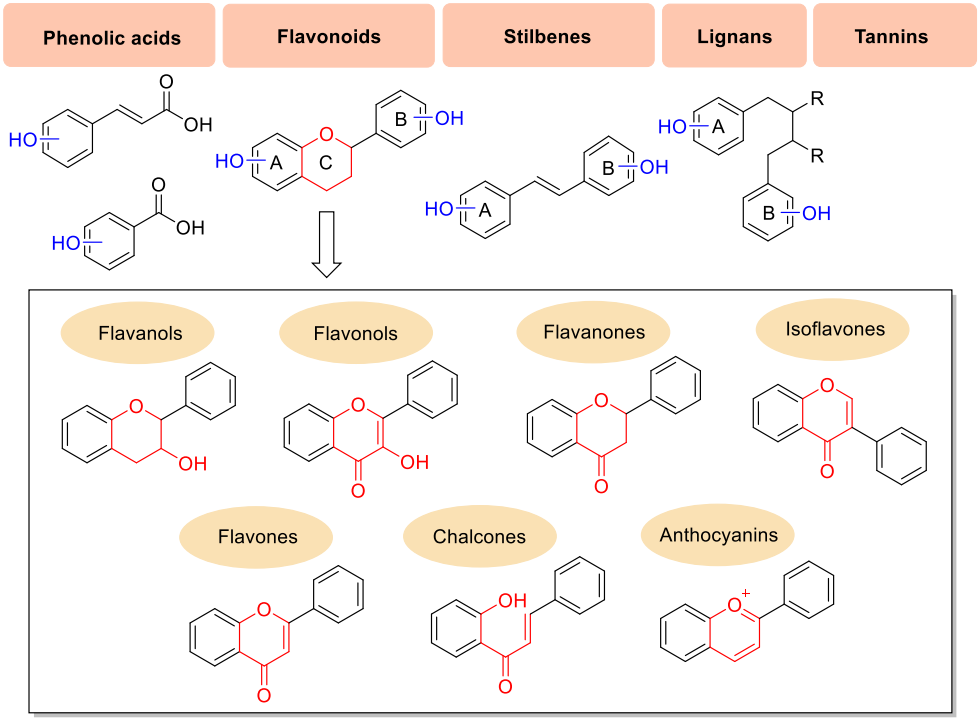

Figure 1.11. Type of polyphenols and their chemical structures.

1.2.4. Lipids

Plant lipids are mainly composed of triglycerides (**Figure 1.12**). A triglyceride consists of two main regions, which are the fatty chains and the ester region. Plant lipids are the crucial source of fatty acids and glycerol production.[21]

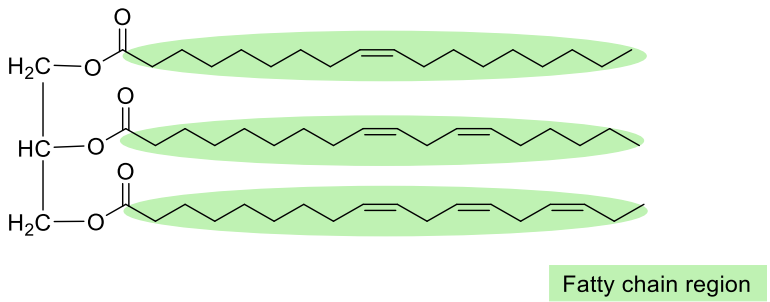

Figure 1.12. Chemical structure of triglyceride.

Fatty acids can be classified as saturated or unsaturated, based on the presence of double bonds in their hydrocarbon chains. The degree of unsaturation influences the physical form of lipids. Unsaturated lipids, which contain one or more double bonds, are typically liquid at room temperature, whereas saturated lipids, which lack double bonds, are generally solid at low temperature. Plant-derived fatty lipids are generally composed of fatty acids ranging from C_{14} to C_{20} with diverse fatty chains.[21] The most common fatty acids found in plants include stearic, palmitic, oleic, linoleic, and linolenic acids with different composition based on the source of raw materials.[21] **Figure 1.13** illustrates the chemical structures and formulas of some common plant fatty acids.[21]

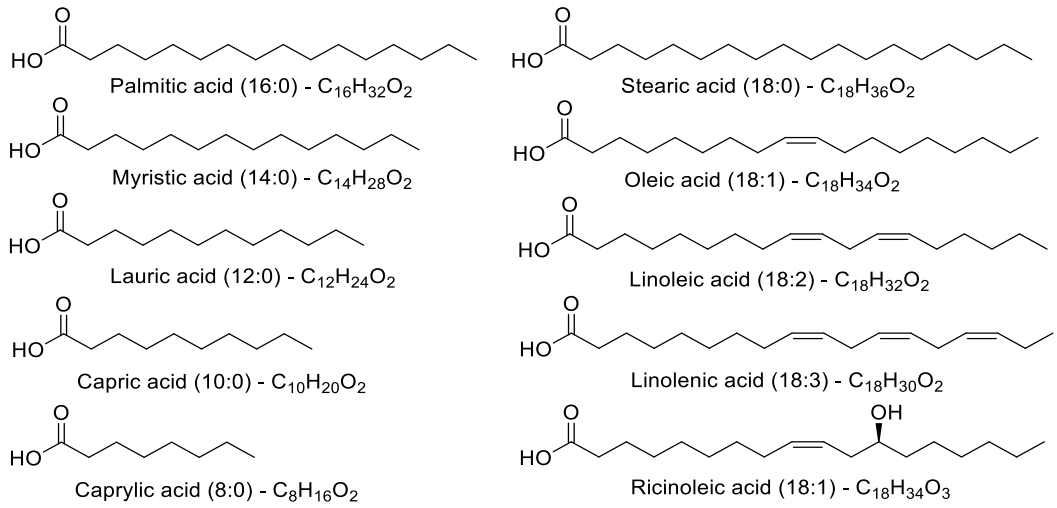

Figure 1.13. Chemical structure of common fatty acids with degree of unsaturation (No. of carbons: No. of double bonds) and chemical formula ($C_xH_yO_z$).[21]

1.2.5. Inorganic components

Biomass also contains inorganic constituents, which may occur in crystalline, semi-crystalline, or amorphous forms. These inorganic components commonly include alkali and alkaline earth metal species such as calcium, potassium, magnesium, and sodium, as well as silica and mineral salts. Although generally present in relatively small amounts, they can significantly influence biomass processing and conversion behaviour by altering pH, exhibiting catalytic behaviour during thermochemical processes such as pyrolysis and gasification, and influencing heat transfer and microwave absorption during hydrothermal or microwave-assisted treatments. In thermal treatment such as pyrolysis or gasification, alkaline or alkaline earth metal species play a crucial role as catalysts, where cations promote depolymerization, dehydration, decarboxylation, demethylation, decarbonylation of biopolymer chains. In addition, during thermal conversion, inorganic species may contribute to equipment wear because alkali or alkaline earth metals can

promote fouling, slagging, and reactor corrosion, as well as the release of undesirable emissions.

1.3. Microwave-assisted hydrothermal extraction

Hydrothermal process was first introduced in the geological field to describe the behaviour of water under conditions of high pressure and temperature, particularly in relation to the formation of rocks and minerals within the Earth's crust.[31,32] Geologists simulated such hydrothermal conditions and applied them in crystal growth, mining, and metallurgy.[31,32] Inspired by these natural processes occurring beneath the seafloor and within rock layers, researchers have extended the concept to biomass conversion, simulating hydrothermal processing for the production of fossil fuel-like products.[33,34] To explore its wider applications, hydrothermal technology has been adapted into artificial processes for biomass conversion.

The hydrothermal process can be categorised based on the processing conditions into hydrothermal carbonisation (HTC), hydrothermal liquefaction (HTL), and hydrothermal gasification (HTG).[31] HTC is generally conducted at a range of temperatures from 130 to 250 °C with the self-generated pressure between 1 and 5 MPa, producing a solid carbon-rich material known as hydrochar from biomass.[31] HTL is carried out at higher temperatures and higher pressure compared to HTC. The hot pressurised water at approximately 250 to 374 °C and 4 to 22 MPa, allowed nonpolar matters in biomass to dissolve and disperse into liquid phase.[31] This enhances biomass degradation and depolymerisation, yielding bio-oils along with polar organics such as phenols, organic acids, furfurals and other platform molecules.[32] HTG is conducted under supercritical water conditions, with the temperatures above 374 °C and pressure higher than 22 MPa, favouring the production of gaseous products such as H_2, CH_4, CO, and CO_2 from biomass.[31]

Overall, the hydrothermal process is one of the thermochemical conversion processes of biomass, typically carried out in closed systems under pressures ranging from 1 to 40 MPa and temperatures between 130 and 600 °C. Under these conditions, water exhibits the significant changes in behaviour and properties compared to room temperature water (see **Figure 1.14** and **Table 1.1**).[31] The increase in thermal conductivity (λ) of water under the elevated temperatures and pressures of HTC and HTL enhances heat transfer during hydrothermal processes. This improved thermal performance contributes to the energy efficiency and cost-effectiveness of hydrothermal conversion of biomass.[31,35]

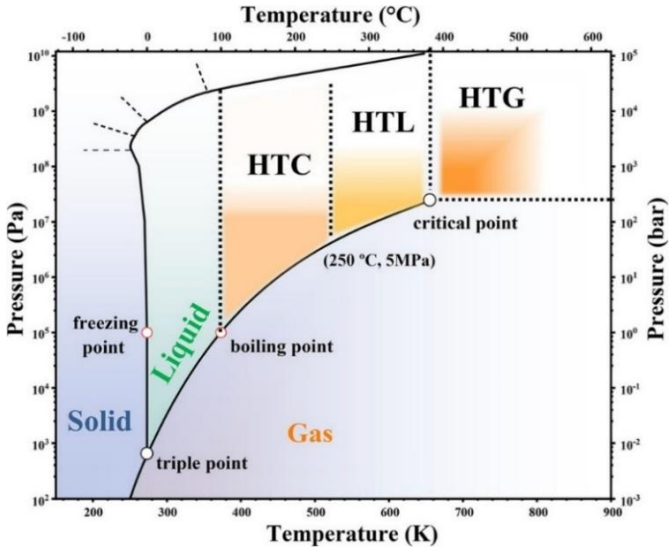

Figure 1.14. Phase diagram of water and hydrothermal conditions.[31]

In addition, the decrease in viscosity (η) and dielectric constant (ε) under hydrothermal conditions enhances the solvent properties of water (**Table 1.1**), facilitating the diffusion and dissolution of a wide range of polar and non-polar biomass-derived compounds.[31,35] The reduction in the logarithmic form of the ionic product (pK_w) further promotes water dissociation, generating higher content of hydronium (H^+) and hydroxide (OH^-) ions. With these property changes in hot pressurised water, namely subcritical and supercritical water, under hydrothermal conditions allow water to function as a catalyst, solvent, and reactant, facilitating biomass conversion through dehydration, decarboxylation, hydrolysis, condensation, aromatisation, and depolymerisation.[31,35] Therefore, the subcritical and supercritical water can serve as an efficient medium for the conversion of biomass into biochemicals, biofuels, and biomaterials.[31]

Table 1.1. Water properties at room temperature and hydrothermal conditions, adapted from Zhang et al.[31]

Properties	**Room temperature water**	**HTC**	**HTL**	**HTG**
Temperature, T (°C)	25	130	250	400
Pressure, P (MPa)	0.1	1	5	50
Thermal conductivity, λ (W/m.K.10^3)	607.50	685.24	619.14	451.30
Viscosity, η (10^{-6} Pa.s)	890.45	213.13	106.58	68.02
Dielectric constant, ε	78.50	49.37	27.15	12.16
Ionic product, pK_w	14.00	12.16	11.20	11.56

Recently, microwave-assisted hydrothermal treatment for the valorisation of biomass has attracted increasing attention due to its cost and energy efficiency, rapid processing, high selectivity, and controllability.[36] Microwaves, a form of electromagnetic radiation, can effectively promote the hydrothermal conversion of biomass because water molecules directly absorb microwave energy and convert into heat, making in rapid and direct heating.[31,36,37] In conventional heating, heat is transferred from the external surface inward through conduction and convection, which often causes the biomass surface to reach higher temperatures than the inside (**Figure 1.15**).[31,37] In contrast, microwave heating proceeds in the opposite manner, in which energy is absorbed directly by the material, allowing heating to occur from the inside out. Microwave heating of biomass, operating with the frequency range of 300 MHz to 300 GHz occurs through dipole rotation and ionic conduction mechanisms involving water molecules, biomass components, and electrolytes.[31,37] In addition, the presence of electrolytes in biomass, such as inorganic salts, facilitates the conversion of electromagnetic energy into heat within the aqueous medium.[31] This enhanced heating efficiency promotes biomass depolymerisation and degradation, thereby facilitating the release of internal compounds and accelerating the biomass conversion into biomass-derived products.[31,37]

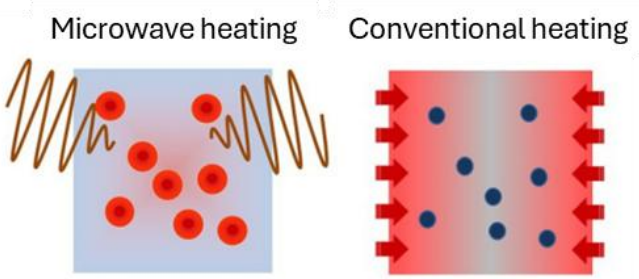

Figure 1.15. Heating pattern in microwave and conventional heating, adapted from Tsubaki et al.[37]

1.4. Aims and Objectives

Unavoidable food supply chain (UFSC) waste, including agro-industrial and agricultural byproducts, is an interesting second-generation, renewable feedstock, which also adheres to green chemistry principle 7 (the use of renewable feedstock). Globally, approximately 1.05 billion tonnes of food waste, including non-edible parts, which can be viewed as a source of biobased chemicals, materials and energy, is produced per annum.[38]

This research explores the valorisation of three agro-industrial and agricultural byproducts using microwave hydrothermal extraction as a core technology as described earlier in **section 1.3**, namely:

i. Feedstock 1: Blackcurrant pomace

Currants (*Ribes*) are small berries classified into black, red, and white varieties. They are concerned as an important ingredient in a healthy diet, as they are rich in bioactive nutrients such as vitamins, polyphenols, sterols and minerals.[39] The majority of currants, approximately 98.6%, are cultivated across European countries, with Russian and Poland being the leading producers.[40] In 2023, global production reached approximately 760,000 tonnes, of which around 130,000 tonnes were blackcurrants, grown primarily in Poland and the United Kingdom (UK).[40,41]

Blackcurrants (*Ribes nigrum*), small purple berries, are regarded as the most valuable among currants and other berries due to its high content of phytochemicals, specifically anthocyanins, exhibiting antioxidants, antimicrobials, and anti-inflammatory.[39,42] **Figure 1.16** illustrates a variety of blackcurrant products available in the UK market.

Figure 1.16. Blackcurrant and blackcurrant-derived products available in the UK on Amazon (https://www.amazon.co.uk/) based on the keyword "blackcurrant product"

Only up to 10% of blackcurrants are consumed as fresh product, while the majority are processed into products such as juice, jam and concentrates. Industrial processing generates substantial amounts of currant pomace, approximately 25-30% of the initial fresh weight, which corresponds to an annual production of 150,000-200,000 tonnes (see **Figure 1.17**).[43,44] Despite its high content of valuable compounds, pomace from the food industry is often discarded through landfilling, composting, or incineration, with smaller portions used as fertilisers or animal feed.[44] Given its abundance and rich composition of bioactive compounds, and biopolymers, currant pomace represents a promising resource for valorisation into high-value products, offering both economic and environmental benefits.

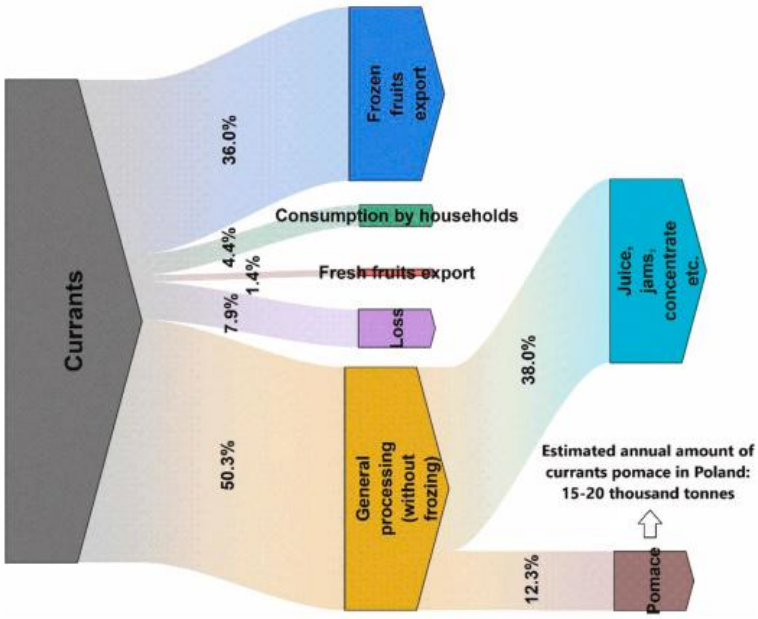

Figure 1.17. Sankey diagram illustrating the use of currants in Poland.[43]

1.4.1. Aim I (A1): Valorisation of blackcurrant pomace

Blackcurrant pomace, a large-volume by-product of industrial harvesting and processing, primarily consists of cellulose, lignin, hemicellulose, pectin, polyphenols, fat and ash. Research interest in blackcurrant pomace has grown steadily between 2015 and 2025. (see **Figure 1.18**). The latter have been extensively studied for their bioactive properties, such as antioxidancy.[45–48] A few studies have investigated the potential to convert blackcurrant pomace into biofuels, e.g., bio-oil and biochar.[49–52] Alba *et al*. report methods for fractionating dietary fibres, including soluble dietary fibre, insoluble dietary fibre, and lignin, from blackcurrants.[53] However, the extraction methods described in previous studies involve conventional heating, acidic conditions, alkaline conditions, and the use of chelating agents, which may have environmental implications.[53]

Citric acid (CA) is an example of a biobased renewable organic acid obtained from fermentation and has been utilised in various biomass pretreatment and extraction processes. It is effective in extraction of pectin and removing impurities such as lignin, hemicellulose, ash and inorganic matter from lignocellulosic feedstocks, facilitating the breakdown of fibre bundles into smaller units.[54–58]

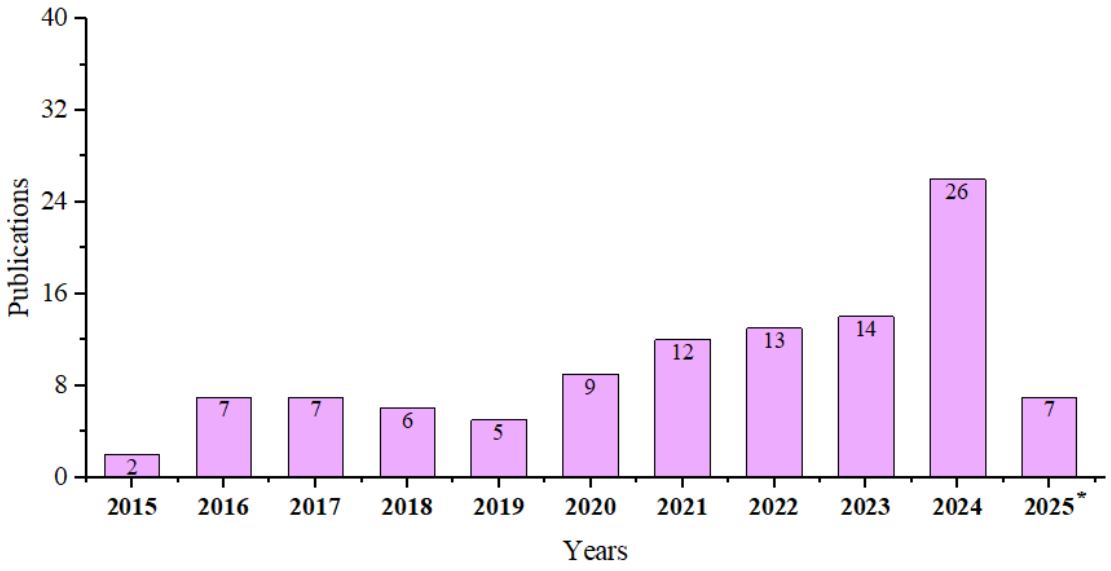

Figure 1.18. Number of papers published annually in the Web of Science (https://www.webofscience.com/) based on the keyword "blackcurrant pomace" between 2015-2025.

Microwave hydrothermal treatment (MHT) is known as a rapid and energy-efficient technique compared to the conventional methods. It allows to produce biopolymers, e.g., pectin and cellulose, that are free from chemical or biological additives and have undergone defibrillation. By utilising microwave energy, this process effectively and specifically eliminates hemicellulose, pectin, and amorphous cellulose from the biomass. This approach has been successfully applied to various biomass sources for production of pectineus and cellulosic materials.[59–62]

Thus, given its large volume and chemical richness, blackcurrant pomace is an important economic biorefinery feedstock. Herein, the aim is to fractionate blackcurrant pomace into biopolymers, and bioactive compounds using green alternative processing, including citric acid extraction and MHT (see **Figure 1.19**). This process adds further value to the eco-friendly blackcurrant waste biorefinery *via* a zero-waste approach. Initially, pectin will be isolated using water (thermal heating), conventional acid (HCl), citric acid (0.2-0.8M) and microwave-assisted hydrothermal processing at temperatures ranging from 100 °C to 160 °C. Thereafter, the depectinated blackcurrant residues obtained will be subjected to microwave hydrothermal reprocessing at 160 °C to yield defibrillated celluloses. Meanwhile, hydrolysates obtained during pectin isolation, considered rich in bioactive compounds, will be collected as anthocyanin-rich fractions. The total phenolic content (TPC), total flavonoid content (TFC), total anthocyanin content (TAC), and antioxidant ability will be evaluated and compared with the conventional solvent extracts

obtained using heptane, ethanol, water, and ethanol/water. Finally, pH-sensitive films will be developed from the fractionated blackcurrant pomace, further expanding its potential applications.

Objective A1 (i): *Characterisation of blackcurrant pomace*

The chemical composition of blackcurrant pomace varies with its origin, pretreatment processes, and the proportion of plant parts that contains in the materials, as pomace typically includes seeds, stems, and skins. **Table 1.2** summarises the chemical compositions of blackcurrant pomace obtained from different sources, such as Poland, the UK, Austria, and Sweden. Dietary fibre, primarily consisted of lignin, cellulose, hemicellulose and pectin, represent the major fraction of blackcurrant pomace, followed by protein, fat, and ash. While overall composition differs among origins and parts of BC, including pomace, skin, seeds, and stem, variations in fat content can be possibly due to differences in seed content.

To estimate the chemical composition of the blackcurrant pomace prior to fractionation, moisture and ash content analysis, Klason lignin analysis, elemental analysis (CHN), attenuated total reflectance infrared spectroscopy (ATR-IR), and thermogravimetric analysis (TGA), will be conducted (see **Figure 1.19).**

Table 1.2. Compositions of blackcurrant pomace from different sources.

Composition (wt.%)	**Poland[53,63,64]**	**UK[53]**	**Austria[65]**	**Sweden[66]**
Moisture	7.5	3.2	-	-
Ash	3.3	2.8	-	-
Fat	2.5 - 5.9	10.8	16.2	-
Protein	11.1 – 12.6	13.3	17.4	-
Polysaccharides [a]	38.7 – 47.2	38.7	-	14.1
Cellulose	12.0 – 17.2	13.6	-	-
Hemicellulose	14.4 – 25.3	14.5	-	-
Pectin	2.7 – 15.6	10.6	-	-
Soluble dietary fibre (SDF)	30	25	6.9	-
Insoluble dietary fibre (IDF)	46.9	47.4	58.6	-
Klason lignin	37.9 – 59.3	35.7	-	41.9

[a] includes cellulose, pectin, and hemicellulose

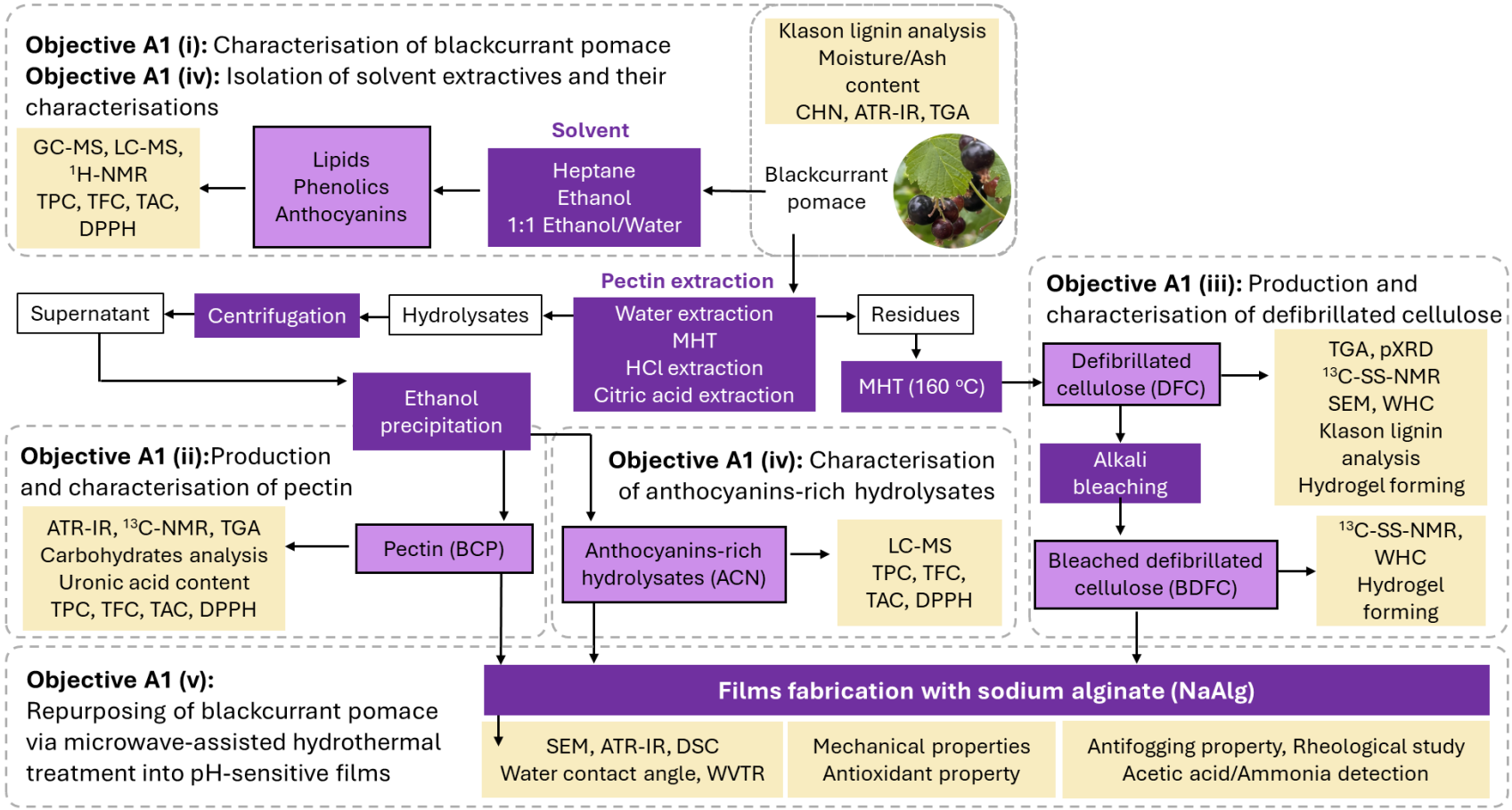

Figure 1.19. Process diagram illustrating the overall aims of blackcurrant pomace valorisation.

Objective A1 (ii): *Production and characterisation of pectin*

Pectin is widely applied in various industries, including food, pharmaceuticals, cosmetics, as well as in the development of edible packaging, paper substitution, foams, and plasticisers.[54,67] In addition, pectin is considered as a dietary fibre due to its natural origin and established safety for human nutrition.[67] The functional properties of pectin are determined by its chemical structure, particularly the gel-forming ability. High-methoxy (HM) pectin forms gel in the presence of sugars and acidic pH, while low-methoxy (LM) pectin can gel within a broader pH range (2-9.5) when divalent cations are present. [54,67] With its unique properties, pectin is not only used as a gelling agent, but also as an emulsifier, stabiliser, and thickening agent in food industry, and in cosmetic and skincare products. [54,67]

Unlike commercial pectin, which commonly derived from citrus and apple, blackcurrant pectin displays distinct structural characteristics. It contains a high content of rhamnogalacturonans (highly branched pectin), as well as anthocyanins and calcium bound within its structure.[68,69] Alba *et al*. identified blackcurrant pomace, a by-product of industrial juice processing, as a promising alternative source of pectin. Acid-soluble and calcium-bound pectin were isolated, characterised by a low degree of esterification (11-38%), a galacturonic acid content of 45-57%, and relatively small amounts of neutral sugars, suggesting a less branched pectin structure.[53]

Ćorović *et al*. fractionated acid-soluble and calcium-bound pectin from blackcurrant pomace for potential cosmetic applications. Instead of using HCl, citric acid was used as an alternative reagent for the acid-soluble pectin extraction. The isolated acid-soluble and calcium-bound pectin fractions exhibited comparable degree of esterification with approximately 49% and 51%, respectively. Both fractions demonstrated excellent emulsifier properties, as well as water and oil-holding capacities, making them suitable for using as cosmetic ingredients. Interestingly, the citric-acid pectin showed a significantly higher galacturonic acid content (72%) compared to the calcium-bound fraction (48%). In addition, it displayed three times greater antioxidant activity, with a tenfold increase in phenolic content, and selective antimicrobial activity, suppressing the growth of *Staphylococcus aureus* (a skin pathogen), while stimulating *Staphylococcus epidermidis* (a beneficial skin bacteria).[54]

As mentioned earlier, MHT has been successfully employed for pectin isolation. In this study, blackcurrant pectin will be fractionated from blackcurrant pomace using MHT at different temperatures (100-160°C) and compared with conventional extraction

methods, including water, HCl (0.2M), and citric acid (0.2-0.8M) extraction. The isolated pectin fractions will be characterised using ATR-IR, TGA, ^{13}C nuclear magnetic resonance (^{13}C NMR) spectroscopy, and carbohydrate analysis. In addition, uronic acid content, TPC, TFC, TAC, and antioxidant activity will also be determined (see **Figure 1.19**).

Objective A1 (iii): *Production and characterisation of defibrillated cellulose*

Cellulose, the most abundant renewable polymer, is often regarded as a sustainable and long-lasting alternative to synthetic polymers. It offers numerous benefits such as cost-effectiveness, environmental friendliness, compatibility with living organisms, biodegradability, and its widespread use in various industries.[70–72] Cellulose can be isolated *via* chemical or mechanochemical pretreatment. Typically, cellulose is obtained through strong mineral acid hydrolysis to remove non-crystalline components and achieve a highly crystalline structure.[70–72] However, the use of mineral acid creates a significant environmental hazard. Additionally, sugar dehydration products, such as furfural and 5-hydroxymethylfurfural (5-HMF), can form as by-products during the hydrolysis of sugars under harsh conditions. The presence of these compounds in hydrolysates acts primarily to inhibit microbial metabolism, negatively impacting biosynthesis processes. This inhibition can lead to substantial productivity losses and cost inefficiencies and make industrial processes economically unfeasible.[73]

De Melo *et al*. demonstrated acid-free microwave hydrothermal fractionation of pectin and cellulose materials from biomass.[59] The industrial production of pectin uses hydrochloric acid (HCl, pKa approx. −6) at 80 °C, which is highly corrosive and generates significant amounts of aqueous acidic waste. All traces of mineral acid need to be removed prior to pectin use in certain applications, for example, food and food packaging. The activation of lignocellulosic substances, such as spent pea biomass, cassava peel, and almond hull, can be achieved through MHT, operated at temperatures ranging from 120 to 220 °C.[60–62]

Thus, herein, blackcurrant residue after pectin extractions, involving conventional water, HCl, citric acid at various concentrations, and MHT at various processing temperatures, will be reprocessed with MHT at 160 °C for production of defibrillated celluloses (DFCs). (see **Figure 1.19**). The microwave processing temperatures used are based on existing knowledge of acid-free microwave-assisted pectin extraction and hemicellulose and cellulose decomposition temperatures. [60–62] Optimal pectin isolation is approx. 140 °C, and optimum cellulose decomposition is typically in excess of 190 °C, which leads to the formation of humins, chars and pseudo-lignins.[59,60,74] Thus, restricting

the upper temperature to 160 °C avoids decomposition of cellulose and ensures higher removal of hemicellulose. Therefore, defibrillated celluloses with higher cellulose content will be envisaged.

The changes in the composition, structure, and morphology of DFCs using various analytical techniques, including scanning electron microscope (SEM), TGA, powder X-ray diffraction (pXRD), and solid-state ^{13}C CP/MAS NMR, will be examined. The specific aims of this study are (i) to examine and compare the effectiveness of water, HCl, citric acid and acid-free microwave-assisted extraction conditions at moderate temperatures on the extraction of lignocellulosic materials from blackcurrant pomace, with the goal to valorise food waste through a sustainable and green approach; (ii) assess the physicochemical properties of the resulting lignocellulose, including crystallinity, morphology, and chemical and structural compositions; (iii) evaluate the thermal and rheological properties to identify potential applications.

Objective A1 (iv): *Isolation of solvent extractives and characterisation of anthocyanins-rich hydrolysates*

Blackcurrant is well-known as a rich source of bioactive compounds, particularly anthocyanins (ACNs), phenolic acids, flavonols, condensed tannins, and hydrolysable tannins.[46,75] Extensive research has focused on the extraction of ACNs, as they not only provide a wide range of biological benefits such as antioxidant, anti-inflammatory, and antimicrobials,[39,42] but also enhance the sensory qualities of foods.[75,76] This makes them valuable for pharmaceutical applications as well as for use as a natural food colourant (E136).[75,76]

Regarding conventional extraction methods, polar solvents such as water, methanol, ethanol, or acetone are commonly employed for extracting ACNs from blackcurrant or its pomace.[77] Although methanol and acetone are highly effective extraction solvents, their use in food products is prohibited due to their toxicity and potential health hazards.[76,77] In contrast, ethanol and water are considered safe and widely accepted for food applications. In addition, mixtures of ethanol and water (40%, 60%, or 96% of ethanol) demonstrated better extraction ability than a single solvent, with 60% of ethanol yielding the highest ACNs content among all ethanol-water mixtures.[75,78] Among all ACNs, cyanidin-3-glucoside (C3G), cyanidin-3-rutinoside (C3R), delphinidin-3-glucoside (D3G), and delphinidin-3-rutinoside (D3R) were identified as the main ACNs (see **Figure 1.20**), accounting for 92-97% of total ACNs content.[78] Additionally, extraction under acidic conditions has been shown to further enhance ACNs yield.[79,80]

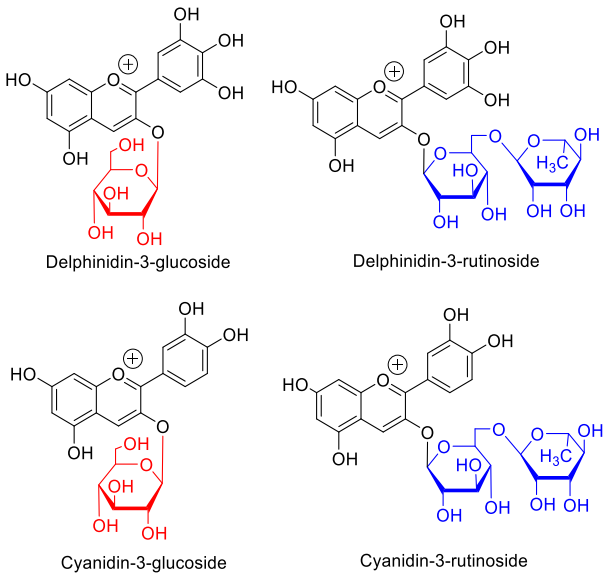

Figure 1.20. Chemical structures of four main anthocyanins found in blackcurrant.

Conventional solvent extraction however, is time and energy consuming, costly, low selectivity, and require for high purity solvent and evaporation after extraction.[73] To overcome these drawbacks, alternative non-conventional methods such as ultrasound-assisted extraction (UAE),[47,76,81–83] microwave-assisted extraction (MAE),[84] enzyme-assisted extraction (EAE),[85,86] and pulsed electric field assisted extraction (PFE),[87] have been extensively studied for ACNs extraction from blackcurrant and its pomace. These methods have demonstrated reduced solvent consumption and shorter processing times, while achieving comparable or even improved ACNs yields compared to conventional extraction.[75]

MAE has been reported to enhance ACN yield from blackcurrant marc by more than 20% when performed under acidic conditions or ethanol-water mixtures.[84,88] However, several factors, including microwave power, time, pH, and the solid-to-liquid ratio, significantly influence the efficiency of ACNs recovery.[84,88]

In this work, we aim to recover blackcurrant pomace hydrolysates obtained after pectin extraction *via* acid-free MHT at 100-160°C, and conventional acid extraction (0.2M HCl, and 0.2 – 0.8M citric acid), which are expected to be rich in ACNs. The recovered ACN-rich fractions from MHT will be characterised and compared with those obtained through conventional solvent extractions using heptane, ethyl acetate, ethanol, and ethanol-water mixtures as solvents. Liquid chromatography-mass spectrometry (LC-MS) will be used to determine the presence of ACNs in the extracts. Additionally, TPC, TFC, TAC, and antioxidant activity will also be investigated.

Objective A1 (v): *Repurposing of blackcurrant pomace via microwave-assisted hydrothermal treatment into pH-sensitive films*

Food labelling is a major cause of confusion that contributes to food waste. Phrases such as “Best by”, “Use by”, and “Sell by”,[89] typically do not provide real-time information on freshness, safety, or quality of food. Approximately, 20% of all edible items are discarded by consumers due to confusion about the meanings of the different labels.[90] To monitor food quality in real-time, colorimetric methods have been introduced, as they are simple, cost-effective, require no additional readout devices, and can be easily incorporated into food packaging.[91] The growth of microorganisms leads to the release of volatile organic compounds such as organic acids and amines, resulting in pH changes.[92,93] The microbial degradation of nitrogen-containing compounds and protein in meat or seafood can increase volatile organic amines. Food freshness can be evaluated by measuring the release of total volatile basic nitrogen (TVB-N) and the biogenic amine index (BAI), which are commonly used as spoilage indicators.[92]

Unavoidable food supply chain byproducts such as agro-industrial waste are valuable sources of bioactive compounds and structural biopolymers.[94] Blackcurrant pomace, a major product after juice processing, which particularly consists of ACNs, pectin, and cellulose, presents a significant opportunity for value-added applications in sustainable material development. The demand for biodegradable and functional packaging materials is growing, led to an upsurge in research focused on converting such biomass into active films with tailored properties.[95–97]

Current research on blackcurrant pomace has largely focused on the separation of natural colorants (ACNs) or directly using pomace powder as an ACNs source in combination with various biopolymers to develop biobased packaging.[95–99] However, the residual biomass remaining after extraction is overlooked, although it is potentially converted into value-added products. Moreover, conventional extraction method for biopolymers such as pectin and cellulose typically involve harsh chemicals, which can pose environmental and sustainability concerns.[53]

Microwave hydrothermal extraction has been reported as an environmentally friendly and efficient method for the isolation of pectin and defibrillated cellulose from various biomass sources.[59,60,100] Compared to conventional techniques, it offers better energy efficiency, shorter processing times, and reduced chemical usage. In addition to its effectiveness for biopolymer recovery, microwave-assisted extraction has also shown

promising results in enhancing the extraction of bioactive compounds, including phenolics and ACNs, due to improved cell wall disruption and solvent penetration.[84,101]

ACN, pH-responsive pigments, have been widely studied for their application in pH-sensitive intelligent films, offering added antioxidant and antibacterial benefit.[95,96,102] Incorporating ACN into films can lead to a colour change at different pH levels, making them effective indicators for monitoring food spoilage, such as in fish, shrimp, pork, and beef.[95,96,102] Additionally, combining ACN extracts with other biopolymers, such as starch, agar and cellulose, is both biodegradable and safe for handling and applicable in the food industry.[95–97]

Several techniques, including biopolymer blending,[95,103] crosslinking,[103,104] and reinforcement adding,[71,105] have been proposed for improving film properties. For instance, Gohil *et al*. and Nešić *et al*. introduced the synergistic effect of NaAlg-pectin blending under calcium chloride or zinc chloride crosslink, where the carboxyl groups of NaAlg and pectin interact with calcium ions or zinc ions, creating the "Egg box" model. The unique physical crosslink of the amorphous molecular structure of the "Egg box" resembles the structure of the synthetic semicrystalline polymers, called "Fringed-Micellar", resulting in improved mechanical properties.[103,106] Rezvanian *et* al. further investigated the optimal condition of crosslinking for NaAlg-Pectin hydrogel film, in which 0.5% calcium chloride positively affected mechanical properties.[107] Moreover, Lei *et al*. introduced cellulose nanocrystals as a reinforcement agent to NaAlg-pectin smart films incorporated with extracted red cabbage ACN. The optimally prepared film demonstrated a pH-indicator film that can be used for shrimp freshness monitoring with less water solubility and enhanced strength.[108]

In this study, blackcurrant pomace will be explored as a single source of pH-responsive ACN, pectin as a biopolymer and, DFC as a filler/reinforcement agent in the production of pH-sensitive sodium alginate films. Importantly, all three components will be simultaneously extracted using MHT, demonstrating a more environmentally friendly and energy-efficient alternative to conventional extraction methods.

ii. Feedstock 2: Extruded ginger pomace

Ginger (*Zingiber officinale*) is a flowering plant native to Southeast Asia whose root is commonly used as a spice or flavouring in foods, fragrances as well as in traditional and modern medicine due to its distinctive pharmacological and nutritional values.[109,110] Ginger extracts are rich in high-value oleoresins, which exhibit unique antioxidant, antimicrobial, anti-inflammatory and anticoagulant properties.[111] Thus, the global popularity of ginger

and its extract is increasing. According to the Food and Agriculture Organization of the United Nations (FAOSTAT), global ginger production reached 4.9 million tonnes in 2023, with Asia accounting for 79% of total cultivation.[40] In the same year, imports of ginger into the European market exceeded 168,000 tonnes, with expected to grow further due to the widespread use of ginger in the food and beverage industry (see **Figure 1.21**) and its recognised health benefits.[112]

Figure 1.21. Ginger and examples of ginger-derived products available in the UK on Amazon (https://www.amazon.co.uk/) based on the keyword "ginger product"

As ginger is rich in oleoresins and widely used as a spice in culinary applications, there has been a corresponding rise in the ginger oleoresin industry. However, ginger high-value oils, containing oleoresin represent only 4-10wt.%, meaning that large volumes of spent ginger biomass are generated as by-products of extraction.[74,113] Traditionally, ginger waste, including stalks and leaves, is directly sent to landfills, incinerated and/or used as low-value animal feed (ginger waste meal).[113,114] Due to the adverse environmental effects of producing such a large volume of ginger waste, including, but not limited to, decomposition to greenhouse gases, there is a strong incentive to find alternatives to disposal.

Currently, the re-utilisation of spent ginger waste for high-value chemicals, materials and bioenergy beyond simple biomass burning or composting, is limited but now beginning to increase (see **Figure 1.22**). Due to some of the unique compounds present in ginger oils, ginger waste also represents an excellent opportunity for valorisation.

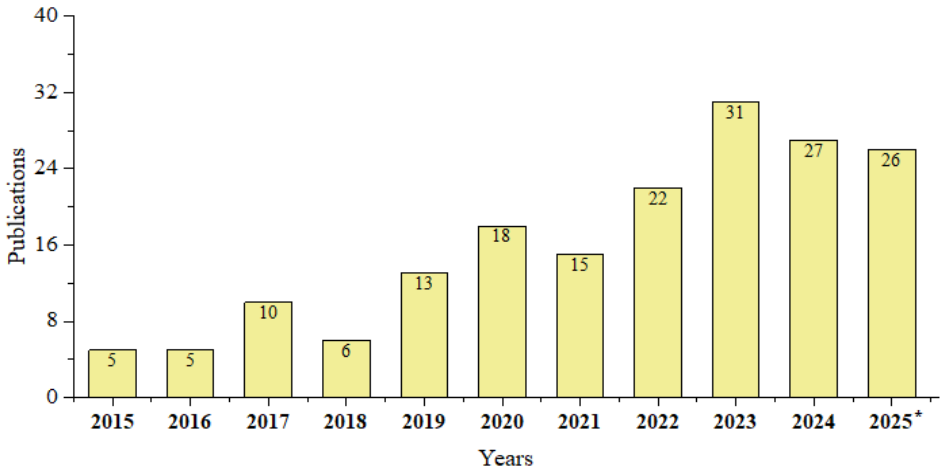

Figure 1.22. Number of papers published annually in the Web of Science (https://www.webofscience.com/) based on the keyword "ginger waste" between 2015-2025.

1.4.2. Aim II (A2): Valorisation of extruded ginger pomace

As consumer behaviour continues to shift towards a healthier lifestyle, there is a growing reduction in the consumption of processed foods, preservatives, and artificial additives.[112] Ginger fits well into this trend, as it is widely recognised as a functional food, a natural ingredient, and a traditional remedy. This is demonstrated by the increasing availability of ginger shots in mainstream supermarkets across European countries.[112] Therefore, the aim of this section is to explore the valorisation of ginger pomace, generated as a by-product of juice production, into biochemicals and biomaterials with the framework of zero waste biorefinery development (see **Figure 1.23**).

Ginger pomace will first be subjected to supercritical carbon dioxide ($scCO_2$) extraction for the recovery of ginger oil. The resulting oil-free residue will then undergo double microwave-assisted hydrothermal treatment (MHT) to investigate the characteristics and properties of defibrillated cellulose (DFC). In addition, given that ginger is a starch-rich plant, starch and protein hydrolysates will also be recovered as valuable by-products.

Objective A2 (i): *Characterisation of extruded ginger pomace*

Ginger waste can vary in composition depending on its source and processing method. In an industrial context, ginger peel, stems, and leaves may also be classified as 'ginger waste'. Stems and leaves, which are generated as residues after harvesting, have little or no commercial value; however, they do contain proteins and polysaccharides such as sugars, starch, cellulose, hemicellulose, and lignin.[115–117] **Table 1.3** provides an example

of the composition of ginger wastes produced both at the farm gate (stems and leaves) and during secondary processing, such as oleoresin extraction.[113,117]

To better understand the composition of ginger pomace, our study's waste raw material, generated from juice processing prior to further valorisation, characterisation methods including moisture and ash content analysis, Klason lignin analysis, CHN, ATR-IR, TGA, and pXRD will be applied (see **Figure 1.23**). These techniques will provide a comprehensive profile of the physicochemical properties of ginger pomace.

Table 1.3. Type and composition (%) of ginger waste

Compositions (%)	**Spent ginger[113]**	**Ginger stem[117]**
Ash	9.37 – 10.32	-
Protein	11.74 – 13.02	-
Starch	47.23 – 50.79	-
Pectin	1.63 – 2.09	-
Cellulose	3.84 – 4.32	48.48
Sugar	4.14 – 4.52	-
Hemicellulose	-	31.50
Lignin	-	18.30

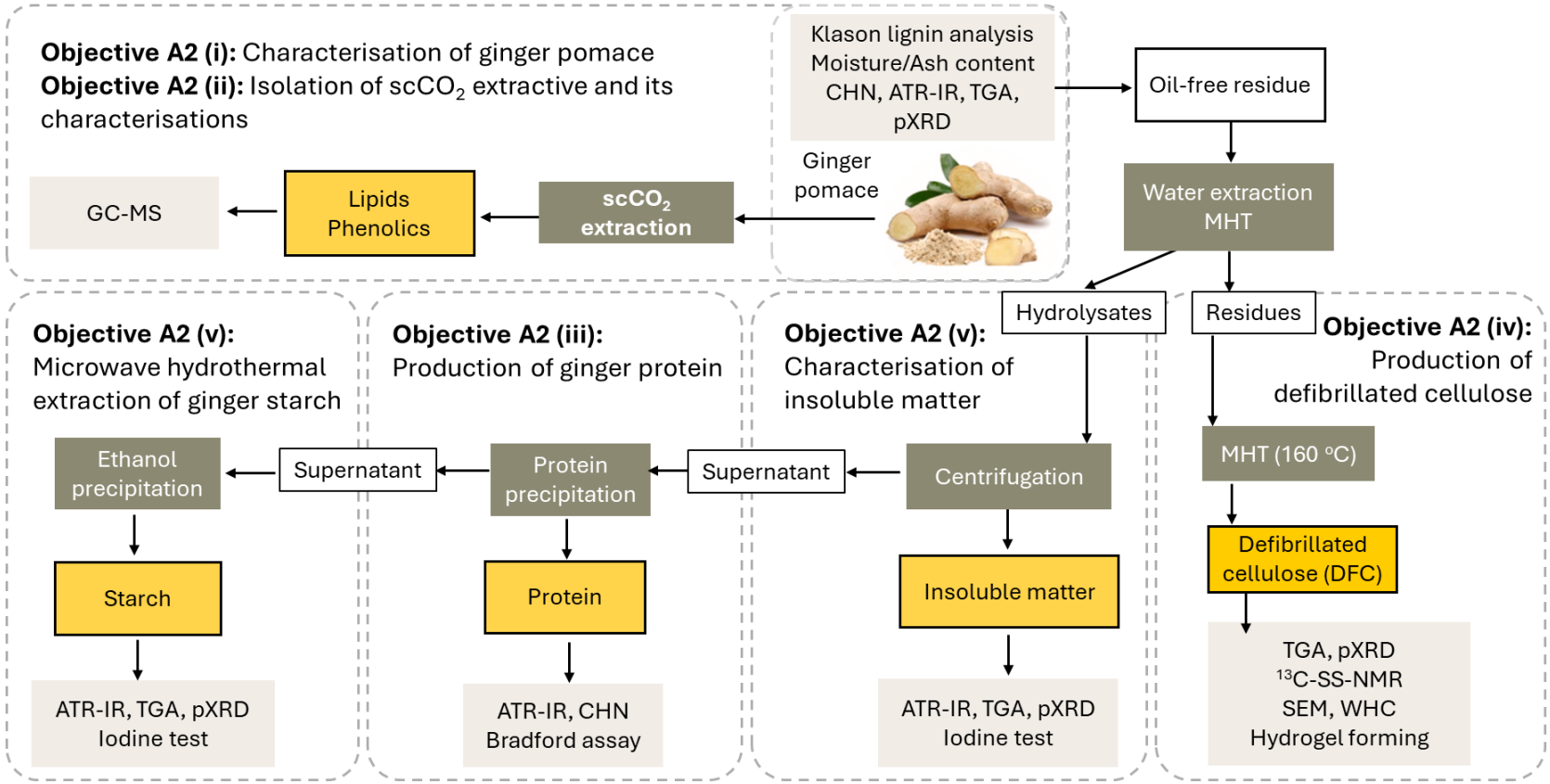

Figure 1.23. Process diagram illustrating the overall aims of extruded ginger pomace valorisation.

Objective A2 (ii): *Isolation of $scCO_2$ extractive and its characterisations*

Historical and/or traditional extraction technologies for the extraction of essential oils have been reliant on cold pressing or the use of hot solvents such as water (steam distillation), ethanol and hexane (either reflux or Soxhlet). The latter are energy-intensive processes and, in the case of hexane, under regulatory watch as it is a suspected reprotoxic chemical. Thus, there is a significant interest in finding effective green extraction methods for ginger oil, such as $scCO_2$, subcritical water extraction (SWE), MAE, and UAE. **Table 1.4** summarises a variety of green extraction methods for ginger waste and their resultant extractives.

Carbon dioxide (CO_2) is widely used in industry as a green solvent because it leaves no residual trace solvent in the products or post-extraction residues, has high diffusivity and solvation capacity, and can be recycled and is food grade approved, notably already in use in the industry for decaffeination of coffee.[118,119] CO_2 typically enters a supercritical phase at temperature and pressure exceed 31°C and 72.79 atm (7.38 MPa), exhibiting both gas-like and liquid-like properties (**Figure 1.24**).[119] As a non-polar solvent, its solvating power can be tuned by adjusting temperature and pressure, thereby enhancing extraction selectivity for target compounds. In addition, particle size of raw materials, solvent flow rate, and the presence of a co-solvent play significant roles in determining overall extraction efficiency.[119] Increasing pressure raises the density of CO_2, improving its solvating capacity and extraction yield; however, excessive pressure also increases operational costs.[120] On the other hand, increasing temperature decreases CO_2 density, but increase solute vapour pressure and diffusion rates.[121] Reducing particle size of raw material increases surface area, enhancing mass transfer and facilitating faster solute release into the solvent. Similarly, increasing solvent flow rate ensures sufficient contact between CO_2 and material, improving extraction efficiency.[119] Moreover, the use of co-solvents (e.g., polar solvents such as ethanol) increases polarity such that more polar compounds can be extracted.[74,122]

Table 1.4. Summary of green extraction technologies for ginger oil recovery

Feedstock	Extraction techniques	Solvent	Essential oil yield	References
Spent ginger waste	Soxhlet scCO$_2$	Heptane CO$_2$ CO$_2$ – Ethanol	4 %w [a] 2.51 %w [a] 4.12 %w [a]	[74]
Ginger pulp	Subcritical water	Water	0.50 mg/g [b]	[123]
Ginger rhizome peel	Subcritical water	Water	1.06 mg/g [b]	
Fresh ginger rhizome	Solvent-free MAE	-	1.12 %w	[124]
	Microwave-assisted hydrodistillation	Water	1.71 %w	[125]
	MAE	1-decyl-3-methy-limidazolium bromide	0.72%w	[126]
Dried ginger	UAE	Water–Ethanol	27.53 mg/g [b], 3.05 %w	[127,128]
		Ethanol	213.58 mg/g extract [b]	[129]
	MAE	Water	0.51%w	[130]
	Microwave steam diffusion	Water	0.57%w	
	Microwave-Ultrasonic steam diffusion	Water	0.95%w	
	Microwave-assisted hydrodistillation	Water	1.85 %w	[131]
	Low-temperature continuous phase transition	-	4.90 %w	[132]
	Subcritical propane	Propane	2.06%w	[122]
	scCO$_2$	CO$_2$	1.54%w, 413.45 mg/g extract [b]	[122,129]
		CO$_2$ – Ethanol	6.06%w	[122]
Ginger powder after scCO$_2$ extraction	scCO$_2$	CO$_2$ – Ethanol	6.42%w	
Ginger powder after scCO$_2$ - EtOH extraction	scCO$_2$	CO$_2$ – Ethanol	3.20%w	
Red ginger rhizome pulp	Enzymatic extraction	Isolated cow rumen enzymes	26.28% [c]	[133]

[a] Percentage of each component is calculated as peak area of analyte divided by peak area of total ion chromatogram times 100, [b] The highest yield of 6-gingerol and 6-shogaol, [c] The highest yield of zingiberene.

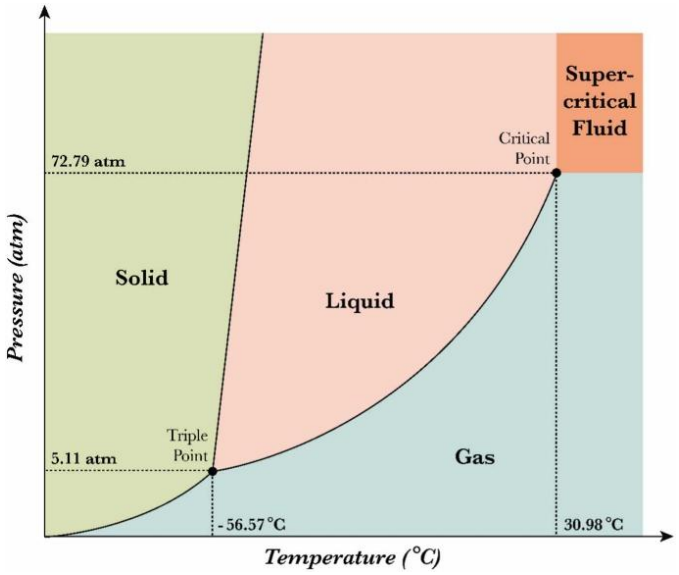

Figure 1.24. Phase diagram of carbon dioxide (CO_2).[119]

Gao *et al*. recently compared the conventional Soxhlet extraction of spent industrial ginger waste using hot heptane (Soxhlet) with respect to $scCO_2$ and $scCO_2$-EtOH as a greener methodology. Heptane was used in preference to hexane due to its reprotoxic concerns but also because the polarity of carbon dioxide mimics that of heptane. Interestingly, the yield of ginger oil from Soxhlet extraction and $scCO_2$-EtOH extraction were similar (approximately 4 %w), but the $scCO_2$ and $scCO_2$-EtOH techniques extracted more compounds beyond zingiberene, gingerols, shogaols, α-curcumene, β-bisabolene and β-sesquiphellandrene (see **Figure 1.25**). The high diffusivity and solvation power of $scCO_2$ and $scCO_2$-EtOH compared to hot heptane extraction enabled a richer fraction of products to be isolated.[74]

Spyrou *et al*. investigated the use of subcritical propane, $scCO_2$ and $scCO_2$-EtOH for ginger essential oil extraction. The results supported that $scCO_2$ with ethanol as co-solvent achieved the highest essential oil yield (6.06 %w) from dried ginger among all green extraction methods evaluated (see **Table G1**). The essential oil obtained from $scCO_2$ and $scCO_2$-EtOH exhibited similar chemical profile, containing the major compounds typically found in ginger, namely zingiberene, zingerone, gingerols, α-curcumene, β-bisabolene and β-sesquiphellandrene (see **Figure 1.25**); however, less variety of compounds were observed compared to subcritical propane's extract.[122] Additionally, primary and secondary repeat extractions of the residual ginger with $scCO_2$-EtOH demonstrate the potential for circular economy approaches, yielding up to 6.42 wt.% recovery of essential oil.[122]

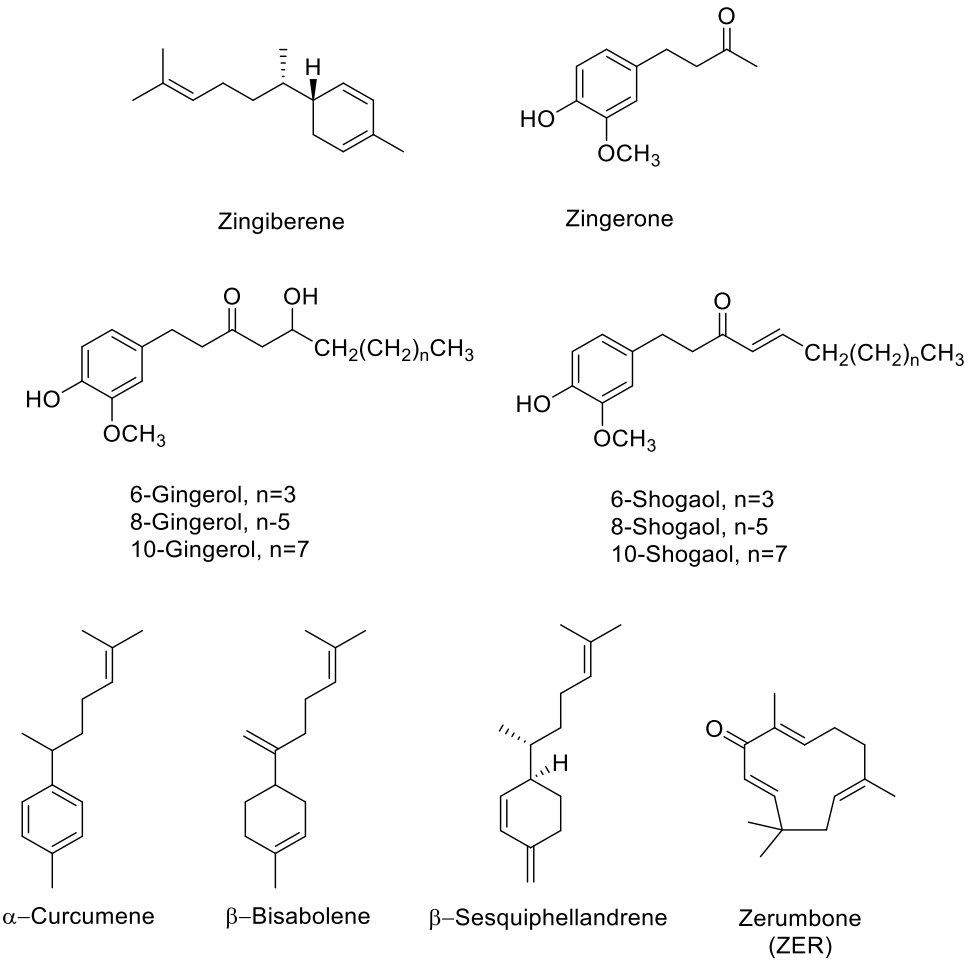

Figure 1.25. Exemplar chemicals found in essential oils and oleoresins from ginger

To minimise the use of organic solvents, $scCO_2$ extraction as a proven green extraction method, will be used to recover the essential oil/lipid from ginger pomace under a single condition, operating with 10% ethanol co-solvent at 35°C and 350 bar, prior to fractionation of the ginger pomace. The extracts will be primarily characterised using gas chromatography-mass spectrometry (GC-MS).

Objective A2 (iii): *Production of microwave-assisted hydrothermal protein*

Plant-based proteins have recently gained increasing attention in human diet as an alternative substitute for animal proteins. Plant-based proteins offer more sustainable options, unlike animal proteins, which are costly, have available limitation, and have a relation to climate change, biodiversity loss, freshwater depletion, and various human health issues.[134]

Ginger is well-known for its bioactive compounds and widely used in cooking; however, research on ginger protein remains limited. In 1973, ginger protein was first reported to possess proteolytic activity and was identified as a protease called

"Zingibain".[135] Zingibain has been studied for its roles in meat tenderisation, milk clotting, and its strong ability to hydrolyse collagen and cysteine-containing proteins.[135–139] Importantly, Zingibain has shown potential as a substitute for rennin, an essential enzyme traditionally derived from ruminants for cheese production, thereby offering promising applications in the dairy industry.[136–138] Moreover, ginger extract, which contains Zingibain, has demonstrated superior effectiveness in enhancing the colour, texture, and sensory attributes of meat compared with other plant-derived proteases such as papain, ficin, bromelain, and kiwifruit protease. This highlights its potential for improving meat quality in both household and industrial settings.[139] Beyond its enzymatic activity, ginger protein has also been reported to exhibit antifungal properties,[140] and ability to improve growth performance, immunity, gut health, and nutrient digestibility in Japanese quails and broiler chickens.[141–143]

Conventional protein extraction from plants sometimes provides low extraction yield. The non-conventional cell disruptive methods such as EAE, MAE, UAE, high pressure-assisted extraction (HPE), PFE, and homogenisation have been explored as alternatives to improve both protein yield and nutritional quality.[134,144] MAE offers a cost-effective and efficient for protein and carbohydrate extraction. This technique is recognised as a green and environmentally friendly method that disrupts cell walls using low energy input, shorten processing times, and requires no hazardous chemicals. Microwaves selectively interact with polar molecules, generating intracellular heating. The resulting heat and pressure buildup within the cells leads to cell wall rupture, thereby facilitating and enhancing the release of intracellular proteins and carbohydrates.[74,145] Therefore, MAE has been employed to improve the efficiency of protein and carbohydrate extraction from various agro-industrial food wastes, including spent ginger, brewer's spent grain, spent coffee grounds, and kale stems.[74,145]

In this study, ginger protein will be isolated from the hydrolysates obtained from conventional water extraction and MHT at different extraction temperatures (see **Table 1.5** and **Figure 1.23**). The isolated fractions will be characterised by ATR-IR and CHN analysis, while protein content will be quantified using the Bradford colorimetric assay.

Objective A2 (iv): *Production of defibrillated cellulose from extruded ginger pomace*

Cellulose, a biomaterial, contains both crystalline and amorphous regions dependent upon the packing arrangement of individual strands, which are held together *via* extensive intra- and inter-molecular hydrogen bonding rendering it insoluble in cold

water. Cellulose in this form is often regarded as passive, but through chemical and physical manipulation, the structure of cellulose can be altered, making it an active material (defibrillated and nanocelluloses) with functional properties.[146–148] Currently, there is a significant interest in producing nanocelluloses from ginger and ginger wastes for applications in high strength materials, packaging, and pharmaceuticals.[149–154] Defibrillation of celluloses and production of nanocelluloses from ginger waste are commonly carried out using conventional treatments, including alkalisation, bleaching, and acid hydrolysis, which require harsh chemical conditions, generating considerable amounts of acidic and basic aqueous waste streams.[117,154–157] However, this is an essential niche of research to consider green alternative methods, given the emerging importance of nanocellulose as a biomaterial and environmental concerns.

Interestingly, Gao *et al*. reported on the successful production of porous microfibrillated cellulose (MFC) in the absence of any harsh chemical or extensive mechanical processing. They used acid-free hydrothermal microwave processing (120-200 °C, 30 min) to afford MFCs. The MFCs yield decreased from 21.6% to 7.8% when the extraction temperature was increased. Conversely, the crystallinity index of the MFCs increased by up to 20% due to the leaching of amorphous cellulose and degradation of hemicellulose with increasing the processing temperature. The resultant materials were able to form hydrogels and thus can foresee applications as rheology modifiers.[74]

In this work, to explore the influence of low-to-moderate MHT temperatures on the simultaneous fractionation of defibrillated cellulose and temperature-sensitive compounds such as proteins will be investigated. Acid-free MHT at 60-120 °C will be applied to oil-free ginger residue. Meanwhile, conventional water extraction will be carried out as a control experiment. The ginger residue obtained at 60 °C will further be subject to a secondary acid-free MHT at 160 °C to produce defibrillated cellulose (see **Figure 1.23**). In addition, proteins and starch will subsequently be isolated from the hydrolysate by-products (see **objective A2 (iv)** and **objective A2 (v)**). The resulting defibrillated celluloses will be characterised using TGA, pXRD, solid-state ^{13}C CP/MAS NMR, and SEM. In addition, water holding capacity (WHC) and hydrogel-forming ability of ginger defibrillated celluloses will also be evaluated.

Objective A2 (v): *Characterisation of insoluble matter and soluble starch in hydrolysates*

Starch is a naturally occurring carbohydrate polymer widely utilised in food, pharmaceutical, and industrial applications due to its thickening, stabilising, and binding properties.[158] Among various sources of starch, ginger has attracted growing interest as an

alternative, owing to its unique physicochemical characteristics and potential functional benefits.[159,160] Ginger starch can be extracted primarily from the rhizomes through processes involving washing, peeling, grinding, sedimentation, and drying, which yield a fine powder suitable for further use.[161,162] Beyond its role as a food ingredient, ginger starch has found applications in food packaging films, and as a functional additive in food products, making it a versatile and valuable natural resource.[163–167]

Processing methods, such as cooking, freezing, and microwave processing significantly affect yield, structure and functional properties of starch.[168–171] Microwave processing has been reported to modify the crystalline and granular morphology of starch, for examples, converting potato starch from type B to type A.[172] In addition, it enhances functional properties of starch, including water and oil holding capacity, swelling capacity, emulsifying activity and stability. These changes make starch more suitable for applications as stable aqueous dispersion in food and biotechnology applications.[171–174]

Ginger starch is commonly isolated from fresh ginger; however, by-products such as spent ginger from oleoresin extraction and ginger pomace also represent important sources of starch and other biopolymers. Madeneni *et al*. investigated the physicochemical and functional properties of starch recovered from spent ginger using a sedimentation method. The isolated starch contained approximately 26% amylose, exhibited a high gelatinization temperature (88 °C), and showed 45% *in vitro* digestibility, corresponding to a low glycemic index (GI < 55). These characteristics suggest that spent ginger starch is suitable as a stabilising agent or food additive in high-temperature processing, such as ultra-high temperature (UHT) and sterilised products.[160] Recently, Gao *et al*. reported the recovery of starch from spent ginger hydrolysates derived after MHT (120-200°C), achieving yields of up to 48.6%. However, significant starch decomposition was observed at 200°C with only 1.95% yield of starch.[74]

In this part, to primarily investigate the change of ginger pomace starch characteristics of under conventional water extraction and low MHT temperatures, starch, including insoluble matter and soluble starch, will be isolated from the hydrolysates (see **Figure 1.23**). The recovered insoluble matters and soluble starch will be characterised using ATR-IR, TGA, and pXRD. Amylose content will also be evaluated through iodine test and blue value.

iii. Feedstock 3: Extruded aeroponically grown Coriander and Thai Basil roots

Coriander (*Coriandrum sativum*) and Thai basil (*Ocimum basilicum var. thyrsiflora*) are widely used spices in Asian cuisine. Apart from its culinary use, coriander and Thai basil also recognised as a medicinal plant.[175–177] They are rich in linalool, fatty acids, and bioactive phytochemicals such as terpene, gallic acid, thymol, and bornyl acetate.[175,176,178] These compounds are associated with diverse health benefits, including anticancer, neuroprotective, anti-inflammatory, cardioprotective, and migraine-relieving effects.[175] Thus, with its remarkable health-promoting properties and the growing global interest in healthy cuisine, the demand for coriander and Thai basil continues to rise. **Figure 1.26** reveals examples of coriander and Thai basil products, including essential oils and food ingredients available in the UK market.

In 2023, coriander production, combined with that of related spices such as anise, badian, cumin, caraway, fennel, and juniper berries, reached 2.8 million tonnes worldwide. These crops are cultivated extensively across Asia, followed by Americas, Africa, and Europe, requiring approximately 2.3 million hectares of production area annually.[40] Due to the climate change, the production and quality of leafy crops have been affected. To overcome this challenge, the controlled-environment cultivation systems, with precisely controllable lighting, climate, and enclosed growing space such as hydroponics, aeroponics, and vertical farming, have gained increasing attention.[175,179,180] These cultivation systems offer significant environmental benefits, particularly in terms of soil and water conservation.[179]

Figure 1.26. Coriander, Thai basil and examples of their products available in the UK on Amazon (https://www.amazon.co.uk/) based on the keyword "coriander product" and "Thai basil product"

Aeroponics is a modern, soilless, cultivation system in which plant roots are suspended in air and supplied with a fine mist of nutrient solution. This method enables efficient use of water and nutrients while ensuring optimal oxygen availability to the roots, offering great potential for enhancing resource efficiency and addressing global food

security challenges.[181,182] In addition, in comparison to hydroponic and peatmoss slab systems, aeroponics has been reported to provide the most nutrition uptake, highest growth rate, and most cost-efficiency with the production cost of approximately 2.93 Egyptian pound per kilogram (≈ 0.06 USD).[183] Recent studies have demonstrated that aeroponically grown leafy crops, including basil, exhibit enhanced growth performance, higher essential oil yield, and comparable phenolics content compared with conventionally cultivated plants,[183,184] highlighting the potential of aeroponic systems for producing high-quality basil and coriander under sustainable and controlled conditions.

1.4.3. Aim III (A3): Valorisation of aeroponic coriander and Thai basil root wastes

Coriander roots, which have a stronger flavour than the leaves, are commonly used in cooking and traditional medicine,[175] while Thai basil have very limited documented uses. Most studies have primarily focused on their aerial parts, particularly the leaves and seeds, for essential oil extraction, chemical composition analysis, and bioactivity evaluation.[175] Moreover, the roots are believed to contain valuable essential oils with potential bioactive properties. **Figure 1.27** presents recent research on coriander roots and Thai basil roots, particularly in relation to their cultivation systems; however, studies on the chemical composition of coriander and Thai basil roots remain limited.

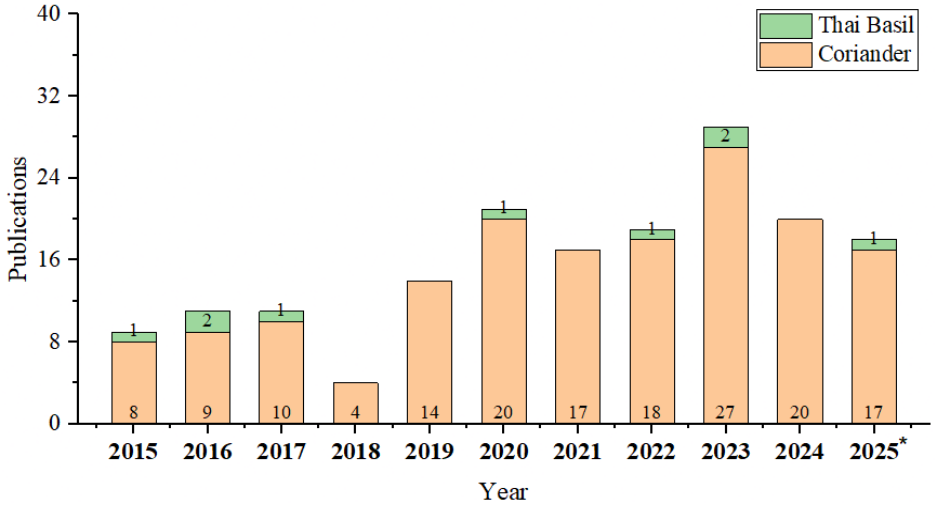

Figure 1.27. Number of papers published annually in the Web of Science (https://www.webofscience.com/) based on the keyword "Coriander root" and "Thai Basil root" between 2015-2025.

To the best of our knowledge, no research has yet investigated the chemical composition of aeroponically grown coriander and Thai basil roots. These roots are

typically discarded after aeroponic cultivation. Therefore, this study aims to valorise aeroponically grown roots of coriander and Thai basil into value-added biochemicals and biopolymers using green extraction technologies, including $scCO_2$ extraction and MHT, to demonstrate a sustainable and zero-waste approach (see **Figure 1.28**). Coriander and Thai basil roots will first be subjected to $scCO_2$ for lipids/essential oils extraction. The resulting oil-free residue will then undergo double MHT to investigate the characteristics and properties of defibrillated cellulose. In addition, protein will also be isolated from hydrolysates as valuable by-products.

Objective A3 (i): *Characterisation of extruded aeroponic coriander and Thai basil roots*

As mentioned earlier, different type of plant and plant parts vary in their chemical compositions. Aeroponically grown coriander and Thai basil roots, which are often regarded as lignocellulosic-rich wastes, represent a potential source of valuable biochemicals and biopolymers; however, their chemical compositions have not yet been investigated by any researchers. In this section, the compositional analysis of these roots, including moisture and ash content, Klason lignin content, carbohydrates content, and protein content will be evaluated using several analytical techniques such as CHN, ATR-IR, TGA, and pXRD.

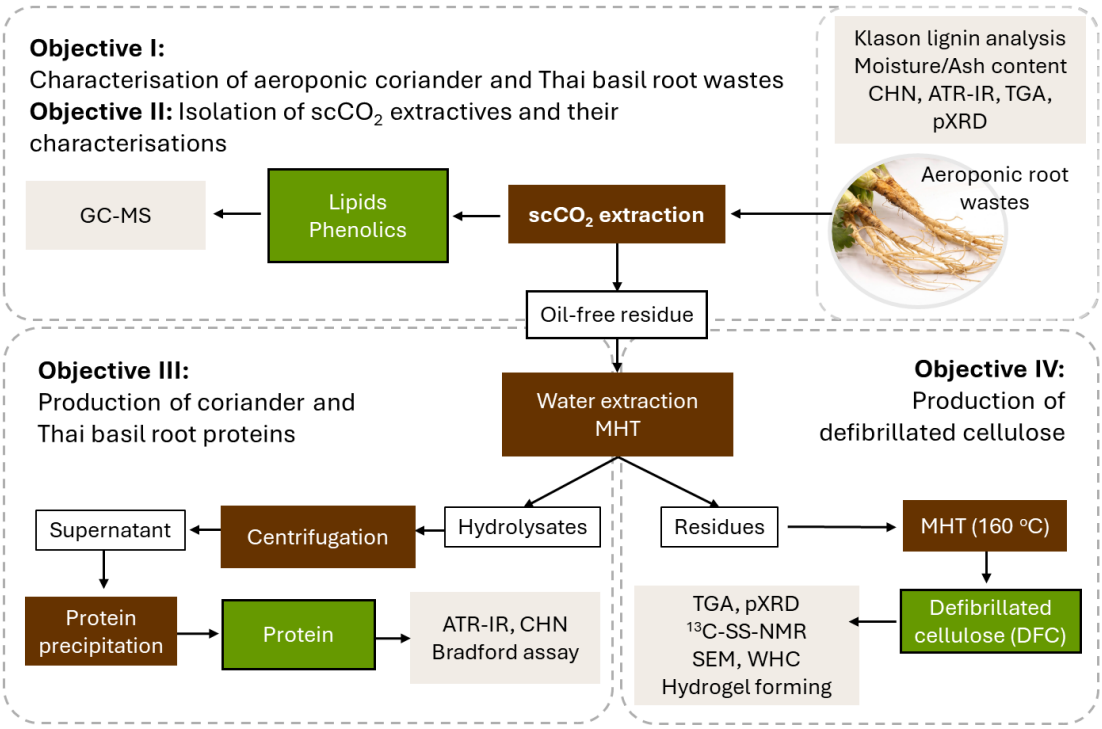

Figure 1.28. Process diagram illustrating the overall aims of extruded aeroponic coriander and Thai basil roots valorisation.

Objective A3 (ii): *Isolation of $scCO_2$ extractives and their characterisation*

Coriander essential oil has a long history of use in traditional medicine and is commonly derived from the seeds. It is a triglyceride oil containing unusual components such as petroselinic acid and linalool.[185] Essential oil can be isolated from various parts of the coriander plant, including the seeds, leaves, flowers, and roots; however, the chemical composition, particularly the fatty acid and bioactive compound profiles, differs significantly depending on the plant part used.[175,185,186] In addition, modern culinary trends have contributed to the worldwide spread of various herbs, such as Thai basil, a species native to South and Southeast Asia that has seen growing popularity in European markets.[176] This popularity is largely attributed to its unique aroma, resulting from its distinctive essential oil composition, containing estragole as a main compound, along with smaller amounts of other volatiles such as linalool and camphor.[176] **Table 1.6** summarises examples of chemical compositions of coriander and Thai basil essential oils.

The chemical composition of essential oils is significantly affected by the extraction methods. Hydrodistillation and steam distillation are conventional methods commonly used for essential oil extraction, typically carried out at high temperatures for long period.[187] However, the prolonged exposure to heat during hydrodistillation or steam distillation can lead to thermal degradation of chemical compounds, thereby reducing the overall yield of essential oils.[187] Thus, alternative methods such as microwave-assisted hydrodistillation, ultrasonic-assisted extraction, Soxhlet, subcritical water, and supercritical fluid extraction have been investigated to minimise thermal degradation and shorten extraction time.[175,187]

$scCO_2$ extraction is considered as a green and sustainable technique for essential oil extraction, offering several advantages including non-toxicity, the absence of solvent residues in the final product, chemical inactive, and non-flammability.[188] Among methods such as hydrodistillation, Soxhlet extraction, dynamic headspace, solvent extraction, and steam distillation, $scCO_2$ extraction has been reported to produce the highest coriander essential oil yield, up to 4.5% from coriander fruits, while minimising non-volatile contamination.[189] Furthermore, the chemical composition of coriander essential oil obtained *via* $scCO_2$ extraction can be influenced by parameters such as pressure, temperature, and flow rate.[188]

$scCO_2$ extraction combined with the addition of a polar co-solvent, such as ethanol or propanol, has been shown to enhance essential oil yield and improve the extraction efficiency of bioactive compounds from spices.[74,122,190] As mentioned earlier, there is a lack

of information regarding the chemical composition of essential oils and lipids derived from the roots of coriander and Thai basil, particularly those cultivated under aeroponic conditions. In this section, we aim to highlight the potential of using a green extraction technique, $scCO_2$ extraction with ethanol co-solvent, for the recovery of valuable essential oils from aeroponically grown plant residues, specifically the roots of coriander and Thai basil. This approach not only promotes the sustainable utilisation of agricultural by-products but also aligns with environmentally friendly extraction practices that minimise solvent use and thermal degradation of bioactive compounds. The chemical compositions of essential oils and lipids from aeroponically grown coriander and Thai basil will be analysed using GC-MS.

Table 1.5. Examples of chemical compounds in coriander and Thai basil essential oils.

Constituent	**Concentration (%)**				
	Coriander seeds [175,185,187,191]	Coriander leaf [175,185,187,192]	Coriander flower [175,185]	Coriander root[186]	Thai Basil [176,178]
Linalool [a]	58.0-80.3	0-13	-	-	0.2-0.3
Geranial [a]	0.5-3.0	-	-	-	19.1
Terpinene [a]	0.3-11.2	0.9-3.1	-	-	0.1-0.3
Pinene [a]	0.2-10.9	1.9-2.5	-	0.5-1.5	0.3-0.9
Thujene [a]	-	-	-	0.5-7.3	-
Cymene [a]	0.1-8.1	-	-	-	-
3-carene [a]	-	-	-	-	0.7-1.5
Ocimene [a]	-	-	-	-	0.6-1.4
Camphor [a]	3.0-5.1	-	-	0.1-0.4	0.1-0.4
Geranyl acetate [a]	0.2-10	-	-	-	-
Linalyl acetate [a]	0.1-9	-	-	0-0.6	-
Estragole [a]	-	-	-	-	47.7-94.4
Neral [a]	-	-	-	-	15.9
Decanal [a]	-	5.1-19.1	-	6.6-13.4	-
trans-2-decenal [a]	-	12.0-35.0	-	3.9-14.4	-
2-decen-1-ol [a]	-	12.3	-	0.5-0.9	-
Cyclodecane [a]	-	12.2	-	-	-
2-dodecenal [a]	-	10.7-14.0	-	30.8-38.3	-
Dodecanal [a]	-	4.1	-	1.3-4.8	-
Dodecan-1-ol [a]	-	3.1	-	-	-
Borneol [a]	-	-	-	3.1-6.4	-
Coumaran [a]	-	-	15.4	-	-
Methyl palmitate [a]	-	-	10.3	-	-

Eupatoriochromene A [a]	-	-	9.4	-	-
4-vinylguaiacol [a]	-	-	8.8	-	-
2,3,5,6-tetrafluroanisole [a]	-	-	8.6	-	-
2,6-dimethyl-3-aminobenzoquinone [a]	-	-	6.8	-	-
Fatty acid					
Dodecanoic acid (12:0) [a]	-	-	5.0	-	-
2-decenoic acid (10:1) [a]	-	30.8	-	-	-
Pentadecylic acid (15:0) [b]	-	-	-	1.1-4.2	-
Palmitic acid (16:0) [b]	5.3	12.5-14.9	-	18.2-26.1	-
Palmitoleic acid (16:1 c9) [b]	0.3	0.7-3	-	0.4-2.7	-
Heptadecanoic acid (17:1) [b]	-	13.4-16.1	-	-	-
Stearic acid (18:0) [b]	3.1	0.6-0.9	-	2.2-5.9	-
Petroselinic acid (18:1 c6)	68.5	-	-	-	-
Oleic acid (18:1 c9) [b]	7.6	2.5-8.7	-	17.2-26.6	-
Linoleic acid (18:2 c6) [b]	13.0	15.3-19.7	-	42.3-49.5	-
Linolenic acid (18:3 c3) [b]	-	37.4-43.2	-	0.3-5.5	-
Stearidonic acid (18:4 c3) [b]	-	2.3-7.7	-	0.4-0.7	-

[a] Constitution in essential oil, [b] Constitution in total fatty acids

Objective A3 (iii): *Production of coriander and Thai basil root proteins*

Coriander and basil are primarily cultivated for their fruits, which are widely used as spices and as sources of essential oils.[193,194] The essential oil extracted from coriander and basil seeds contain a high concentration of linalool (29.1-80%),[185,187,191,194] a bioactive compound known for its antiproliferative, antibacterial, antifungal, anticancer, and neuroprotective properties.[193] Although highly valuable, the yield of these essential oils is relatively low, typically 0.3-1.2% from coriander seeds and 1.5-3.2% from basil leaves.[193,195]

Apart from essential oils, both seeds contain other nutritionally valuable components. Coriander seeds consist of approximately 55% carbohydrates, 17.8-21.9% lipids, and 12.4-13.1% protein,[193,196] while basil seeds contain about 43.9% carbohydrates,

33% lipids, and 10% protein.[197] The protein content of coriander and basil seeds is comparable to that of several cereal grains, such as rice (8.5%), barley (9.2%), wheat (14%), and corn (14%).[198] Therefore, valorising these remaining fractions after essential oil extraction presents opportunities to develop value-added and sustainable products. Plant-derived proteins, in particular, offer a low-cost, eco-friendly source of nutrients that can enhance the nutritional quality of various food applications.[198] However, studies on coriander and basil proteins remain limited.

Rohr *et al*. examined the chemical composition and nutritive value of coriander seed oil meal, finding it is high protein content and suitable for inclusion in the diets of cows, sheep, and fallow deer.[199] Nazir *et al*. were among the first to isolate protein from basil seed meal, obtaining an extract with 89% protein content. They also examined its foaming and emulsifying properties, suggesting that basil protein could be a promising functional food ingredient.[198] Similarly, Aluko *et al*. investigated the functional properties of coriander protein, including its emulsifying and foaming capacities, in defatted flour and protein concentrate across a range of pH values. Their findings suggested that coriander protein could serve as a key ingredient in acidic food emulsions.[200]

More recently, Hojilla-Evangelista *et al*. extracted protein from coriander fruit, seed, and seed press cake using a combined process of steam distillation, dehulling, and screw pressing. Their study revealed that dehulling significantly increased the protein content of the extracts, whereas steam distillation affected protein yield but did not impair its foaming, emulsifying, or heat-coagulability properties. In addition, the coriander protein extracts exhibited amino acid compositions comparable to their starting materials and amino acid scores higher than those of their starting meals and soybean protein, highlighting their promising nutritional potential.[201]

MAE is a proven green extraction technology and an effective cell-disruptive technique that enhances protein recovery while minimising environmental impact. It has shown high extraction efficiency across a wide range of biological sources, including cereals, oilseeds, pulses, algae, and agro-industrial by-products.[145,202] The protein yield achieved through MAE depends on several factors, such as the origin of the raw material, microwave power, temperature, extraction time, and solid-to-liquid ratio.[202] With respect to temperature optimisation, relatively low temperatures (46-65 °C) are generally favourable for protein extraction, as excessive heat can lead to thermal denaturation, particularly soybeans and herbal roots.[145] MAE performed under alkaline conditions has been reported

to improve protein recovery from brewer's spent grain, spent coffee grounds, and kale stems;[145] however, alkaline conditions may also enhance protein denaturation, cross-linking, hydrolysis of peptide bonds, and amino acids degradation, which can negatively affect protein functionality and nutritional quality.[203]

Previous studies have primarily focused on the extraction of essential oils and proteins from the aerial parts of coriander and basil; however, research on their root components remains limited.[175,178,198,200,201] In this study, we aimed to fractionate and recover proteins from coriander and Thai basil root wastes generated from aeroponic cultivation using a chemical-free MAE method, and to compare the efficiency with conventional water extraction. The isolated root proteins will be characterised using ATR-IR, CHN, and Bradford assay.

Objective A3 (iv): *Microwave-assisted hydrothermal defibrillation of cellulose from extruded aeroponic coriander and Thai basil roots*.

Lignocellulosic plants such as coriander and Thai basil primarily consist of cellulose, hemicellulose, lignin, proteins, fats, and minerals.[175] Research on these plants has mainly focused on extracting high-value essential oils.[193–195] However, the post-extraction residues remain rich in cellulose, the most abundant biopolymer in these materials, which has received limited attention due to its relatively low economic value compared to essential oils. [193,196,197]

Defibrillated celluloses (DFC), including microcellulose and nanocellulose, have recently attracted interest due to their functional properties, such as high colloidal and thermal stability, mechanical strength, and biodegradability. These characteristics make cellulose a promising material for a wide range of industrial applications, for example, coatings, optically transparent films, aerogels, rheology modifiers, filtration membranes, packaging materials, and molecular scaffolds.[195] Conventionally, nanocellulose is isolated from cellulose-rich biomass through intensive chemical and mechanical treatment.[151–153] On the other hand, MHT is considered as a rapid and energy-efficient method, that enables DFC extraction under chemical-free conditions.[59–62] The application of microwave energy induces dielectric heating of intracellular water, generating internal pressure that disrupts cell walls.[145,202] In addition, the hydrothermal condition promotes hydrothermolysis of polysaccharides and the selective removal of hemicellulose, pectins, and amorphous cellulose, resulting in cellulose fibres with enhanced crystallinity.[59–62] This approach has

been successfully demonstrated with diverse biomass sources, including orange peel,[59] cassava and almond peel,[62] and spent pea residue.[60]

Previous studies on MHT extraction of biomass have shown that optimal pectin isolation occurs at approximately 140 °C, while significant cellulose degradation typically begins above 190 °C, leading to the formation of humins, chars, and pseudo-lignins.[59–62] Therefore, maintaining the microwave temperature below 160 °C effectively minimises cellulose degradation while facilitating extensive hemicellulose removal, ultimately yielding defibrillated cellulose with higher purity and crystallinity.

In this part, DFC will be isolated from extruded aeroponically grown coriander and Thai basil roots using MHT at 160 °C. Prior to MHT, essential oils and protein fractions will be sequentially extracted via $scCO_2$ extraction and MAE at 60 °C, respectively. The resulting DFC will be characterised by TGA, pXRD, solid-state ^{13}C CP/MAS NMR, and SEM. In addition, the WHC and hydrogel-forming ability of the isolated DFCs will also be evaluated to assess their functional performance.

Chapter 2: Experimental

2.1. Chemicals

All chemicals were purchased from Sigma-Aldrich, Alfa, and/or Fisher chemicals and were utilised without any additional purification. Solvents used in this work were analytical or HPLC grade. Deionised water was used from an in-house building tap.

2.2. Blackcurrant pomace

Blackcurrant (*Ribes nigrum*) pomace (**BC**), an industrial derived product, was provided by Lucozade Ribena Suntory Ltd., UK. The as-received BC, consisting of skin, seeds, and stems, was dried (ambient condition, 7 days), milled using a coffee grinder, sieved (a stainless-steel mesh, ≤ 2 mm) and stored in air-tight bags prior to use. The ready-to-use BC is showed in **Figure 2.1**.

2.3. Extruded ginger pomace, aeroponically grown coriander and Thai basil roots

Organic fresh ginger (*Zingiber officinale*) rhizome was sourced by Real Foods retailer, UK, whereas aeroponically grown microgreen coriander (*Coriandrum sativum*) and Thai basil (*Ocimum basilicum var. thyrsiflora*) roots were supplied by Grow it York, an aeroponic vertical farm in the UK. The fresh ginger rhizome, containing rhizome, roots, and skin, coriander or Thai basil roots was extruded through a twin-screw press juicer (Angelia 7500 Series). Thereafter, the extruded ginger pomace (**GP**), coriander roots (**CR**), and Thai basil roots (**ThB**) obtained after juice processing, were air-dried (ambient condition, 7 days), milled using a Retsch Knife Mill (Grindomix GM300), and sieved through a stainless-steel mesh (≤ 250 µm). The appearance of GP, CR and ThB is presented in **Figure 2.1**.

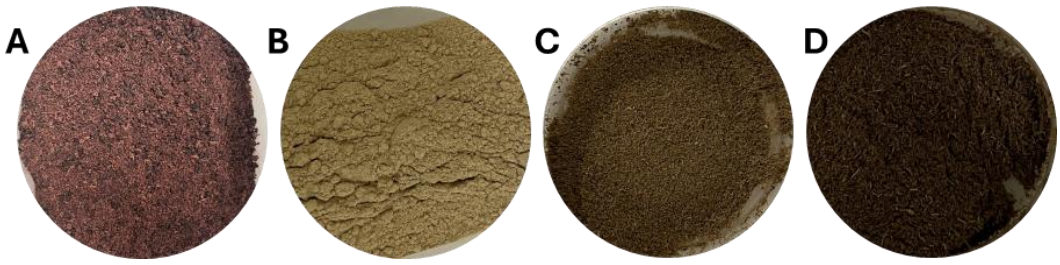

*Figure 2.1. Raw materials: blackcurrant pomace, BC (**A**), extruded ginger pomace, GP (**B**), extruded aeroponic coriander roots, CR (**C**), extruded aeroponic Thai basil roots, ThB (**D**)*

2.4. Compositional analysis of biomass and biomass-derived products

2.4.1. Moisture and ash content

Moisture and ash content analysis were determined based on the standard NREL method. [204,205] Biomass samples (1 g, W), including BC, GP, CR, and ThB, were placed into pre-dry crucibles (W_C) and put into an oven (105 °C, overnight). The dried samples within crucibles were cooled down in a desiccator and the weight were recorded (W_{C1}). Thereafter, the dried samples in crucibles (W_{C1}) were then put into a muffle furnace under an air atmosphere (575 °C, 6 h). The crucibles were cooled down in a desiccator and recorded the weight (W_{C2}). The moisture and ash content were calculated using the following equation:

$$Moisture\ content\ (\%) = \frac{W-(W_{C1}-W_C)}{W} \times 100 \qquad \textit{(Equation 2.1)}$$

$$Ash\ content\ (\%) = \frac{W_{C2}-W_C}{W} \times 100 \qquad \textit{(Equation 2.2)}$$

2.4.2. Klason lignin and carbohydrate analysis

Klason lignin and carbohydrate analysis were determined based on the standard NREL method with little modification.[206] Biomass, pectin or DFC samples (100 mg, W) were mixed with 72% H_2SO_4 (1 mL) and subjected to shaking in a water bath (40 °C, 2 h). Thereafter, the mixtures were supplemented with deionised water (28 mL) to make a final concentration of 4% H_2SO_4 and then autoclaved (121 °C, 1 h). The resulting hydrolysed sample was filtered through a vacuum filter crucible (W_0). The resulting liquid was then subjected to carbohydrate analysis using HPLC-RID (see **Section 2.7.4.2**).

Following this, the solid residues were rinsed with distilled water and subsequently dried in an oven (105 °C, overnight). After cooling within a desiccator, the weight of the crucible containing the solid residue was recorded (W_1). The calculation of lignin content was performed using the following equation:

$$Klason\ lignin\ (\%) = \frac{W_1-W_0}{W} \times 100 \qquad \textit{(Equation 2.3)}$$

2.5. Extraction and defibrillation methodologies

2.5.1. Conventional solvent extraction (heptane, ethanol, and ethanol-water)

Conventional solvent extraction was performed with BC to extract bioactive compounds such as phenolics. BC (40 g) and solvent (heptane, ethanol, or 1:1 Ethanol-Water, 200 mL) were heated (reflux, 2 h). Thereafter, the heptane or ethanol mixture was vacuum filtered through a Buchner funnel, whilst the 1:1 ethanol-water mixture was filtrated through a stainless-steel mesh and centrifuged (3500 rpm, 10 min) to separate the fine residue out. The heptane or ethanol filtrate was evaporated to dryness using a rotary evaporator and vacuum dry, whilst the 1:1 ethanol-water filtrate was evaporated and freeze dried to dryness. Further purification was performed on the ethanol extract, in which ethyl acetate (50 mL) was added, stirred (room temperature, 1 h), and filtered through a filter paper (gravity) to separate the extract into ethanol-ethyl acetate soluble and ethanol-ethyl acetate insoluble. BC solvent extracts were named as shown in **Table 2.1**.

2.5.2. Supercritical carbon dioxide extraction ($scCO_2$)

$scCO_2$ was used to extract lipids and essential oils from GR, CR, and ThB. The $scCO_2$ extraction with 10% ethanol as a co-solvent was performed using a laboratory-scale $scCO_2$ extraction system (SciMed, Stockport, UK), following the method described by Gao *et al*.[74] Biomass samples (100 g) were loaded into the Soxhlet thimbles, and the tops of the thimbles were covered with cotton wool before being placed into the extraction vessel. CO_2 and ethanol co-solvent were pressurised into the extractor (350 bar, 35 °C, 2 h). Flow rate of CO_2 and ethanol were set at 15 and 1.5 g/min, respectively, to ensure a 10% co-solvent ratio. The $scCO_2$ extracts were named as in the following in **Table 2.2**.

2.5.3. Conventional water extraction

Conventional water extraction was carried out as a control experiment for pectin extraction from BC. BC (40 g) was heated in deionised water (200 mL) and stirred under reflux for 2 h. Conventional water extraction was also conducted as a control experiment for protein and starch extraction from $scCO_2$ extracted GP, and for protein extraction from $scCO_2$ extracted CR and ThB. GP, CR, or ThB (10 g) was stirred in deionised water (150 mL, 50 °C, 2 h). The hydrolysates derived from the extraction were subjected to protein or carbohydrate precipitation (see **Section 2.5**), while solid residues were washed with hot water, hot ethanol, room temperature ethanol, and acetone. The washed residues were

then air-dried under a fume hood for 2 days and stored for further defibrillated cellulose (DFC) extraction (see **Section 2.4.6**).

2.5.4. Conventional acid extraction

Conventional acid extraction was conducted for pectin extraction from BC. BC (40 g) and acid solutions (200 mL: 0.2M HCl or 0.2-0.8M citric acid) were performed (80 °C, 2 h). Thereafter, hydrolysates were retained for pectin precipitation (see **Section 2.5.1**), whilst solid residues were washed, as described in **Section 2.4.3**, and kept aside for DFC extraction (see **Section 2.4.6**).

2.5.5. Microwave-assisted (MAE) and hydrothermal extraction (MHT)

Acid-free microwave hydrothermal extraction (MHT) was conducted for pectin extraction from BC. BC (20 g) was mixed with deionised water (300 mL) and placed into a 750-mL PTFE microwave vessel. The mixture was performed using a Milestone Synthwave Microwave at temperatures ranging from 100°C to 160°C, with a 15 min ramping time, 15 min holding time, 10 bar nitrogen pressure, and 60% stirring.

Acid-free microwave-assisted extraction (MAE) and MHT were also applied for protein and starch extraction from $scCO_2$ extracted GP, and for protein extraction from $scCO_2$ extracted CR and ThB. The $scCO_2$ extracted GP, CR, or ThB (10 g) was mixed with deionised water (350 mL) and placed into a 750-mL PTFE microwave vessel. The mixture was processed using the Milestone Synthwave Microwave using 15 min ramping time, 15 min holding time, 10 bar nitrogen and 60% stirring, with the microwave temperatures of 60°C to 120°C for GP, and 80 °C for CR and ThB.

Thereafter, the BC hydrolysates were collected for pectin precipitation (see **Section 2.5.1**), GP hydrolysates for protein and starch isolation (see **Section 2.5.2** and **2.5.3**), and CR and ThB hydrolysates for protein isolation (see **Section 2.5.2**). On the other hand, the remaining solid residues were washed, as described in **Section 2.4.3**, and set aside for DFC extraction (see **Section 2.4.6**).

Table 2.1. Summary of blackcurrant pomace (BC) extract sample names and conditions.

Extraction condition	**Sample name**				
	Solvent extract	**Pectin (BCP)**	**Hydrolysate (BCH)**	**DFC***	**Bleached DFC****
Solvent extraction					
Heptane (reflux, 2 h)	BCHt	-	-	-	-
Ethanol (reflux, 2 h)	BCEt	-	-	-	-
1:1 Ethanol-Water (reflux, 2 h)	ETW	-	-	-	-
Ethanol (reflux, 2 h) – ethyl acetate (soluble fraction)	BCEt-F1	-	-	-	-
Ethanol (reflux, 2 h) – ethyl acetate (insoluble fraction)	BCEt-F2	-	-	-	-
Conventional extraction					
Water (reflux, 2 h)	-	BCP-W	BCH-W	DFC-W	BDFC-W
HCl (0.2M, 80 °C, 2 h)	-	BCP-H	BCH-H	DFC-H	BDFC-H
Citric acid (0.2M, 80 °C, 2 h)	-	BCP-C1	BCH-C1	DFC-C1	BDFC-C1
Citric acid (0.4M, 80 °C, 2 h)	-	BCP-C2	BCH-C2	DFC-C2	BDFC-C2
Citric acid (0.6M, 80 °C, 2 h)	-	BCP-C3	BCH-C3	DFC-C3	BDFC-C3
Citric acid (0.8M, 80 °C, 2 h)	-	BCP-C4	BCH-C4	DFC-C4	BDFC-C4
Microwave hydrothermal extraction (MHT)					
MHT (100 °C, 15 min)	-	BCP-M1	BCH-M1	DFC-M1	BDFC-M1
MHT (120 °C, 15 min)	-	BCP-M2	BCH-M2	DFC-M2	BDFC-M2
MHT (140 °C, 15 min)	-	BCP-M3	BCH-M3	DFC-M3	BDFC-M3
MHT (160 °C, 15 min)	-	BCP-M4	BCH-M4	DFC-M4	BDFC-M4

*Conventional extractions or MHTs, followed by MHT (160 °C, 15 min)

** Conventional extractions or MHTs, followed by MHT (160 °C, 15 min) and 6%v/v H_2O_2 at pH 11.5

Table 2.2. Summary of extruded ginger pomace (GP), coriander root (CR), and Thai basil root (ThB) extract sample names and conditions

Biomass source	**Extraction condition**	**Sample name**				
		Lipids/Oils	**Protein**	**Insoluble starch**	**Soluble starch**	**Residue/DFC**
GP	$scCO_2$-10% ethanol (350 bar, 35 °C, 2 h)	GP-Oil	-	-	-	-
	$scCO_2$-10% ethanol – Water (50 °C, 2 h)	-	GPP-W	GPI-W	-	GPR-W
	$scCO_2$-10% ethanol – MAE (60 °C, 15 min)	-	GPP-MW60	GPI-MW60	-	GPR-MW60
	$scCO_2$-10% ethanol – MAE (80 °C, 15 min)	-	GPP-MW80	GPI-MW80	GPS-MW80	GPR-MW80
	$scCO_2$-10% ethanol – MHT (100 °C, 15 min)	-	GPP-MW100	GPI-MW100	GPS-MW100	GPR-MW100
	$scCO_2$-10% ethanol – MHT (120 °C, 15 min)	-	-	GPI-MW120	GPS-MW120	GPR-MW120
	$scCO_2$-10% ethanol – MAE (60 °C, 15 min) – MHT (160 °C, 15 min)		-	-	-	DFC-GP60
CR	$scCO_2$-10% ethanol (350 bar, 35 °C, 2 h)	scCR	-	-	-	-
	$scCO_2$-10% ethanol – Water (50 °C, 2 h)	-	CRP-W	-	-	CRR-W
	$scCO_2$-10% ethanol – MAE (80 °C, 15 min)	-	CRP-MW80	-	-	CRR-MW80
	$scCO_2$-10% ethanol – MAE (80 °C, 15 min) – MHT (160 °C, 15 min)		-	-	-	DFC-CR80
ThB	$scCO_2$-10% ethanol (350 bar, 35 °C, 2 h)	scThB	-	-	-	-
	$scCO_2$-10% ethanol – Water (50 °C, 2 h)	-	ThBP-W	-	-	ThBR-W
	$scCO_2$-10% ethanol – MAE (80 °C, 15 min)	-	ThBP-MW80	-	-	ThBR-MW80
	$scCO_2$-10% ethanol – MAE (80 °C, 15 min) – MHT (160 °C, 15 min)		-	-	-	DFC-ThB80

2.5.6. Microwave-assisted hydrothermal production of defibrillated cellulose

The solid residues obtained after protein or carbohydrate extraction from BC, GP, CR or ThB were mixed with deionised water at a solid-to-liquid ratio of 1:20 (g/mL) for BC residues and 1:35 (g/mL) for GP, CR and ThB residues. The mixtures were subjected to defibrillated cellulose (DFC) extraction using a Milestone Synthwave Microwave at a temperature of 160°C, with a 15 min ramping time, 15 min holding time, 10 bar nitrogen pressure, and 60% stirring. Then, the mixtures were filtered, and solid residues were then washed with hot water, hot ethanol, room temperature ethanol, and acetone. The washed residues were then air-dried under a fume hood (2 days), ground and sieved (250 µm), and named as DFC (see **Table 2.1** and **2.2**).

The DFC derived from BC were further bleached with a slightly modified method suggested by Alba *et al*.[53] The DFC were bleached with 6% v/v H_2O_2 with the solid-to-liquid ratio of 1:20 (g/mL) at pH 11.5 (adjusted by 6M NaOH), 60 °C for 2 h, followed by room temperature for 16 h. The bleached DFC (named as BDFC, see **Table 2.1**) were centrifuged (3500 rpm, 20 min). The solid fractions were washed with deionised water (3 times), followed by 5% w/v acetic acid, water, ethanol, and acetone, then air-dried (2 days), ground and sieved (250 µm).

2.6. Isolation of protein and carbohydrates

2.6.1. Pectin precipitation (obtained from blackcurrant pomace)

BC hydrolysate obtained after filtration through a stainless-steel mesh was centrifuged (3500 rpm, 4°C, 10 min) to remove fine residues. Thereafter, supernatant was then treated with ethanol at a supernatant-to-ethanol ratio of 1:2 and stored overnight in the refrigerator.[207] The pectin pallet was collected by centrifugation (3500 rpm, 4°C, 20 min). The pallet was washed with hot ethanol, followed by ethanol at room temperature. After vacuum filtration, the washed pectin (named as BCP, see **Table 2.1**) was freeze-dried to dryness and ground into powder for further characterisation. Besides, the supernatant (named as blackcurrant hydrolysate; BCH, see **Table 2.1**) was evaporated and freeze-dried to dryness for further characterisation.

2.6.2. Protein precipitation (obtained from extruded ginger pomace, coriander and Thai basil roots)

GR, CR and ThB hydrolysate obtained after filtration through a stainless-steel mesh was centrifuged (3500 rpm, 4°C, 10 min) to remove fine residue. Then, supernatant was adjusted to pH 4.5 (isoelectric point of protein) by adding 1M HCl and centrifuge (3500 rpm, 4°C, 20 min).[144] The precipitate was freeze-dried and considered as protein fraction (see **Table 2.2** for sample names). In addition, as ginger contain high content of starch, supernatant after protein precipitation was subjected to starch isolation (see **Section 2.5.3**).

2.6.3. Starch precipitation (obtained from extruded ginger pomace)

Fine residue obtained from GR hydrolysate after centrifugation (3500 rpm, 4°C, 10 min) was considered as insoluble starch, while supernatant after protein precipitation (**Section 2.5.2**) was treated with ethanol a supernatant-to-ethanol ratio of 1:2, stored overnight in the refrigerator, and then centrifuge (3500 rpm, 4°C, 20 min). The precipitate was freeze-dried and considered as soluble starch. Both insoluble starch and soluble starch were named as shown in **Table 2.2**.

2.7. Film fabrication

Blackcurrant extracts, including BCP-M1 (pectin), BCH-M1 (anthocyanin-rich hydrolysate), and BDFC-M1 (bleached defibrillated cellulose) obtained from MHT at 100 °C were chosen as additives in sodium alginate (NaAlg) film. NaAlg-BCP aqueous solutions (4 wt.%. in deionised water 30 mL) of NaAlg-to-BCP ratios of 100:0, 90:10, 80:20, and 50:50, were prepared, and stirred vigorously (800 rpm, 40°C, 3 h). Thereafter, glycerol (0.625 g), and BDFC-M1 suspension (0% or 2 wt.%., 1.25 mL), or BCH-M1 solution (0% or 0.5 wt.%., 1.25 mL) were added into the polymer mixture. The entire mixture was then mixed (800 rpm, 40°C, 30 min) and then was sonicated in degas mode (room temperature, 20 min). The film solutions were carefully poured into 9 mm-diameter petri dishes (10 g) and set to cast in an oven (50°C, 20 h).

Filter papers (9 mm diameter) were soaked overnight in a 0.5%$CaCl_2$-7%glycerol solution and were placed on top of the previously oven-dried films for 2 min to facilitate crosslinking. The crosslinked films were dried in a fume hood at ambient temperature overnight and then stored in plastic zip lock bags. The prepared films were labelled as shown in **Table 2.3**.

Table 2.3. Composition of NaAlg-BCP films

Sample code	NaAlg: BCP ratio	Additives (%)
NaAlg	100: 0	-
NaAlg-BCP10	90: 10	-
NaAlg-BCP20	80: 20	-
NaAlg-BCP50	50: 50	-
NaAlg-DFC	80: 20	BDFC-M1 (2%)
NaAlg-ACN	80: 20	BCH-M1 (0.5%)

2.8. Instrumental analysis for characterisation of antioxidant compounds, protein and carbohydrates

2.8.1. Attenuated total reflection infrared spectroscopy (ATR-IR)

ATR-IR analysis of BC, CR, and ThB extracts, and film samples was carried out using a Perkin Elmer Spectrum 400 IR. Prior to record, the sapphire window and tip were cleaned with isopropanol. Thereafter, moisture and CO_2 background from the surrounded atmosphere were corrected. Small amount of samples were placed directly on top of the sapphire window. The spectra were scanned and recorded from 4000 to 600 cm^{-1}, with the force gauge between 100 and 120, and 4 scans per sample.

2.8.1.1. Determination of pectin degree of esterification

BC pectin spectra were recorded using the method mentioned in **Section 2.8.1**. The absorbance peak at wavenumber around 1720-1740 cm^{-1} were considered as the peak of esterified C=O (-COOR, A_{1730}), while at wavenumber around 1600-1620 cm^{-1} were considered as non-esterified C=O or C=O of carboxyl group (-COOH, A_{1620}). Degree of esterification (DE) of BC pectin was determined using the following equation:[208]

$$DE\ (\%) = \frac{A_{1730}}{A_{1730} + A_{1610}} \times 100 \qquad \textit{(Equation 2.4)}$$

2.8.2. Elemental analysis (CHN)

Elemental analyses were performed by Dr. Graeme McAllister and Dr. Scott Hicks, Department of Chemistry, University of York using an Exeter Analytical Inc. CE-440 analyser. The sample was placed in a nickel sleeve, injected into a high temperature furnace (975 °C), and burnt in high purity oxygen under static conditions. The results reported are the average

of duplicate. Protein content can be estimated by multiplying 6.25 to nitrogen content (N × 6.25).[209]

2.8.3. Gas chromatography and mass spectrometry (GC-MS)

Gas chromatographic measurements were made with an Agilent Technologies 6890 gas chromatograph, fitted with a Rxi-5HT capillary column (30 m 250 mm x 0.25 mm nominal). Helium was used as the carrier gas at a flow rate of 2.2 mL/min with a split ratio of 10:1, an injection temperature of 250°C and a 2 µl injection. The initial oven temperature was 30°C and was increased instantly at a rate of 50°C/min to 300°C and held at this temperature for 5 minutes, with a total run time of 13.3 minutes.

Mass spectrometric measurements were made with an Agilent 5973 mass spectrometer, with electron ionisation and quadrupole mass analyser. Masses were scanned over 50 m/z to 550 m/z, with a solvent delay of 3 minutes. Total run time of 13.34 minutes. MS data analysed using NIST library version 2.2 (2017).

2.8.4. High performance liquid chromatography (HPLC)

2.8.4.1. Identification of anthocyanins in blackcurrant pomace hydrolysate

The identification of anthocyanins in the blackcurrant hydrolysate samples was conducted using a LC-DAD-ESI/MS/MS separation method described by Šimerdová *et al*.[210] with a slight modification. Sample solutions (20 mg/mL) were performed on a Thermo Scientific UltiMate 3000 Rapid Separation system equipped with a Bruker high-capacity ion trap (HCT1) mass spectrometer. The compounds were separated on a C18 analytical column (150 × 2.1 mm, 2.7 µm particle size) with an injection volume of 10 µl. The column was operated at 50°C with the elution solvents A (2% formic acid in water) and B (100% methanol) and a flow rate of 0.8 mL/min. The gradient was: 0-4 min, 5-20% B; 4-8 min, 20-25% B; 8-10 min, 25-90% B, 10-10.15 min, 90% B; 10.15-10.30 min, 90-5% B, and finally reconditioning of the column (10.30-13 min, 5% B). Four types of anthocyanins were detected at a wavelength of 520 nm with a total run time of 13 min. Anthocyanins was identified by comparing retention times, UV-Visible absorption spectra, and detected molecular weight and fragmentations with the literatures.[210–214]

2.8.4.2. Carbohydrate analysis

Carbohydrate analysis was operated by Dr. Richard Gammons, Department of Chemistry, University of York using high performance liquid chromatography equipped

with refractive index detector (HPLC-RID) on an Agilent 1260 equipped with an Agilent Hi-Plex H+ column (300 × 7.7 mm, 8 µm particle size) (Agilent Technologies, Santa Clara, CA, USA). The analytical conditions included a reverse-phase system with 0.005 M H_2SO_4 as the mobile phase, an injection volume of 5 µL, a flow rate of 0.4 mL/min, and column and detector temperatures set at 60 °C and 55 °C, respectively. The total run time for this procedure was 30 min.

2.8.5. Nuclear magnetic resonance spectroscopy (NMR)

2.8.5.1. ^{1}H-NMR

^{1}H NMR was operated using JEOL ECS400 MHz spectrometer at 298K (25 °C) for 8 scans. Solvent extract or $scCO_2$ extract samples (10 mg) were dissolved in Chloroform-D (1.5 mL) and filtered through standard bore cotton prior to submit.

2.8.5.2. ^{13}C-NMR

^{13}C NMR of BCP was operated by Dr. Heather Fish, Department of Chemistry, University of York on a Bruker AVIIIHD 500 spectrometer at 125 MHz, 343 K (70 °C), and 30,000 scans. BCP samples (50 mg) were dissolved in deuterium water (D_2O, 2 mL). The sample solutions were then filtered through standard bore cotton before being submitted.

2.8.5.3. Solid state ^{13}C CP/MAS NMR

Solid state ^{13}C cross polarisation magic angle spinning (^{13}C CP/MAS NMR) analysis was performed on BC, GR, CR, ThB, DFC and BDFC samples by Dr. Ryan Barker and Jolyon Glynn, Department of Chemistry, University of York on a Bruker Avance III HD spectrometer (400 MHz). Sample spectra were acquired using the 400 MHz spectrometer equipped with a 4 mm H(F)/X/Y triple-resonance probe and 9.4T ascend superconducting magnet (Bruker, Bremen, Germany). The spinning rate was set at 20 kHz, with a contact time of 1 ms and a recycle delay of 8 s. A total of 8500 scans were accumulated. The spectra were analysed using MestReNova×64 software version 14.3.1.31739.

2.8.6. Ultraviolet-visible (UV-Vis) spectroscopy

2.8.6.1. Determination of uronic acid content in blackcurrant pectin

The uronic acid (UA) content of BCP was determined by the metahydroxyldiphenyl or 3-phenylphenol (MHDP).[215] Sample solutions (40 µg/mL, 0.5 mL) were mixed with cold sodium tetraborate in concentrated H_2SO_4 (0.0125 M, 3 mL). The solution was then heated in a water bath (95 °C, 5 min). Thereafter, the mixture was cooled within an ice-water bath,

and a MHDP solution (0.15% MHDP in 0.5% NaOH, 0.05 mL) was added into the mixture and mixed using a vortex mixer. After a 15-minute incubation, the absorbance values of the samples were measured using a Jasso 500 UV-Vis spectrophotometer at 530 nm. A blank solution composed of distilled water (0.5 mL), sodium tetraborate in H_2SO_4 (3 mL), and 0.5% NaOH (0.05 mL) was prepared. A standard curve of galacturonic acid (0-80 μg/mL) was generated (y = 0.0036X - 0.0266, R^2 = 0.9500, see **Appendix 1**). The percentage of UA was determined using the following equation:

$$UA\ (\%wt) = \frac{m}{M} \times Fc \times Df \times 100 \qquad \textit{(Equation 2.5)}$$

where m (mg) is mass of uronic acid determined by the calibration curve, Ms (mg) is mass of sample, Fc is a correction factor when galacturonic acid monohydrate is used as standard (0.830), and Df is a dilution factor.

2.8.6.2. Determination of protein in ginger, coriander and Thai basil protein extracts (Bradford assay)

Protein content in GR, CR and ThB protein extracts was determined using Bradford assay. Sample solutions (1 mg/mL, 15 μL) was mixed with Coomassie Plus reagent (1.5 mL) and incubate for 10 min. The absorbance of the samples was determined using a Shimadzu UV-Vis spectrophotometer at 595 nm. Deionised water was used as a blank solution and a calibration curve of albumin standard (0-2000 μg/mL) was plotted (y = 0.0002X + 0.5751, R^2 = 0.9977, see **Appendix 2**). The protein content was calculated using the following equation:

$$Protein\ content\ (\%\ or\ g/100\ g\ sample) = \frac{m}{Ms} \times Df \times 100 \qquad \textit{(Equation 2.6)}$$

where m (g) is mass of protein determined by the calibration curve, M (g) is mass of protein extract sample, and Df is a dilution factor.

2.8.6.3. Determination of starch in insoluble and soluble ginger starch extracts (iodine-binding test)

Amylose and amylopectin content in insoluble and soluble ginger starch extracts were determined by Iodine-binding method with little modifications.[216] Starch samples (50 mg) was dispersed in ethanol (0.5 mL), then mixed with NaOH solution (0.09M, 5 mL) and heated in a shaking water bath (85 °C, 10 min), followed by autoclave (121 °C, 1 h). The solution was transferred to a 50-mL volumetric flask and made up to 50 mL with deionised water, making a final concentration of 1 mg/mL starch solution. The starch solution (1

mg/mL, 0.5 mL) was adjusted the pH to 3.5 by adding HCl solution (0.1M), mixed with freshly prepared iodine reagent (2 mg/mL I_2 + 20 mg/mL KI, 0.5 mL) and deionised water (5 mL). The mixed solution was incubated in dark area (room temperature, 20 min). The absorbance of sample solution was recorded using a Shimadzu UV-Vis spectrophotometer at 720 nm. The mixed solution without starch sample was used as a blank solution. Calibration curves of a mixture of amylose and amylopectin obtained from potato at different ratios (100:0 to 0:100) were plotted (y = 0.4587X - 0.0115, R^2 = 0.9518 for amylose standard; y = -0.4541X + 0.4481, R^2 = 0.9554 for amylopectin standard, see **Appendix 3** and **4**). The content of amylose and amylopectin (%) in samples was obtained from calibration curves.

2.8.7. Antioxidant activity

2.8.7.1. Determination of total phenolic content (TPC)

The total phenolic content (TPC) in the blackcurrant hydrolysate was determined following a modified literature method.[217] Gallic acid solution/sample solution (0.5 mL) was mixed with 1N Folin-Ciocalteu Reagent (0.5 mL). Na_2CO_3 solution (2%w/v, 9 mL) was added to the mixture and allowed to stand for 25 min at room temperature. A standard curve of gallic acid (0-0.01 mg/mL) was plotted (y = 99.043X + 0.084, R^2 = 0.9998, see **Appendix 5**) and the content of phenolic compounds were measured at 730 nm using a Jasso 500 UV-vis spectrophotometer with deionised water as reference. The result was expressed as mg gallic acid (GA) equivalents per gram of dried weight sample (mg GA/g dry weight). The TPC of the extracts was calculated using the following equation:

$$TPC\ or\ TFC = \frac{c \times V}{m} \qquad \textit{(Equation 2.7)}$$

where, c is the sample concentration before dilution (mg/mL), V is the volume (mL) of the solvent used for dissolving, and m represents the weight (g) of the dried sample.

2.8.7.2. Determination of total flavonoid content (TFC)

Total flavonoid content (TFC) was determined using Alara *et al*. method.[217] Standard quercetin solutions/sample solution (0.5 mL) was mixed with ethanol (9 mL). Then, $AlCl_3$ (2%w/v, 0.5 mL) was added and incubate (room temperature, 1 h). A standard curve of quercetin (0-0.01 mg/ml) was plotted (y = 62.682X + 0.0194, R^2 = 0.9925, see **Appendix 6**). The TFC was measured at 420 nm using a Jasso 500 UV-vis spectrophotometer and ethanol was use as a reference. The result was expressed as mg quercetin equivalents per gram of dried weight sample (mg QT/g dry weight). The TFC of the extracts were calculated using the equation 2.7.

2.8.7.3. Determination of total anthocyanin content (TAC)

The total anthocyanin content (TAC) was determined according to the AOAC protocol.[218,219] Blackcurrant hydrolysate (1 mg/mL, 1.5 mL) was mixed with potassium chloride buffer (0.2 M, pH 1.0, 1 mL), and another portion (1.5 mL) was mixed with sodium acetate buffer (0.2 M, pH 4.5, 1 mL). Then, dilute the mixtures by adding deionised water (2 mL) and absorbance was recorded using a Jasso 500 UV-Visible spectrophotometer at wavelengths of 520 and 700 nm, for solutions at pH 1.0 and pH 4.5, respectively. The TAC was expressed as cyanidin-3-glucoside equivalents (C3G mg/g), and was calculated using the following equation:

$$TAC\ \left(C3G\,\frac{mg}{g}\right) = \frac{A \times MW \times DF \times V}{\varepsilon \times l \times W} \qquad \textit{(Equation 2.8)}$$

where, A is $(A_{520nm} - A_{700nm})pH1.0 - (A_{520nm} - A_{700nm})pH4.5$, MW is molecular weight of C3G (449.2 g/mol), DF is the dilution factor, V is the volume of solvent (mL), W is the sample weight (mg), l is the path length (cm), and ε is the molar extinction coefficient of C3G (26,900 L/mol·cm).

2.8.7.4. 2,2-diphenyl-1-picrylhydrazyl (DPPH) antioxidant assay

The DPPH assay was carried out using the method reported by Do *et al*.[220] Blackcurrant hydrolysates (0.12 mg/mL, 2.5 mL) were mixed with DPPH solution (0.3 mM, 2.5 mL). The mixtures were incubated in the dark area (room temperature, 20 min). The absorbance of mixtures (A_{sample}) and control solution (2.5 mL DPPH + 2.5 mL ethanol, $A_{control}$) were measured at 517 nm using a Jasso 500 UV-Visible spectrophotometer and ethanol was used as a reference.

The antioxidant activity of the films was investigated by the DPPH assay.[220,221] The absorbance of a freshly prepared DPPH solution in ethanol (0.025 mM) was measured at 517 nm ($A_{control}$). Then, small pieces of films (0.3 cm × 2.0 cm) were placed in the DPPH solution and incubated in a dark area (room temperature, 1 h). The absorbance of each film (A_{sample}) in the DPPH solution was measured using a Jasco 500 spectrophotometer at 517 nm. DPPH inhibition was calculated by the following equation:

$$DPPH\ inhibition\ (\%) = \frac{A_{control} - A_{sample}}{A_{control}} \times 100 \qquad \textit{(Equation 2.9)}$$

2.8.7.5. pH-responsive analysis of blackcurrant hydrolysate

The pH-responsive colour of the BCH-M1 was investigated by measuring their absorption spectrum in buffer solutions from pH 1 to 11. The spectra were determined using a Jasso 500 UV-Visible spectrophotometer from 400 to 700 nm.

2.8.8. Thermogravimetric analysis (TGA)

Thermogravimetric analysis (TGA) of the biomass and biomass-derived samples were carried out using the Stanton Redcroft STA625 (Stanton Instruments Ltd., London, UK). In this process, samples (10 mg) were placed into an aluminium pan and compared against an empty reference aluminium pan while being exposed to a nitrogen gas atmosphere. The temperature was incrementally raised from 25 °C to 625 °C at a rate of 10 °C/min.[60] The resulting data were then analysed using Origin software version 2022bSr1.

2.8.9. Scanning electron microscopy (SEM)

The microstructure study of DFC was conducted by Dr. Karen Hodgkinson, Department of Biology, the University of York. A small quantity of the DFC samples was applied onto a carbon tab affixed to an SEM stub. Subsequently, the SEM stubs underwent sputter coating with a 5 nm layer of gold/palladium using a Polaron SC7640 sputter coating apparatus (Quorum Technologies Ltd., East Sussex, UK). The specimens were then visualized using a Jeol JSM 6490LV scanning electron microscope, which operated at 5 kV (JEOL Ltd., Tokyo, Japan).

The microstructure study of films was conducted by Dr. Pual Gunning, Department of Biology, the University of York, using a scanning electron microscopy (JEOL JSM 7800F Prime Field Emission Gun Scanning Electron Microscope, (FEGSEM)) at 5kV accelerating voltage. Samples were prepared by mounting on 12.5 mm diameter aluminium pin-stubs (Agar Scientific Uk Ltd.,), using carbon-rich self-adhesive discs (Agar Scientific Uk Ltd.,). Cross-sections were prepared by cryo-fracturing using liquid nitrogen. All of the mounted samples were sputter coated with platinum in a Safematic CCU-10 sputter coater.

2.8.10. Powder X-ray diffraction (pXRD)

Powder X-ray diffraction (pXRD) analysis of the DFC samples was conducted using the Panalytical Aeris powder X-ray diffractometer. This instrument employed a Beta nickel source filter and operated with a scan speed of 0.2°/s at room temperature. The samples were scanned within a range of 2θ = 5-40°.[60] The spectra were plotted using Origin software

version 2022bSr1. The crystallinity index (CrI) of native biomass and DFC samples was calculated using the Segal equation:[222]

$$CrI\ (\%) = \frac{I_t - I_a}{I_t} \times 100 \qquad \textit{(Equation 2.10)}$$

where I_t represents the total intensity of the major crystalline peak at 2θ = 22° and I_a is the intensity of amorphous region at 2θ = 18°. The CrI was calculated from the baseline subtracted curve fit using Origin software version 2022bSr1.

2.9. Rheological studies

2.9.1. BDFC hydrogel from BC

Amplitude sweep tests of hydrogels were conducted using a stress-controlled rheometer (Anton Paar Physica, MCR-301 rheometer, Graz, Austria) equipped with a serrated parallel-plate measuring system (25 mm diameter, 1 mm gap) at room temperature (25 °C), with an angular frequency (ω) of 10 rad/s and amplitude strain (γ) ranging from 0.001% to 1000%. Data points were collected at a frequency of 6 points per decade, resulting in a total of 37 measuring points. To conduct this test, stable hydrogels were prepared from BDFC-H, BDFC-C1–C4 (7.5 wt.%) and BDFC-M1-M4 (5 wt.%). These hydrogels were subjected to increasing shear strain (γ, %) while maintaining a constant angular frequency. The relationship between the increasing shear strain and the storage modulus (G') and loss modulus (G"), which describes the solid-like and liquid-like viscoelastic behaviour of the hydrogel, respectively, was plotted, and the linear viscoelastic region (LVR) of each sample was identified.

Flow and thixotropic analyses of BDFC hydrogels were conducted with a Kinexus rheometer (Malvern Instruments Ltd., Malvern, UK) equipped with a smooth-plate measuring system (20 mm diameter, 1 mm gap) at 25 °C. Flow curves were measured from 0.1 to 100 s^{-1} (forward) and then 100 to 0.1 s^{-1} (backward) in 2 min. Thixotropic tests were conducted by step test while applying a shear rate of 0.1 s^{-1} for 100 s, followed by shearing at a rate of 100 s^{-1} for 10 s and, finally, at a 0.1 s^{-1} rate for 5 min to observe the viscosity recovery.

2.9.2. Film-forming solution

Flow curve, amplitude sweep and frequency sweep analysis, and creep and recovery test were conducted with a Kinexus rheometer (Malvern Instruments Ltd.,

Malvern, UK) equipped with a cone plate measuring system (CP4/40, 40 mm diameter, 0.1448 mm gap) at 25 °C. Flow curves were measured from 1 to 1000 s^{-1} in 2 min. Amplitude sweep test was conducted at an angular frequency (ω) of 1 Hz and shear strain (γ) ranging from 0.1% to 100%. Frequency sweep test was evaluated at a shear strain of 0.5% (within the LVR) and frequency ranging from 0.1 to 10 Hz. Creep and recovery test were conducted at a gap of 1mm by step test while applying a shear stress of 0.5 Pa for 180 s, followed by removing shear stress for 180 s to observe the strain recovery.

2.10. Properties tests

2.10.1. Water holding capacity (WHC) of DFC and BDFC

The determination of WHC was conducted following the modified literature procedures.[223,224] The samples (0.2 g) were suspended in deionised water (10 mL) within a centrifuge tube. Subsequently, the mixture was agitated using a vortex mixer (2000 rpm, 1 min), subjected to sonication (30 °C, 20 min), and allowed to stand overnight (room temperature). Afterward, centrifugation was performed (3900 rpm, 20 min), and the liquid fraction was carefully decanted. WHC (g water/ g sample) was determined by using the following equation:

$$WHC = \frac{Weight\ of\ wet\ sediment - Weight\ of\ sample}{Weight\ of\ sample} \qquad \textit{(Equation 2.11)}$$

2.10.2. Hydrogel formation of DFC and BDFC

DFC and BDFC samples were mixed with deionised water (2.5 mL) at concentrations of 5 wt.% and 7.5 wt.%. Subsequently, the mixture was vortexed (2000 rpm, 1 min) and sonicated (30 °C, 20 min). The mixtures were left undisturbed (room temperature, 18 h), and the stability of the hydrogel was assessed by qualitatively evaluating gel strength through the inversion of the gel vial for 30 min.

2.10.3. Physical properties of films

The film thickness was measured with a digital micrometre at seventeen different points within every 1 cm interval across the film samples. The moisture content was calculated using the following equation and measured four times for each sample:

$$Moisture\ content\ (\%) = \frac{W_0 - W}{W_0} \times 100 \qquad \textit{(Equation 2.12)}$$

where, W_0 is the initial weight of films, and W is the weight of film after drying.

2.10.4. Mechanical properties of films

Tensile properties were evaluated using an Instron 3367 device (Instron). Dog bone-shaped specimens (20 mm in length, 3 mm in width) were obtained from the films and tested at a speed of 4 mm/min. The tensile properties were determined based on the thickness of the film, which was calculated for each sample using the mean thickness. The results were presented as mean values and standard deviations derived from five measurements.

2.10.5. Water contact angle analysis of films

The hydrophilicity of the film was measured using Attension Theta tensiometer using the sessile drop method and Young-Laplace analysis mode. Films were cut into (1 cm x 1 cm) pieces and deionized water droplets (1 µL) were tested on each film samples. Each sample was measured five times in the ambient atmosphere. Water contact angle analysis was performed on ImageJ program (version 1.54g) with drop analysis plugin.

2.10.6. Water vapour transmission properties of films

The water vapour transmission rate (WVTR) and water vapour permeability (WVP) of the NaAlg-BCP films were measured using the dry cup method, modified according to Azmi *et al.*,[225] and based on the ASTM E96 standard. Glass vials with a transmission area of 64 mm^2 were used for the measurement. The NaAlg-BCP films were placed in a desiccator maintained at 25 °C with a saturated magnesium nitrate solution to control the relative humidity at 50% ± 5% for 24 h. A digital ThermoPro TP49 hygrometer (ThermoPro, China) was placed inside the desiccator to monitor real-time temperature and humidity. Anhydrous calcium chloride was added to the vial to maintain a relative humidity of 0%. Silicone grease was applied to the rim of the vial, and the NaAlg-BCP films were placed on top. The initial weight of the vial with the films was recorded, after which the vial was stored in a desiccator maintained at 50% RH and 25 °C. The weight of the vial was monitored daily for 7 days. The WVTR and WVP were calculated using the following equation:

$$WVTR = \frac{\Delta m}{\Delta t \cdot A} \qquad \textit{(Equation 2.13)}$$

$$WVP = WVTR\ (\frac{L}{\Delta p}) \qquad \textit{(Equation 2.14)}$$

where $\frac{\Delta m}{\Delta t}$ is the weight gain over time, A is the transmission area of the film, L is the film thickness, and Δp is the difference in water vapour partial pressure across the film.[226]

2.10.7. Antifogging property of films

The antifogging property of NaAlg-BCP films was investigated using the hot-fog test.[227] Water (0.75 mL) was added to a 3-ml vial, and silicone grease was applied to the rim of the vial to ensure a proper seal. The NaAlg-BCP films were then placed over the vial openings. The vial was heated (60°C, 3 h) to induce condensation. The transparency of each sample was visually evaluated and scored on a scale from A (completely transparent) to D (fully fogged with coalesced water droplets) (**Figure 2.2**). A glass slide was used as a control.

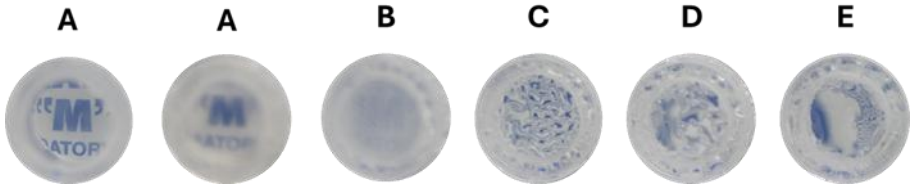

Figure 2.2. Pictures of different scores based on surface appearance after fogging test. (A) transparent surface; (B) fogging surface with reduced transparency; (C) fogging surface exhibiting small, discrete water droplets; (D) surface with reduced transparency and medium-sized, discrete water droplets; (E) surface exhibiting coalesced water droplets.

2.10.8. Acetic acid and ammonia detection of films

The capability of the films to detect CH_3COOH and NH_3 vapour was evaluated using the method described by Ferri *et al*.[221] Films were cut and put into the hole of vial cap, containing CH_3COOH or NH_3 solution (10%v/v, 2 mL). The vials were allowed to stand in the fume hood for 6 h to investigate any colour change of films. NaAlg-BCP50 film was selected for further sensitivity testing with varying concentrations (500ppm, 1, 5, 10%v/v) of NH_3. The NaAlg-BCP50 film after exposure under NH_3 (10%v/v, 6 h) was chosen for colour reversible test with CH_3COOH (10%v/v). The colour transitions were quantified using the CIELab colour space system, which measures colours with Cartesian coordinates (L*, a*, and b*). Photos were taken under consistent conditions, and the total colour difference (ΔE) was calculated using the following equation:

$$\Delta E = \sqrt{(L_{1^*} - L_{2^*})^2 + (a_{1^*} - a_{2^*})^2 + (b_{1^*} - b_{2^*})^2} \qquad \textit{(Equation 2.15)}$$

When the value of ΔE is greater than 5, the observer can clearly perceive two different colours.

2.10.9. Anthocyanin stability in film metrics

Freshly prepared NaAlg-BCP50 films (n = 3) were used to investigate colour changes over time. Prior to analysis, photographs of the films were taken and recorded as Day 0. The films were then stored in a plastic incubator (Gilson digital mini incubator) at 25 °C and photographed daily at 24 h intervals for 14 days. Colour measurements were quantified using the CIELab colour space system. All photos were taken under consistent lighting and camera settings to ensure accuracy.

2.10.10. Thermal stability of films

Differential Scanning Calorimetry was conducted using MDSC, TA Instruments. The film samples (about 5-6 mg) were heated in a hermetically-sealed aluminium pan under a nitrogen atmosphere, from 40 to 300 °C at a heating rate of 10 °C/min. An empty sealed aluminium pan was used as reference and the instrument was calibrated with an indium standard.[102]

2.11. Statistical analysis

Statistical analysis was performed on a one-way analysis of variance (ANOVA) with Tukey's test at a 0.05 significance level using IBM SPSS Statistics program (version 29.0.2.0). Yield, compositional analysis, degree of esterification of BCP, uronic acid content, total phenolic content (TPC), total flavonoid content (TFC), total anthocyanin content (TAC), protein content, amylose and amylopectin contents, DPPH antioxidant activity, Klason lignin and sugar composition of DFC, water-holding capacity, and the physical and functional properties of films were analysed in triplicate (n = 3), whereas elemental analysis was performed in duplicate (n = 2).

Chapter 3: Results and Discussion

This chapter is divided into 2 sections based on the aims mentioned in chapter 1, including:

Section 1: Aim I (A1) Valorisation of blackcurrant pomace.

Section 2: Aim II (A2) Valorisation of extruded ginger pomace and Aim III (A3) Valorisation of extruded aeroponically grown coriander and Thai basil roots: A comparative study.

3.1. Valorisation of blackcurrant pomace (A1)

3.1.1. Characterisation of blackcurrant pomace (Objective A1 (i))

The chemical and elemental compositions of dried blackcurrant pomace (BC) are reported in **Table 3.1**. Moisture, ash, protein, and Klason lignin content in BC are aligned well with the literatures, where BC was reported to contain about 3.2 – 7.5 wt.% moisture, 2.8 – 3.3 wt.% ash, 11.1 – 17.4 wt.% protein, and 35.7 – 59.3 wt.% lignin.[53,63–66] However, polysaccharide content determined in this study (12.07 wt.%), including cellulose, hemicellulose, and pectin, is significantly lower than the literatures, which ranged from 14.1 – 47.2 wt.%.[53,64,66]

Table 3.1. Compositional and elemental analysis of blackcurrant pomace

Composition (wt.%)	
Moisture [a]	7.57 ± 0.17 [b]
Ash [a]	2.46 ± 0.17 [a]
Protein (N × 6.25) [a]	10.66 ± 0.31 [c]
Cellulose [a, b]	8.74 ± 0.52 [b]
Hemicellulose [a, b]	1.62 ± 0.69 [a]
Pectin [a, b]	1.71 ± 0.94 [a]
Klason lignin [a]	46.80 ± 2.61 [d]
Elemental content (wt.%)	
C	48.43 ± 0.13 [D]
H	5.58 ± 0.04 [B]
N	1.71 ± 0.05 [A]
Remainder	44.30 ± 0.15 [C]

[a] Estimated via the NREL method,[204–206,209] [b] based on HPLC analysis of carbohydrates and sugars in acid-hydrolysed BC. Values are presented as mean ± SD (composition, n = 3; elemental content, n = 2). Letters indicate the significant differences ($p < 0.05$).

The variation in the reported polysaccharide contents of BC may be due to different analysis method used, for example, Alba *et al*. reported that fractionated polysaccharides, including acid-soluble pectin (2.9 – 5.8 wt.%), calcium-bound pectin (7.7 – 9.8 wt.%), hemicellulose (14.4 – 14.5 wt.%) and cellulose (13.6 – 17.2 wt.%) in BC ranged from 38.7 – 47.2 wt.%, depending on its origin,[53] whilst Wądrzyk *et al*. estimated a polysaccharide content of

37.8 wt.%, comprising hemicellulose (7.4 wt.%) and cellulose (30.4 wt.%), using a Fibretherm analyser.[43] Nawirska *et al.* reported 40.0 wt.% polysaccharides, consisting of pectin (2.7 wt.%), hemicellulose (25.3 wt.%), and cellulose (12.0 wt.%), through acid and enzymatic hydrolysis.[64] In contrast, Jakobsdottir *et al.* estimated the dietary fibre polysaccharides (14.1 wt.%) using an enzymatic method.[66]

In this study, pectin, hemicellulose, and cellulose were estimated using the NREL standard method, based on their constituent monomers generated through acid hydrolysis and subsequently analysed by HPLC.[206] Therefore, the low content of polysaccharides obtained in the acid-hydrolysed BC hydrolysate may be attributed to incomplete hydrolysis of polysaccharides and acid-induced precipitation,[228] which could result in the production of short-chain polysaccharides or oligosaccharides that are not fully detected by this method. Complementary analytical techniques, such as thermogravimetric analysis (TGA), discussed in **Section 3.1.1.1**, provide a broader assessment of total carbohydrate content. The higher polysaccharide values obtained by TGA compared to those reported in **Table 3.1** from HPLC analysis further support the likelihood that HPLC-based monomer quantification underestimates the total polysaccharide content in BC.

In addition, the total compositional analysis reported in **Table 3.1** accounts for only approximately 79% of the sample. Beyond incomplete polysaccharide hydrolysis, the remaining fraction may consist of other components, potentially including lipids such as fatty acids and/or triglycerides, as discussed in **Section 3.1.1.2.**

3.1.1.1. Thermogravimetric analysis of blackcurrant pomace

Thermogravimetric analysis (TGA) of BC was conducted to confirm the presence of polysaccharides in BC. (see **Figure 3.1**). The TGA thermogram of BC exhibits three main phases ranging from 25 - 150°C (phase A), 150 - 625°C (phase B) and over 625°C (phase C). The mass loss observed in phase A (3.9 wt.%) may attribute to the evaporation of water and volatile compounds. Phase B reveals a rapid mass loss of 40.1 wt.%, corresponding to thermal decomposition of polysaccharide and lignin. Phase C represents the residual fixed carbon and inorganic matters, accounting for 56.0 wt.%.

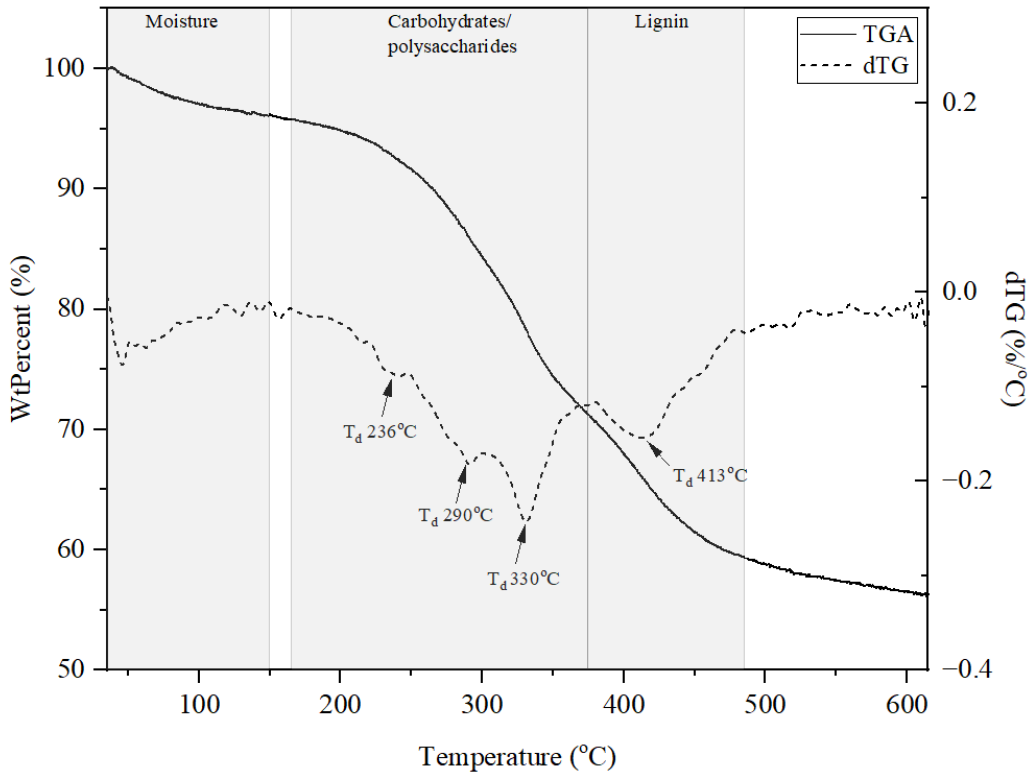

Figure 3.1. TGA and dTG thermogram of blackcurrant pomace.

According to previous studies, the thermal degradation of polysaccharides and lignin occurs within temperature ranges of 220 – 240 ˚C for pectin, 220 – 315 ˚C for hemicellulose, 315 – 400 ˚C for cellulose, and 160 – 500 ˚C and 750 - 800˚C for lignin.[100,229,230] The derivative thermogravimetric (dTG) curve further reveals characteristic degradation peaks corresponding to pectin (240 ˚C), hemicellulose (290 ˚C), cellulose (330 ˚C), and lignin (413 ˚C) in BC. In addition, the mass loss of approximately 23.3 wt.%, observed between 220 – 380 ˚C, attributed to the decomposition of polysaccharides including pectin, hemicellulose, and cellulose, which aligns with the reported polysaccharides content in BC.[53,64,66] However, the polysaccharide content determined by TGA is considerably higher than the values reported in **Table 3.1**, which were determined based on their constituent monomers. This could be because of incomplete hydrolysis of the polysaccharides, resulting in limited release of their constituent monomers.

3.1.1.2. IR spectroscopy analysis of blackcurrant pomace

IR spectroscopy analysis of BC was performed to identify the functional groups associated with its chemical constituents. The IR spectra and the corresponding peak assignments are presented in **Figure 3.2** and **Table 3.1**. A broad band peak observed around

3280 cm^{-1} corresponds to the -OH stretching of carboxylic acids (-COOH) or hydroxyl groups (-ROH), indicating the presence of fatty acids or structural hydroxy-containing molecules in BC. The presence of fatty acids and glycerides/triglycerides is further supported by characteristic peaks at 3010 cm^{-1} (sp^2-C-H stretching of unsaturated fatty acids), 2922 and 2853 cm^{-1} (-C-H stretching of fatty acids/glycerides), 1742 cm^{-1} (-C=O stretching of esters/glycerides), 1627 cm^{-1} (-C=O stretching of carboxylic acids/fatty acids), 1533 cm^{-1} (-C=C stretching of alkenes), and 1376 cm^{-1} (-C-H bending of alkanes).[231–233]

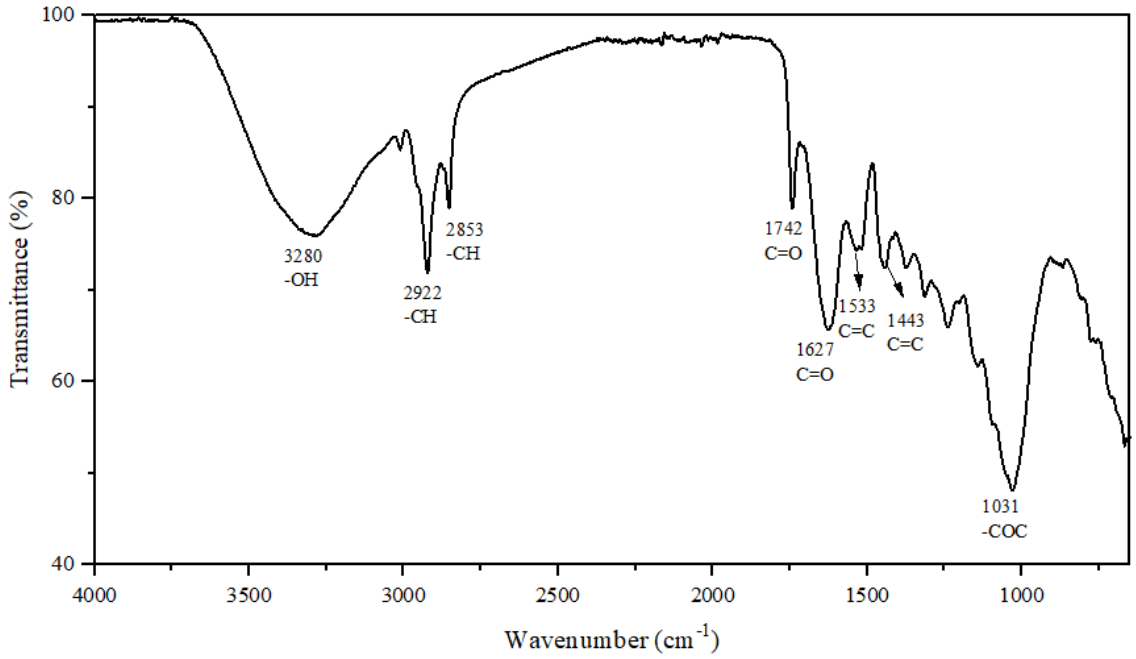

Figure 3.2. IR spectra of blackcurrant pomace.

Given the large amount of lignin presented in **Table 3.**1, lignin or phenolic compounds in BC also present in IR analysis, as evidenced by absorbance bands at 3280 cm^{-1} (-O-H stretching of phenolics), 3010 cm^{-1} (sp^2-C-H stretching of lignin), and 1533 and 1443 cm^{-1} (-C=C stretching of aromatics).[231,234] In addition, typical bands associated with polysaccharides present at 3280 cm^{-1} (-O-H stretching), 2922 and 2853 cm^{-1} (-C-H stretching), 1376 cm^{-1} (-C-H bending), and 1031 cm^{-1} (-C-O stretching of glycosidic linkages), indicate the presence of cellulose, hemicellulose, and pectin.[100,231,235] Vibrations appearing at 1742 and 1627 cm^{-1} (-C=O stretching of esters and carboxylic acids, respectively), also suggest the presence of hemicellulose and pectin.[100,235]

Table 3.2. Summary of bands (cm^{-1}) found in IR spectra of blackcurrant pomace

Wavenumber (cm^{-1})	Assignment
3280 (broad)	O-H stretching vibration of hydroxyl groups (-COOH or -ROH)
3010	sp^2 C-H stretching vibration of unsaturated fatty acids or lignin/aromatics
2922	Asymmetric C-H stretching vibration of -CH, $-CH_2$ and $-CH_3$
2853	Asymmetric C-H stretching vibration of -CH, $-CH_2$ and $-CH_3$
1742	C=O stretching vibration of esters of glycerides, pectin, and/or hemicellulose
1627	C=O stretching vibration of carboxylic acid of fatty acids, pectin, and/or hemicellulose
1533	C=C stretching vibration of alkenes or aromatics
1443	C=C stretching vibration of aromatics
1376	C-H bending vibration of alkanes
1031	C-O stretching vibration of ethers/glycosidic linkages

3.1.2. Production and characterisation of pectin from blackcurrant pomace via HCl, citric acid, water and acid-free microwave hydrothermal conditions (Objective A1 (ii))

3.1.2.1. Pectin yield

Variations in pectin yield, purity, structure, and functional properties are influenced by extraction methods, pre-treatment steps, and initial pectin content of raw materials. The appearance, yield (wt.%) and degree of esterification (DE, %) of the isolated pectin from BC pomace (BCP) under different extraction conditions, including conventional HCl, citric acid, water extractions, and acid-free microwave hydrothermal extractions (MHT), are presented in **Figure 3.3**, with corresponding sample names are summarised in **Table 2.1**. Overall, the yield of BCP ranges from 2.04 – 3.86 wt.%, which is similar with the reported values in literatures (2.9 – 9.8 wt.%).[53,54]

The highest pectin yield is observed from conventional HCl extraction (BCP-H, 3.86 wt.%), as expected. Strong mineral acids such as HCl effectively disrupt plant cell walls,

facilitating the release of intracellular components and resulting in increasing yield. BCP extracted using citric acid, a bio-based organic acid, at different concentrations (0.2 – 0.8M; BCP-C1 to BCP-C4) yield 2.04 – 3.41 wt.%. Higher concentrations of citric acid result in increased BCP yields, with BCP-C3 (3.39 wt.%) and BCP-C4 (3.41 wt.%) comparable to BCP-H (3.86 wt.%), while BCP-C1 (2.04 wt.%) and BCP-C2 (2.37 wt.%) are similar to the conventional water-extracted control (BCP-W, 2.28 wt.%, see **Figure 3.3**). Thus, the optimal condition for BCP extraction using citric acid is at 0.6M (BCP-C3) as yield is not significantly different to BCP-C4, while using less acid. The trend of increasing yield with higher citric acid concentration aligns with previous findings on durian pectin extraction, where citric acid concentrations between 0.0001 and 1.0 M produced significantly higher yields at 1.0 M.[215] This could be because of stronger acid hydrolysis at higher concentrations facilitates the release of impurities such as hemicellulose, starch, ash, and pectin-organic acid complexes from plant cell walls.[215,236,237]

Regarding acid-free MHT at different microwave (MW) temperatures (100 – 160°C, BCP-M1 to BCP-M4), higher MW temperatures led to increased pectin yields, peaking at 140 °C (BCP-M3, 3.07 wt.%). This might be due to the formation of organic acids from biomass components during hydrothermal treatment, creating a mildly acidic environment that promotes pectin solubilisation and partial hydrolysis of cell wall components, thereby positively enhancing pectin extraction. However, the yield significantly drops at 160 °C (BCP-M4, 2.05 wt.%, see **Figure 3.3B**), possibly due to the thermal degradation of pectin.

Therefore, the optimal MHT extraction based on BCP yield was identified as 140 °C (BCP-M3, 3.07 wt.%), which was slightly lower than BCP-H (3.86 wt.%), BCP-C3 (3.39 wt.%), and BCP-C4 (3.41 wt.%), however, not significantly different. This finding aligns with the reported pectin yields from mango peel, and lemon and orange residues extracted through MHT at 140 °C under fixed solid-to-liquid ratios (1:10 for mango peel and 1:6 for lemon and orange residues) and fixed MW holding times (10 min for mango peel and 15 min for lemon and orange residues).[100,238] Nevertheless, yield can also be significantly influenced by solid-to-liquid ratio, MW holding time, and MW power. Therefore, further optimisation of these factors could reduce solvent use, time, energy, and cost, thereby enhancing the efficiency of BCP extraction.

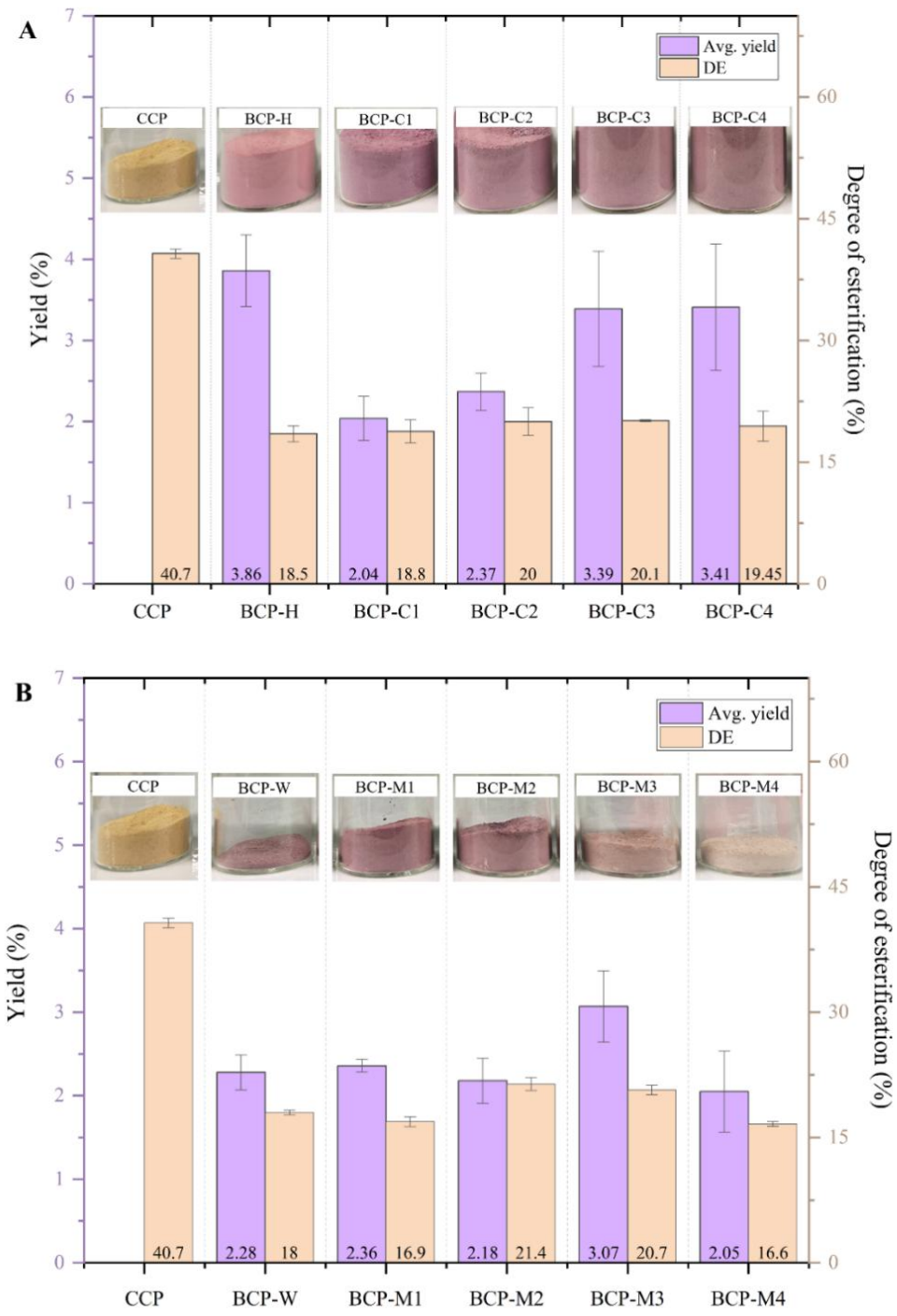

Figure 3.3. Appearance, yield and degree of esterification of commercial citrus pectin (CCP), acid derived BCP (A), and free-acid derived BCP (B); Values are presented as mean ± SD (n = 3).

3.1.2.2. Degree of esterification of BCP

The DE, an essential characteristic of pectin, was calculated using the IR spectroscopic method and is presented in **Figure 3.3**.[208] Commercial citrus pectin (CCP; DE of 40.7%), was used as a control sample, while BCP exhibited DE values ranging from 16.6 – 21.1%. Both CCP and BCP were categorised as low methoxy (LM) pectin (DE < 50%). Interestingly, all BCP exhibited a pale pink colour (see **Figure 3.3**), which may indicate the presence of bound anthocyanins. The presence of the anthocyanin-bound pectin in BCP is supported by Salleh *et al.,* who observed this type of pectin derived from blackcurrant juice.[68] As the MW temperature increased to 160 °C, the pink colour lessened, suggesting that higher temperatures may lead to the degradation of pectin-bound anthocyanins.[239]

The DE values obtained for BCP are consistent with the work reported by Alba *et al.,* where BC pomace-derived pectin was identified as LM type with DE of 11 – 38%.[53] However, the DE of BCP in this study is significantly lower than citric acid-extracted pectin from BC pomace (48.7 – 51.3%) reported by Ćorović *et al*.,[54] and also lower than pectin derived from BC juice, (65.2%) as reported by Salleh *et al*.[68] Differences in the DE of BCP among studies may be due to differences in the methods of determination and pre-treatment of raw materials. In this study, a comparable titration method,[240] was also evaluated; however, it was found to be unsuitable for determining the DE of BCP due to the presence of anthocyanins, pH-responsive pigments bound within the pectin structure. The presence of these anthocyanin-bound compounds interfered with the titration process, making it impossible to accurately determine the DE of BCP (see **Appendix 7**).

Regarding the effect of extraction methods on the DE of BCP, acid-derived BCP (BCP-H and BCP-C1 to BCP-C4) exhibited similar DE results, ranging from 18.5 – 20.1%, with citric acid concentrations (0.2 – 0.8M) showing no significant influence (see **Figure 3.3A**). In contrast, for MHT extraction, the DE of BCP slightly increased with the increasing MW temperature, peaking at 120 °C (DE, 21.3%), followed by a plateau at 140 °C (DE, 20.7%); thereafter, it decreased at 160 °C (DE, 16.3%).

3.1.2.3. Purity and sugar composition of BCP

Table 3.3 shows the purity of the extracted BCP based on their uronic acid content. The uronic acid content of all BCP samples ranges from 38.70 – 61.26%, which is below 65%, indicating low purity. Among all acid-extracted BCP, BCP-H exhibits the lowest uronic acid content (38.70%). Increasing the concentration of citric acid initially led to higher uronic acid contents in the extracted pectin (BCP-C1 to BCP-C3; 47.21 – 49.06%), but the value decrease to 43.99% for BCP-C4. The reduction in uronic acid content at higher acid strengths and concentrations may be due to the co-extraction of non-pectin polysaccharides, such as hemicellulose or starch, which can also be precipitated in ethanol.[241] In addition, strong acids may hydrolyse pectin into smaller molecules that are not precipitable with ethanol, resulting in lower uronic acid content found in samples.[242]

For the acid-free extraction, the control water-extracted BCP (BCP-W) contains 42.84% uronic acid, while the uronic acid content of MHT-extracted pectin ranges from 37.32 – 61.26%. The uronic acid content slightly increases with increasing MW temperature, peaking at 120 °C (61.26%); thereafter, a subsequent drop to 37.32% is observed at 160 °C, which could be due to the thermal degradation of pectin. The trend of uronic acid content of BCP is consistent with the galacturonic acid (GalA) content determined by HPLC analysis of acid-hydrolysed BCP (see **Figure 3.4**). However, the uronic acid content is significantly higher than GalA content. This can be explained by the presence of anthocyanins in BCP, which react with H_2SO_4, one of the chemicals used in the uronic acid-MHDP assay, producing red flavylium cations. These cations absorb light in a similar wavelength range (450 – 550 nm; λ_{max} at 495 nm, see **Figure 3.24**) as the assay measurement wavelength (530 nm), thereby leading to an overestimation of uronic acid content.

Table 3.3. Purity of BCP based on uronic acid content (%)

Sample	Uronic acid content (%)
BCP-H	38.70 ± 0.40 [a]
BCP-C1	47.91 ± 1.44 [c]
BCP-C2	47.21 ± 1.05 [c]
BCP-C3	49.06 ± 0.80 [c]
BCP-C4	43.99 ± 0.69 [b]
BCP-W	42.84 ± 0.40 [b]
BCP-M1	59.88 ± 1.20 [d]
BCP-M2	61.26 ± 0.69 [e]
BCP-M3	49.52 ± 1.38 [c]
BCP-M4	37.32 ± 1.05 [a]

Values are presented as mean ± SD (n = 3). Letters indicate the significant differences ($p < 0.05$).

Based on the sugar analysis of acid-hydrolysed BCP (**Figure 3.4**), the presence of galacturonic acid (GalA), rhamnose (Rham), and arabinose (Ara) indicates the existence of pectin and its branched side chains. Meanwhile, the detection of glucose (Glu) and mannose (Man*), including xylose and fructose, suggests the presence of starch and hemicellulose within the extracted soluble polysaccharide fraction. GalA is the main monosaccharide found among all samples, confirming that pectin is the major component in the extracted BCP, with the HCl-extracted sample (BCP-H) contained the highest GalA content (50.59%). Meanwhile, citric acid-extracted pectin exhibits 36.45 – 40.01% GalA with increasing citric acid concentrations; however, the proportions of other components, such as Glu and Man* also increase. These results suggest that citric acid is less selective for pectin extraction, as higher concentrations tend to promote the co-extraction of other soluble polysaccharides.

For MHT-extracted pectin, the highest GalA content is observed at 100 °C (BCP-M1, 48.59%), which also higher than that of the control water-extracted pectin (BCP-W, 42.59%). As the MW temperature increased, the contents of GalA, Rha, and Ara gradually decreased, suggesting thermal degradation of the pectin backbone and its branched side chains. In contrast, the contents of Glu and Man* increased with rising temperature from 9.41 – 43.16%

and 5.63 – 12.70%, respectively, suggesting that lower MW temperature (below 160°C) are more selective for pectin extraction.

Table 3.4. Linearity of BCP based on ratio of GalA and Rham + Ara

Sample	GalA (%)	Rham + Ara (%)	Linearity (GalA: Rham + Ara)
BCP-H	50.59	7.48	6.76
BCP-C1	36.45	6.79	5.37
BCP-C2	38.29	7.56	5.06
BCP-C3	40.01	6.49	6.16
BCP-C4	41.70	4.79	8.71
BCP-W	42.59	10.46	4.07
BCP-M1	48.59	7.87	6.17
BCP-M2	45.01	8.39	5.36
BCP-M3	39.05	3.81	10.25
BCP-M4	13.18	1.47	8.97

Values are presented as single measurements (n = 1); therefore, no statistical comparison among samples was performed.

In addition, to indicate linearity of BCP, the ratio of GalA (pectin backbone) and sum of Rham and Ara (pectin side chain) are summarised in **Table 3.4**. At the same acid concentration of HCl and citric acid, BCP-H exhibits higher linearity (6.76) than BCP-C1 (5.37). This difference can be attributed to the weaker acidity and bulkier molecular structure of citric acid, which may limit hydrolysis efficiency through steric hindrance. Meanwhile, at higher citric acid concentrations (0.2 – 0.8M), the linearity of BCP also increased (5.06 – 8.71), suggesting partial hydrolysis of pectin side chains. Similarly, increasing MW temperatures (100 - 140°C) resulted in higher linearity (5.36 – 10.25), indicating the thermal degradation of pectin side chains. However, at MW temperature of 160°C, the linearity drops to 8.97, suggesting that excessive thermal exposure may lead to degradation of the main pectin backbone.

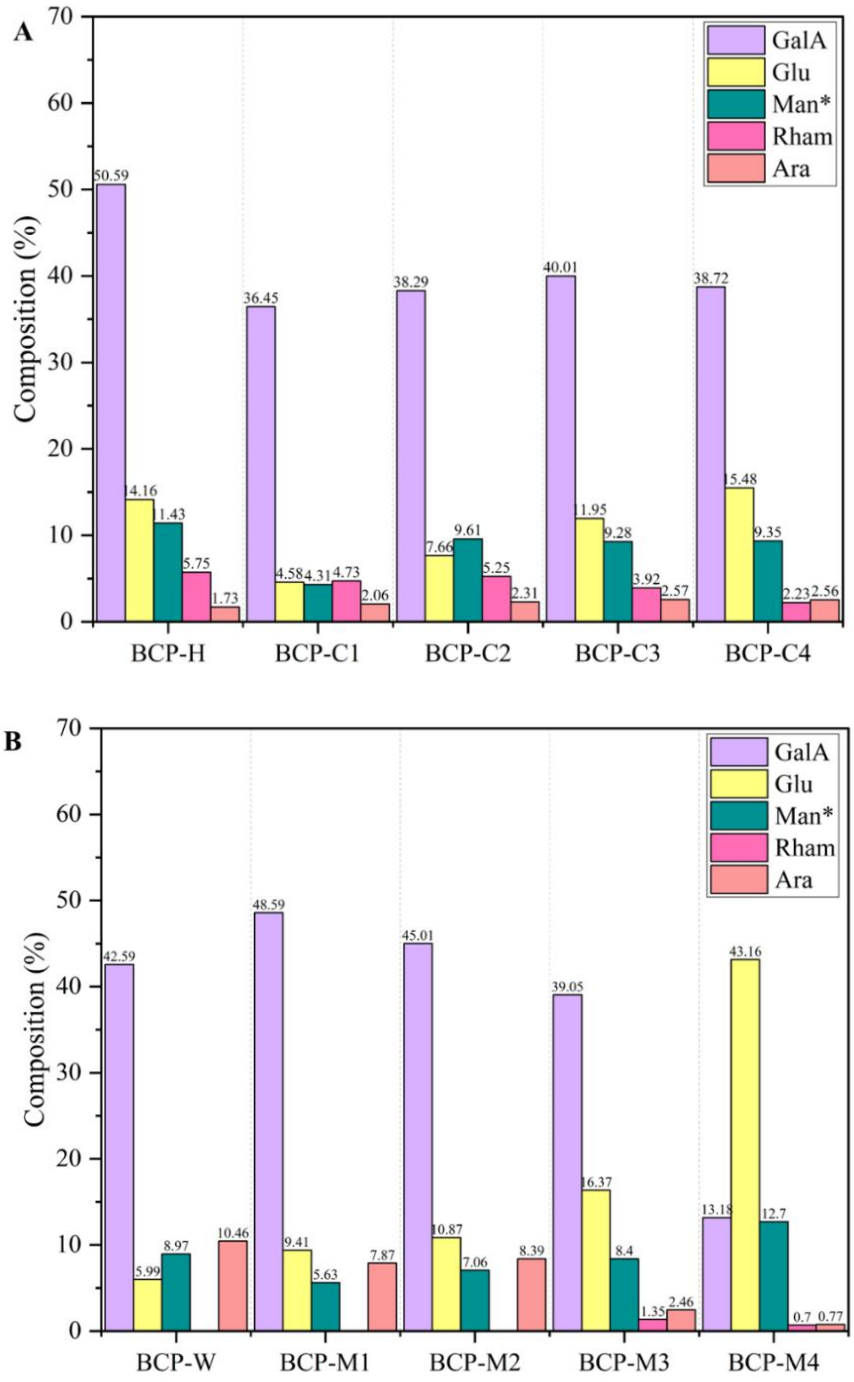

Figure 3.4. Sugar composition (%) of acid derived BCP (A), and free-acid derived BCP (B) based on total soluble acid-hydrolysed BCP; Man includes mannose, xylose and fructose. Values are presented as single measurements (n = 1); therefore, no statistical comparison among samples was performed.*

3.1.2.4. ATR-IR spectroscopy analysis of BCP

Figure 3.5 displays the ATR-IR spectra of CCP, acid-derived BCP (BCP-H, and BCP-C1 – C4), and acid-free derived BCP (BCP-W, and BCP-M1 – M4). All samples exhibit a broad absorbance band centred at around 3330 cm^{-1}, corresponding to the O-H stretching of uronic or galacturonic acid, the C–H stretching band at approximately 2920 cm^{-1}, the characteristic carbonyl absorbances of pectin at around 1730 cm^{-1} (-$COOCH_3$) and 1610 cm^{-1} (-COOH), and the intense band at 1013 cm^{-1}, attributing to C–O–C stretching of glycosidic bond.[53,54,215]

The relative intensities of the two major carbonyl bands at around 1730 cm^{-1} and 1610 cm^{-1} varies with citric acid concentrations and MW temperatures, which were used to determine the DE in **section 3.1.2.2**. In addition, a shift of the carbonyl vibration toward higher wavenumber (to 1650 cm^{-1}) and an increased intensity of the peak near 1540 cm^{-1} were observed at higher citric acid concentrations and HCl-extracted sample (BCP-H), indicating possible extraction of protein under acid conditions, in which bands at around 1650 cm^{-1} and 1540 cm^{-1} corresponds to amide I (C=O stretching) and amide II (N-H bending), respectively.[243,244] These peaks were also observed in the acid-extracted soy hull pectin and grape pomace pectin.[245,246] Moreover, BCP-H exhibits 19.50% protein, whileBCP-C1 to C4 exhibit levels of protein from below the detection limit (0.01% N, equivalent to 0.0625% protein) to 11.16% (see **Table 3.5**). The increasing of protein content also corresponds to the increasing of vibrational intensities of 1650 cm^{-1} and 1540 cm^{-1} (see **Figure 3.5**). For MHT-derived BCP, the intensities between these two carbonyl bands are similar for BCP-M1 to M3 (MHT at 100 – 140°C), then the peaks at 1730 cm^{-1} and 1610 cm^{-1} decrease at 160°C, suggesting the degradation of pectin at this MW temperature. Therefore, MHT at 100 - 140°C is more selective for pectin extraction.

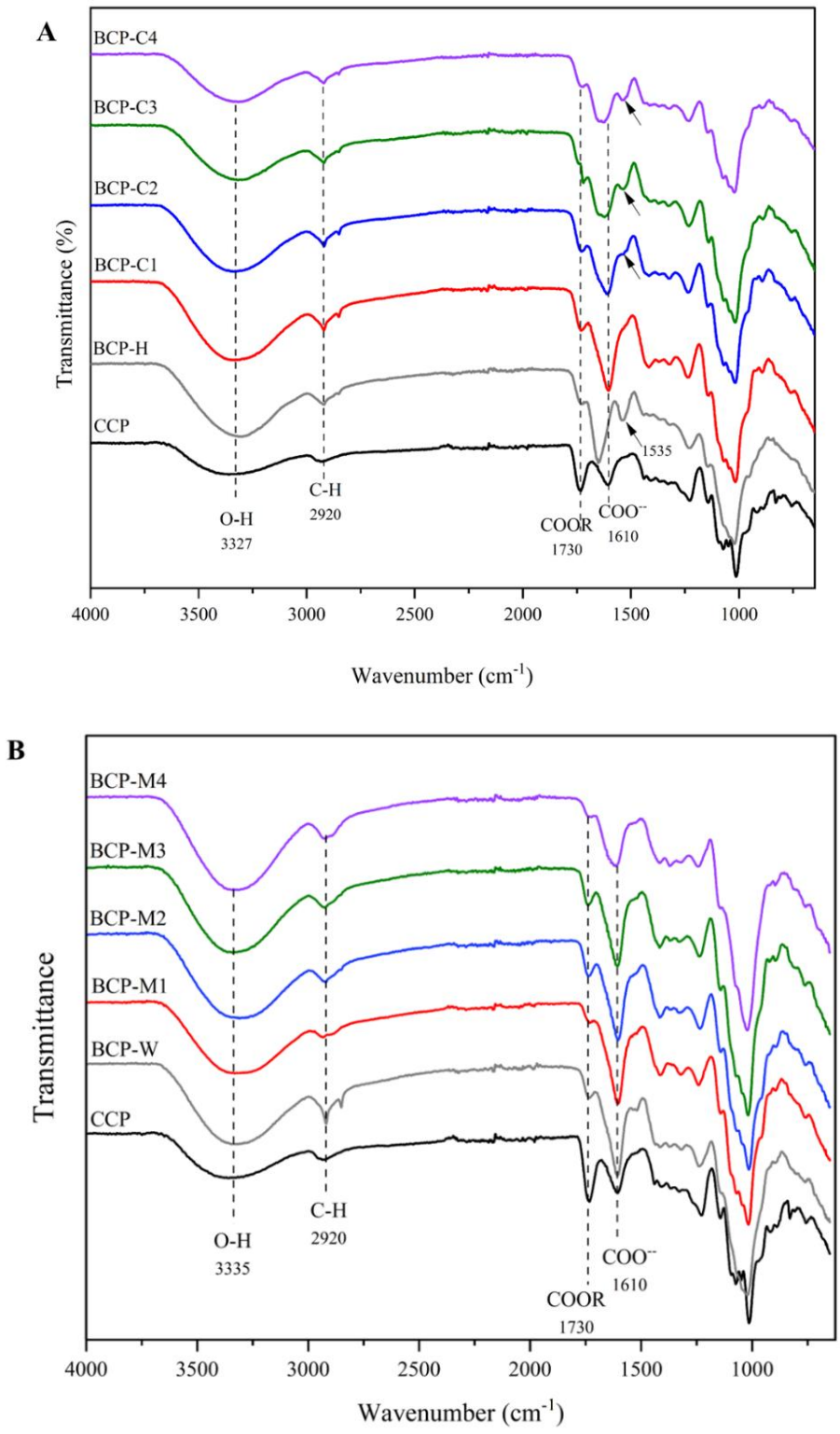

*Figure 3.5. IR spectra of commercial citrus pectin (CCP), acid-derived BCP (**A**), and acid-free derived BCP (**B**).*

Table 3.5. Elemental composition and protein content of BCP

Sample	C (%)	H (%)	N (%)	Protein* (%)
BCP-H	34.70 ± 0.01[a]	4.28 ± 0.46[a]	3.12 ± 0.13[d]	19.50 ± 0.80[d]
BCP-C1	37.66 ± 0.04[d]	4.67 ± 0.19[a]	n.d.	n.d.
BCP-C2	38.55 ± 0.11[e]	4.86 ± 0.25[a]	0.18 ± 0.25[a]	1.13 ± 1.59[a]
BCP-C3	38.82 ± 0.04[e]	4.84 ± 0.10[a]	1.21 ± 0.05[b]	7.53 ± 0.31[b]
BCP-C4	39.54 ± 0.18[f]	4.98 ± 0.07[a]	1.79 ± 0.33[c]	11.16 ± 2.08[c]
BCP-W	35.56 ± 0.02[b]	4.87 ± 0.16[a]	n.d.	n.d.
BCP-M1	34.59 ± 0.07[a]	4.05 ± 0.49[a]	n.d.	n.d.
BCP-M2	35.85 ± 0.01[b]	4.51 ± 0.02[a]	n.d.	n.d.
BCP-M3	36.66 ± 0.09[c]	4.38 ± 0.25[a]	n.d.	n.d.
BCP-M4	37.51 ± 0.04[d]	4.79 ± 0.20[a]	n.d.	n.d.

* Protein content was estimated from N×6.25. Values are presented as mean ± SD (n = 2). Letters indicate the significant differences ($p < 0.05$).

3.1.2.5. Nuclear magnetic resonance spectroscopy (NMR) analysis of BCP

Liquid ^{13}C NMR spectroscopic studies were performed on the CCP and BCP, shown in **Figure 3.6**, and a comprehensive summary of the NMR signals based on CCP and their corresponding regions is presented in **Table 3.6**.[68,100,247] The resonance in the regions of δ60–80 ppm and δ97–105 ppm was characteristic of C2–C5 of monosaccharides and C1 (anomeric) of monosaccharides, respectively. Additionally, the resonances at δ52.7 and δ170.5 ppm were attributed to the CH_3 of methyl ester and C6 of galacturonic acid, respectively. Notably, these resonances decreased when the MW processing temperature exceeded 140 °C, which is indicative of thermal degradation and the decarboxylation of homogalacturonan (HG) or pectin backbone.

For acid-derived BCP, the characteristic resonance at δ52.7 ppm was observed in all BCP-H and BCP-C1 to C4 with lower intensity compared to CCP and BCP-M1 to M3. Meanwhile, the resonance at δ170.5 ppm was difficult to observe. This could be because of low purity of pectin in acid-derived BCP, which is in good accordance with uronic acid and sugar analysis results.

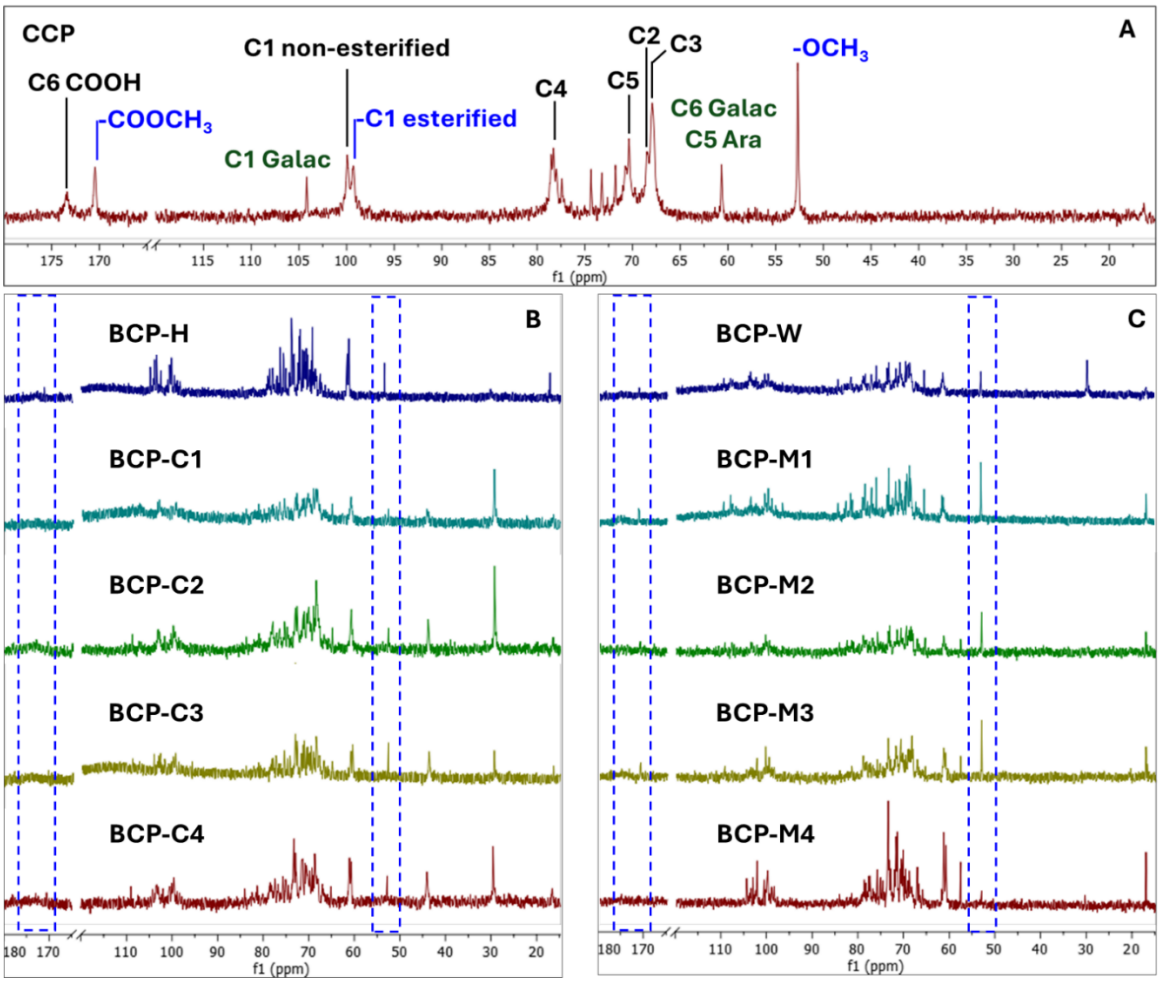

Figure 3.6. ^{13}C NMR spectra of commercial citrus pectin (CCP); black and blue signals define GalA (A), acid derived BCP (B), and free-acid derived BCP (C).

Table 3.6. Summary of ^{13}C NMR signals of pectin based on CCP.

Chemical shift (δ, ppm)	Assignment
173.4	Non-esterified carbonyl GalA (–COOH)
170.5	Esterified carbonyl GalA (–$COOCH_3$)
104.2	C1 Galactose
99.9	C1 GalA non-esterified
99.3	C1 GalA esterified
78.3	C4 GalA
71.8	C5 GalA
68.5	C2 GalA
67.9	C3 GalA
84.1–61.1	C2 to C5 of GalA and sugar residues
60.7	C6 Galactose or C5 Arabinose
52.7	Methyl GalA (–$COOCH_3$)

3.1.2.6. Thermogravimetric analysis of BCP

TGA was performed to assess the thermal stability of the BCP in comparison with CCP (see **Figure 3.7**). All the BCP display three distinct degradation temperatures, which are 25–150 °C, 220–280 °C, and 280–350 °C, corresponding to loss of moisture and volatile compounds, pectin, and hemicellulose or starch, respectively. However, as CCP has been industrially purified it demonstrated a less-pronounced mass loss between 280 and 350 °C, whereas BCP exhibited a higher mass percentage loss within this temperature range.

The dTG of acid-derived BCP (BCP-H and BCP-C1 to C4) reveals that BCP-H has a pronounced decomposition peak between 220–280 °C, while BCP-C1 to C4 exhibit two main decomposition peaks 220–280 °C, and 280–350 °C, in which the intensity of the peak at 280–350 °C is more pronounced with increasing citric acid concentrations. These results supported that BCP-H has higher pectin purity than BCP-C1 to C4. In addition, higher citric acid concentrations have more ability to extract other polysaccharides, such as hemicellulose or starch, which is in a good accordance with the sugar analysis of BCP (see **section 3.1.2.3**)

Interestingly, the dTG of MHT-derived BCP (BCP-M1 to M4) displays a shift in the decomposition peak from 230–310 °C to 250–350 °C, with increasing temperature. The most pronounced shift occurred for pectin processed at 160 °C, suggesting a significant change in the structure of pectin or hydrolysis.[100] At this temperature, other polysaccharides such as hemicellulose and starch also appear to become more soluble. In addition, sugar composition analysis (**Figure 3.4**) supports this observation, as a significant decrease in GalA content at 160 °C indicates reduced pectin recovery. In contrast, the concentrations of Glu and Man*, monomers of hemicellulose or starch, showed a marked increase at this temperature.

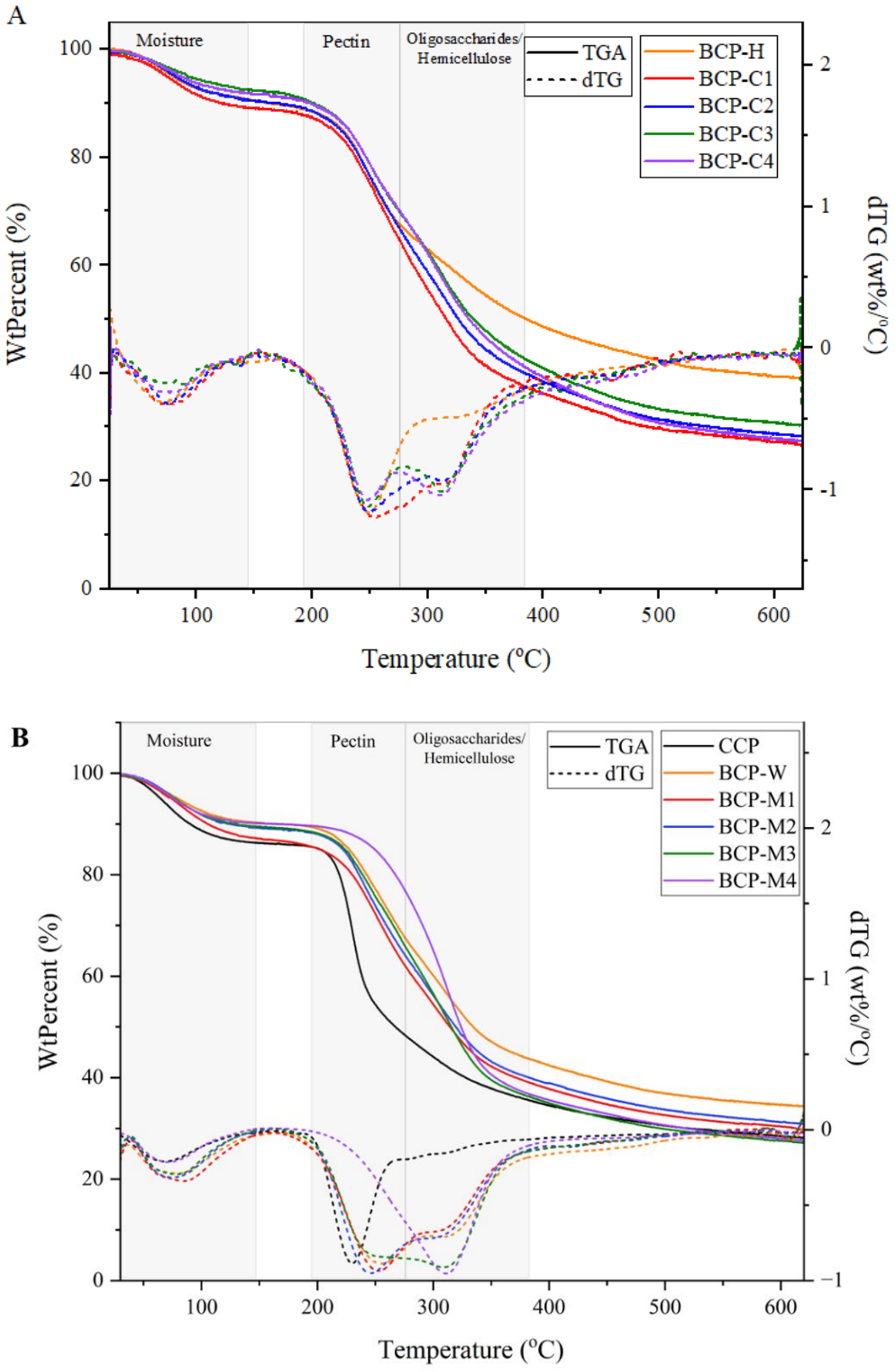

Figure 3.7. TGA and dTG thermogram of CCP, acid-derived BCP (A), and acid-free derived BCP (B).

3.1.2.7. Total anthocyanin content and antioxidant of BCP

Total anthocyanin content (TAC) was determined by colorimetric analysis based on the colour change of anthocyanins (ACN) at pH 1 and pH 4.5 to confirm the presence of anthocyanin-bound BCP (**Table 3.7**). At pH 1, most BCP samples exhibited a pronounced red colour, which can be attributed to the conversion of ACN into the red flavylium cation form at pH < 3,[248] confirming the presence of anthocyanin-bound pectin. However, for most acid-derived BCP samples, including BCP-H, and BCP-C2 to C4, cloudy solutions were observed at pH 4.5 and pH 1 (see **Appendix 8**), likely due to protein precipitation below the isoelectric point (pH 4.5).[144] The presence of protein in theses samples had also been confirmed by IR analysis and elemental analysis (see **section 3.1.2.4**). Protein precipitation interfered with TAC measurement, leading to false-negative TAC values for BCP-H and BCP-C2 to C4. In contrast, acid-free derived BCP samples exhibited TAC values ranging from 0.01 to 0.77 mg C3G/g. TAC decreased with increasing MW treatment temperature, consistent with the fading of the pale pink colour observed in BCP-M1 to BCP-M4 (**Figure 3.3B**).

Table 3.7. Total phenolic content (TPC), total flavonoid content (TFC), anthocyanin content (TAC) and antioxidant activity of BCP.

Sample	TPC (mg GA/g)	TFC (mg QT/g)	TAC (mg C3G/g)	Antioxidant (DPPH inhibition, %)
BCP-H	15.01 ± 0.79^{a}	n.d.	-0.50 ± 0.30*^{c}	21.1 ± 3.4^{bc}
BCP-C1	37.40 ± 0.99^{e}	n.d.	0.38 ± 0.06^{fg}	45.2 ± 2.2^{e}
BCP-C2	38.78 ± 1.40^{e}	n.d.	-0.98 ± 0.12*^{a}	45.0 ± 1.3^{e}
BCP-C3	35.03 ± 1.21^{d}	n.d.	-0.67 ± 0.08*^{b}	30.4 ± 2.8^{d}
BCP-C4	29.44 ± 0.95^{c}	n.d.	-0.69 ± 0.35*^{b}	23.4 ± 2.9^{c}
BCP-W	46.13 ± 1.36^{g}	n.d.	0.59 ± 0.03^{h}	61.3 ± 0.5^{f}
BCP-M1	37.24 ± 0.64^{e}	n.d.	0.77 ± 0.49^{h}	42.9 ± 1.9^{e}
BCP-M2	33.82 ± 0.69^{d}	n.d.	0.41 ± 0.03^{g}	17.4 ± 0.7^{b}
BCP-M3	33.27 ± 0.67^{d}	n.d.	0.17 ± 0.06^{ef}	14.3 ± 1.2^{ab}
BCP-M4	21.35 ± 0.57^{b}	n.d.	0.01 ± 0.01^{de}	3.6 ± 0.8^{a}

*Cloudy solutions were observed at pH 4.5, GA refers to gallic acid equivalent, QT refers to quercetin equivalent, C3G refers to cyanidin-3-glucoside equivalent. Values are presented as mean ± SD (n = 3). Letters indicate the significant differences ($p < 0.05$).

Total phenolic content (TPC), total flavonoid content (TFC), and antioxidant activity (DPPH inhibition, %) of BCP were also determined and are presented in **Table 3.7**. Overall, the antioxidant activity of BCP was primarily attributed to the presence of phenolic compounds and anthocyanins, as flavonoids were not detected (n.d.) in any of the samples. The TPC and antioxidant activity of BCP ranged from 15.01 – 46.13 mg GA/g and from 14.3% – 61.3% DPPH inhibition, respectively. A consistent trend was observed between TPC and antioxidant activity, with BCP-W showing the highest TPC (46.13 mg GA/g) and antioxidant activity (61.3% DPPH inhibition). Both TPC and antioxidant activity decreased with increasing citric acid concentration and MW treatment temperature, suggesting the breakdown of phenolic–pectin linkages.

3.1.3. Microwave-assisted production of defibrillated celluloses from blackcurrant pomace via HCl, citric acid and acid-free conditions (Objective A1 (iii))

This part reports the characterisation of the isolated defibrillated cellulose (DFC) samples obtained from the microwave hydrothermal reprocessing at 160 °C on depectinated blackcurrant residues, produced from pectin extraction via water, MHT, HCl and citric acid (see **section 3.1.2**). Yield of DFC samples derived from depectinated blackcurrant residues ranges from 58.8 – 85.3 wt.%; DFC-H, 58.8 wt.%; DFC-C1, 61.3 wt.%, DFC-C2, 61.6 wt.%; DFC-C3, 60.9 wt.%; DFC-C4, 59.6 wt.%; DFC-W, 68.9 wt.%; DFC-M1, 74.6 wt.%; DFC-M2, 80.3 wt.%; DFC-M3, 80.1 wt.%; DFC-M4, 85.3 wt.%.

3.1.3.1. *Microstructure analysis*

Scanning electron microscopy (SEM) analysis was used to visualise the morphology of commercial microcrystalline cellulose (CMC), DFC-H obtained after 0.2M HCl pectin extraction, followed by MW reprocessing at 160 °C, DFC-C1 to C4 obtained after 0.2 – 0.8 M citric acid, followed by MW reprocessing at 160 °C, and DFC-M1 to M4 derived after MHT at 100 – 160 °C, followed by MW reprocessing at 160 °C (**Figure 3.8**). All isolated DFC from blackcurrant pomace exhibited mainly bulk and rough pallet-like characteristics in different shapes and sizes. The DFC-C1 to C4 surfaces appeared more open-like and smoother as the concentration of citric acid increased; however, the differences were not significant. This suggests that the degree of hydrolysis may not have varied much with change in citric acid concentration. Bondancia *et al*. found that cellulose isolated under shorter reaction times (1.5

h) with 65 wt.% citric acid did not undergo complete hydrolysis.[249] The size and morphology of the cellulose derived from different citric acid conditions may be influenced by reaction time rather than the concentration of citric acid. Interestingly, although Fouad *et al*. and Trache *et al*. suggest a link between smooth surfaces with loss of hemicellulosic and lignin components, detailed IR spectra of the fibres pre- and post-treatment (see **Figure 3.2** and **Figure 3.9**) revealed no significant correlation.[250,251] DFC-H and DFC-C1 to C4 revealed a smoother surface and smaller sizes compared to DFC-W and DFC-M1 to M4. The smaller particle size observed in acid-derived DFC may be due to the breakdown of the internal structure of cellulose, in particular the amorphous regions, during acid hydrolysis in the acid pretreatment step. On the other hand, DFC-M1 to M4 exhibited a flaky surface and uneven bundle structure, with increasing MW temperatures indicating the defibrillation of the fibre bundles.

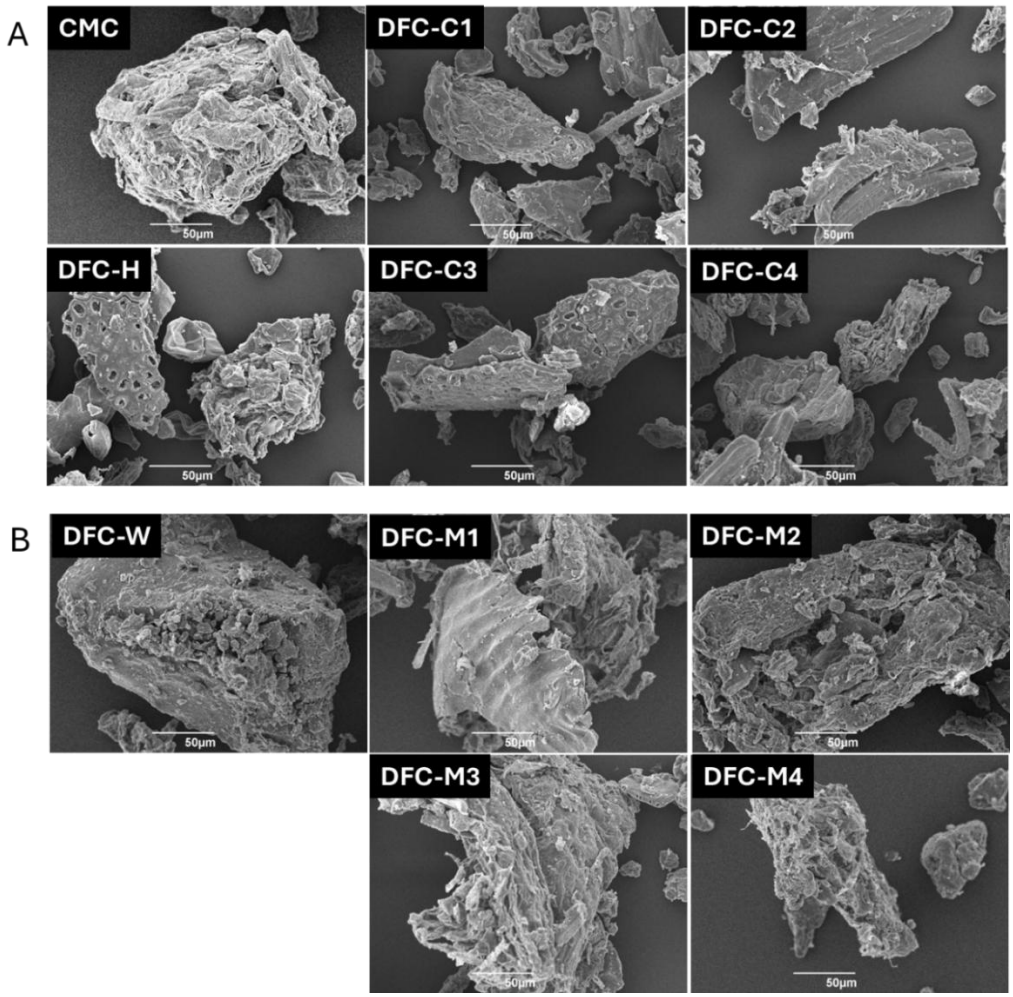

Figure 3.8. SEM images of commercial microcrystalline cellulose (CMC), acid-pretreat derived DFC (A), and acid-free derived DFC (B) at 500× magnification.

3.1.3.2. ATR-IR spectroscopic analysis of DFC

ATR-IR spectra of the isolated DFC from blackcurrant pomace are revealed in **Figure 3.9**. All DFC samples show the main characteristic transmittance peaks associated with the structure of cellulose; broad O-H stretching centred at around 3310 cm^{-1}, C-H stretching at approximately 2920 cm^{-1}. Additional cellulose-related bands were found at roughly 1030 cm^{-1}, corresponding to C-O stretching.[231–233] In addition, the evidence for the presence of hemicellulose, pectin and lignin were observed in all isolated DFC. A small peak at around 1520 cm^{-1} can be confirmed to be an absorption peak of aromatic skeleton,[231,234] which in the corresponds to lignin. The peaks at around 1735 cm^{-1} and 1620-1640 cm^{-1} can be assigned to the carbonyl group in hemicellulose and pectin.[231–233] However, peaks correspond to hemicellulose or pectin are less pronounced compared to raw material (BC pomace; **Figure 3.2**), confirming that those polysaccharides are extracted in the pectin extraction step.

3.1.3.3. Thermogravimetric analysis of DFC

The TGA of DFC samples is presented in **Figure 3.10**. All DFC samples contain mainly cellulose with the main mass loss between 280 – 380 °C, followed by lignin (380 – 475 °C), and peak shoulder below 280 °C, corresponding to residual hemicellulose or oligosaccharides.

Regarding thermal behaviour of DFC, the maximum degradation temperature (T_d) was observed at 336 °C. For acid-pretreat derived DFC, including DFC-H and DFC-C1 to C4, the T_d of these samples (318 – 325 °C) are lower than CMC (336 °C) and BC pomace (330 °C, see **Figure 3.1**). In addition, T_d decreased with increasing citric acid concentrations. Specifically, the T_d values for acid-derived DFC (DFC-H: 318 °C, DFC-C1: 325 °C, DFC-C2: 322 °C, DFC-C3: 324 °C, and DFC-C4: 325 °C) were 5 – 12 °C lower than BC pomace (330 °C), and 11 – 18 °C lower than CMC (336 °C).

In contrast, acid-free derived DFC, including BCP-W, and DFC-M1 to M4, exhibited T_d values (DFC-W: 350 °C, DFC-M1: 345 °C, DFC-M2: 346 °C, DFC-M3: 347 °C, and DFC-M4: 348 °C), approximately 15 – 20 °C higher than that of BC pomace (330 °C), and 5 – 14 °C higher than CMC (336 °C). This suggests that the MW pretreatment for pectin removal has less impact on cellulose structure, preserving its thermal stability.[59] These findings align well with studies on defibrillated cellulose obtained from various sources via acid-free MHT, where T_d values ranged from 340 to 374 °C.[59,60,62] Additionally, the presence of lignin, as evidenced in **Figure 3.11**, contributes to increased thermal stability.[252]

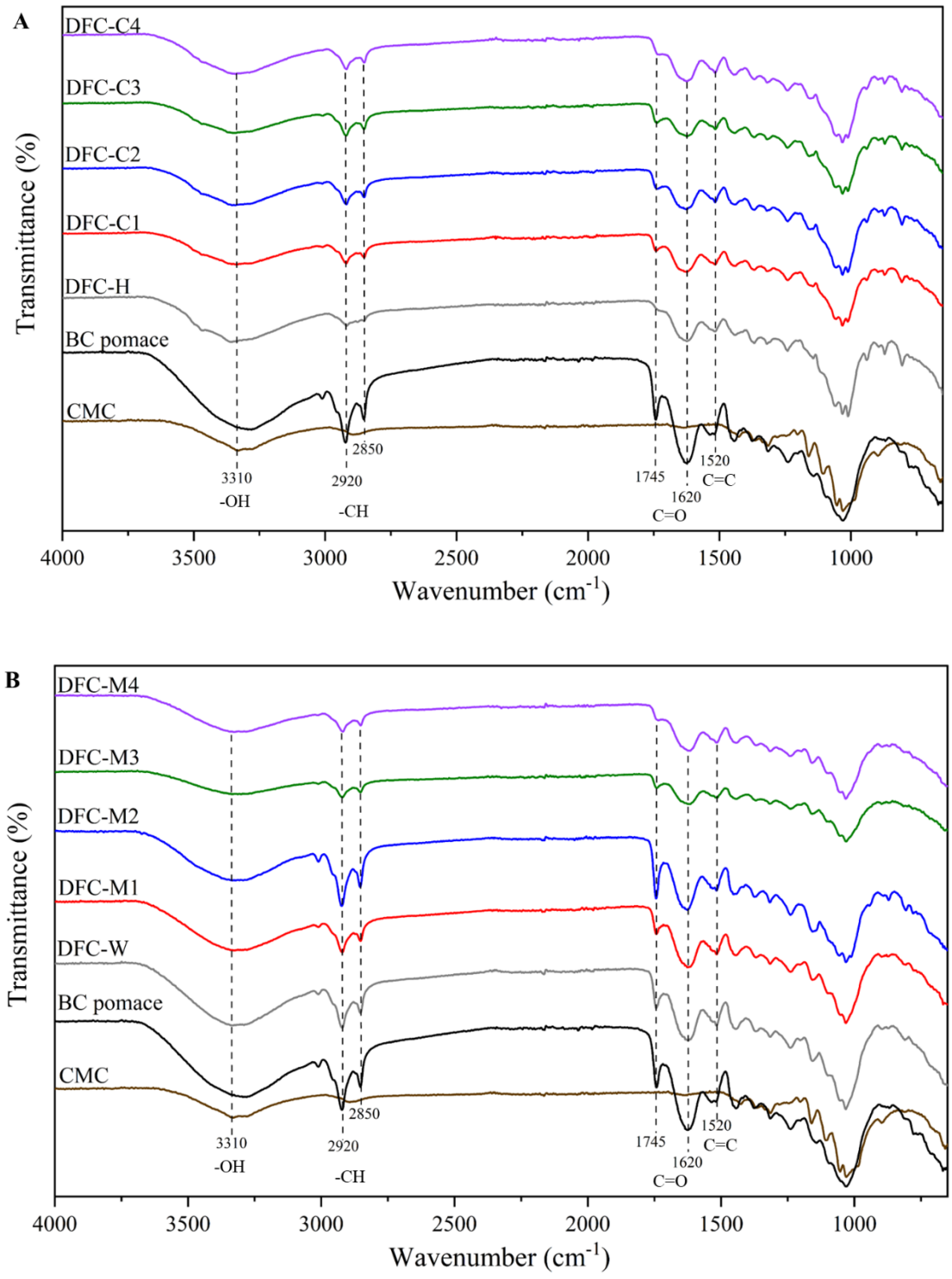

Figure 3.9. ATR-IR spectra of commercial microcrystalline cellulose (CMC), BC pomace, acid-pretreat derived DFC (A), and acid-free derived DFC (B).

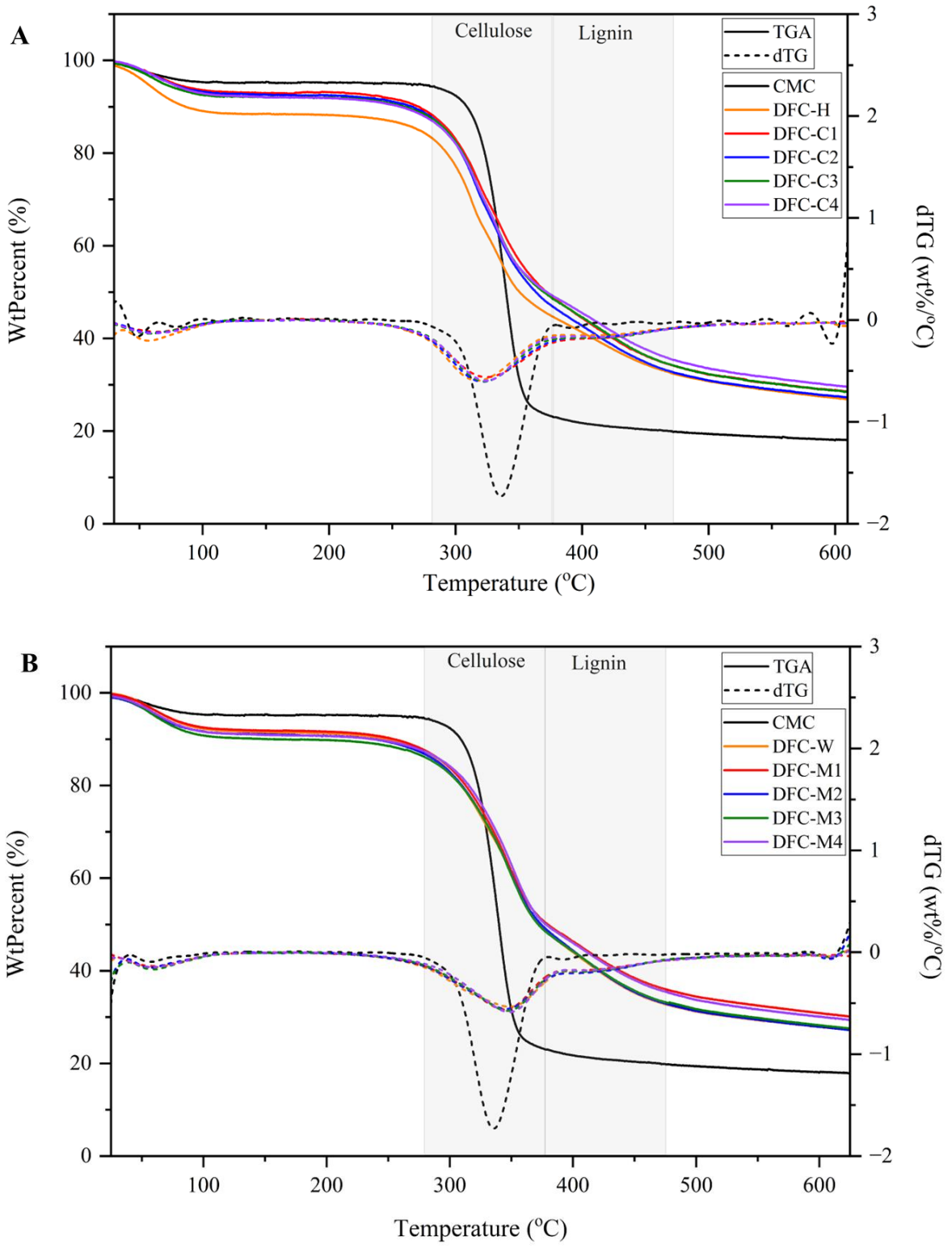

Figure 3.10. TGA and dTG thermogram of CMC, acid-pretreat derived DFC (A), and acid-free derived DFC (B).

3.1.3.4. Klason lignin and sugar analysis of DFC

Lignin and sugar analyses of native BC pomace and DFC samples were conducted to evaluate the impact of pretreatment on removing amorphous non-cellulosic structures (see **Figure 3.11**). All DFC displayed elevated levels of glucose, compared to untreated BC pomace. This increase in glucose suggests that impurities such as hemicellulose, pectin, and lignin were partially removed during pretreatment, leading to a higher observed cellulose content. Moreover, DFC-M1 to M4 exhibited lower concentrations of xylose, denoted as Man*, and GalA, monomers of hemicellulose and pectin, respectively, compared to DFC-H and DFC-C1 to C4. This observation indicates that double MHT processing may be more effective in breaking down hemicellulose and pectin in lignocellulosic biomass than the acid-MHT process, likely due to thermal degradation.

However, lignin content seems slightly increased in acid-derived DFC (45.1 – 49.5%) and acid-free derived DFC (49.4 – 58.3%), compared to BC pomace (46.8%). This can be explained by the complexity of lignin structure, which makes it resistant to degradation during these processes, whereas other components, such as pectin and hemicellulose, are more susceptible to degradation. Additionally, it is possible that pseudo-lignin from 5-hydroxymethyl furfural (5-HMF) and furfural formed at high microwave processing temperatures, which can be observed in microwave-assisted production of defibrillated cellulose from other biomass sources.[36,60,62]

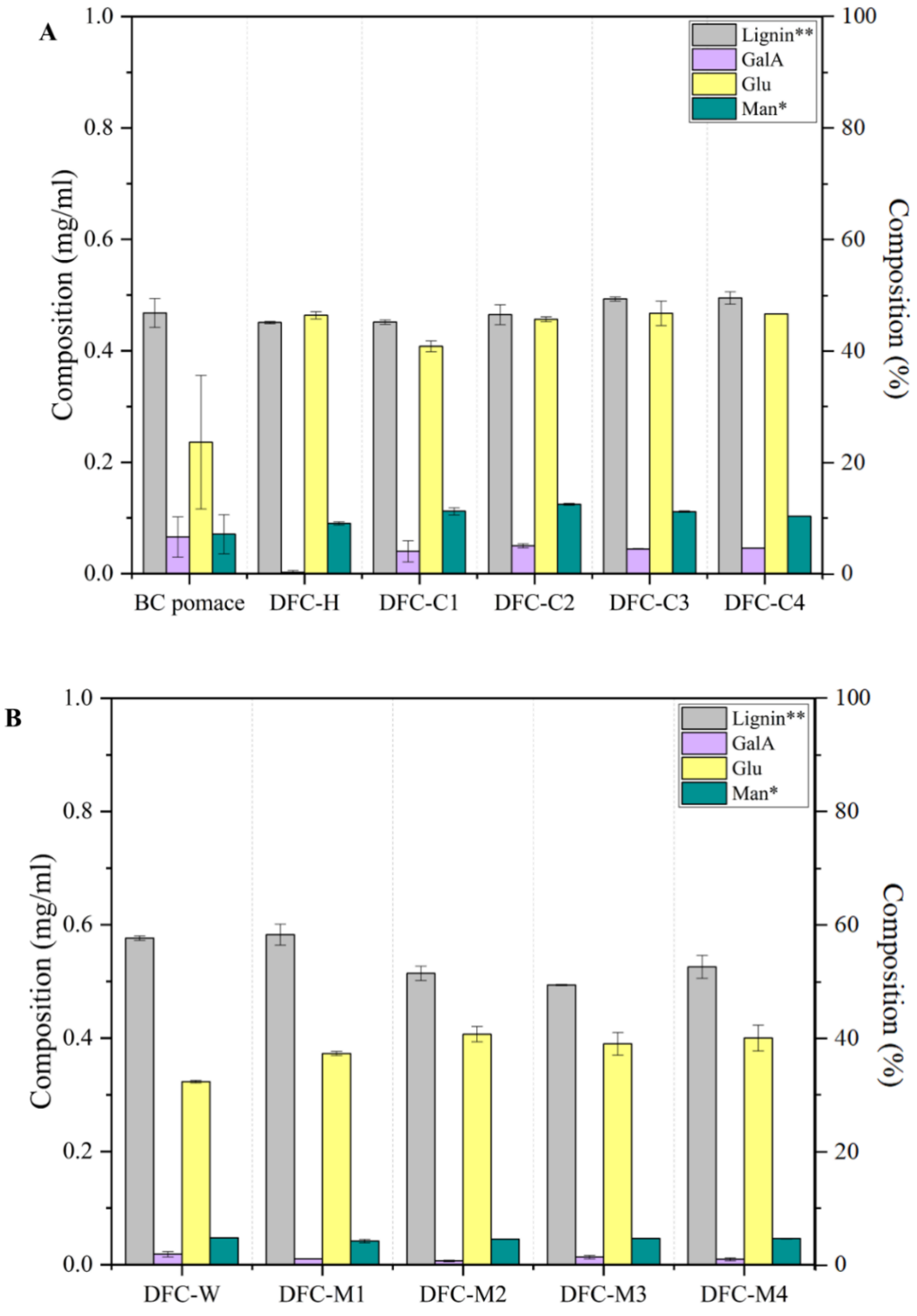

Figure 3.11. Klason lignin and sugar composition of BC pomace, acid-derived DFC (A), and free-acid derived DFC (B); Man includes mannose, xylose, and fructose, Lignin** (%) is estimated based on weight of raw material, and sugar content (mg/ml) in acid-hydrolysed samples is estimated by HPLC. Values are presented as mean ± SD (n = 3). Letters indicate the significant differences ($p < 0.05$).*

3.1.3.5. Powder X-ray diffraction (pXRD) analysis of DFC

The XRD diffractogram of native BC pomace (**Figure 3.12**) showed a primary broad peak with high intensity between 20° and 22°, a secondary broad peak between 15° and 17°, and a low-intensity peak at 34.5°, reflecting a predominantly cellulosic composition.[253] This is also observed in various biomass types, such as coffee husk, corn cob, teff straw and sweet sorghum stalk.[254] After subjecting BC pomace to acid pretreatments (0.2M HCl, or 0.2 – 0.8M citric acid), followed by MHT reprocessing, the resulting DFC-H, and DFC-C1 to C4 (**Figure 3.12A**) showed a change in their XRD patterns. The characteristic peaks observed at approximately 15°, 16°, 20.1°, and 22.3° are indicative of ($1\underline{1}0$), (110), (200) of cellulose I, and (110), (020) of cellulose II. However, the peak at 12.5°, corresponding to ($1\underline{1}0$) of cellulose II, was not observed.[253,255–257] On the other hand, acid-free derived DFC (**Figure 3.12B**) exhibited XRD patterns similar to that of native BC pomace. These findings suggest citric acid pretreatment modifies the structure of cellulose more than microwave pretreatment. However, this observation is inconsistent with the literature, which reported that citric acid treatment did not alter the crystalline structure of cellulose.[258,259]

Lorentzian deconvolution was employed to examine the crystalline pattern of DFC-C1 to C4. Upon pretreatment of BC pomace with citric acid (0.2 – 0.8M), the intensity of the diffraction peak of the (110) plane of cellulose I in DFC-C1 to C4 (**Figure 3.12C**) was found to be higher. With increasing citric acid concentration, the crystalline plane (110) of cellulose II was observed to be shifted to the (020) plane. This indicated that citric acid contributes to enhancing the change in the crystalline plane of cellulose. However, the crystalline plane of acid-free derived DFC (**Figure 3.12B**) remained unchanged compared to native BC pomace, indicating that the crystalline structure of cellulose is not affected by microwave treatment.

There could be another possibility of Xylan crystal contained in acid-derived DFC-H, and DFC-C1 to C4, as lignocellulosic materials are very complex and sugar analysis revealed higher xylose content, denoted as Man*, in DFC-H, and DFC-C1 to C4 compared to native BC pomace, DFC-W, and DFC-M1 to M4 (see **section 3.1.3.4**). DFC-H, and DFC-C1 to C4 exhibit the reflections at around 15.8°, 18.1°, 20.1°, 21.5°, 24.4°, and 26.6°, likely matched with the reflections of the Xylan hydrate crystal reported by Johnson *et al*.[260]

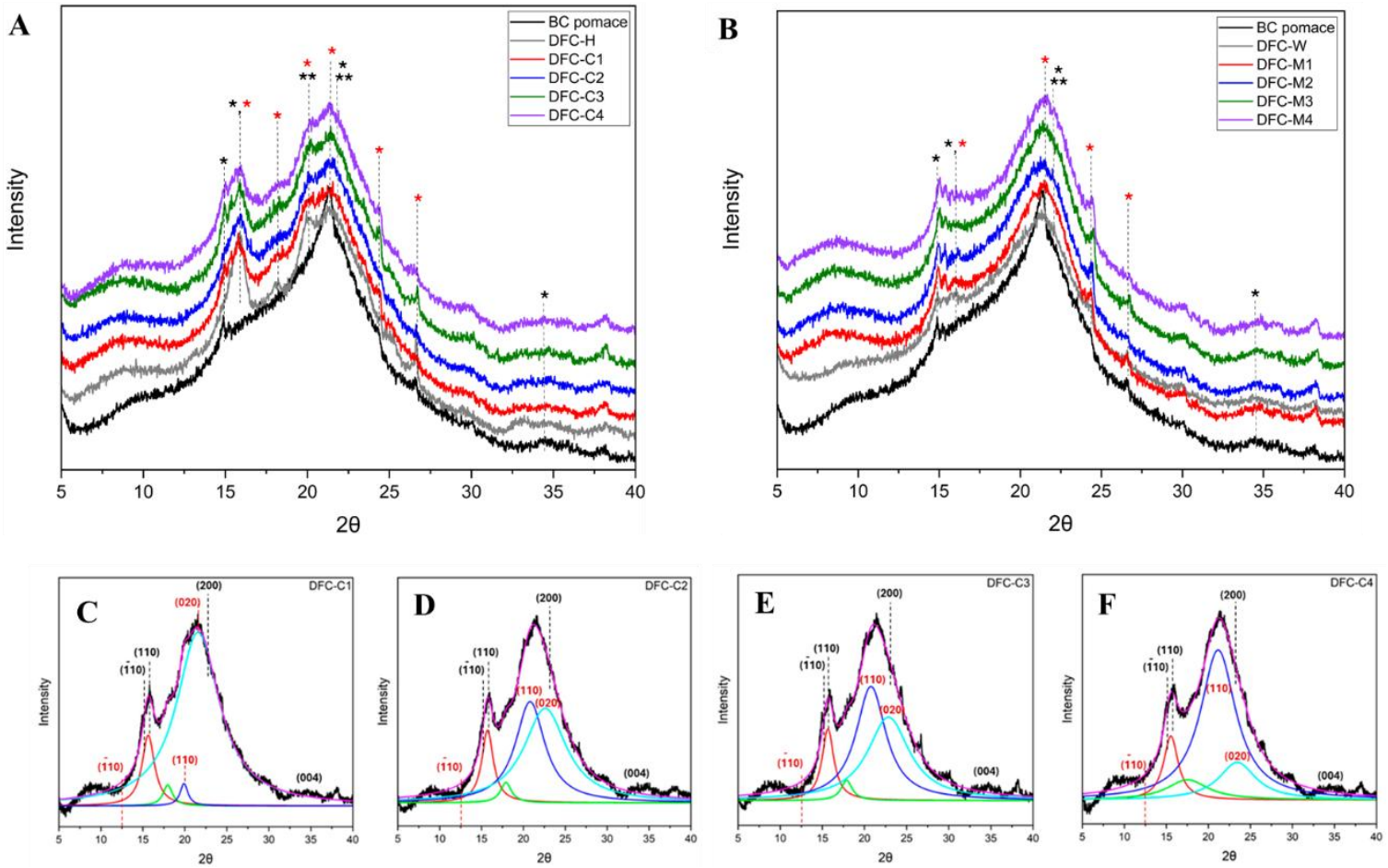

*Figure 3.12. X-ray diffractograms of BC pomace, acid-derived DFC (A), acid-free derived DFC (B); * and ** refer to cellulose I and II, respectively, based on French et al., 2014,[255] and * refers to Xylan hydrate crystal based on Johnson et al., 2023.,[260] and XRD deconvolution of DFC-C1 to C4 (C – F); crystalline plane of cellulose I (black) and cellulose II (red) based on French et al., 2014.[255]*

Regarding the crystalline index (CrI), BC pomace exhibited a CrI of 38.8%, while all DFC samples showed an increase in CrI after pretreatment, ranging from 40.0 to 56.0% (**Table 3.8**). This suggests that acid pretreatment together with MHT reprocessing and double MHT processing induced the changes in the crystallinity index of BC pomace. However, the CrI of DFC-C1 to C4 remained consistent between 43.0% and 44.2%, suggesting that varying citric acid concentrations prior to MHT reprocessing have a minimal impact on the cellulose crystallinity index. In contrast, varying MW temperatures before MHT reprocessing significantly enhanced crystallinity, with the CrI reaching up to 56.0%.

Table 3.8. Crystalline index (CrI, %) of BC pomace and DFC samples.

Sample	CrI (%)	Sample	CrI (%)
BC pomace	38.8		
DFC-H	40.0	**DFC-W**	52.4
DFC-C1	43.1	**DFC-M1**	47.2
DFC-C2	43.5	**DFC-M2**	42.4
DFC-C3	44.2	**DFC-M3**	51.1
DFC-C4	43.0	**DFC-M4**	56.0

Values are presented as single measurements (n = 1); therefore, no statistical comparison among samples was performed.

3.1.3.6. Solid state ^{13}C CP/MAS NMR analysis of DFC

^{13}C CP/MAS NMR spectroscopy was conducted to help characterise the structures of DFCs (**Figure 3.13**). A comprehensive summary of the NMR signals of lignocellulose based on CMC, and Xylan, and their corresponding regions is presented in **Table 3.9**.[261–267] All spectra revealed the presence of C1–C6 of cellulose signals, observed within the range of δ60 to δ120 ppm. Additionally, signals observed in the range of δ20 to δ35 ppm suggested potential evidence of the aliphatic region, supporting the presence of fatty acids or triglycerides and aligning with the IR spectrum (see **Figure 3.9**).[59,261,262] The signals at δ56 ppm and δ174 ppm may be attributed to the methoxy (-OCH_3) group and carbonyl (C=O) group, respectively, in ester bonds of lignin regions.[261] The aromatic signals of lignin ranging from δ110 to δ160 ppm were detected.[263]

The untreated BC pomace and acid-free derived DFCs presented an NMR pattern of cellulose I (**Figure 3.13C**).[264] However, a different pattern emerged in acid-derived DFC (**Figure 3.13D**). There was a splitting peak observed for C1 (at δ102 and δ105 ppm) and C4 (at δ82, 84, and 89 ppm), along with four sub-peaks in the regions of C2, C3, and C5. This difference might be explained by a partial conversion of cellulose I to cellulose II. The characteristic four sub-peaks in the C2, C3, and C5 regions appeared along with the presence of a peak at C6 (δ62 ppm) resembling cellulose II morphology.[264,268,269] The characteristic peak of C6 for cellulose I (at δ65 ppm) was also present,[270] suggesting that the cellulose underwent a partial conversion rather than a complete transformation from cellulose I to cellulose II during the acid pretreatment step.

Table 3.9. Summary of ^{13}C NMR signals of lignocellulose based on CMC and Xylan.

Chemical shift (δ, ppm)	Assignment
174	carbonyl esters of lignin
110 - 160	Aromatics
105	C1 cellulose
102	C1 Xylan (XnC1)
89	C4 crystalline cellulose (C4 Cr)
84	C4 amorphous cellulose (C4 Am)
82	C4 Xylan (XnC4)
75, 73, 72	C2 to C5 cellulose
75, 74	C2, C3 Xylan (XnC2, XnC3)
65	C6 crystalline cellulose (C6 Cr)
63	C5 Xylan (XnC5)
62	C6 amorphous cellulose (C6 Am)

Another possibility is the folding of Xylan structures occurring during the treatment, as evidenced by the presence of peaks at δ105, 72, 75, 82, and 64 ppm, corresponding to XnC1 to XnC5 of twofold Xylan, respectively. In addition, the XnC1 to XnC5 signals of threefold Xylan appeared at δ102, 73, 74, 77, and 63 ppm, respectively.[271] Twofold Xylan can be bound with cellulose microfibrils, which effectively extend the crystalline region in the cellulose system, resulting in better resistance to the microbial hydrolysis process.[271] On the other hand, self-assembled crystal hydrate Xylan can readily form in aqueous solution, in which threefold Xylan may occur in crystalline hydrate form.[260] It can be seen that the folded Xylan signals are prominent in acid-pretreated DFC (**Figure 3.13C**). This may be explained by the treatment of BC pomace in the first step with citric acid or HCl, which can remove sidechain uronic acids of

Xylan, resulting in less solubility of Xylan in water, making it readily self-assembled into twofold, threefold Xylan or Xylan hydrate form. The effect of the Xylan sidechains on the formation of Xylan hydrate crystals has been explained by Johnson *et al*.[260] The presence of xylose in carbohydrate analysis can further confirm the presence of Xylan in DFC samples (see **section 3.1.3.4**).

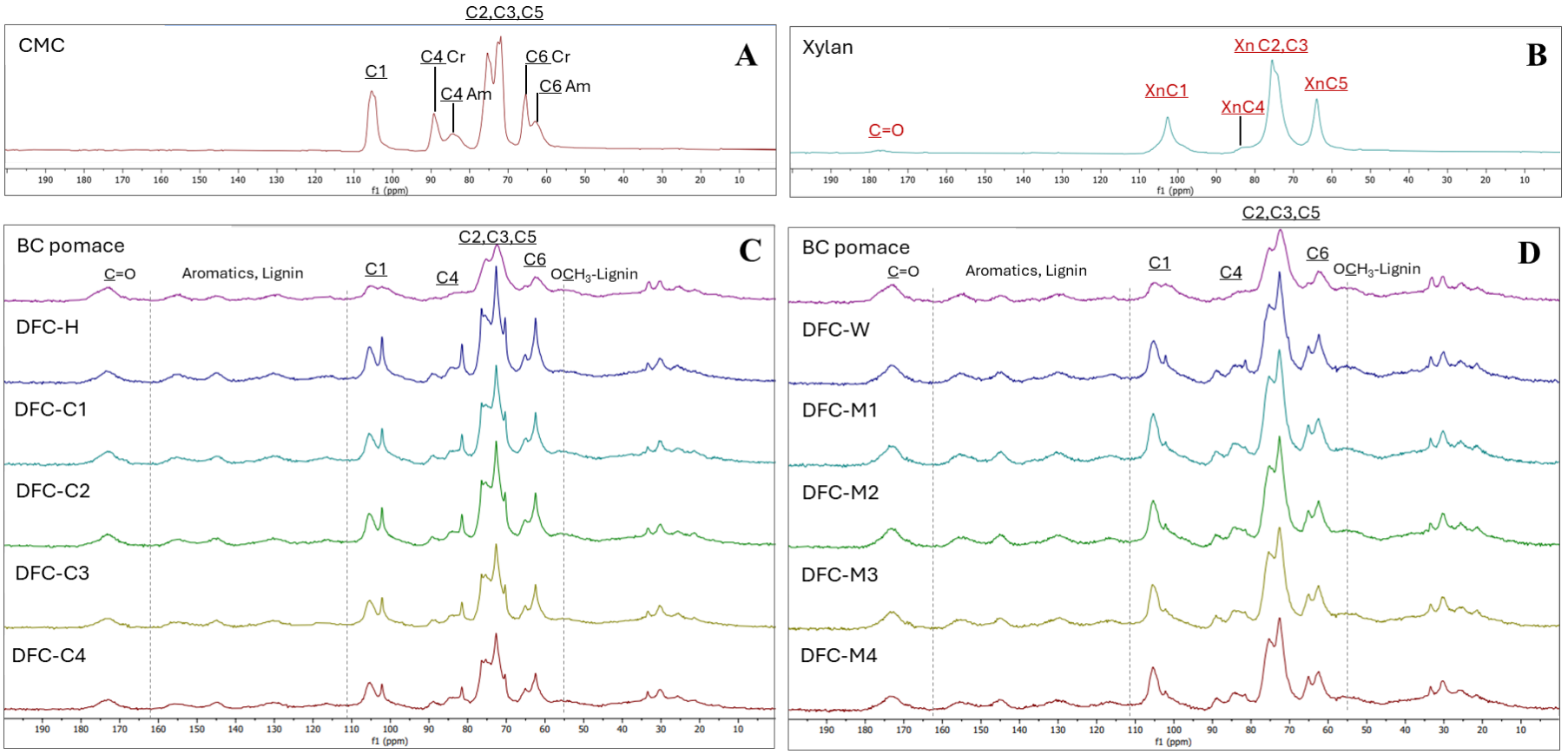

Figure 3.13. Solid state ^{13}C CP/MAS NMR spectra of BC pomace, commercial microcrystalline cellulose (CMC) (A), Xylan (B), acid-derived DFC (C) and acid-free derived DFC (D).

3.1.3.7. Water-holding capacity (WHC) and hydrogel formation

The WHC and hydrogel formation capability of the DFC and their bleached samples (BDFC) are showed in **Table 3.10** and **Figure 3.14**. The higher WHC was observed in acid-derived DFC samples (DFC-H, DFC-C1 to C4; 5.12–5.60 g/g), followed by acid-free derived DFC samples (DFC-W, DFC-M1 to M4; 4.77–5.13 g/g). These values are below those obtained from defibrillated celluloses derived from orange peel and pea waste using acid-free MHT.[59,60] This implies that the DFCs produced from BCP through both acid and MHT pretreatments may not have the same WHC. This difference in WHC may be attributed to the elevated lignin content (approximately 45.1 – 58.3%; **Figure 3.11**) present in the resulting DFCs, as also evidenced in solid state ^{13}C CP/MAS NMR spectra (**Figure 3.13**), and TGA thermograms (**Figure 3.10**), resulting in the interference of hydrogen bonding between polysaccharides and water molecules. Upon the presence of lignin content, alkaline bleaching was performed for delignification of DFC samples. As expected, the WHC of bleached DFC (BDFC) samples increases to 8.97 – 9.69 g/g for acid-derived BDFC; BDFC-H, BDFC-C1 to C4, and 7.95 – 10.86 g/g for acid-free derived BDFC; BDFC-W, BDFC-M1 to M4.

The ability to form hydrogels was tested with CMC, unbleached DFC samples, and bleached DFC samples at concentrations of 2.5%, 5% and 7.5%. CMC and all DFCs derived from BC pomace did not afford a stable hydrogel at any concentration, which may be due to the residual lignin present in DFC samples and high crystalline structure of CMC. Thereafter, alkali bleaching of all DFCs resulted in the formation of stable hydrogels at a concentration of 5% with BDFC-M1 to M4 (**Figure 3.14B**), and the acid-derived BDFC series (BDFC-H, BDFC-C1 to C4) gelling at 7.5% (**Figure 3.14A**). Interestingly, the ^{13}C CP/MAS NMR spectra (**Appendix 9**) of the acid-derived BDFC series (BDFC-H and BDFC-C1 to C4) revealed more crystalline Xylan hydrate, whilst the BDFC-M1 to M4 series revealed less rigid Xylan structures. The latter show propensity to form gels at 5% in water, whilst the former form gels at 7.5% in water. Thus, it appears that cellulose with less rigid Xylan is more favourable for hydrogel formation.

Table 3.10. Water holding capacity (WHC) of DFC and bleached DFC (BDFC) samples

Sample	WHC (g/g)	Sample	WHC (g/g)
DFC-H	5.12 ± 0.17^{ab}	**BDFC-H**	8.97 ± 0.44^{c}
DFC-C1	5.42 ± 0.40^{bc}	**BDFC-C1**	9.69 ± 0.69^{d}
DFC-C2	5.60 ± 0.31^{c}	**BDFC-C2**	8.58 ± 0.01^{b}
DFC-C3	5.38 ± 0.45^{abc}	**BDFC-C3**	8.60 ± 0.29^{b}
DFC-C4	5.48 ± 0.14^{c}	**BDFC-C4**	9.63 ± 0.19^{d}
DFC-W	5.13 ± 0.27^{ab}	**BDFC-W**	7.95 ± 0.47^{a}
DFC-M1	4.77 ± 0.14^{a}	**BDFC-M1**	10.28 ± 0.17^{e}
DFC-M2	5.00 ± 0.24^{a}	**BDFC-M2**	9.83 ± 0.29^{de}
DFC-M3	4.89 ± 0.24^{a}	**BDFC-M3**	9.67 ± 0.59^{d}
DFC-M4	4.91 ± 0.10^{a}	**BDFC-M4**	10.86 ± 0.44^{f}

Values are presented as mean ± SD (n = 3). Letters indicate the significant differences ($p < 0.05$).

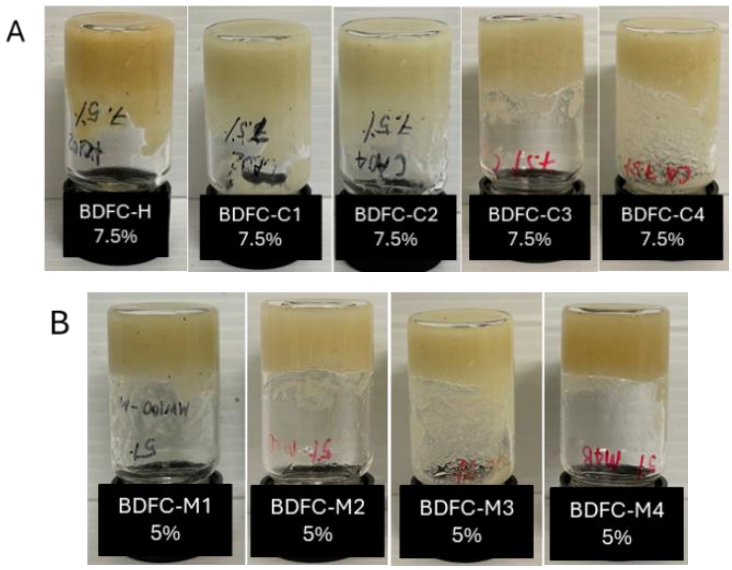

Figure 3.14. Hydrogel formation of acid-derived BDFC samples at 7.5% (A), and acid-free MHT BDFC samples at 5% (B).

3.1.3.8. Rheological studies of hydrogels

The amplitude sweep test, also known as a strain sweep test, is a common oscillatory rheology test used to analyse the viscoelastic properties of hydrogels. To conduct this test, stable hydrogels were prepared from BDFC-H and BDFC-C1 to C4 (7.5%) and BDFC-M1 to M4 (5%). These hydrogels were subjected to increasing shear strain (γ, %) while maintaining a constant angular frequency. The relationship between the increasing shear strain and the storage modulus (G') and loss modulus (G"), describing the solid-like and liquid-like viscoelastic behaviour of the hydrogel, respectively, was plotted. **Figure 3.15A** displays the rheological amplitude sweep curves of the hydrogels derived from 7.5% of BDFC-H and BDFC-C1 to C4 and 5% of BDFC-M1 to M4.

Within the initial phase of small shear strain, the hydrogels exhibited a linear viscoelastic region (LVR). During this region, all hydrogels displayed solid-like viscoelastic behaviour (G' > G"), indicating that the hydrogel behaved more like a solid than a fluid, with elastic behaviour dominating over viscous behaviour. As the shear strain increased, both G' and G" decreased, suggesting that the hydrogel network structure underwent deformation and then reached a crossover point or flow point (G' = G") at a shear strain between 147% and 316%. Past the crossover point, G" value became higher over G', indicating that the hydrogel began to exhibit fluid-like behaviour.[272] The yield point, marking the point at which G' begins to decrease, was found at a shear strain of 0.1% and was comparable between both classes of materials. The ability of cellulose to form gels depends on the degree of fibrillation and surface charge, the increase of both fibrillation and specific surface area can enhance the water holding capacity of fibrillated cellulose.[273,274] However, G' for BDFC-H, and BDFC-C1 to C4 were comparable and higher than that of DFC-M1 to M4, may be due to the higher concentration of the former, resulting in increased gel strength in the hydrogel. The hydrogels made from bleached DFC-C1-C4 (7.5%) and bleached DFC-M1-M4 (5%) exhibited rheological behaviour similar to that of high-consistency enzymatic fibrillated cellulose (HefCel) gel, in which the LVR and yield point occurred at shear strains below 1%, and the flow point was observed beyond 100% strain.[275] Additionally, HefCel cannot form a stable gel at concentrations below 7%.[275]

Flow and thixotropic analyses were performed to investigate the flow behaviour and time-dependent structural changes in BDFC hydrogels, presented in **Figure 3.15B** and **3.15C**,

respectively. The viscosity of all BDFC samples decreases with increasing shear rate, indicating shear thinning behaviour. This phenomenon is linked to the network of defibrillated cellulose disruption under shear action, leading to the aggregation or breakdown of the system and subsequent reduction in viscosity.[276] In addition, subsequently reducing the shear rate allows the network to reform, resulting in an increase in viscosity, and a hysteresis loop within the overall flow curve was observed (**Figure 3.15B(i)** and **3.15B(ii)**), indicating thixotropic behaviour in BDFC hydrogel samples derived from BC pomace. These behaviours have also been found in microfibrillated suspensions of pea hull fibre.[277] However, we note a slightly unusual hysteresis loop showing crossover for sample BDFC-M3 (**Figure 3.15B(ii)**), which may be due to the presence of an artefact in the sample, for example, microscopic particulate matter.

The thixotropy test was conducted to monitor viscosity and structural changes of bleached DFC hydrogels over time. In **Figure 3.15C(i)** and **3.15C(ii)**, it can be seen that all bleached DFC hydrogels gradually decreased with time at a shear rate of 0.1 s^{-1}, and a deep drop was observed with the application of a high shear rate (100 s^{-1}). Then, the bleached DFC hydrogels showed increased viscosity with time, representing the time-dependent behaviour. However, hydrogels derived from bleached MW-DFCs showed lower time-dependent behaviour than bleached CA-DFCs. This again can be explained by the difference in concentration of bleached DFCs in hydrogels, in which 5 wt% MW-DFCs and 7.5 wt% CA-DFCs were prepared, resulting in a stronger and more viscous network structure in bleached CA-DFCs. Both types of bleached DFCs can be considered for industrial food applications, as they show reformed structures over time and can be applied as both functional and nutritional substances.

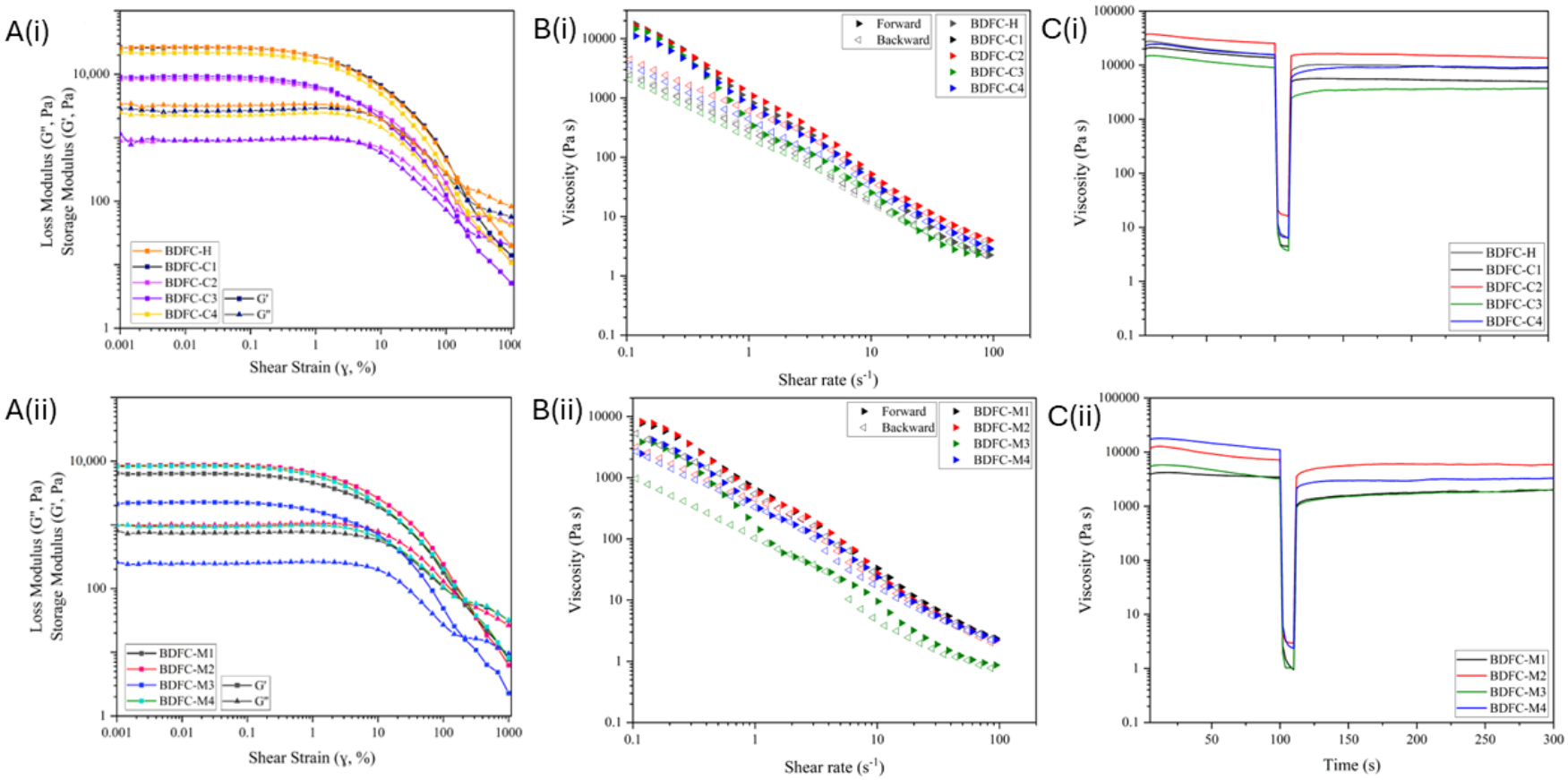

Figure 3.15. Amplitude sweep curves (A), flow curves (B), and thixotropic curves (C) of acid-derived BDFC (i), and acid-free derived BDFC (ii).

3.1.4. Isolation of solvent extractives and characterisation of anthocyanins (ACN)-rich hydrolysates (Objective A1 (iv))

Blackcurrant hydrolysates (BCH), by-products obtained from BC pomace after pectin isolation (**section 3.1.2**), were freeze-dried and retained for further characterisation, as they were expected to contain bioactive compounds with potential antioxidant activity. Solvent extracts of BC pomace prepared using heptane (BCHt), ethanol (BCEt), and a 1:1 ethanol-water mixture (ETW) were included as comparable samples. Additionally, the BCEt extract was further purified with ethyl acetate to yield two fractions: an ethanol–ethyl acetate soluble fraction (BCEt-F1) and an insoluble fraction (BCEt-F2), both of which were also used as comparable samples.

3.1.4.1. Yield of solvent extracts and ACN-rich hydrolysates

The yields and appearances of BC pomace extracts and hydrolysates are shown in **Figure 3.16**. Solvent extractions using solvents of varying polarity (heptane, ethanol, and a 1:1 ethanol-water mixture) produced yields ranging from 3.1 to 8.5 wt.% (**Figure 3.16A**). Among these, the ethanol-water extract (ETW, 8.5 wt.%) showed the highest yield, with 1.5 times more extract than the ethanol extract (BCEt, 5.7 wt.%) and 2.7 times more than the heptane extract (BCHt, 3.1 wt.%). This trend reflects the higher polarity of the ethanol-water solvent, which enables more efficient extraction of polar compounds such as water-soluble carbohydrates, sugars, and highly polar pigments. In contrast, the non-polar solvent (heptane) selectively extracts non-polar constituents such as fats and lipids, which typically account for 2.5 - 16.2 wt.% of BC pomace.[53,63–65] Meanwhile, ethanol is well known to enable to extract non-polar and polar compounds. To further separate these components within the ethanol extract (BCEt), ethyl acetate was employed. The non-polar, ethanol-ethyl acetate soluble fraction (BCEt-F1, 3.3 wt.%) yielded 1.8 times higher than the polar, ethanol-ethyl acetate insoluble fraction (BCEt-F2, 1.8 wt.%). In addition, non-polar extracts (BCHt and BCEt-F1) exhibited totally different colour (dark green) compared to polar extracts (BCEt, BCEt-F2, and ETW; dark purple or dark red).

Acid-free hydrolysates obtained from water extraction and MHT (100 – 160 °C) yield 4.9 – 11.0 wt.%, with higher yields were observed with increasing MW temperatures (see **Figure 3.16B**). These results indicate that higher MW temperatures promote the extraction of additional compounds, possibly due to the formation of organic acids from polysaccharide

components during hydrothermal treatment. The resulting mildly acidic environment may facilitate the hydrolysis of cell wall components, thereby enhancing the release of soluble compounds.

The water-extracted hydrolysate (BCH-W, 4.9 wt.%), a control sample, yielded 1.7 times lower than ETW. This is consistent with the literature that solvent mixtures exhibit more efficient extraction than a single solvent.[75,78] The relatively low yield of BCH-W is also expected, as soluble polysaccharides such as pectin had already been removed in a previous step (**section 3.1.2**). Interestingly, the colour change in MHT hydrolysates (BCH-M1 to M4) was observed with increasing MW temperatures, shifting from dark purple to brown. This change could be due to the thermal degradation of anthocyanins (ACNs), the natural purple pigment.[239] This observation is consistent with the colour changes observed in extracted BCP obtained from MHT (100 – 160 °C; see **Figure 3.3B**).

Acid-derived hydrolysates yielded 14.2 – 66.2 wt.% (**Figure 3.16C**), which is significantly higher than both the solvent extract group (1.8 – 8.5 wt.%) and the acid-free hydrolysate group (4.9 – 11.0 wt.%). These elevated yields are likely due to the strong hydrolysis ability of the acid, which facilitates the release of more compounds into the hydrolysates. However, traces of acid were also present in the resulting hydrolysates, indicating that additional purification would be necessary before further application.

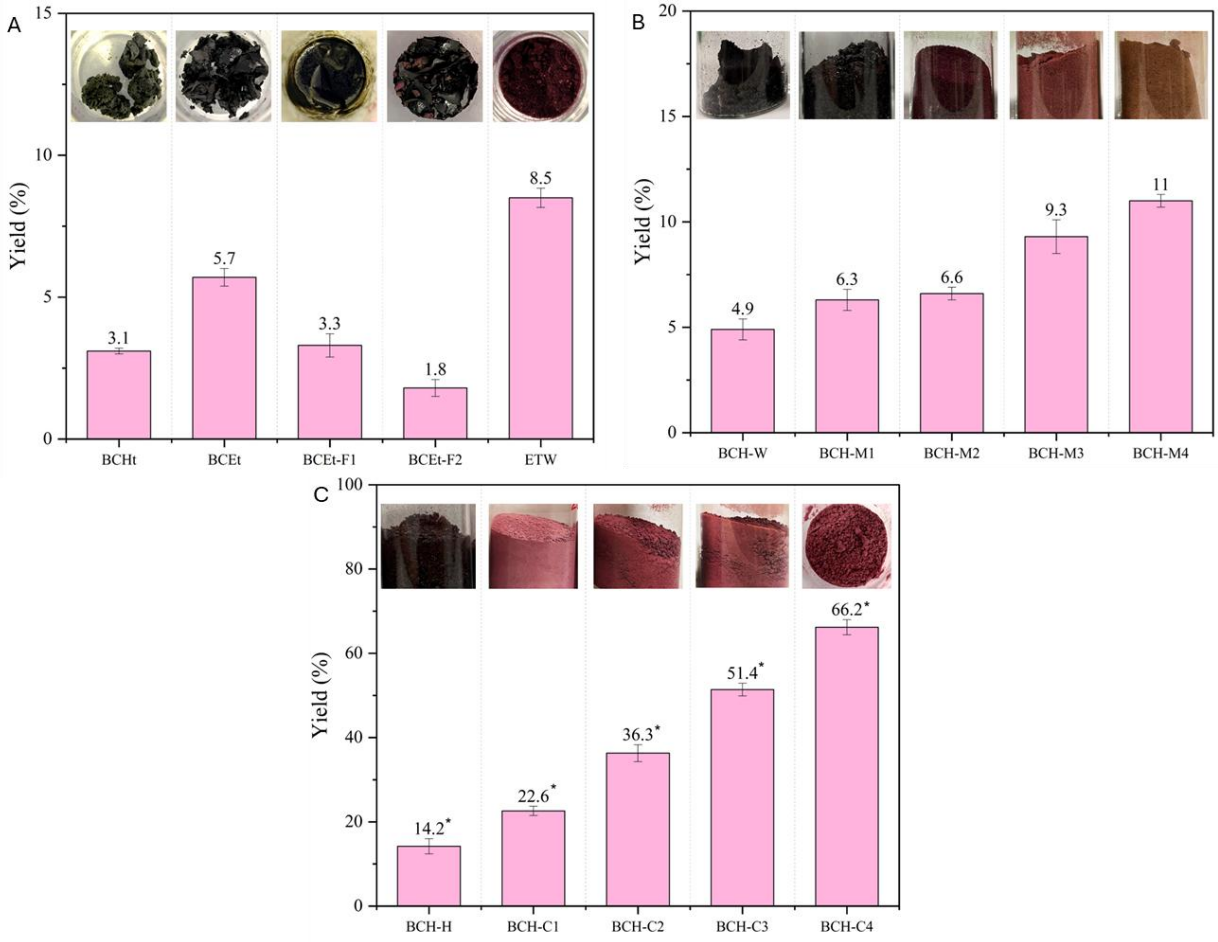

*Figure 3.16. Yield and appearance of solvent extracts (A), acid-free BCH (B), and acid-derived BCH (C); * contained acid traces. Values are presented as mean ± SD (n = 3). Letters indicate the significant differences ($p < 0.05$).*

3.1.4.2. TPC, TFC, TAC, and antioxidant activity of solvent extracts and ACN-rich hydrolysates

The total phenolic content (TPC) of the solvent extracts and BCH was determined using the Folin-Ciocalteu assay, with results expressed as gallic acid equivalents (mg GA/g). Total flavonoid content (TFC) was measured using the $AlCl_3$ assay and reported as quercetin equivalents (mg QT/g). Total anthocyanin content (TAC) was quantified using the pH differential method and expressed as cyanidin-3-glucoside equivalents (mg C3G/g). Antioxidant activity was assessed using the DPPH assay and reported as percent DPPH inhibition (%). The results for TPC, TFC, TAC, and antioxidant activity are summarised in **Table 3.11**.

Table 3.11. TPC, TFC, TAC, and antioxidant activity of solvent extracts and BCH.

Sample	TPC (mg GA/g)	TFC (mg QT/g)	TAC (mg C3G/g)	Antioxidant (DPPH inhibition, %)
Solvent extracts				
BCHt	14.60 ± 1.87^{a}	6.06 ± 0.95^{b}	n.d.	0.0 ± 0.1^{a}
BCEt	30.46 ± 0.54^{c}	19.46 ± 0.95^{c}	10.77 ± 2.67^{i}	46.3 ± 2.7^{c}
BCEt-F1	26.35 ± 1.56^{b}	20.54 ± 0.83^{c}	n.d.	22.1 ± 0.8^{b}
BCEt-F2	44.45 ± 0.24^{d}	20.01 ± 0.41^{c}	83.29 ± 6.38^{k}	91.0 ± 3.1^{k}
ETW	28.30 ± 6.94^{bc}	2.18 ± 1.05^{a}	15.32 ± 2.15^{j}	66.0 ± 1.6^{e}
Acid-free hydrolysates				
BCH-W	10.43 ± 3.92^{a}	n.d.	3.32 ± 2.15^{efg}	56.9 ± 1.4^{d}
BCH-M1	94.31 ± 0.35^{e}	n.d.	7.22 ± 0.66^{h}	85.3 ± 0.1^{h}
BCH-M2	163.82 ± 3.92^{g}	n.d.	4.21 ± 0.53^{g}	85.0 ± 0.4^{h}
BCH-M3	195.54 ± 4.06^{h}	n.d.	0.78 ± 0.04^{a}	86.3 ± 0.5^{i}
BCH-M4	131.07 ± 3.01^{f}	n.d.	n.d.	68.7 ± 0.3^{f}
Acid-derived hydrolysates				
BCH-H	n.d.	n.d.	1.69 ± 0.46^{e}	83.3 ± 1.0^{g}
BCH-C1	n.d.	n.d.	2.68 ± 0.03^{f}	89.4 ± 0.5^{j}
BCH-C2	n.d.	n.d.	1.12 ± 0.03^{d}	89.3 ± 0.3^{j}
BCH-C3	n.d.	n.d.	0.90 ± 0.12^{c}	88.9 ± 0.7^{j}
BCH-C4	n.d.	n.d.	0.93 ± 0.05^{b}	82.2 ± 0.5^{g}

Values are presented as mean ± SD (n = 3). Letters indicate the significant differences ($p < 0.05$).

TPC of solvent extracts and acid-free BCH ranged from 14.60 – 44.45 mg GA/g, and 10.43 – 195.54 mg GA/g, respectively, while TPC was not detected in acid-derived BCH. TFC was observed in only organic solvent extracts, ranging from 2.18 – 20.54 mg QT/g, whereas aqueous solvent extracts were not detected. Meanwhile, TAC was detected in polar solvent extracts, with BCEt and ETW containing 10.77 and 15.32 mg C3G/g, respectively. Further purification of BCEt with ethyl acetate enhanced the TAC by approximately 8 folds, producing BCEt-F2 with 83.29 mg C3G/g. TAC ranged from 0.78 – 7.22 mg C3G/g in acid-free BCH and from 0.90 – 2.68 mg C3G/g in acid-derived BCH.

Interestingly, a great increase in both TPC and TAC was observed in the MHT hydrolysate obtained at 100 °C (BCH-M1) compared with the conventional water hydrolysate (BCH-W). This likely due to the microwave (MW) interaction with polar molecules (water) within the blackcurrant pomace cell walls, generating rapid internal heating that promotes biomass depolymerisation and degradation, thereby facilitating the release of polar compounds such as phenolics and anthocyanins into the hydrolysate. With increasing MHT temperatures (100 - 160 °C), TPC rose from 94.31 mg GA/g (BCH-M1; 100 °C) to 195.54 mg GA/g (BCH-M3; 140 °C), before decreasing to 131.07 mg GA/g (BCH-M4; 160 °C). These results are in good accordance with the literature, showing that microwave-assisted extraction of blackcurrant helps improve phenolic content compared to conventional hot solvent extraction, in which the TPC increased from 31.25 (conventional solvent extraction) to 41.77 mg GA/g (deionised water, microwave, 780 W, 60 min),[101] and from 26.32 (conventional solvent extraction) to 40.19 mg/g (microwave, 600W, 10 min).[278] The TPC yield significantly increases to 58.60 mg/g when microwave-assisted aqueous two-phase extraction was applied.[278] In contrast, TAC decreased progressively with increasing temperature, declining from 7.22 mg C3G/g (BCH-M1; 100 °C) to undetectable (BCH-M4; 160 °C). Although hydrothermal treatment generally promotes the conversion of biomass components into organic acids, creating a mildly acidic environment in which anthocyanins are relatively stable due to the predominance of the flavylium cation form, prolonged exposure to elevated temperatures under severe hydrothermal conditions may still accelerate anthocyanin degradation.

In addition, the increasing TPC trend observed between MHT 100 – 140 °C can be explained by (i) the thermal degradation of ACNs into phenolic compounds. The plausible mechanism of Delphinidin and Cyanidin conversion, the primary ACNs found in blackcurrant, are illustrated based on Oancea and Jiang *et al.* (**Figure 3.17**).[279,280] Phenolic acids such as gallic acid, protocatechuic acid, and 4-hydroxybenzoic acid, are produced through the C2-C3 bond cleavage, whereas phloroglucinaldehyde is generated via C3-C4 bond cleavage of Delphinidin or Cyanidin through hydrolytic cleavage and autoxidative reaction.[280] (ii) Hydrothermal conversion of cellulose- and hemicellulose-derived monomers, such as glucose and xylose, into hydroxymethylfurfural (HMF) or furfural through dehydration at evaluated MHT temperature. These aromatic compounds are soluble in the aqueous phase, thereby elevating the measured TPC values (**Figure 3.18**).[281,282]

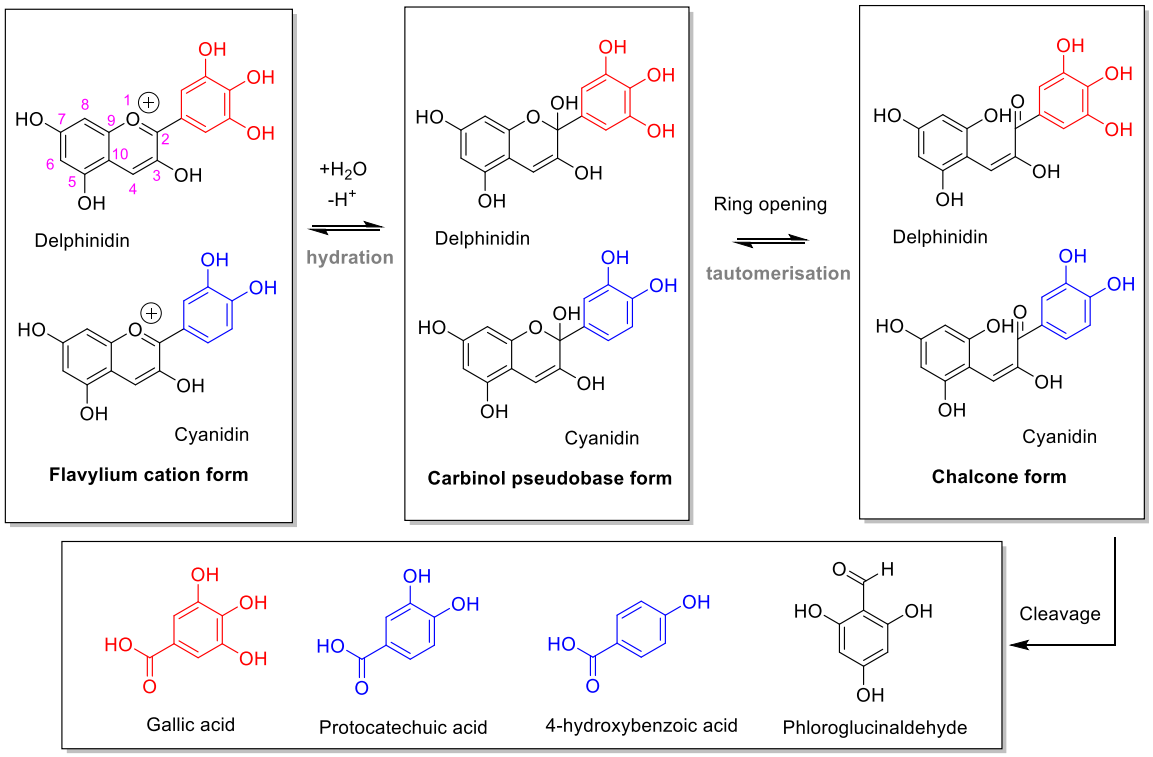

Figure 3.17. Plausible mechanism of thermal degradation of Delphinidin and Cyanidin.[279,280]

At 160 °C, however, the TPC of BCH-M4 decreased to 131.07 mg GA/g. This reduction is likely due to the partial polymerisation or condensation of HMF and furfural with other compounds, including phenolics and aldehydes, forming high-molecular-weight polymeric substances known as humins (**Figure 3.18**).[282] Humins are insoluble in water and were likely removed along with the solid BC residue. The formation of humins or pseudo-lignin is commonly reported at temperatures of 160 °C and above during MHT, particularly in microfibrillated cellulose production.[60,238]

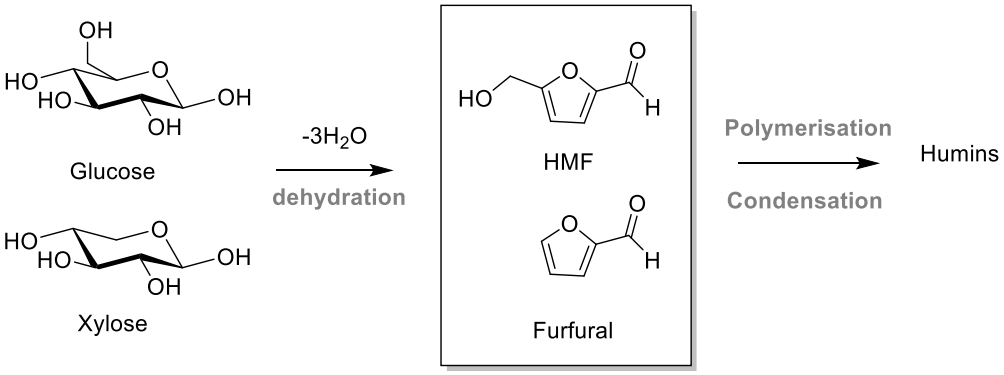

Figure 3.18. Conversion pathway of glucose and xylose to humins.[281,282]

Antioxidant activity of the solvent extracts and BCH samples was evaluated at a concentration of 200 ppm. The solvent extracts showed a wide range of antioxidant activity, from 0.0% to 91.0% DPPH inhibition. Among them, BCEt-F2 exhibited the highest activity, followed by ETW, BCEt, BCEt-F1, and BCHt. The antioxidant activity observed in these extracts was likely influenced by both anthocyanins (ACNs) and phenolics. In contrast, antioxidant activity in acid-free BCH appeared to be driven primarily by phenolics, while in acid-derived BCH it was largely influenced by ACNs, with DPPH inhibition values of 56.9–86.3% and 82.2–89.4%, respectively.

Interestingly, although acid-derived BCH showed high antioxidant activity (up to 89.3% DPPH inhibition), its TAC was relatively low (0.90 – 2.68 mg C3G/g), and both TPC and TFC were undetectable. This discrepancy may be explained by the formation of aggregated, water-insoluble complexes of phenolics and other compounds under the strongly acidic conditions during the freeze-drying of unneutrallised hydrolysates (as observed experimentally; **Appendix 8**). Such aggregation can cause false-negative results in TPC, TFC, and TAC assays, which are designed to measure soluble free phenolics, flavonoids, and anthocyanins rather than their bound or polymerised forms.

3.1.4.3. Characterisation of anthocyanins in solvent extracts and BC pomace hydrolysates.

Given the special properties of ACNs as natural pigments, pH-responsive compounds, antioxidant compounds, and their presence in most of BC pomace solvent extracts and hydrolysates (see **section 3.1.4.2**), further characterisation of ACNs was evaluated using high performance liquid chromatography-diode array detector-mass spectrometry (HPLC-DAD-MS/MS), following the method based on Šimerdová *et al.*[210] Chromatograms of major ACNs in solvent extracts and BCH are presented in **Figure 3.19** and their analyses are summarised in **Table 3.12**. In addition, the insets within each chromatogram illustrate the relative proportions of each ACNs among the total detected ACNs, based on peak areas (**Figure 3.19**).

Table 3.12. Summary of HPLC-DAD-MS data for blackcurrant anthocyanins in the solvent extracts and BCH, including retention time, molecular weight, molecular formula, fragmentation patterns, and absorbance maxima.

Identified compound	t_R (min)	Molecular Formula	Molecular Weight	$[M+H]^+$ (m/z)	Fragmentations MS^2 (m/z)	Absorbance (nm)
D3G	6.4	$C_{21}H_{21}O_{12}^+$	465.3865	465	465, 303	526
D3R	7.0	$C_{27}H_{31}O_{16}^+$	611.5285	611	611, 465, 303	526
C3G	7.6	$C_{21}H_{21}O_{11}^+$	449.3875	449	449, 287	518
C3R	8.4	$C_{27}H_{31}O_{15}^+$	595.5295	595	595, 449, 287	518

Across all solvent extracts and BCH samples, four major ACNs were identified, which are delphinidin-3-glucoside (D3G), delphinidin-3-rutinoside (D3R), cyanidin-3-glucoside (C3G), and cyanidin-3-rutinoside (C3R). These compounds were confirmed through their mass spectra and fragmentation patterns (**Appendix 10**). The types of ACNs detected in this study align well with previous literature; however, the retention times observed in our chromatograms appear slightly earlier than those reported by Šimerdová *et al.*[210]

It is obviously seen that among all solvent extracts, the ETW shows the highest intensities of the four ACNs, followed by BCEt, while the signals disappear completely in BCHt (**Figure 3.19A**). Further purification of BCEt sample with ethyl acetate increased the intensities of all four ACNs in the BCEt-F2 fraction to levels higher than those in ETW, whereas the BCEt-F1 fraction showed no detectable ACNs. Similar trend was observed in the TAC analysis (**section 3.1.4.2**), where ACNs were not detected in BCHt or BCEt-F1, and the highest TAC was observed in BCEt-F2, followed by ETW and BCEt. With respect to the relative proportions of each ACN, the glucoside forms of delphinidin and cyanidin (D3G and C3G) appear to dissolve preferentially in less polar solvents (e.g., ethanol). Their percentages were higher in BCEt and BCEt-F2, ranging from 21.8 – 22.3% for D3G and 8.6 – 9.7% for C3G, compared with ETW (D3G: 16.9%; C3G: 5.9%).

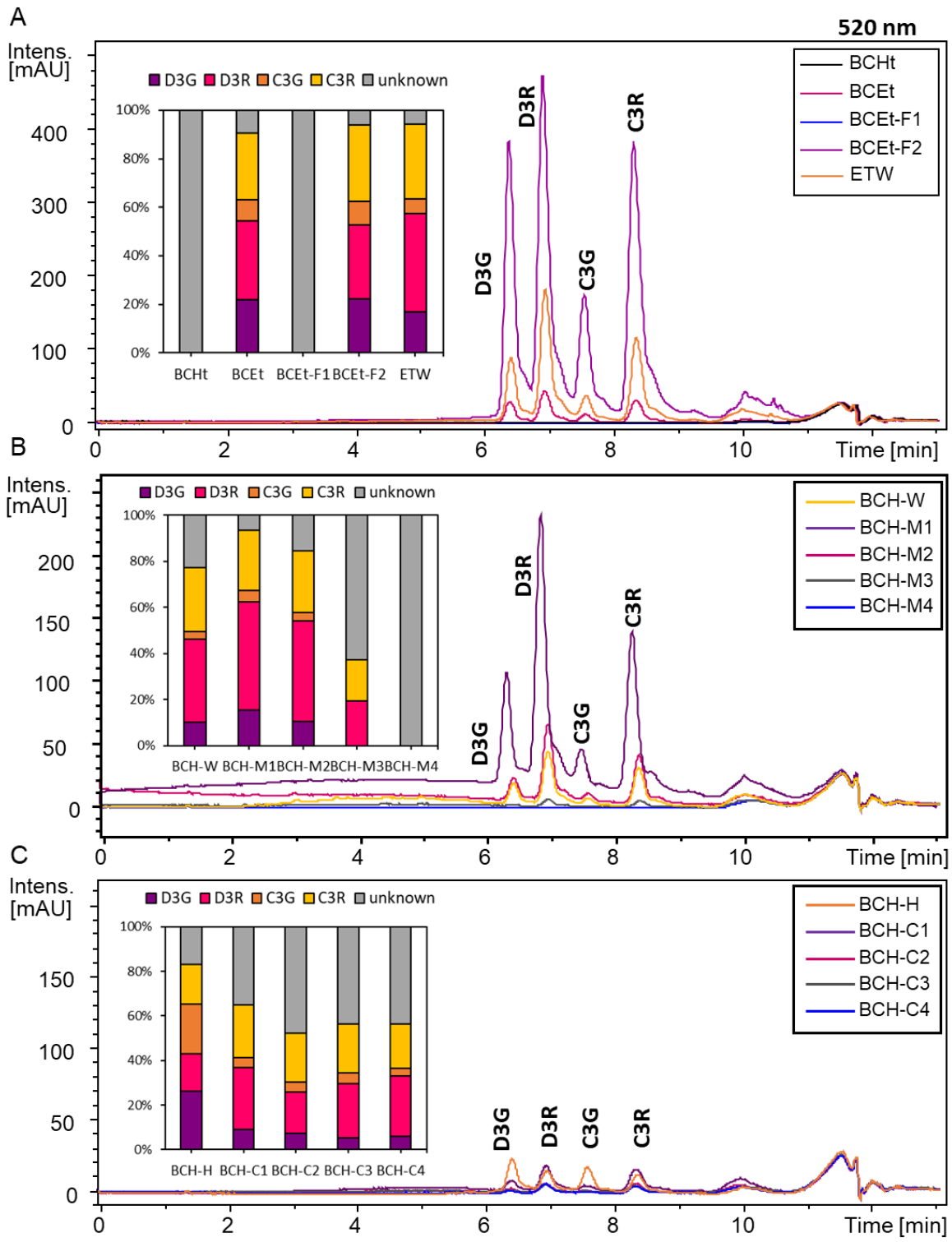

Figure 3.19. Chromatograms of anthocyanins detected at 520 nm in solvent extracts (A), acid-free BCH (B), acid-derived BCH (C). Insets within each chromatogram illustrate the relative percentage of each anthocyanin among the total detected.

Interestingly, the HPLC-DAD-MS/MS results support the TAC findings for BCH (**section 3.1.4.2**). Acid-free BCH samples show higher ACN intensities than acid-derived BCH (see **Figures 3.19B** and **3.19C**). In addition, BCH-M1 exhibited stronger ACN signals than BCH-W, and a decreasing trend in ACN intensities was observed with increasing MHT temperature. In the BCH-W sample, the four ACNs accounted for 10.3% D3G, 35.9% D3R, 3.2% C3G, and 28.0% C3R. These values suggest that the rutinoside forms preferentially dissolve in more polar solvents (such as water), in contrast to the ethanol-based BCEt extracts. MHT at 100 °C (BCH-M1) improved ACN extraction, increasing the relative proportions to 15.5% D3G, 47.0% D3R, 4.8% C3G, and 26.2% C3R. All four ACNs increased in BCH-M1 compared with BCH-W, indicating that MHT at 100 °C enhances ACN extraction, but not specific in each ACN.

With increasing MHT temperatures from 100 – 160 °C, the intensities of all four ACNs progressively declined and were completely absent at 160 °C (BCH-M4), likely due to thermal degradation, as previously discussed in **section 3.1.4.2**. At 140 °C (BCH-M3), only D3R and C3R remained detectable. This may indicate that these ACNs are either more thermally resistant than their glucoside counterparts or are present in higher initial concentrations in BC pomace, causing them to degrade more slowly.

Interestingly, increasing citric acid concentrations (0.2 – 0.8 M; BCH-C1 to C4) did not noticeably alter the relative proportions of the four ACNs (**Figure 3.19C**). In these samples, the rutinoside forms (D3R and C3R) consistently appeared in higher proportions than the glucoside forms (D3G and C3G), similar to the patterns observed in the solvent extracts (**Figure 3.19A**) and acid-free BCH samples (**Figure 3.19B**). In contrast, extraction with 0.2 M HCl significantly changed the proportions of four ACNs in BCH-H (**Figure 3.19C**), where the glucoside forms (D3G; 26.1% and C3G; 22.2%) were higher than the rutinoside forms (D3R; 16.9% and C3R; 18.0%). This shift can be attributed to the strong acid hydrolysis capability of HCl, which is sufficient to hydrolyse the glycosidic linkage between glucose and rhamnose in the rutinoside forms, leading to the removal of the rhamnose moiety and the formation of the corresponding glucosides (D3G and C3G). The proposed fragmentations of D3G, C3G, D3R, and C3R, based on their mass spectrometric patterns (see **Table 3.12**), are illustrated in **Figure 3.20**.

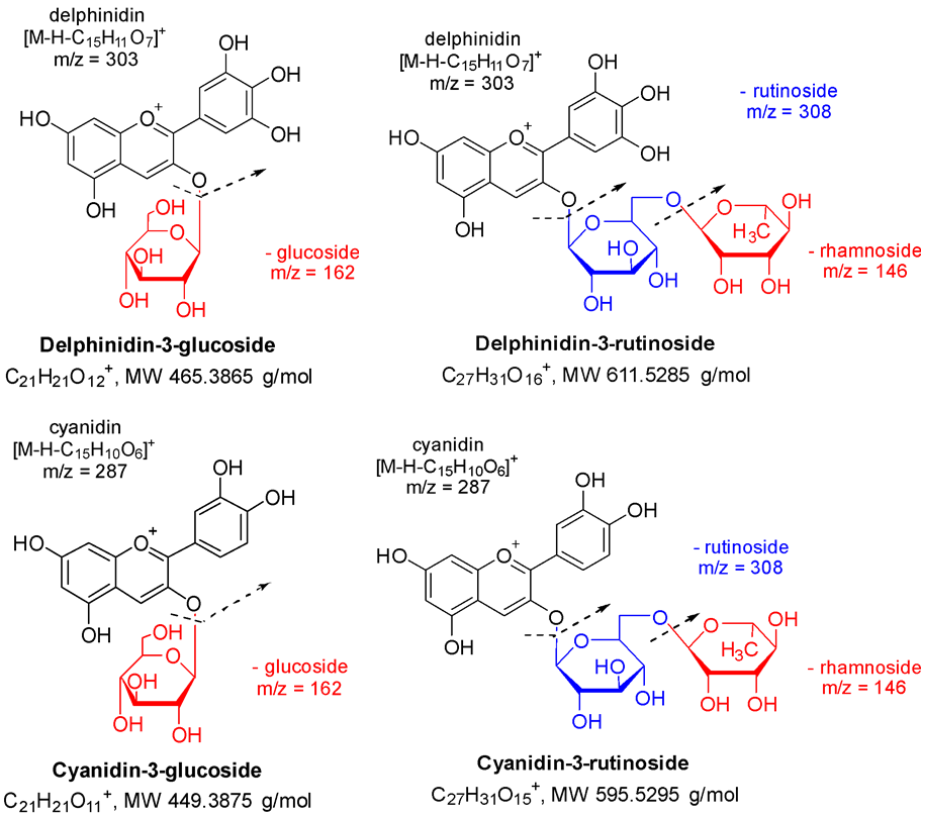

Figure 3.20. Proposed fragmentation patterns of delphinidin-3-glucoside (D3G), delphinidin-3-rutinoside (D3R), cyanidin-3-glucoside (C3G), and cyanidin-3-rutinoside (C3R).

3.1.4.4. Characterisation of solvent extracts and BC pomace hydrolysates.

Apart from determination of aromatic compounds such as phenolics, flavonoids, and anthocyanins, other types of compounds in solvent extracts and BCH were preliminary scanned through proton nuclear magnetic resonance (^{1}H-NMR). The ^{1}H-NMR spectra of the solvent extracts and BCH were illustrated in **Figure 3.21**and **Figure 3.22**, respectively. *Singlet* signals at δ 2.16 ppm, δ 4.7 ppm (*broad*), and δ 7.26 ppm correspond to residual acetone, D_2O solvent, and $CDCl_3$ solvent, respectively. Additional signals at δ 1.06 ppm (*triplet*), δ 3.49 ppm (*quartet*), and δ 4.7 ppm (*broad*) represent the CH_3, CH_2, and OH groups of residual ethanol or ethanol-D_2 solvent. These solvent-related signals can be ignored.

The ^{1}H-NMR spectra of BCHt, BCEt, and BCEt-F1 display similar patterns characteristic of plant oils, particularly triglycerides and their hydrolysis products, fatty acids (**Figure 3.21**). The major peaks and their assignments, based on typical triglyceride structures, are summarised in **Table 3.13**.[283,284] These spectra highlight several key signals commonly

associated with triglycerides or free fatty acids, which are expected components resulting from triglyceride hydrolysis.

Table 3.13. Summary of ^{1}H NMR signals of blackcurrant heptane extract (BCHt) and ethanol extracts (BCEt and BCEt-F1).

Signal	Chemical shift (δ, ppm)	Assignment
A	0.89 (*m*)	Terminal -CH_3 of fatty acids or triglycerides
B	0.97 (*m*)	Terminal -CH_3 of fatty acids or triglycerides
C	1.22 – 1.42 (*m*)	Long chain CH_2
D	1.52 – 1.70 (*m*)	β-CH_2 to carbonyl
E	1.94 – 2.14 (*m*)	CH_2 groups adjacent to C=C double bonds
F	2.33 (*m*)	α-CH_2 to carbonyl
G	2.77 – 2.80 (*m*)	CH_2 between two double bonds (polyunsaturated region)
H	4.10, 4.30 (*dd, dd*)	Glycerol -OCH_2
I	5.26 (*m*)	Glycerol -OCH
J	5.36 (*m*)	Protons on the C=C double bonds of fatty acids or triglycerides

However, due to the complex composition of oils and triglycerides, ^{1}H-NMR analysis alone could only provide preliminary identification of compound types present in BCHt, BCEt, and BCEt-F1 extracts. More detailed structural characterisation will further discuss in GC-MS analysis section. The results also indicate that heptane is more selective for extracting triglycerides and fatty acids than ethanol. Although ethanol is a polar solvent, making triglycerides less soluble under normal conditions, its use under reflux improves their solubility and enables partial extraction. Furthermore, additional purification of BCEt using ethyl acetate to obtain the ethanol-ethyl acetate-soluble fraction (BCEt-F1) increases the purity of triglycerides and fatty acids in the final extract.

Ethanol can extract a broader range of compounds which are not only triglycerides and fatty acids, but also aromatic compounds, citric acid and sugars. This is evident in the ^{1}H-NMR spectra of the ethanol-ethyl acetate-insoluble fraction (BCEt-F2), which reveals the signals corresponding to citric acid (*dd*, δ2.73 ppm), sugar region (δ3.3 - 5.5 ppm), and aromatic region

(δ5.5 - 8.5 ppm) (**Figure 3.21** and **Table 3.14**). The ETW extract displays a similar spectral profile to BCEt-F2. The presence of sugars in both BCEt-F2 and ETW is further supported by the sugar analysis results (**Appendix 11**).

Based on solvent polarity, it is obvious that heptane selectively extracts non-polar compounds such as triglycerides and fatty acids. In contrast, ethanol-water preferentially extract polar compounds such as citric acid and sugars. Ethanol can extract a broader range of compounds in both non-polar and polar compounds.

Table 3.14. Summary of ^{1}H NMR signals of blackcurrant ethanol extracts (BCEt-F2), ethanol-water extract (ETW), and blackcurrant pomace hydrolysates (BCH).

Chemical shift (δ, ppm)	**Assignment**
2.50 – 3.00 (*dd*)	-CH_2 of citric acid
3.30 – 5.30	Sugars or polysaccharides
5.50 – 8.50	Aromatics

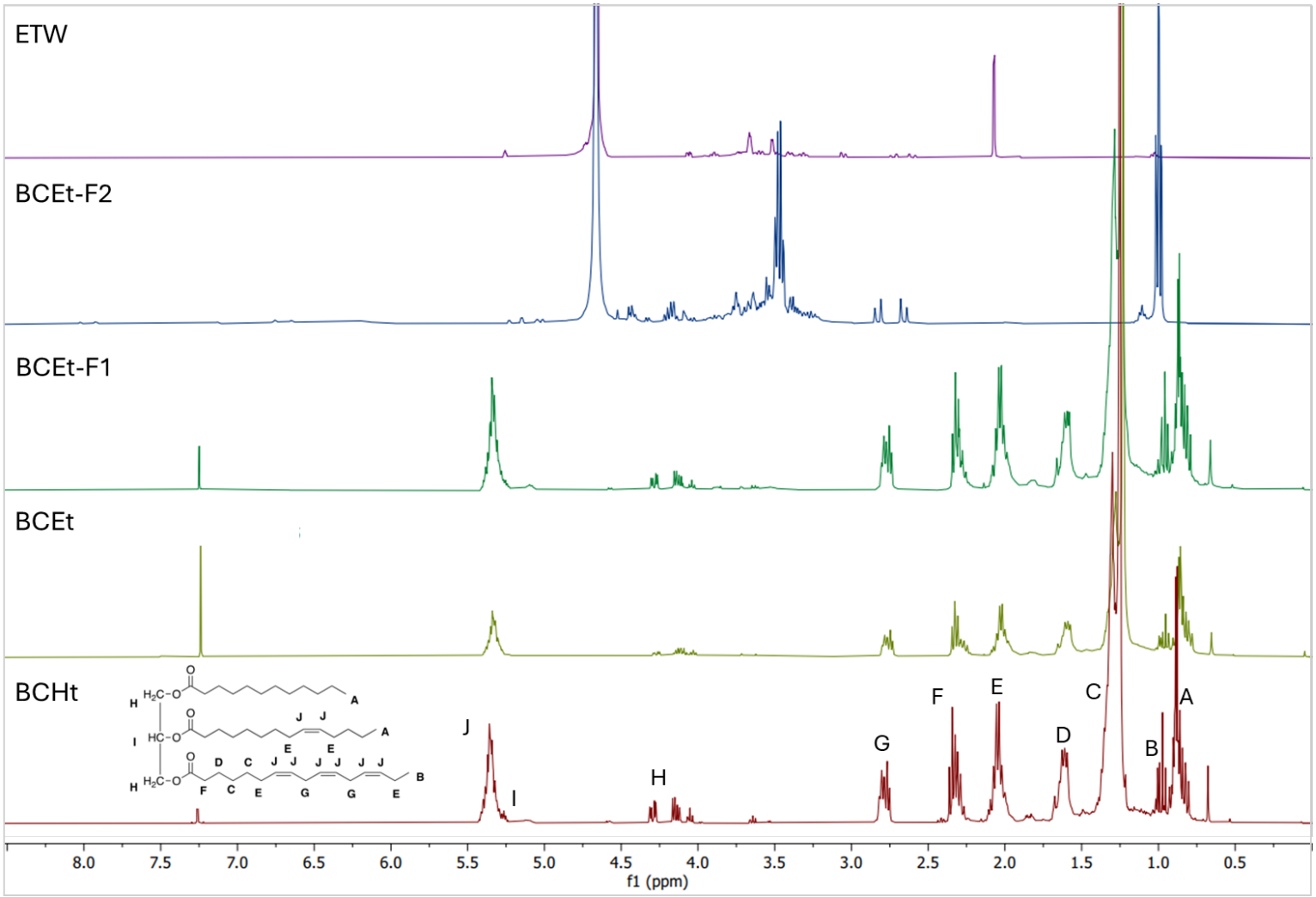

Figure 3.21. ^{1}H-NMR spectra of solvent extracts; BCHt, BCEt, and BCEt-F1 in $CDCl_3$, BCEt-F2 in ethanol-D2, and ETW in D_2O.

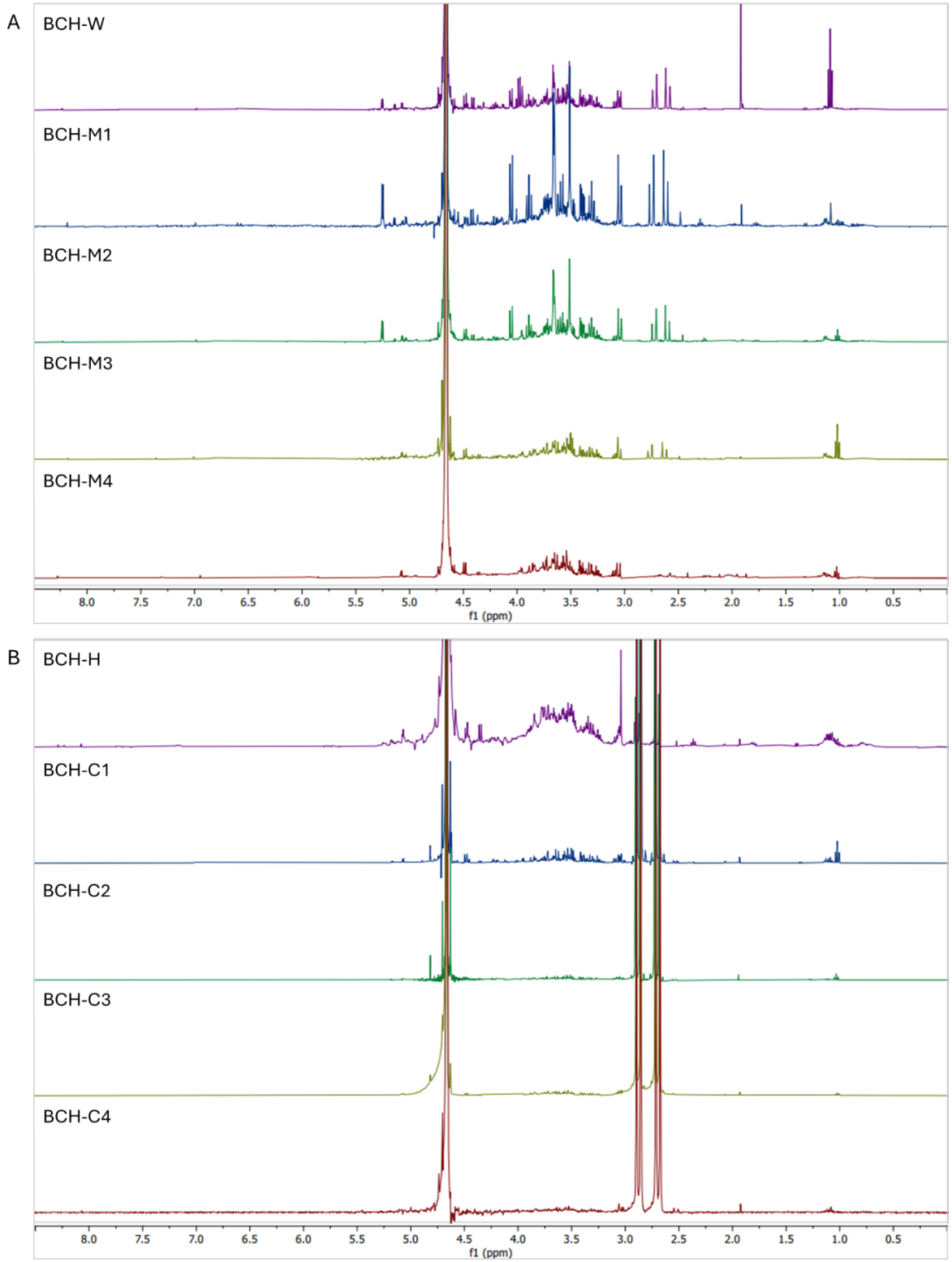

Figure 3.22. ^{1}H-NMR spectra of acid-free BCH (A), and acid-derived BCH (B) in D_2O.

The ^{1}H-NMR spectra of both acid-free and acid-derived BCH show two dominant chemical-shift regions: δ2.50 - 3.00 ppm, corresponding to citric acid, and δ3.30 - 5.30 ppm, corresponding to sugars or polysaccharides (**Figure 3.22** and **Table 3.14**). The presence of sugars and polysaccharides in both acid-free and acid-derived BCH were further confirmed by the sugar analysis results (**Appendix 11**). In acid-free BCH, additional low-intensity signals appear in the aromatic region (δ5.50 - 8.50 ppm), although these are much weaker than the two major regions (**Figure 3.22A**). Between BCH-W and BCH-M1, the intensities of the δ2.50 - 3.00 ppm and δ3.30 - 5.30 ppm regions are stronger in BCH-M1, indicating that MHT at 100 °C enhances the extraction of these compounds compared with conventional water extraction.

With increasing MHT temperatures, the intensities of both major regions are less pronounced, with the signals between δ2.50 - 3.00 ppm disappear at MHT 160 °C, suggesting thermal degradation of citric acid. In contrast, the signals between δ2.50 – 3.00 ppm is more pronounced in acid-derived BCH, especially the citric acid-derived BCH (BCH-C1 to C4), indicating citric acid trace in hydrolysates (**Figure 3.22B**).

The two *doublet* (d) signals observed between δ2.50 - 3.00 ppm, is assumed to be a signal of citric acid. A commercial citric acid sample was analysed by ^{1}H-NMR as a reference (**Appendix 12**), and its interpretation was based on the known chemical structure of citric acid (**Figure 3.23**). Although citric acid possesses a plane of symmetry, analysis using the Newman projection reveals the methylene protons (H_A and H_B) as diastereotopic protons (**Figure 3.23B**). Therefore, these diastereotopic protons were observed as *doublet (d)* signals, with the geminal splitting patterns occurred through AB coupling system and 2nd-order coupling ($\Delta\nu_{AB}/J < 10$),[285] showing the coupling constant ($^{2}J_{AB}$ and $^{2}J_{BA}$) of 16 Hz with resonance distance ($\Delta\delta_{AB}$) of 0.18 ppm (**Table 3.15**).

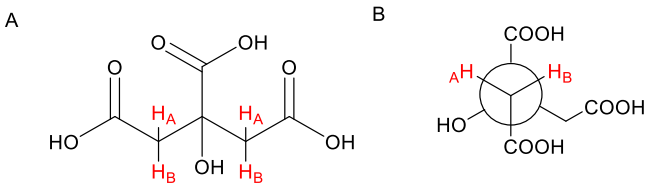

Figure 3.23. Chemical structure of citric acid: plane (A) and Newman projection (B).

The chemical shift, multiplicity, and coupling constants of this signal in both commercial citric acid and BCH samples are summarised in **Table 3.15**. In the reference sample, citric acid exhibits the resonance at δ2.87, 2.69 (*d,d*, $\Delta\delta_{AB}$ *= 0.18 ppm,* $^2J_{AB}$ *= 16 Hz*). Acid-derived BCH samples show very similar resonance with chemical shifts at around δ2.88, 2.70 (*d, d*, $\Delta\delta_{AB}$ *= 0.18 ppm,* $^2J_{AB}$ *= 16 Hz*). In contrast, acid-free BCH samples display a lower chemical shift and $\Delta\delta_{AB}$, showing at around δ2.74, 2.62 (*d*, *d*, $\Delta\delta_{AB}$ *= 0.13 ppm,* $^2J_{AB}$ *= 16 Hz*). This change can be explained by the ionisation state of citric acid under different pH conditions, in which the citric acid signal shifted downfield (higher δ) at lower pH, and the distance between the δ of H_A and H_B increased accordingly.[286]

Table 3.15. Summary of chemical shift, multiplicity, coupling constant of ^{1}H NMR signal of citric acid and BCH (D_2O, 400 MHz) at δ2.50 – 3.00 ppm.

Sample	**Multiplicity**	**Chemical shift (δ, ppm)**	**Coupling constant (^2J, Hz)**	**Distance between H_A and H_B ($\Delta\delta_{AB}$, ppm and $\Delta\nu_{AB}$, Hz)**
Citric acid	*d, d*	2.87, 2.69	$^2J_{AB}$, $^2J_{BA}$ = 16 Hz	0.18 ppm, 72 Hz
Acid-free BCH				
BCH-W	*d, d*	2.72, 2.60	$^2J_{AB}$, $^2J_{BA}$ = 16 Hz	0.12 ppm, 48 Hz
BCH-M1	*d, d*	2.75, 2.62	$^2J_{AB}$, $^2J_{BA}$ = 16 Hz	0.13 ppm, 52 Hz
BCH-M2	*d, d*	2.73, 2.61	$^2J_{AB}$, $^2J_{BA}$ = 16 Hz	0.12 ppm, 48 Hz
BCH-M3	*d, d*	2.77, 2.63	$^2J_{AB}$, $^2J_{BA}$ = 16 Hz	0.14 ppm, 56 Hz
BCH-M4	*d, d*	n.d.	n.d.	-
Acid-derived BCH				
BCH-H	*d, d*	2.89, 2.71	$^2J_{AB}$, $^2J_{BA}$ = 16 Hz	0.18 ppm, 72 Hz
BCH-C1	*d, d*	2.87, 2.70	$^2J_{AB}$, $^2J_{BA}$ = 16 Hz	0.17 ppm, 68 Hz
BCH-C2	*d, d*	2.89, 2.71	$^2J_{AB}$, $^2J_{BA}$ = 16 Hz	0.18 ppm, 72 Hz
BCH-C3	*d, d*	2.88, 2.70	$^2J_{AB}$, $^2J_{BA}$ = 16 Hz	0.18 ppm, 72 Hz
BCH-C4	*d, d*	2.88, 2.70	$^2J_{AB}$, $^2J_{BA}$ = 16 Hz	0.18 ppm, 72 Hz

Gas chromatography-mass spectrometry (GC-MS) results for BCHt, BCEt, and BCEt-F1 support the ^{1}H-NMR findings, confirming that fatty acids are the major components of these extracts (**Table 3.16**). The chromatograms and mass spectra for BCHt, BCEt, and BCEt-F1 are provided in **Appendix 13**, **14**, and **15**, respectively. Linoleic acid and palmitic acid were identified as the two predominant fatty acids in BCHt, with tetracosane appearing as the third major compound. Similarly, linoleic acid and palmitic acid were also the most abundant fatty acids in BCEt and BCEt-F1. Interestingly, the ethyl ester forms of both palmitic acid and linoleic acid were detected in these samples. This suggests that esterification occurred during extraction, in which palmitic and linoleic acids reacted with ethanol under reflux conditions, where ethanol served both as the solvent and as the alcohol reagent. The citric acid naturally presented in BC pomace (identified earlier through ^{1}H-NMR) likely acted as an acid catalyst, facilitating the esterification process.

Table 3.16. Major identified compounds in BCHt, BCEt, and BCEt-F1.

Compound	**Retention time (t_R, min)**	**Area (%)**		
		BCHt	**BCEt**	**BCEt-F1**
Palmitic acid	5.59	11.18	18.55	12.24
Palmitic acid, ethyl ester	5.64		7.92	2.5
Linoleic acid	6.02	30.49		31.08*
Linoleic acid, ethyl ester	6.05		52.63*	
Oleic Acid	7.32	1.7		
Heptadecane	7.52	1.46	0.96	1.28
Tricosan-2-ol	8.15	2.48		
Tetracosane	8.42	8.66	3.28	4.21
Octacosane	9.32	3.84		

* Mixtures of linoleic acid and linoleic acid ethyl ester were observed.

3.1.4.5. Optical properties of acid-free blackcurrant pomace extracts

Anthocyanins (ACNs) are well-known as pH indicator pigments. Based on our findings, microwave-assisted hydrothermal extraction (MHT) at 100 °C is recommended for ACNs extraction among all studied conditions, which can yield high TAC without requiring any additional mineral acid and organic solvent. The highest TAC value of MHT was found in BCH-M1 (7.22 mg C3G/g; **Table 3.11**). Although the obtained TAC value is lower than that of blackcurrant extract obtained from microwave-assisted acid extraction (20.4 mg C3G/g at 700W, pH 2),[84] it is higher than that of the TAC of microwave-assisted ethanolic extraction (104.09 mg C3G/100g or 1.04 mg C3G/g, 30% ethanol).[287]

The optical properties of the BC pomace ETW extract and MHT hydrolysates (BCH-M1 to M4) across the full pH range were investigated using UV-visible spectroscopy (**Figure 3.24**). The shift in the maximum absorption peak is primarily due to the colour change of BC pomace extracts with pH, influenced by the ionic nature of the ACNs, which can undergo structural transitions in response to changes in pH: from red flavylium cation (pH < 3) to colourless carbinol pseudobase, by hydration (pH 4-5), to blue quinonoidal base (pH 6-9) and, finally to yellow chalcones (pH > 10) (**Figure 3.25)**.[248,288] As the pH of the solution increases from 1 to 11, the maximum absorption peak undergoes a notable hypsochromic (blue) shift from approximately 495 nm to below 400 nm, accompanied by a colour change from red to yellow. BCH-M1 responded well to both acidic and basic pH as similar as the control ETW. In contrast, all other MHT hydrolysates (BCH-M2 to M4) had less ability to respond to acidic pH. Therefore, among all MHT hydrolysates, BCH-M1 is most suitable for pH-responsive applications.

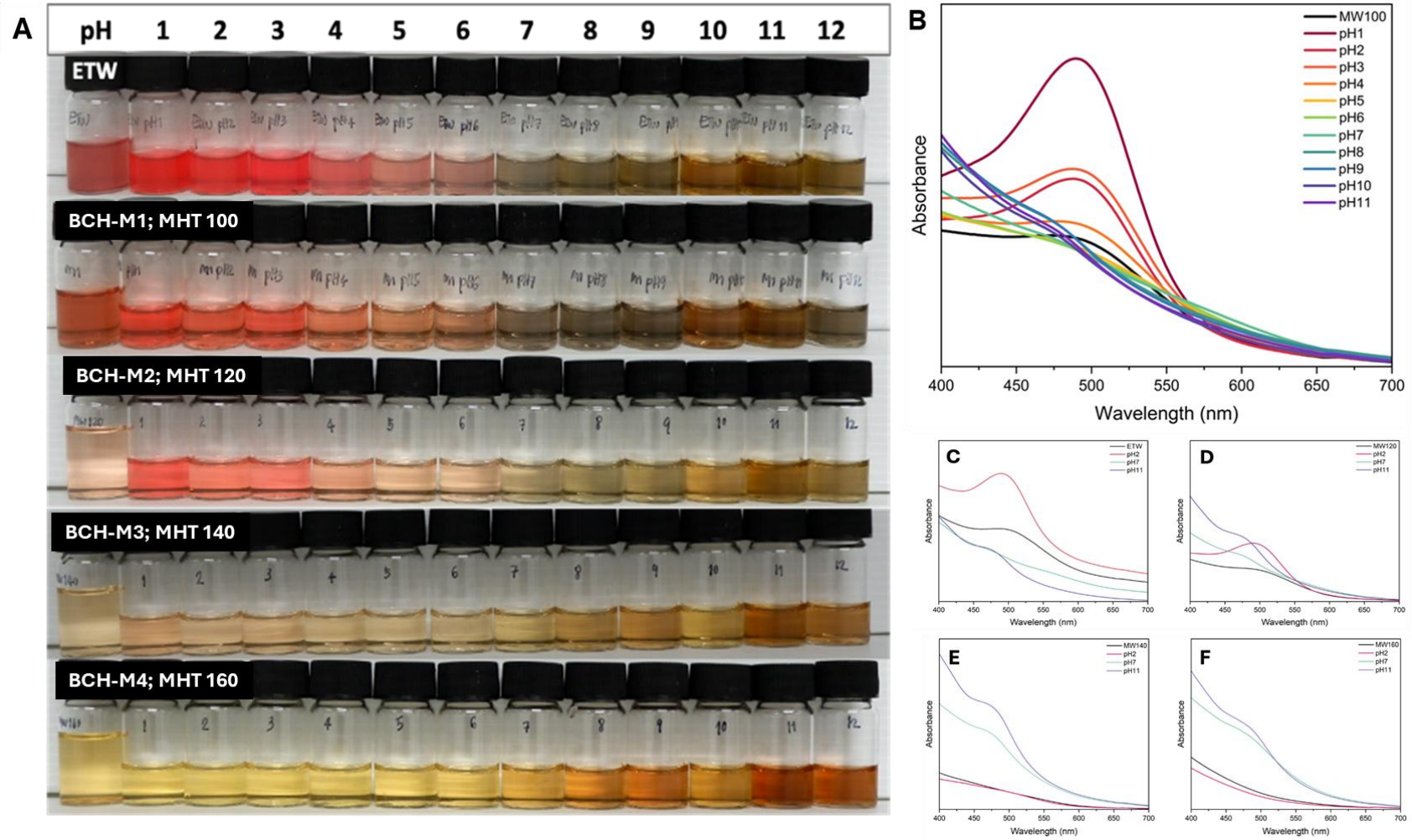

Figure 3.24. Visual appearance of ETW extract and MHT hydrolysates from pH 1 to 12 (A), UV-vis spectra of BCH-M1 from pH 1 to 11 (B), UV-vis spectra of ETW (C), BCH-M2 (D), BCH-M3 (E) and BCH-M4 (F) at original pH approx. 5 (black), pH 2 (red), pH 7 (green), and pH 11(purple).

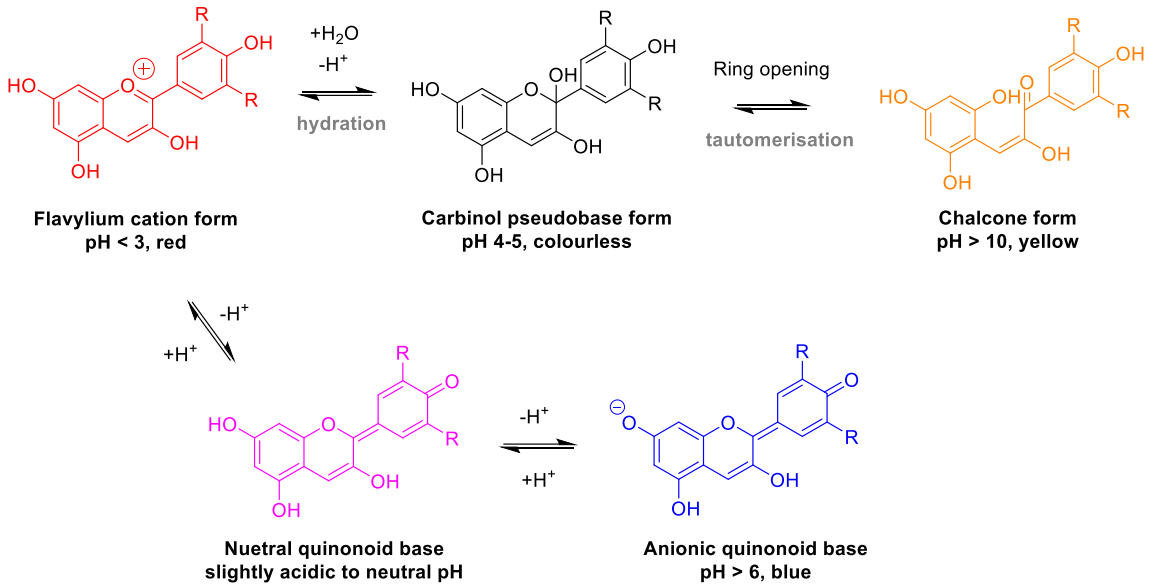

Figure 3.25. Effect of pH on chemical structure of anthocyanin and its colour.[288]

3.1.5. Repurposing of blackcurrant pomace via Microwave-assisted hydrothermal fractionation into pH-sensitive films (Objective A1 (v))

In this section, six different formulations of pH-responsive sodium alginate (NaAlg) films were developed. The sample codes and film compositions are summarised in **Table 2.3**. Based on the findings from earlier experiments, microwave-assisted hydrothermal treatment (MHT) at 100 °C was selected for fractionating blackcurrant (BC) pomace into three key components: blackcurrant pectin (BCP-M1), anthocyanin-rich hydrolysate (BCH-M1), and bleached defibrillated cellulose (BDFC-M1). BCP-M1, identified as low-methoxyl (LM) pectin containing residual anthocyanins (ACNs), served both as a co-biopolymeric matrix and an internal ACN source. BCH-M1, which exhibited strong pH responsiveness under both acidic and basic conditions, functioned as an additional ACN source and pH-responsive agent. BDFC-M1 was incorporated as a reinforcing additive to improve film structure and mechanical property. In this section, BCP-M1 will be referred to as BCP, BDFC-M1 as DFC, and BCH-M1 as ACN.

3.1.5.1. Characterisation of NaAlg and NaAlg-BCP films

The appearance and microstructures of NaAlg and NaAlg-BCP films on surface and cross-section were examined using scanning electron microscopy (SEM) (**Figure 3.26**). All NaAlg and NaAlg-BCP films are transparent. According to the SEM images, the NaAlg film

exhibited an amorphous-like texture, illustrated by smooth surfaces without pores or holes from top to bottom. However, some cracking was observed, likely attributable to the soft nature of the polymer films. The cross-sectional fractures indicating good homogeneity within the films. The interactions between BCP, NaAlg and the Ca^{2+} ions likely contributed to forming a more stable and uniform network, with incorporating 20% BCP revealed the smoothest surface and less cracking (**Figure 3.26**; NaAlg-BCP20). Incorporation of DFC or ACN into the NaAlg-BCP20 film altered its microstructure, giving the surface a rougher and less homogeneous appearance. The addition of DFC or ACN appeared to disrupt the polymer network, resulting in a less structured film and consequently reducing its tensile strength (see later). Similarly, cracking has been observed in the literature when ACN from rose, and blackcurrant was added to NaAlg/apricot peel pectin films and konjac glucomannan/carboxymethyl cellulose films.[106,107]

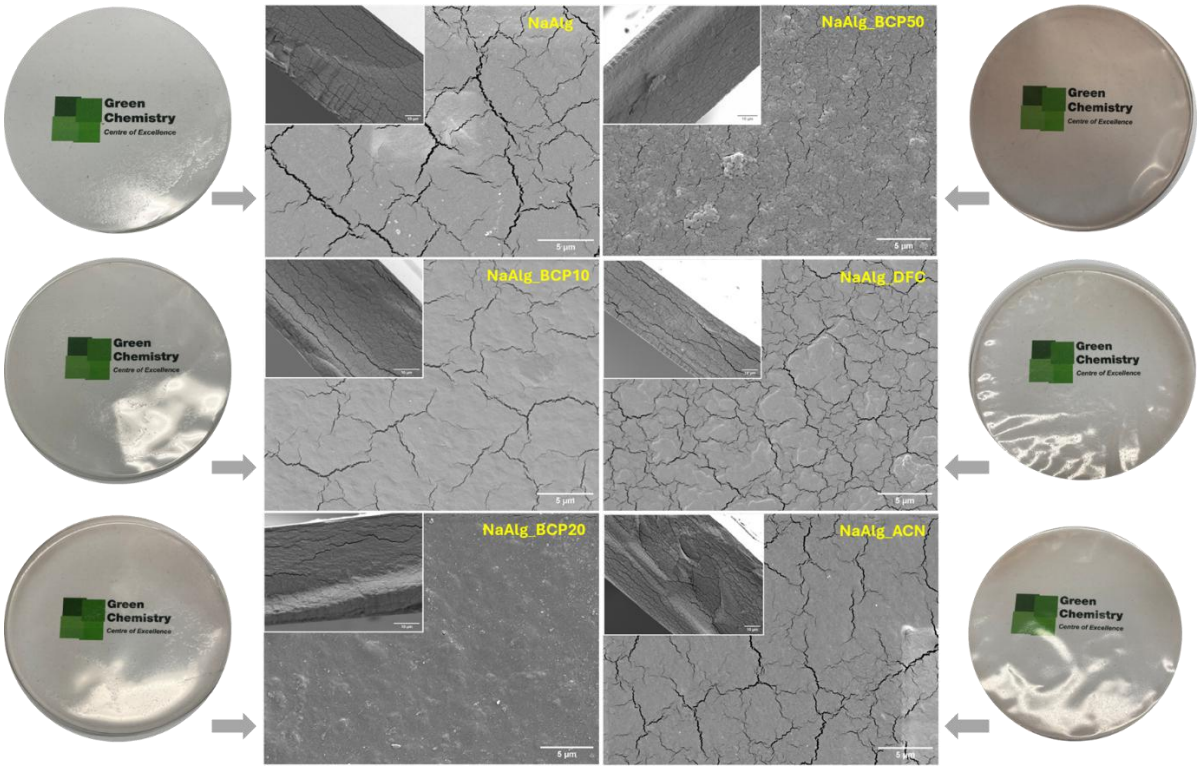

Figure 3.26. Visual appearance and SEM images (inset show cross-section (4000x)) of NaAlg and NaAlg-BCP films.

Attenuated Total Reflectance Infra-Red (ATR-IR) analysis was used to confirm the functional groups present in the films (**Figure 2.37**). All films exhibited the main characteristic absorption bands associated with the structure of NaAlg at around 3267 (O-H stretching), 2920 (C-H stretching), 1605 (COO^- stretching) and 1409 cm^{-1} (C-H bending or C-O stretching).[108,289] After adding BCP, a new band was observed at 1740 cm^{-1} attributable to the methyl ester of galacturonic acid within pectin or possibly the product of esterification of pectin and glycerol. No new significant absorbance bands were observed after adding either DFC or ACN. The O-H stretching band in NaAlg-BCP20 at 3263 cm^{-1} shifted to 3255 cm^{-1} and 3253 cm^{-1} for NaAlg-DFC and NaAlg-ACN, respectively. This change may be due to the incorporation of NaAlg-BCP and DFC or NaAlg-BCP and ACN through hydrogen bonding.[108,290,291]

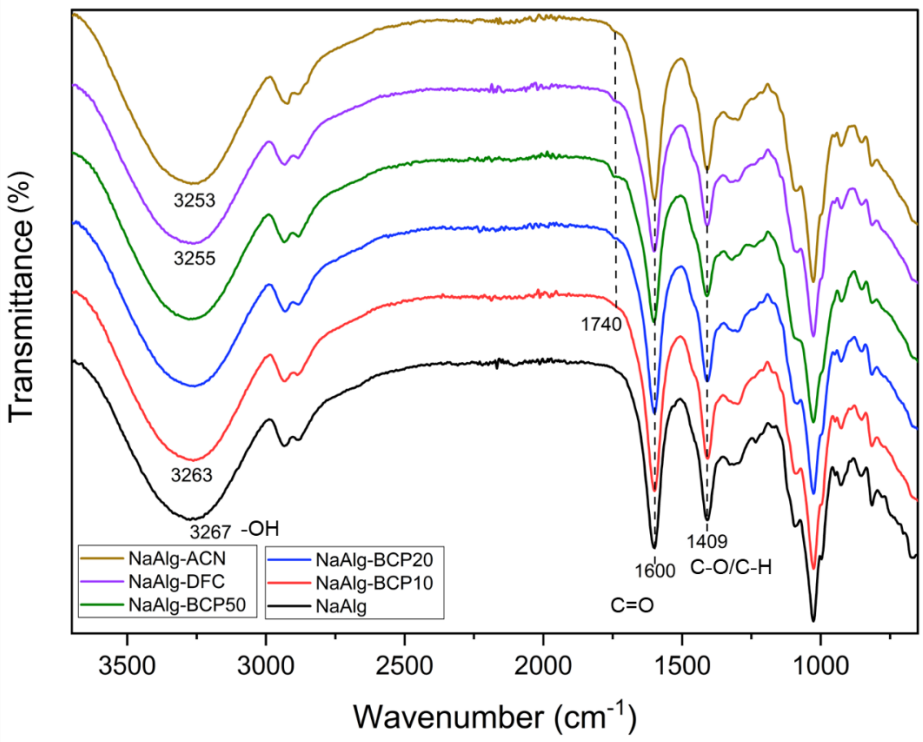

Figure 3.27. ATR-IR spectra of NaAlg and NaAlg-BCP films.

3.1.5.2. Mechanical properties of films

The tensile strength of NaAlg-BCP films ranged from 2.14 to 5.15 MPa, while the tensile strain at break was between 1.86 and 2.98 mm/mm (**Table 3.17**). It was observed that the NaAlg-BCP50 film exhibited the highest tensile strength among all NaAlg-BCP films. However, there was no significant difference between other NaAlg-BCP films. This possibly due to the synergistic effect of NaAlg-BCP blending,[106] where the carboxyl groups of NaAlg and pectin

interact with calcium ions, creating the "Egg box" model. The unique physical crosslink of the amorphous molecular structure of the "Egg box" resembles the structure of the synthetic semicrystalline polymers known as "Fringed-Micellar",[106] may have contributed to the increased strength of the films. This aligns with results from the literature where a similar highest tensile strength trend was found at around 40% pectin content.[106] Moreover, the higher tensile strength of NaAlg film when adding BCP may also be due to hydrogen bonding between molecular polymer chains,[292] and the chemical crosslink between glycerol and non-esterified pectin structures.[293] However, the interaction that improves the tensile strength property of the films leads to a densely packed structure, resulting in reduced tensile strain at break of NaAlg-BCP films with increased BCP content.

The addition of DFC into the NaAlg-BCP20 film resulted in reduce tensile strength and tensile strain at break. This phenomenon may be attributed to the residual insoluble lignin and crystalline Xylan present in DFC (BDFC-M1). Klason lignin analysis indicated that lignin accounted for approximately 17.5%, while residual crystalline Xylan was confirmed by the ^{13}C CP/MAS NMR spectra (**Appendix 9**). The presence of insoluble lignin and crystalline Xylan could interfere with intramolecular interactions between NaAlg/BCP and DFC, potentially leading to a discontinuous polymer network and the formation of defect zones, thereby limiting reinforcement within the film matrix.

Unlike DFC, the addition of ACN decreased the tensile strength of the NaAlg-BCP film; however, a slight increase in tensile strain at break was observed. This could be attributed to the plasticising effect of ACN. As small polyphenolic molecules, ACNs can act as plasticisers by interacting with NaAlg/BCP polymer chains through hydrogen bonding. These interactions enhance chain mobility, leading to increased film flexibility.[294] However, the presence of ACN may also disrupt intramolecular interactions within the polymer matrix, thereby weakening the overall film structure.[294] This finding was consistent with previous studies, which suggested that polyphenols can inhibit the chain interaction in the film structure, thereby reducing the tensile strength.[295]

Table 3.17. Mechanical properties of NaAlg and NaAlg-BCP films.

Sample	Tensile stress (MPa)	Tensile strain at break (ε, mm/mm)
NaAlg	2.90 ± 1.22[a]	2.59 ± 0.40[bc]
NaAlg-BCP10	2.72 ± 0.40[a]	2.98 ± 0.36[c]
NaAlg-BCP20	2.88 ± 1.73[a]	2.22 ± 0.42[ab]
NaAlg-BCP50	5.15 ± 1.60[b]	1.86 ± 0.25[a]
NaAlg-DFC	2.14 ± 0.41[a]	1.88 ± 0.21[a]
NaAlg-ACN	2.26 ± 0.37[a]	2.37 ± 0.26[ab]

Values are presented as mean ± SD (n = 3-6). Lowercase letters indicate the significant differences ($p < 0.05$)

In addition, the tensile strength of the NaAlg and NaAlg-BCP films is significantly lower than the tensile strength of commercial packaging, ranging from around 15 to 70 MPa.[221] This limitation may be influenced by the structural characteristics of NaAlg, which consists of different polymer block types, including homopolymeric blocks (MM or GG) and alternating blocks (MG or GM) (**Figure 3.28**).[296] Among these, GG blocks have a stronger affinity for binding with Ca^{2+} ions, which can enhance crosslinking and improve mechanical strength.[297] Therefore, optimising the ratio of mannuronic acid (M) to guluronic acid (G) monomers and selecting NaAlg with a higher content of GG blocks could be a promising strategy to enhance the tensile strength of NaAlg-BCP films. Moreover, the incorporation of bio-based acid crosslinkers may offer additional mechanical reinforcement. For instance, Singh *et al*. demonstrated that NaAlg/pectin films crosslinked with citric acid and tartaric acid through covalent bonding exhibited tensile strength values of up to 18 MPa.[298]

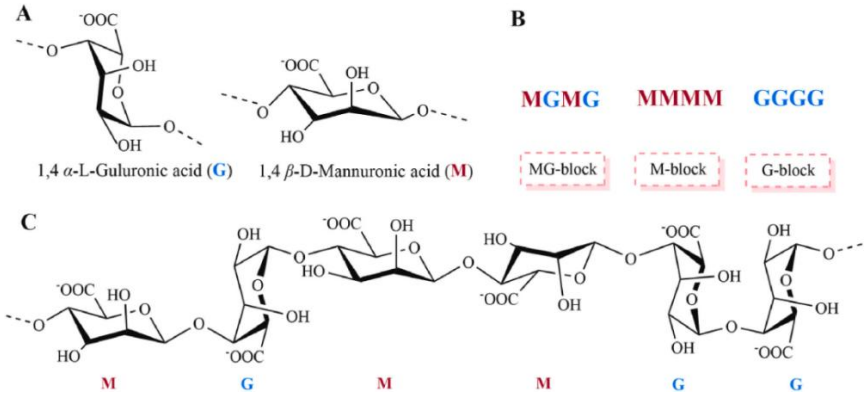

Figure 3.28. Chemical structure of NaAlg; monomers (A), polymeric block types (B), and structural conformation (C).[296]

3.1.5.3. Rheological properties of NaAlg-BCP film-forming solutions

Viscosity significantly influences film properties such as thickness, spread ability, mechanical properties and homogeneity of films.[299,300] All flow curves (**Figure 3.29**) exhibited shear thinning behaviour, in which increasing shear rate decreases shear viscosity. This behaviour indicates the deformation of the entanglement structure and the reduction of intermolecular forces between pectin and NaAlg with increasing shear rate. The weakness of intermolecular forces with increasing shear rate is consistent with berry pectin gel and NaAlg solution.[301,302] Compared with NaAlg solution alone, solutions with higher concentrations of BCP showed lower shear viscosity (**Figure 3.29A**) suggesting that NaAlg primarily dominates the viscosity of NaAlg-BCP solutions.

The shear viscosity on addition of glycerol as a plasticiser (**Figure 3.29B**) was slightly lower than without glycerol in the NaAlg-BCP solutions. The glycerol molecules are able to occupy intermolecular spaces between polymer chains, weakening the ordered polymer network.[299] As expected, the addition of a calcium crosslinker increased the shear viscosity of NaAlg-BCP solutions (**Figure 3.29C**), confirming the formation of "egg box" structures and interlinked network involving NaAlg, BCP and Ca^{2+} ions. The highest shear viscosity among the NaAlg-BCP film-forming solutions containing Ca^{2+} ions was observed in the NaAlg-BCP20 formulation, followed by NaAlg-BCP50, NaAlg-BCP10, NaAlg, NaAlg-ACN, and NaAlg-DFC, respectively. However, no significant differences in shear viscosity were found among NaAlg-BCP10, NaAlg, NaAlg-ACN, and NaAlg-DFC. The shear viscosity results generally correlated well with the tensile strength of the corresponding NaAlg-BCP films. Specifically, NaAlg-BCP10, NaAlg, NaAlg-ACN, and NaAlg-DFC films exhibited no significant differences in tensile strength, while NaAlg-BCP50 showed a relatively higher value.

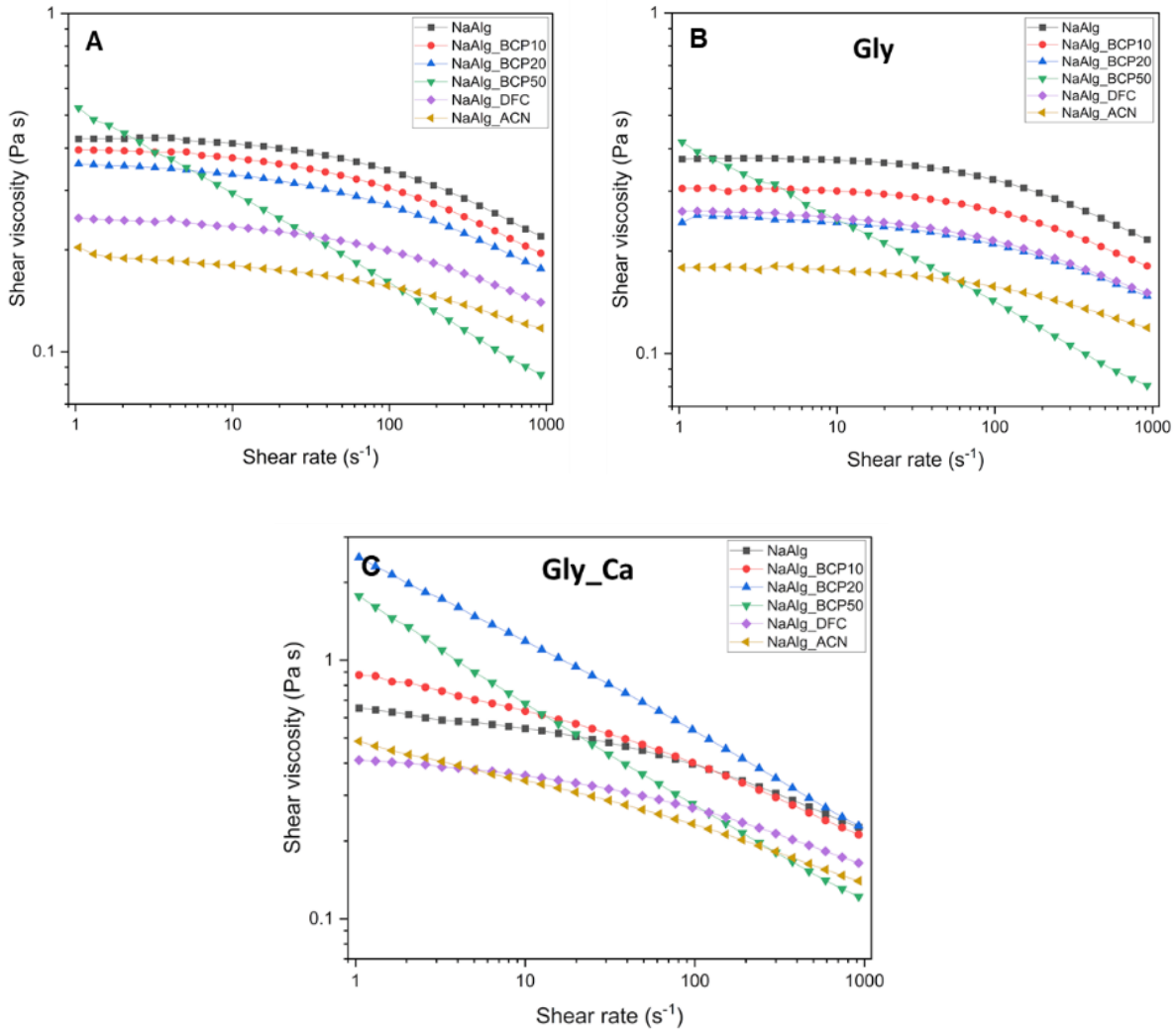

Figure 3.29. Flow curves of NaAlg-BCP film forming solutions: 4% of polymer solution (A), with glycerol adding (B), with glycerol and calcium chloride adding (C).

Amplitude sweep test of the NaAlg-BCP film-forming solutions containing glycerol and $CaCl_2$ (**Figure 3.30A**) was conducted to evaluate the linear viscoelastic region (LVR) and rheological stability of viscoelastic solid/liquid. All curves showed the LVR within a strain of 1% and the crossover point or yield point was not observed in the range of study (strain of 0.1% to 100%). The NaAlg solution predominantly displayed viscoelastic liquid behaviour with higher value of loss modulus (G") over storage modulus (G') was observed.

The frequency sweep test was conducted to observe the change in the stability and microstructure of the film-forming solution during storage or transportation.[299,303] The frequency sweep test of the NaAlg-BCP film-forming solutions containing glycerol and $CaCl_2$

(**Figure 3.30B**) was conducted within the LVR as determined earlier by the amplitude sweep test. The G' and G" of the NaAlg-BCP film-forming solutions increased with increasing frequency (**Figure 3.30B (i and ii)**.

The tan δ, the ratio of loss modulus (G") to storage modulus (G'), reflects the balance between the viscous and elastic behaviour.[304] The tan δ (**Figure 3.30B (iii))** of NaAlg solution was greater than 1, indicating liquid-like behaviour (G">> G'). The tan δ for NaAlg-BCP solutions decreased with increasing BCP content and the addition of DFC or ACN, reflecting a transition from a more liquid-like (G" > G') to a more solid-like matrix (G' > G"). This shift is primarily attributed to the crosslinking of higher content of low methoxy BCP facilitated by Ca^{2+} ions, where enhanced entanglement contributes to an increase in solid-like behaviour.[300] However, the tan δ for NaAlg-BCP50 remained below 1 throughout the entire frequency sweep, signifying consistently solid-like behaviour within the range of study. It can be seen that the viscosity of NaAlg-BCP solutions including glycerol and $CaCl_2$ increased with higher BCP content (**Figure 3.29C**), while tan δ decreased (**Figure 3.30B (iii)**), indicating that adding BCP can improve the elastic property of NaAlg solutions.

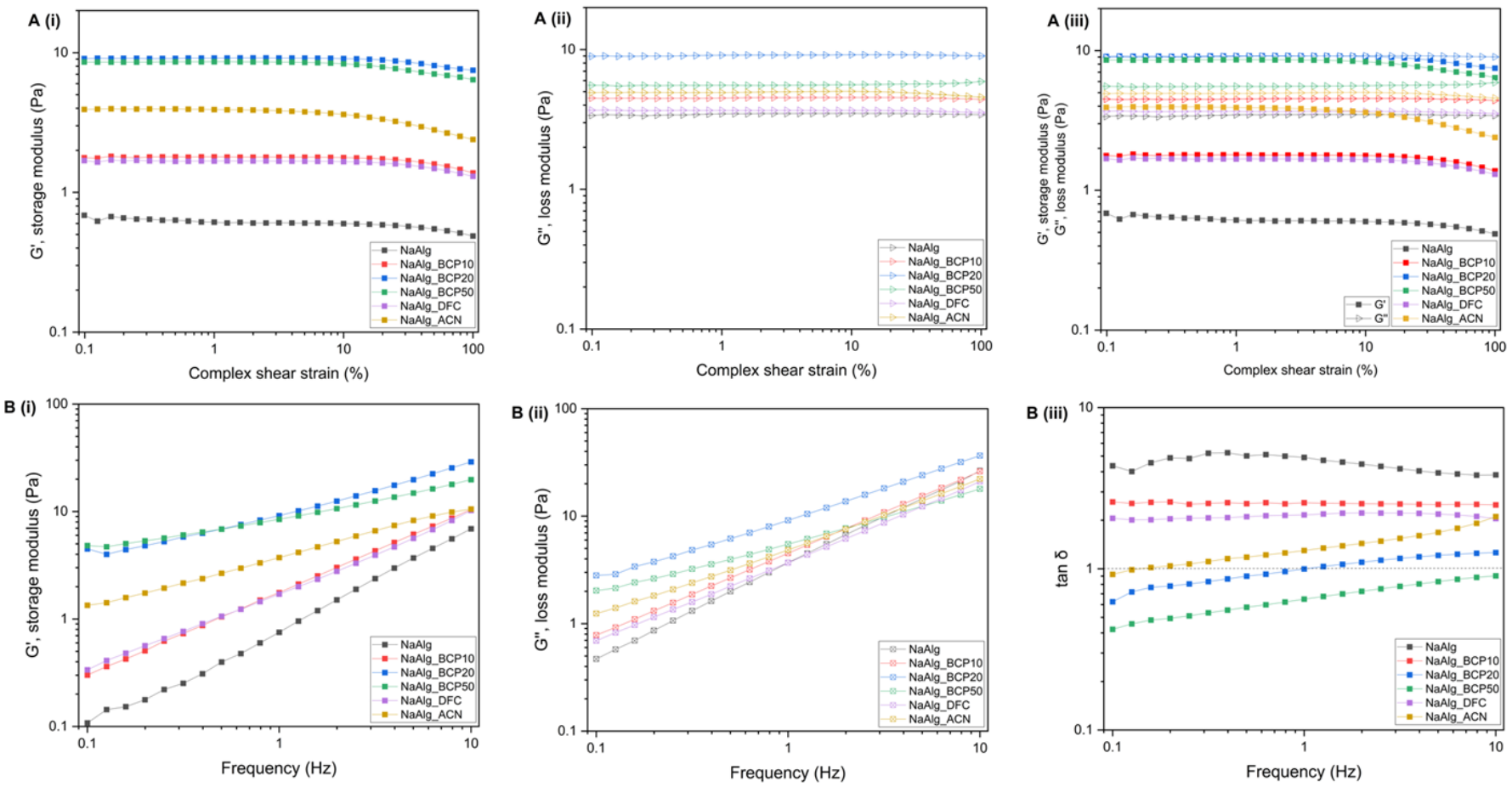

Figure 3.30. Rheological properties of NaAlg-BCP film-forming solutions; Amplitude sweep curves showing (A): Storage modulus (G') (i), Loss modulus (G") (ii), Comparison of storage (G') and loss modulus (G") (iii); Frequency sweep curves showing (B): Storage modulus (G') (i), Loss modulus (G") (ii), Loss tangent (tan δ) (iii).

The creep-recovery test evaluates the elasticity of materials.[305] NaAlg and NaAlg-BCP10 showed a small recovery and largely permanent deformation with the recovery of 1.12% and 0.19%, respectively (**Figure 3.31** and **Table 3.18**), indicating predominantly viscous behaviour with negligible elasticity. As the BCP content increased, the recovery improved significantly with NaAlg-BCP50 exhibiting the highest recovery (93.53%). This reflects a shift towards elastic (solid-like) behaviour due to the enhanced network structure created by BCP, which allows the material to regain its original shape partially. For the NaAlg-BCP20 solution, the addition of DFC or ACN exhibited a reduction in recovery from 64.82% to 9.01% and 4.33%, respectively. This again confirms the decrease in network structure which may be due to DFC or ACN interference.

According to the frequency sweep and creep-recovery tests, increasing the BCP content in NaAlg films resulted in lower tan δ values and higher recovery rates, indicating enhanced elastic behaviour in the film-forming solutions. However, this trend contrasts with the mechanical properties of the final films (**Table 3.17**), where higher BCP content was associated with a decrease in tensile strain at break, suggesting reduced flexibility. This may be due to water loss during film drying, which leads to structural rearrangement and densification of the polymer network, resulting in different mechanical behaviour in the final films.

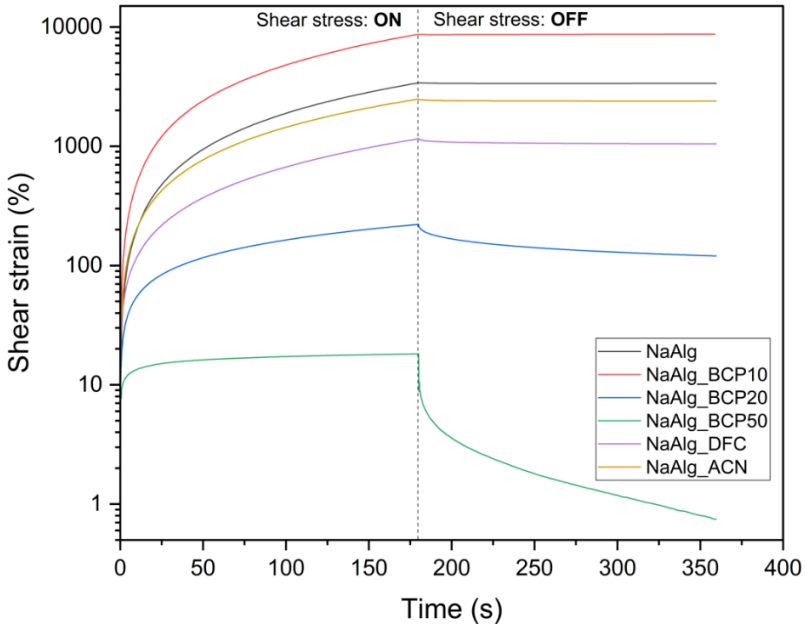

Figure 3.31. The strain (%) experienced by the NaAlg-BCP film-forming solutions when subjected to a creep recovery test at a constant shear of 0.5 Pa.

Table 3.18. Recovery (%) of NaAlg-BCP film-forming solutions.

Sample	Recovery (%) at a shear stress of 0.5 Pa
NaAlg	1.12 ± 0.23^{cd}
NaAlg-BCP10	0.19 ± 0.23^{d}
NaAlg-BCP20	64.82 ± 6.89^{b}
NaAlg-BCP50	93.53 ± 3.29^{a}
NaAlg-DFC	9.01 ± 1.13^{c}
NaAlg-ACN	4.33 ± 0.69^{cd}

Values are presented as mean ± SD (n = 3). Lowercase letters indicate the significant differences ($p < 0.05$)

3.1.5.4. Physical properties of films

The control film (NaAlg) had a thickness of 0.074 mm and had the highest moisture content among all the films (**Table 3.19**). The addition of BCP resulted in no significant difference in thickness compared to the control film. This is in good accordance with previous literature, where no differences in thickness were observed between alginate and alginate-commercial low-methoxy pectin films.[289] The introduction of either DFC or ACN from BC pomace extracts into the NaAlg-BCP20 solution led to a gradual increase in film thickness from 0.065 mm (NaAlg-BCP20) to 0.078 mm (NaAlg-DFC) or 0.077 mm (NaAlg-ACN). This increase in thickness is likely due to the higher dry matter content of DFC and ACN. A similar trend was observed when cellulose nanocrystals were added into NaAlg-Pectin and NaAlg-Pectin-Red cabbage ACN films,[108] as well as when incorporating blackcurrant waste powder into chitosan or pectin films.[98]

The hydrophobicity or hydrophilicity of the surface of the films was determined by water contact angle measurements (**Table 3.19** and **Figure 3.32**). The contact angle of NaAlg film was 21.67° (at 60 s) and increased with increasing BCP concentration. The NaAlg-BCP films showed higher contact angles than NaAlg indicating a relatively more hydrophobic surface in the former. However, all contact angles for the NaAlg-BCP films were less than 90°, indicating that all the films have hydrophilic surfaces.

Table 3.19. Physical, water vapour transmission, and antioxidant properties of NaAlg and NaAlg-BCP films.

Sample	Thickness (mm)	Moisture content (%)	Water contact angle (°) at 60s	WVTR ($\times10^{-3}$ g/s·m^2)	WVP ($\times10^{-11}$ g/m·s·Pa)	DPPH inhibition (%)
NaAlg	0.074 ± 0.011^{ab}	27.75 ± 1.79^{a}	21.67 ± 1.79^{a}	4.35 ± 0.82^{b}	8.53 ± 0.63^{ab}	n.d.
NaAlg-BCP10	0.068 ± 0.008^{ab}	16.53 ± 1.31^{b}	30.71 ± 1.81^{b}	2.16 ± 0.48^{c}	5.54 ± 1.05^{a}	1.50 ± 0.16^{a}
NaAlg-BCP20	0.065 ± 0.010^{a}	14.94 ± 1.41^{b}	38.47 ± 0.75^{c}	3.12 ± 0.42^{bc}	5.74 ± 1.13^{a}	4.55 ± 0.07^{b}
NaAlg-BCP50	0.066 ± 0.009^{ab}	14.54 ± 1.17^{b}	47.02 ± 0.91^{d}	3.94 ± 0.32^{bc}	7.57 ± 0.52^{ab}	25.66 ± 0.11^{e}
NaAlg-DFC	0.078 ± 0.015^{c}	10.72 ± 0.94^{c}	39.06 ± 1.39^{c}	4.22 ± 0.88^{bc}	10.53 ± 2.16^{b}	9.17 ± 0.38^{c}
NaAlg-ACN	0.077 ± 0.012^{bc}	14.70 ± 1.17^{b}	37.98 ± 0.38^{c}	4.64 ± 1.15^{b}	11.21 ± 2.93^{b}	14.53 ± 0.11^{d}

Values are presented as mean ± SD (n = 3-6). Lowercase letters indicate the significant differences ($p < 0.05$)

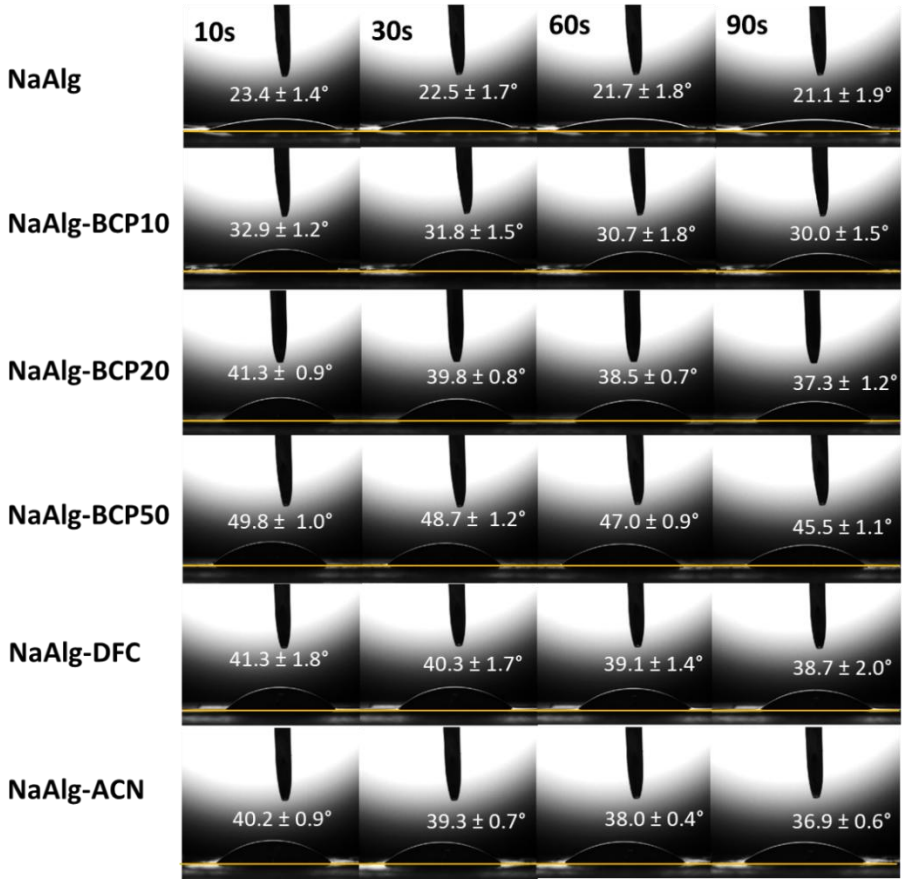

Figure 3.32. Water contact angle analysis of NaAlg and NaAlg-BCP films.

3.1.5.5. Water vapour transmission properties

The water vapor transmission rate (WVTR) and water vapor permeability (WVP) of NaAlg-BCP films reflect the moisture transfer property of film. The WVTR was observed in a range of 2.16 to 4.64 $\times 10^{-3}$ g/s·m^2, while the WVP was ranged from 5.54 to 11.21$\times 10^{-11}$ g/m·s·Pa (**Table 3.19**). A similar trend was observed for both WVTR and WVP, in which the NaAlg film exhibited higher value compared to NaAlg-BCP10, NaAlg-BCP20, and NaAlg-BCP50 films. This reduction can be attributed to the denser network formed between NaAlg and BCP through intramolecular interactions, resulting in lower WVTR and WVP values. However, the addition of DFC or ACN resulted in increased WVTR and WVP values compared to the NaAlg film, possibly due to the accumulation of DFC or ACN within the polymer network, which created greater free volume in the films. The increased free volume facilitated a higher rate of water vapour transmission, thereby enhancing the moisture permeability of films.[225,306]

The WVTR and WVP values of NaAlg-BCP films were lower than the previous findings, where NaAlg-$CaCl_2$ films exhibited higher WVTR values, ranging from 13.38 to 36.70 $\times 10^{-3}$ g/s·m^2,[307] and NaAlg-Pectin-$ZnCl_2$ films showed WVP values between 23.9 and 51.3 $\times 10^{-11}$ g/m·s·Pa.[103] The relatively lower WVTR and WVP values of NaAlg-BCP films compared to NaAlg-$CaCl_2$ films and NaAlg-Pectin-$ZnCl_2$ films may be due to differences in measurement methods. This study employed the dry cup method, whereas the others used the wet cup method,[103,307] which typically yields higher permeability values.[308,309] However, the relatively high WVTR and WVP values of the NaAlg-BCP films, which significant higher than the commercial low-density polyethylene films (WVTR of 7.23×10^{-5} g/s·m^2 and WVP of 8.46×10^{-16} g/m·s·Pa), suggesting their potential to regulate water vapour transmission and reduce condensation, thereby providing antifogging functionality and helping to extend the shelf life of perishable products.[225]

3.1.5.6. Antifogging property

Since the NaAlg-BCP films possess a hydrophilic surface evidenced by water contact angles below 90° and high-water vapour transmission properties, their antifogging behaviour was further evaluated. The fogging test was visually assessed using the NaAlg and NaAlg-BCP films, with a glass slide serving as a control. The results are shown in **Figure 3.33**, scored according to the criteria in **Figure 2.2**, and summarised in **Table 3.20**. At the initial point (t_0), all NaAlg-BCP films and the glass slide appeared completely transparent (score A). The control glass slide revealed fogging surface (score B) within 5 min of water vapor exposure and developed small, discrete water droplets (score C) by 30 min of exposure. With prolonged exposure, an increase in water droplet size was observed (score D-E). In contrast, the NaAlg-BCP films maintained their transparency for up to 20 min under heating. By 30 min, slight crinkling on the film surface and a reduction in transparency were observed (score A-B). Although the reduced transparency was observed, there was no fogging observed on NaAlg-BCP films surface. This condition remained stable up to 180 min of exposure to heated water vapor. The antifogging property of NaAlg-BCP films can be referred to the hydrophilic nature, which enables rapid absorption of water vapor through hydrogen bonding.[225,310] In addition, the relatively high WVTR and WVP values of the films facilitate the transmission of water vapor through the film. As a result, no condensed water droplets were observed on the film surface. Therefore, the hydrophilic nature of the NaAlg-BCP films, combined with their high-water vapour permeability, contributes to their effective antifogging performance.

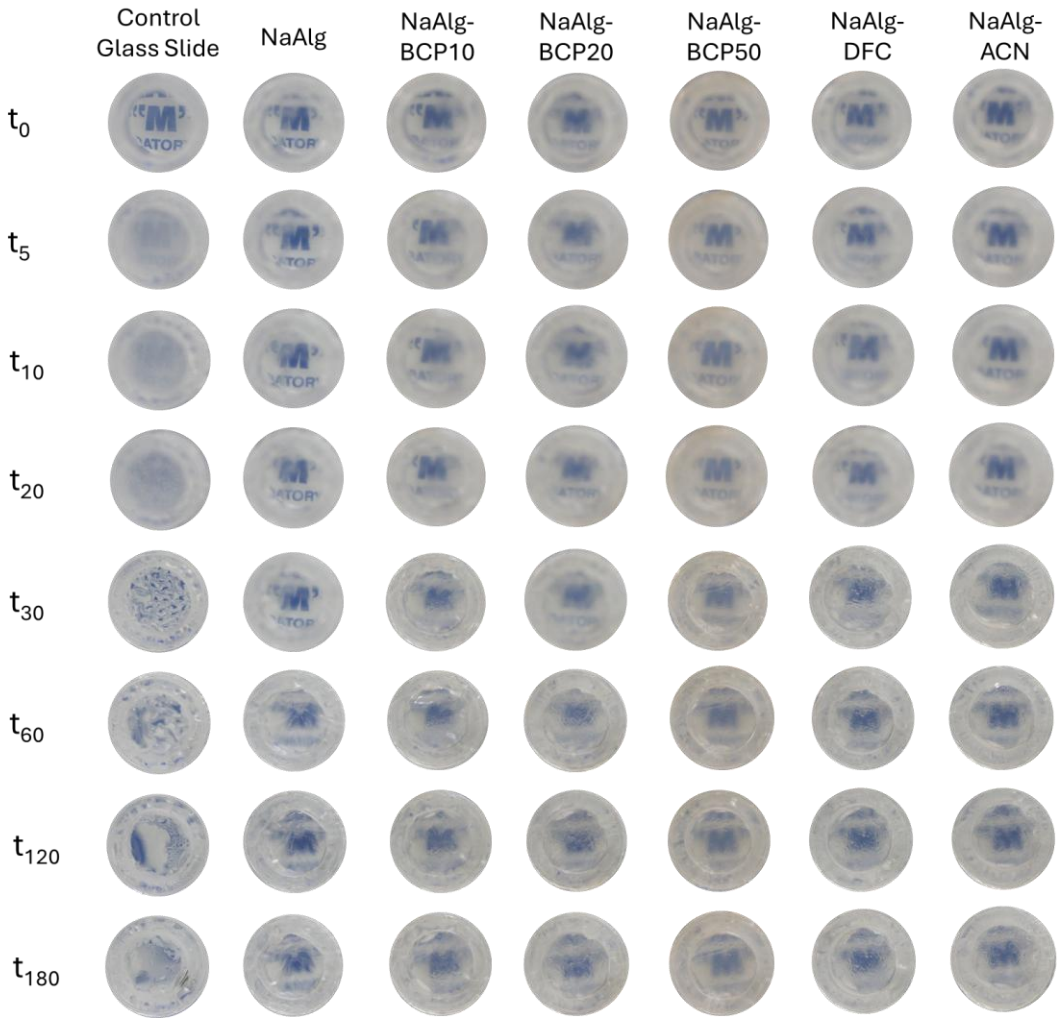

Figure 3.33. Appearance of a glass slide, NaAlg and NaAlg-BCP films under the exposure of water vapour over a 180-min period.

Table 3.20. Antifogging scores (A-E) of glass slide and NaAlg-BCP films over a 180-min period.

Sample	**Test time (min)**							
	t_0	t_5	t_{10}	t_{20}	t_{30}	t_{60}	t_{120}	t_{180}
Glass slide (control)	A	B	B	B	C	D	E	E
NaAlg	A	A	A	A	A	A-B	A-B	A-B
NaAlg-BCP10	A	A	A	A	A-B	A-B	A-B	A-B
NaAlg-BCP20	A	A	A	A	A-B	A-B	A-B	A-B
NaAlg-BCP50	A	A	A	A	A-B	A-B	A-B	A-B
NaAlg-DFC	A	A	A	A	A-B	A-B	A-B	A-B
NaAlg-ACN	A	A	A	A	A-B	A-B	A-B	A-B

3.1.5.7. Antioxidant property of films

The antioxidant activity of NaAlg-BCP films, represented by the percentage of DPPH inhibition, increased with an increase in BCP content (**Table 3.19**). The higher DPPH inhibition of the NaAlg-BCP films may be attributed to the higher ACN-bound or remaining polyphenolics in BCP. Similar results were found in pectin extracted from lemon, pomelo, and pitaya peels.[311] The incorporation of either DFC or ACN into NaAlg-BCP20 films improved the antioxidant activity. This may be due to residual lignin in the DFC, the ACNs in BC extract, or a combination of both factors.[295,312] This suggests that adding BCP to NaAlg film improves both tensile properties and antioxidant activity. NaAlg-BCP50 demonstrated the highest antioxidant activity, possibly attributed to the increased amount of bound ACNs in BCP. While our primary focus is on using blackcurrant ACN as pH indicators for monitoring food quality, their antioxidant capabilities could also be harnessed to extend the shelf life of food products.

3.1.5.8. Volatile NH_3 and CH_3COOH detection

Aqueous CH_3COOH and NH_3 solutions were prepared at a concentration of 10%v/v to demonstrate the ability of NaAlg and NaAlg-BCP films to detect volatile acids and amines within packaging environments. **Figure 3.34** shows the colour changes of the NaAlg-BCP films after 6h of exposure to CH_3COOH and NH_3. A colour change in response to NH_3 is seen in all NaAlg-BCP films, although the ACN fraction had not blended in films such as NaAlg-BCP10, NaAlg-BCP20, and NaAlg-BCP50. The observed colour change can be attributed to conversion of CAN molecules into chalcone molecules,[289,313] due to an increase in pH from the addition of NH_3.[248,288,313] In addition, the darkening of the brown colour may be a result of the ionisation of the phenolic hydroxyl groups in an alkaline system, which has also been observed in the polyhydroxyalkanoate/tannin films.[221] In contrast, the CH_3COOH vapour did not cause significant changes in the film colour. This may be due to the pKa of CH_3COOH being between 3 to 4, which cannot drive the ACN molecules into red flavylium cation structure occurring at pH below 3.[248,288,313] Additionally, International Commission on Illumination (CIE) Lab colour analysis confirmed a significant change in colour of NaAlg-BCP films (**Table 3.21 – 3.23**). The $\Delta E > 5$ indicating that the change could be differentiated by the naked eye for all the NaAlg-BCP films under NH_3 detection (**Figure 3.34**), and the NaAlg-BCP50 film displayed the most significant change (**Table 3.21**).

Further tests with various concentrations of NH_3 solutions (**Table 3.22**) were performed with the NaAlg-BCP50 film. The colour change became visible after 2h of exposure to NH_3 solution, with the light red-brown colour intensifying into a dark brown with prolonged exposure to NH_3 vapours. A concentration of 500 ppm NH_3 was selected to demonstrate the spoilage environment of minced beef or pork, corresponding to the upper limit of the biogenic amine index, which is 500 mg/kg or 500 ppm.[92] This concentration was the lowest level found to induce a visible colour change in the NaAlg-BCP50 film within 6h, with a ΔE value of 7.61. Therefore, NaAlg-BCP50 film has the potential to detect pork or beef spoilage within 6h.

To demonstrate the reusability of NaAlg-BCP films for pH detection, a colour reversible test was performed with the NaAlg-BCP50 film. The film was sequential exposed to 10% NH_3 for 6h, followed by 10% CH_3COOH. Within 2h of exposure to CH_3COOH, a visible colour change was observed, shifting from dark brown to pale brown (**Table 3.23** and **Figure 3.34**). However, the film cannot fully revert to its original colour. This incomplete recovery can be explained by the sensitivity of ACN, which can be degraded under high pH conditions.[289,313]

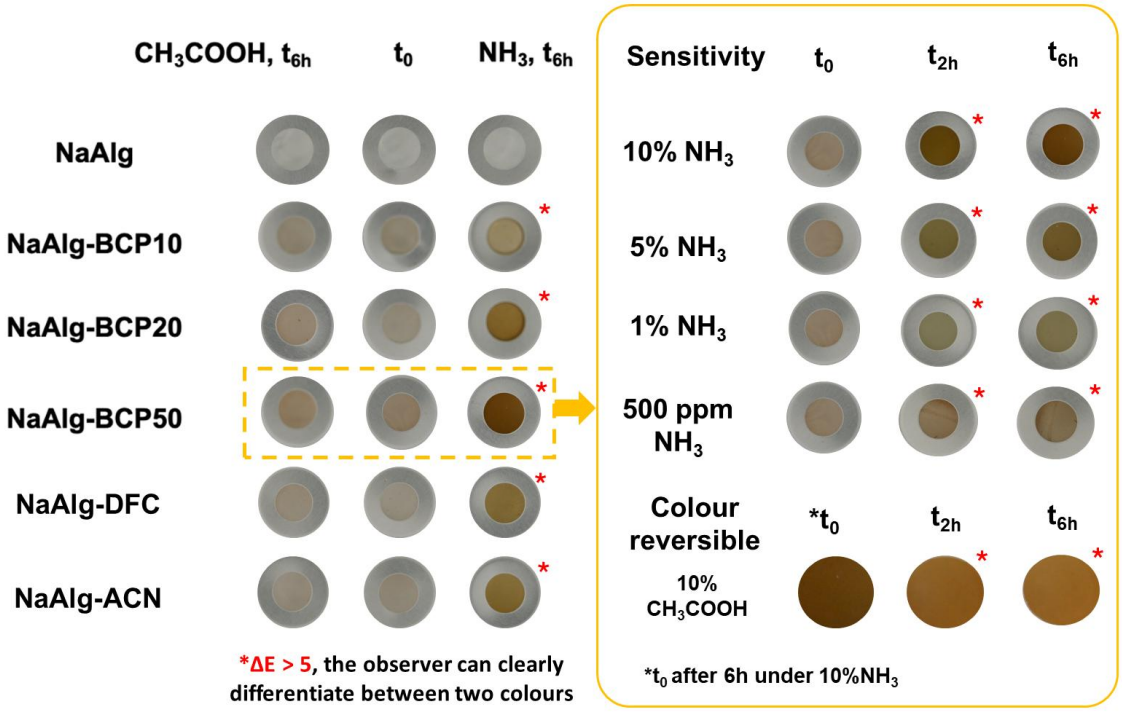

Figure 3.34. Colour change of NaAlg-BCP films after 6h of exposure to acetic acid and ammonia vapours, and colour evolution of the NaAlg-BCP50 film over time in response to different concentrations of ammonia.

Table 3.21. CIE Lab colour analysis of NaAlg and NaAlg-BCP films after exposure to 10% v/v CH_3COOH and NH_3 for 6h.

Conditions	Sample	Colour attributes			Colour difference (ΔE)
		L*	***a****	***b****	
Control at t_0	NaAlg	64.67 ± 0.58^{Aa}	-0.33 ± 0.58^{Ac}	4.33 ± 0.58^{Ac}	n/a
	NaAlg-BCP10	54.67 ± 0.58^{Ad}	0.33 ± 0.58^{Abc}	11.00 ± 0.01^{Bb}	n/a
	NaAlg-BCP20	57.67 ± 0.58^{Abc}	1.33 ± 0.58^{Cb}	9.67 ± 0.58^{Cbc}	n/a
	NaAlg-BCP50	51.67 ± 0.58^{Ae}	3.67 ± 0.58^{Ba}	14.67 ± 0.58^{Ca}	n/a
	NaAlg-DFC	58.67 ± 0.58^{Ab}	0.00 ± 0.01^{Cbc}	8.33 ± 0.58^{Cc}	n/a
	NaAlg-CAN	56.00 ± 0.01^{Acd}	1.00 ± 0.01^{Bbc}	10.33 ± 0.58^{Bb}	n/a
10%CH_3COOH, 6h	NaAlg	64.67 ± 0.58^{Aa}	0.00 ± 0.01^{Ac}	4.67 ± 0.58^{Ae}	0.94 ± 0.82^{Ab}
	NaAlg-BCP10	54.33 ± 0.58^{Ac}	1.00 ± 0.01^{Abc}	11.67 ± 0.58^{Bbc}	1.05 ± 0.92^{Bb}
	NaAlg-BCP20	55.67 ± 0.58^{Abc}	3.67 ± 0.58^{Ba}	13.33 ± 0.58^{Bb}	4.87 ± 0.66^{Bab}
	NaAlg-BCP50	52.33 ± 0.58^{Ad}	4.67 ± 0.58^{Ba}	16.67 ± 0.58^{Ba}	2.49 ± 1.10^{Bab}
	NaAlg-DFC	57.00 ± 0.01^{Ab}	2.00 ± 0.01^{Bb}	11.00 ± 0.01^{Bcd}	3.75 ± 0.65^{Bab}
	NaAlg-CAN	57.00 ± 0.01^{Ab}	1.00 ± 0.01^{Bbc}	9.67 ± 0.58^{Bd}	1.28 ± 1.43^{Bb}
10%NH_3, 6h	NaAlg	66.33 ± 0.58^{Aa}	0.00 ± 0.01^{Ad}	4.00 ± 0.01^{Ad}	1.91 ± 1.01^{Ad}
	NaAlg-BCP10	56.00 ± 0.01^{Ab}	1.33 ± 0.58^{Ad}	21.00 ± 0.01^{Ac}	$10.15 \pm 0.09^{Ac*}$
	NaAlg-BCP20	43.67 ± 0.58^{Bc}	7.67 ± 0.58^{Ab}	36.00 ± 0.01^{Aa}	$30.50 \pm 0.84^{Aa*}$
	NaAlg-BCP50	29.67 ± 1.15^{Bd}	13.33 ± 0.58^{Aa}	34.67 ± 0.58^{Aa}	$31.28 \pm 1.52^{Aa*}$
	NaAlg-DFC	45.00 ± 0.01^{Bc}	5.00 ± 0.01^{Ac}	31.33 ± 0.58^{Ab}	$27.22 \pm 1.11^{Ab*}$
	NaAlg-CAN	45.00 ± 1.00^{Bc}	5.00 ± 0.01^{Ac}	32.33 ± 0.58^{Ab}	$24.93 \pm 1.17^{Ab*}$

Values are presented as mean ± SD (n = 3). Different lowercase letters (a-e) indicate significant differences ($p < 0.05$) between films under the same conditions. Different uppercase letters (A-C) indicate the significant differences ($p < 0.05$) for the same film under different conditions. ΔE > 5 (*) indicates a colour difference noticeable to the human eye.

Table 3.22. CIE Lab colour analysis of the NaAlg-BCP50 film after exposure to NH_3 at varying concentrations, ranging from 10%v/v to 500 ppm, for 2h and 6h.

Conditions	Sample	Colour attributes			Colour difference (ΔE)
		L*	***a****	***b****	
10%NH_3, 6h	NaAlg-BCP50	29.67 ± 1.15^{Ac}	13.33 ± 0.58^{Aa}	34.67 ± 0.58^{Aa}	$31.28 \pm 1.52^{Aa*}$
5%NH_3, 6h	NaAlg-BCP50	36.67 ± 0.58^{Bb}	5.00 ± 0.01^{Ab}	29.00 ± 0.01^{Ab}	$20.80 \pm 0.44^{Ab*}$
1%NH_3, 6h	NaAlg-BCP50	46.67 ± 0.58^{Ba}	0.33 ± 0.58^{Ac}	21.33 ± 0.58^{Ac}	$9.01 \pm 0.79^{Ac*}$
500ppm NH_3, 6h	NaAlg-BCP50	45.67 ± 0.58^{Ba}	3.67 ± 0.58^{Ab}	19.33 ± 0.58^{Ad}	$7.61 \pm 0.35^{Ac*}$
10%NH_3, 2h	NaAlg-BCP50	29.67 ± 0.58^{Ac}	8.33 ± 0.58^{Ba}	35.67 ± 0.58^{Aa}	$30.78 \pm 0.79^{Aa*}$
5%NH_3, 2h	NaAlg-BCP50	40.00 ± 0.01^{Ab}	1.00 ± 0.01^{Bc}	27.00 ± 0.01^{Bb}	$17.20 \pm 0.63^{Bb*}$
1%NH_3, 2h	NaAlg-BCP50	49.00 ± 0.01^{Aa}	-0.67 ± 0.58^{Ad}	18.67 ± 0.58^{Bc}	$6.54 \pm 0.64^{Bc*}$
500ppm NH_3, 2h	NaAlg-BCP50	50.67 ± 0.58^{Aa}	4.67 ± 0.58^{Ab}	19.33 ± 0.58^{Ac}	4.96 ± 0.33^{Bc}

Values are presented as mean ± SD (n = 3). Different lowercase letters (a-e) indicate significant differences ($p < 0.05$) between films exposed to different NH_3 concentrations at the same exposure time. Different uppercase letters (A-C) indicate the significant differences ($p < 0.05$) for the same film exposed to similar NH_3 concentrations at different exposure times. $\Delta E > 5^{(*)}$ indicates the observer may notice the difference between two colours.

Table 3.23. CIE Lab colour analysis of the NaAlg-BCP50 film following sequential exposure to 10% NH_3 and 10% CH_3COOH, for 2h and 6h.

Conditions	**Sample**	**Colour attributes**			**Colour**
		L*	***a****	***b****	**difference (ΔE)**
At t_0	NaAlg-BCP50 after 6h of 10%NH_3 exposure	28.67 ± 1.15^{c}	13.33 ± 0.58^{b}	34.67 ± 0.58^{b}	n/a
10%CH_3COOH, 2h		42.67 ± 0.58^{b}	15.67 ± 0.58^{a}	40.00 ± 1.00^{a}	$15.54 \pm 0.90^{a*}$
10%CH_3COOH, 6h		46.00 ± 0.01^{a}	15.67 ± 0.58^{a}	41.67 ± 0.58^{a}	$18.88 \pm 1.11^{a*}$

Values are presented as mean ± SD (n = 3). Different lowercase letters (a-c) indicate significant differences ($p < 0.05$) between films exposed to the same CH_3COOH concentration at different exposure times. $\Delta E > 5$ (*) indicates a colour difference perceptible to the human eye.

3.1.5.9. Stability of ACN within the films

The stability of ACN can be influenced by various factors such as pH, temperature, light, antioxidants, oxygen, and etc.[314] Due to their excellent pH sensitivity, ACN incorporated into NaAlg-BCP films have successfully demonstrated visible colour changes when exposed to NH_3, representing a high-pH environment. However, several other factors may affect the stability of ACN within the film matrix. Therefore, the NaAlg-BCP50 film was selected for further stability testing to evaluate how the film's colour changes over a 14-day period in a plastic incubator (Gilson digital mini-incubator) at 25 °C and can be seen in **Figure 3.35.** CIE Lab colour analysis (**Table 3.24**) confirmed a gradual colour change in the NaAlg-BCP50 film, with the ΔE value increasing steadily each day. A noticeable visual difference in colour was observed within 10 days (ΔE > 5). As the film was stored in an incubator at 25 °C, its colour change may have been influenced by temperature, light, and air exposure. ACNs are known to be more stable at lower temperatures (2-4 °C).[314,315] The observed brownish coloration can be attributed to the ring opening of ACN into chalcones at elevated temperatures.[316] Moisture in the air can also promote the deglycosylation of ACN into anthocyanidin glycosides, which can then convert into chalcones.[316] Oxygen is another critical factor affecting ACN stability, as its presence can lead to degradation through oxidative reactions or enzymatic activity involving oxidases.[317] Light, particularly high-intensity or UV light, can also induce ring-opening of ACN into chalcones.[314] However, in this study, light was likely not the primary factor contributing to the film's colour change, as the samples were stored in an incubator exposed only to natural light. As a result, the ACN in the film are not stable under ambient conditions, with colour changes occurring within 10 days. Thus, the films should be stored under low temperature, low light and low oxygen conditions to preserve their stability and colour integrity.

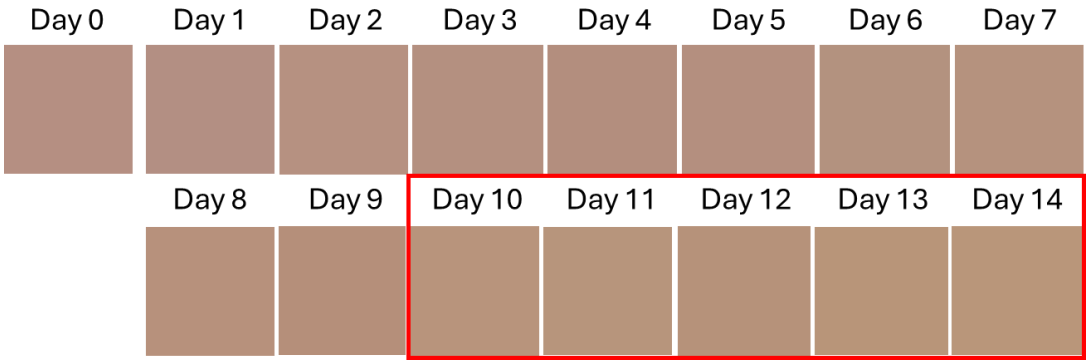

Figure 3.35. Colour changes of the NaAlg-BCP50 film over a 14-day period.

Table 3.24. CIE Lab colour analysis of NaAlg-BCP50 over a 14-days period.

Sample	Conditions	Colour attributes			Colour difference (ΔE)
		L*	***a****	***b****	
NaAlg-BCP50	Day 0	61.67 ± 1.53^{a}	13.00 ± 0.01^{b}	12.67 ± 0.58^{ab}	n/a
	Day 1	63.33 ± 1.53^{ab}	12.00 ± 0.01^{ab}	12.00 ± 0.01^{a}	2.10 ± 0.60^{a}
	Day 2	63.33 ± 0.58^{ab}	12.33 ± 0.58^{ab}	13.33 ± 0.58^{abc}	2.29 ± 1.63^{a}
	Day 3	63.67 ± 0.58^{ab}	11.33 ± 0.58^{ab}	13.33 ± 0.58^{abc}	2.85 ± 0.56^{a}
	Day 4	63.00 ± 1.00^{ab}	12.00 ± 1.00^{ab}	14.33 ± 0.58^{bcde}	2.74 ± 0.87^{a}
	Day 5	63.00 ± 0.01^{ab}	12.33 ± 0.58^{ab}	14.67 ± 0.58^{bcde}	2.91 ± 0.58^{a}
	Day 6	63.33 ± 0.58^{ab}	10.33 ± 0.58^{a}	14.00 ± 0.01^{abcd}	3.68 ± 0.48^{ab}
	Day 7	64.00 ± 0.01^{b}	10.67 ± 0.58^{a}	15.33 ± 0.58^{cdef}	4.36 ± 1.23^{ab}
	Day 8	64.00 ± 0.01^{b}	11.67 ± 1.15^{ab}	16.00 ± 1.00^{defg}	4.51 ± 1.01^{abc}
	Day 9	64.00 ± 1.00^{b}	12.00 ± 1.00^{ab}	16.33 ± 0.58^{efg}	4.57 ± 0.44^{abc}
	Day 10	64.33 ± 0.58^{b}	11.33 ± 0.58^{ab}	17.33 ± 0.58^{fghi}	5.71 ± 0.79^{bcd*}
	Day 11	64.00 ± 0.01^{b}	10.33 ± 0.58^{a}	17.00 ± 1.00^{fgh}	5.74 ± 1.23^{bcd*}
	Day 12	64.00 ± 0.01^{b}	11.33 ± 0.58^{ab}	17.67 ± 0.58^{ghi}	5.90 ± 0.52^{bcd*}
	Day 13	64.33 ± 0.58^{b}	10.67 ± 1.53^{a}	18.67 ± 1.15^{hi}	7.16 ± 0.84^{cd*}
	Day 14	64.33 ± 0.58^{b}	10.67 ± 0.58^{a}	19.33 ± 0.58^{i}	7.72 ± 1.04^{d*}

Values are presented as mean ± SD (n = 3). Different lowercase letters (a-i) indicate significant differences ($p < 0.05$) between films over 14 days. $\Delta E > 5$ (*) indicates a colour difference perceptible to the human eye.

3.1.5.10. Thermal stability of films

Thermal stability is an essential property for understanding how films behave under heat and for evaluating their suitability during manufacturing, storage, and use. The thermal stability of the film-forming compounds and the NaAlg-BCP films was evaluated using differential scanning calorimetry (DSC) under nitrogen gas (**Figure 3.36**). Alginic acid was chosen as a control to compare the thermal stability with NaAlg through DSC. Two small endothermic peaks were observed at 111 °C and 139 °C in alginic acid, while a small peak at 111 °C was not seen in NaAlg (**Figure 3.36A**). The shift of a main sharp endothermic peak to higher temperatures (at 184 °C) was seen in NaAlg when compared to alginic acid (and 173 °C). This tend to be because sodium ions form ionic bonds with alginate, making it more resistant to thermal degradation compared to the weaker hydrogen bonds in alginic acid.[318] For BCP and DFC, a small endothermic peak and a predominant sharp endothermic peak were also observed at 135 °C and 137 °C, and 184 °C and 209 °C, respectively.

However, the DSC curves of alginic acid and NaAlg in this study were inconsistent with the literatures, which typically show a broad endothermic peak at approximately 100 °C corresponding to water evaporation.[104,318] This can be explained by the different DSC lids used as pinhole or perforated lid was used in the literature,[104,318] but sealed pan was used in this study. In pinhole pan, a broad endothermic peak of dehydration, followed by a sharp exothermic crystallisation peak of amorphous structure were observed. In contrast, the sealed pans prevented dehydration, allowing the sample to retain water until it reached 100 °C. Consequently, a sharp endothermic peak and the loss of crystalline structure were observed instead.[319]

Regarding thermal stability of NaAlg and NaAlg-BCP films, The DSC curve of NaAlg-BCP films revealed a small endothermic peak and a predominant sharp endothermic peak, similar to those observed in NaAlg powder. However, these peaks were shifted to 149 °C and 204 °C, respectively, indicating the formation of crosslinks between NaAlg and Ca^{2+} ions. This interaction leads to the development of an “egg-box” structure, which enhances the films’ thermal resistance. As the BCP content in the films increased, the small endothermic peaks shifted to higher temperatures (from 147 °C to 152 °C), while the main sharp peaks shifted lower (from 204 °C to 187 °C). This shift is likely due to the interference caused by the branches

of pectin or anthocyanin-bound pectin in BCP, which hinder the formation of the “egg-box” structure. Moreover, incorporating DFC or ACN into NaAlg-BCP20 films did not affect the small endothermic peak at 150 °C. However, the main endothermic peak shifted higher to 195 °C with DFC addition, and lower to 189 °C when ACN was incorporated. These findings suggest that no significant thermal transitions occur below 147 °C, indicating that all NaAlg-BCP films are well-suited for room temperature storage and relatively high-temperature food heating applications.

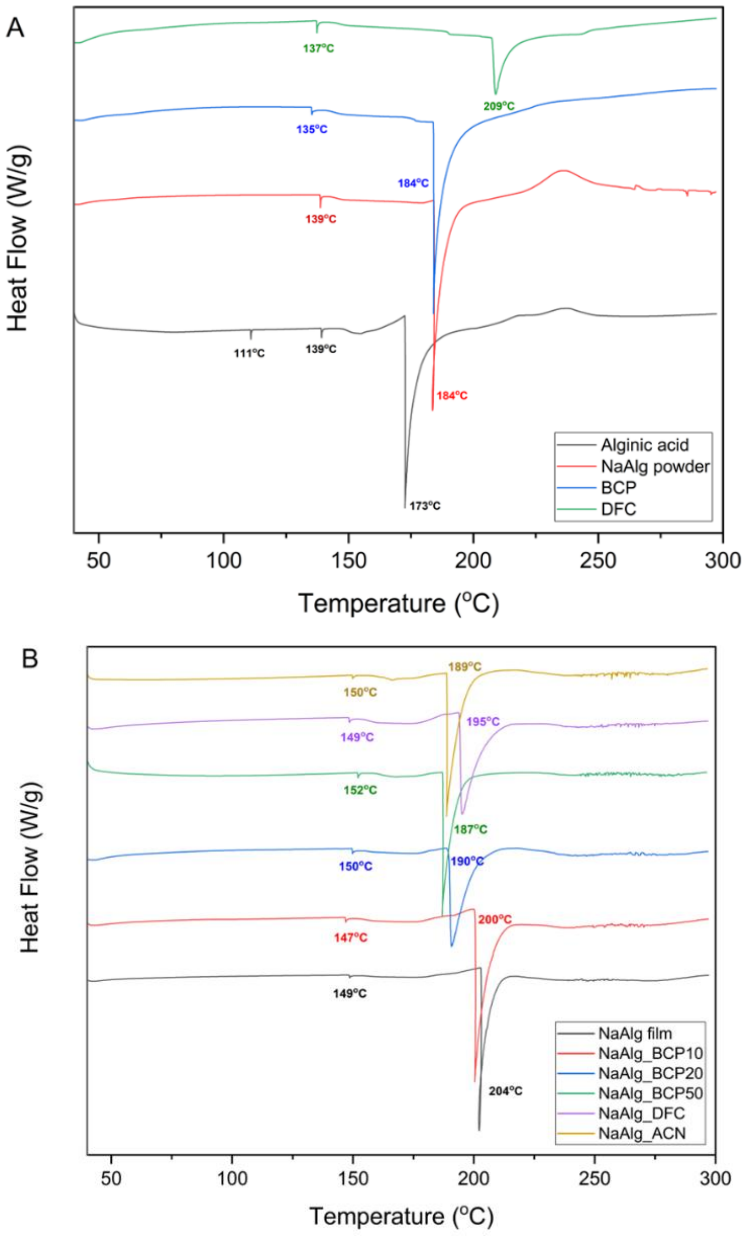

Figure 3.36. Differential scanning calorimetry (DSC) curves of starting materials (A), and NaAlg and NaAlg-BCP films (B).

3.2. Valorisation of extruded ginger pomace (GP) (A2), and extruded aeroponically grown coriander (CR) and Thai basil (ThB) roots (A3): A comparative study

3.2.1. Characterisation of GP, CR and ThB (Objective A2 (i) and A3 (i))

Compositional and elemental analysis of the extruded ginger pomace (GP), coriander root (CR) and Thai basil root (ThB) are shown in **Table 3.25**. The results revealed that GP is a rich source of carbohydrates, containing mainly starch and cellulose (39.52 wt.%). Minor carbohydrates, such as hemicellulose and pectin, were each present at less than 1 wt.%. This trend agrees with the literature, which identified starch as the major carbohydrate component in spent ginger (47.23 – 50.79%).[113] However, the carbohydrate content can vary depending on the ginger source and the pre-treatment applied.

Konar *et al*. analysed spent ginger and found that, in addition of starch, the material contained protein (11.74 – 13.02 %), ash (9.37 – 10.32%), cellulose (3.84 – 4.32%), and pectin (1.63 – 2.09%), with lignin and hemicellulose not detected.[113] In contrast, our GP contained lignin (1.82 wt.%), hemicellulose (0.75 wt.%) and lower levels of ash (3.26 wt.%), protein (3.00 wt.%) and pectin (0.48 wt.%) than those reported by Konar *et al*.[113] It should also be noted that the cellulose and starch contents in our GP sample were estimated from the measured glucose content, the monomer of both polysaccharides, so the reported values represent the combined proportion of these two polysaccharides.

In contrast, CR and ThB consisted primarily of lignocellulosic material, with high contents of lignin (22.42 – 25.61 wt.%), protein (23.31 – 23.41 wt.%), and ash (9.44 – 10.16 wt.%). Compared with coriander seeds and leaves, and basil seeds, which contain protein (11.00 – 21.30% in coriander seeds; 4.05% in coriander leaves; 9.40% in basil seeds) and ash (1.70 – 8.59% in coriander seeds; 1.90% in coriander leaves; 5.20% in basil seeds),[175,320] the extruded, aeroponically grown CR and ThB exhibited higher protein and ash contents. However, it is important to note that protein content was estimated from total nitrogen, which may be influenced by the presence of chlorophyll. Chlorophyll, the green pigment in plants, contains four nitrogen atoms in its chemical structure, potentially leading to an overestimation of protein content.

Table 3.25. Compositional and elemental analysis of extruded ginger pomace (GP), coriander root (CR) and Thai basil root (ThB).

Composition (wt.%)	**Ginger pomace**	**Coriander root**	**Thai basil root**
Moisture [a]	8.99 ± 0.51^{Ce}	7.42 ± 0.62^{Bb}	4.88 ± 0.01^{Ab}
Ash [a]	3.26 ± 0.53^{Ad}	9.44 ± 0.20^{Bc}	10.16 ± 0.50^{Bc}
Protein (N × 6.25) [a]	3.00 ± 0.09^{Ad}	23.31 ± 0.44^{Bd}	23.41 ± 0.57^{Bd}
Cellulose and starch [a, b]	39.52 ± 2.38^{Bf}	9.79 ± 0.38^{Ac}	10.25 ± 1.83^{Ac}
Hemicellulose [a, b]	0.75 ± 0.04^{Ab}	0.99 ± 0.02^{Ba}	1.14 ± 0.51^{ABa}
Pectin [a, b]	0.48 ± 0.04^{Aa}	6.46 ± 0.07^{Bb}	5.01 ± 1.81^{Bb}
Klason lignin [a]	1.82 ± 0.54^{Ac}	22.42 ± 0.66^{Bd}	25.61 ± 0.60^{Ce}
Elemental content (wt.%)			
C	41.18 ± 0.04^{Ac}	42.06 ± 0.05^{Bc}	41.31 ± 0.29^{Ac}
H	6.28 ± 0.01^{Cb}	5.96 ± 0.13^{Bb}	5.71 ± 0.07^{Ab}
N	0.48 ± 0.01^{Aa}	3.73 ± 0.07^{Ba}	3.75 ± 0.09^{Ba}
Remainder	52.06 ± 0.03^{Cd}	48.03 ± 0.18^{Ad}	48.85 ± 0.49^{Bd}

[a] Estimated via NREL method,[204–206,209] [b] estimated from HPLC carbohydrate and sugar analysis of acid hydrolysed BC. Values are presented as mean ± SD (n = 3). Letters indicate the significant differences ($p < 0.05$).

The presence of carbohydrates, primarily starch and cellulose, in GP (**Figure 3.37A**), and lignocellulosic components and ash in CR and ThB (**Figure 3.37B**), was further supported by thermogravimetric analysis (TGA). The TGA thermogram and derivative thermogravimetric (dTG) curve of GP show an initial moisture loss between 25 – 150 °C, followed by a major mass loss occurring between 150 – 400 °C. The main thermal degradation peak (T_d) at 293 °C accounting for 63.48 wt.%, typically associated with the thermal degradation of starch (see **Appendix 18**), and the shoulder observed above 300 °C may correspond specifically to cellulose degradation.[229,230]

For CR and ThB, the TGA and dTG profiles displayed three distinct regions corresponding to moisture loss (25 – 150 °C), carbohydrate and cellulose decomposition (150 – 350 °C), and lignin degradation (350 – 500 °C). Carbohydrate and cellulose region accounted for approximately 43.61 wt.% in CR (T_d = 318 °C) and 41.86 wt.% in ThB (T_d = 323 °C). Lignin contributed 17.28 wt.% in CR and 15.76 wt.% in THB, while fixed carbon and ash made up 31.49 wt.% in CR and 35.44 wt.% in ThB, respectively.

However, the carbohydrates content estimated from TGA (63.48 wt.% for GP; 43.61 wt.% for CR; 41.86 wt.% for ThB), which reflect thermal decomposition behaviour, was higher than the value measured by HPLC (**Table 3.25**). This could be explained by incomplete hydrolysis of polysaccharides during sample preparation for HPLC. Partial hydrolysis can produce short-chain oligosaccharides that are not quantified when estimating cellulose, hemicellulose, and pectin contents, as only the monomeric sugars, such as galacturonic acid, xylose, and glucose, are considered.

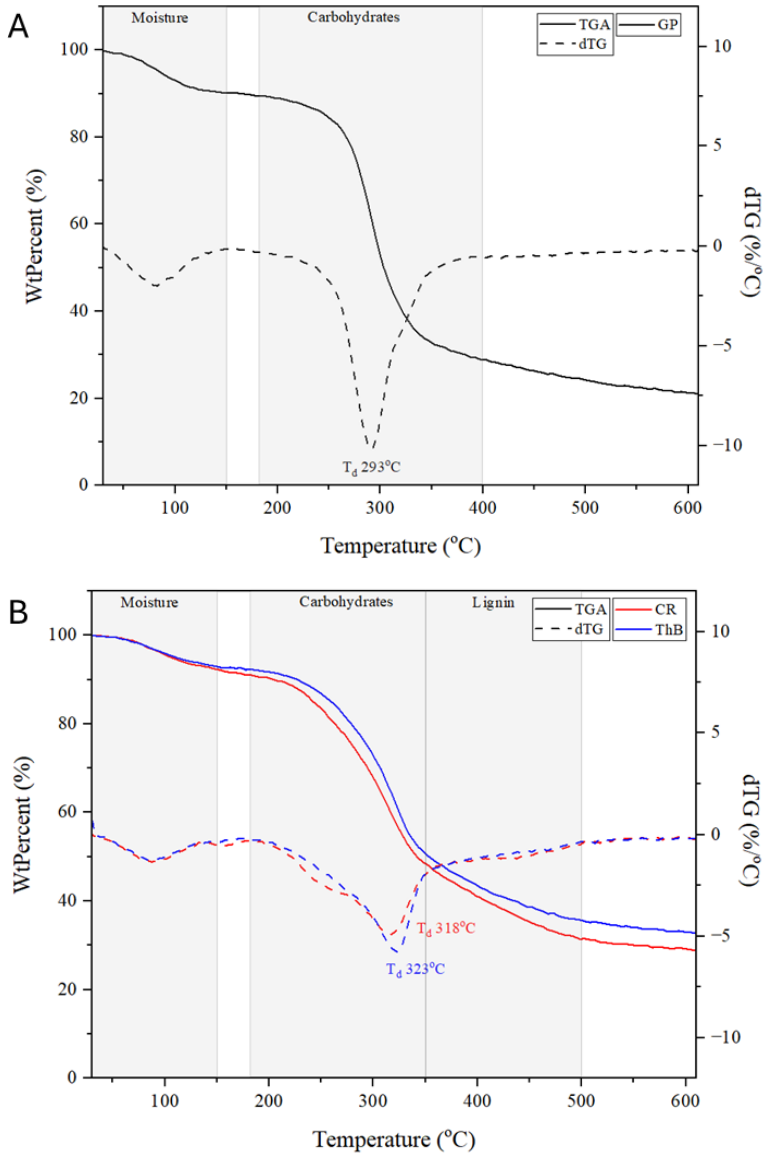

Figure 3.37. TGA and dTG thermograms of GP (A), CR and ThB (B).

IR spectroscopy analysis of GP supported the TGA result, as the detected peaks associated to the functional groups characteristic of carbohydrates (**Figure 3.39**). The presence of carbohydrates is indicated by the broad peak at 3292 cm^{-1} (-OH stretching of hydroxyl groups), 2926 cm^{-1} (-C-H stretching), 1640 cm^{-1} (-C=O stretching of esters), and 996 cm^{-1} (-C-O stretching of glycosidic bond).[161,321] However, the IR spectra closely resemble those reported for ginger starch in the literature, as well as amylose and amylopectin (see **Appendix 18**),[161,322] suggesting that starch is likely the predominant carbohydrate in the extruded ginger pomace.

IR spectra of CR and ThB (**Figure 3.38**) also displayed characteristic carbohydrate signals at 3296 cm^{-1} (-OH stretching), 2921 cm^{-1} (-C-H stretching), 1640 cm^{-1} (-C=O stretching), and 1026 cm^{-1} (-C-O stretching). In addition, the peaks at 3296, 1634, 1536, and 1240 cm^{-1}, associated with N-H stretching of amide bonds (Amide A), C=O stretching (Amide I), N-H bending (Amide II), and N-H bending combined with C-N stretching (Amide III), respectively,[323] were more pronounced compared to GP sample. These enhanced amide signals indicate that CR and ThB contain relatively high protein contents.

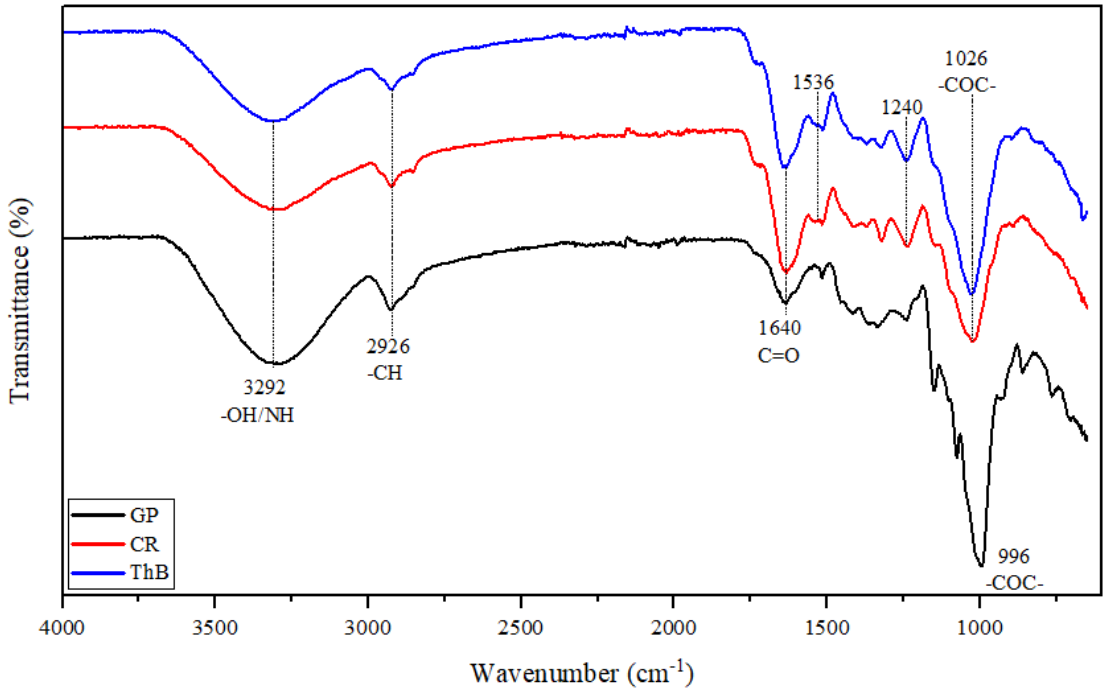

Figure 3.38. IR spectra of GP, CR and ThB.

3.2.2. Supercritical CO_2 ($scCO_2$) extraction and characterisation of GP, CR and ThB extracts (Objective A2 (ii) and A3 (ii))

Prior to fractionating the extruded GP, CR and ThB via acid-free microwave assisted treatment, the ginger essential oil (GP oil), CR extract (scCR), and ThB extract (scThB) were recovered through supercritical CO_2 ($scCO_2$) extraction with 10% ethanol as a co-solvent. This method was selected based on its reported efficiency and considered a green methodology. Literature shows that adding ethanol can significantly enhance essential oil yields (up to 6.06 wt.% in dried ginger, and 4.12 wt.% in spent ginger), compared with $scCO_2$ alone (dried ginger; 1.54 wt.%, spent ginger; 2.51 wt.%).[74,122] In addition, $scCO_2$ extraction of coriander seeds and aerial parts of basil typically yield 0.57 – 7.00 wt.%, and 0.39 – 2.2 wt.% of extract, respectively.[188,190,324,325] The yields of GP oil, scCR and scThB extracts, obtained in this study were only 0.45, 0.42, and 0.37 wt.%, respectively. These relatively low yields may be due to the extrusion process, which disrupts the cell walls and facilitates the release of essential oils into the expressed juice, leaving a reduced amount of extractable oil in the remaining solids.

GP oil, scCR and scThB extracts, were analysed by ^{1}H NMR and IR spectroscopy (**Figure 3.39**) to identify types of compounds present. The ^{1}H NMR spectra of GP oil (**Figure 3.39A**) showed resonances similar to those reported for ginger ethanolic Soxhlet extracts by Bose *et al*.[326] Signals between δ0.50 and δ3.00 ppm likely correspond to alkyl chains of ginger bioactive compounds such as gingerols and shogaols. A *singlet* signal at δ3.75 – 4.00 ppm may be attributed to the -OCH_3 moiety, while *broad singlet* signals between δ5.00 and δ5.75 ppm may be attributed to the -OH protons of alcohols and phenols. In addition, aromatic protons (δ6.00 – 8.00 ppm) were also observed. Although these features are consistent with gingerols and shogaols, the resonances between δ0.50 and δ4.50 ppm may also indicate the presence of fatty acids or triglycerides, similar to those detected and assigned in blackcurrant pomace heptane and ethanolic extracts (see **Figure 3.21** and **Table 3.13**).

Meanwhile, the ^{1}H NMR spectra of scCR and scThB extracts (**Figure 3.39B**) were dominated by signals characteristic of fatty acids and triglycerides between δ0.50 and δ5.50 ppm, with detailed assignments provided in **Table 3.13**.[283,284] Weaker resonances were also observed in the δ6.00 – 8.50 ppm range, indicating the presence of aromatic bioactive compounds, but at lower concentrations.

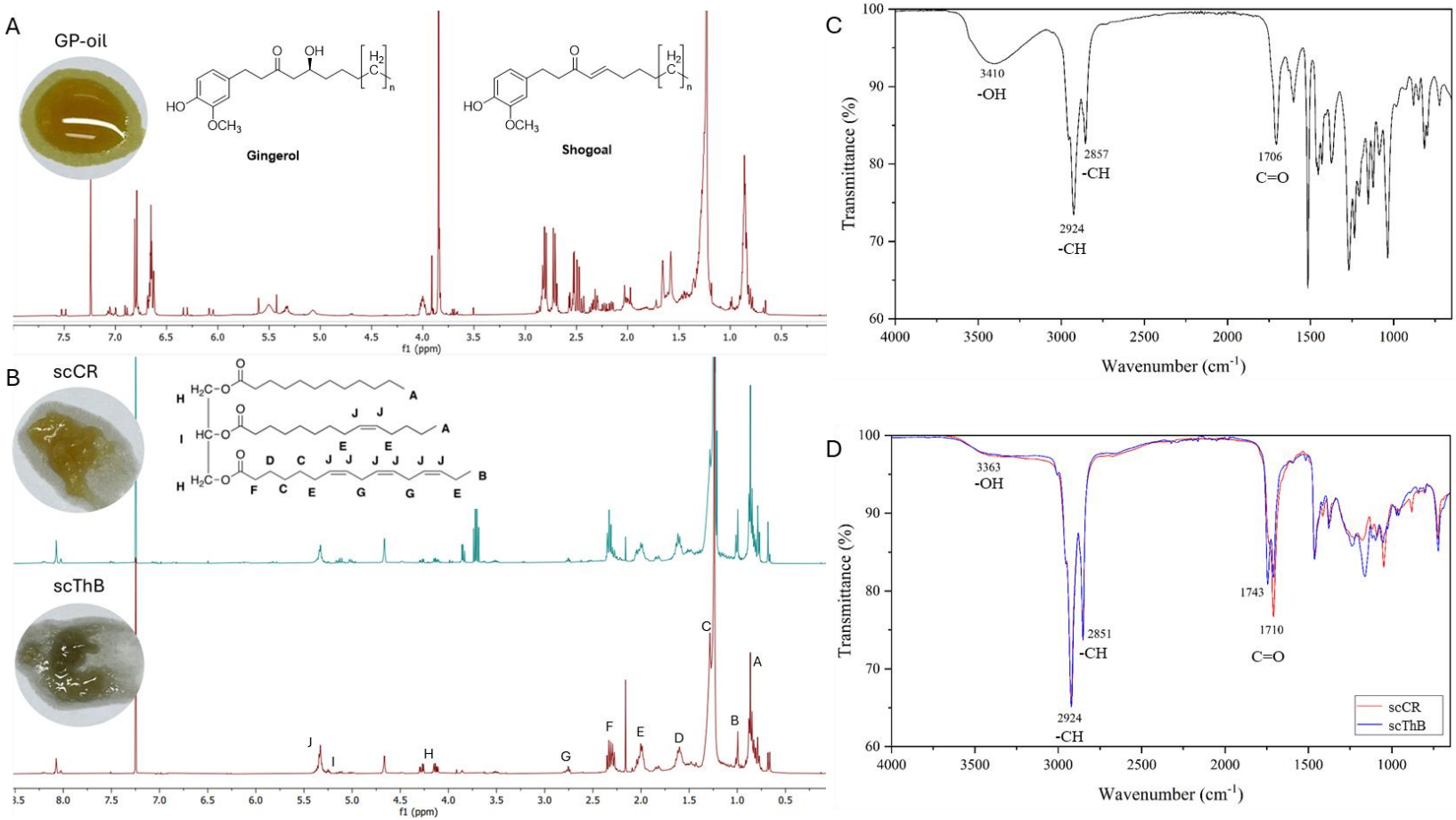

Figure 3.39. Appearance and ^{1}H NMR spectra ($CDCl_3$, 400 MHz) of GP oil (A), scCR and scThB extracts (B), and IR spectra of GP oil (C), scCR and scThB extracts (D).

The IR spectra of GP oil (**Figure 3.39C**) and scCR and scThB extracts (**Figure 3.39D**), showed characteristic absorbance bands at around 3300 – 3400 cm^{-1} (O-H stretching), 2800 – 2900 cm^{-1} (C-H stretching), and 1700 cm^{-1} (-C=O carbonyl stretching), further support the functional groups identified in the ^{1}H NMR analysis. In the scCR and scThB extracts, the relatively strong C-H stretching bands (2800 – 2900 cm^{-1}) and pronounced C=O stretching at approximately 1700 cm^{-1} indicates the presence of long-chain hydrocarbons or long-chain fatty acids within these extracts.

Detailed characterisation of the major compounds contains in GP oil, scCR and scThB extracts were identified using GC-MS (**Table 3.26**). The analysis revealed that palmitic acid, linoleic acid, and several aromatic compounds, specifically Zingerone derivatives (compounds **2**, **4**, **6**, **7**, **9** and **10**), and Shogaols (compounds **3** and **10**), were the predominant constituents (**Table 3.26** and **Figure 3.40**). Interestingly, aromatic compounds accounted for 51.29% of the total composition, while fatty acids were detected only 4.58%. The three most abundant phenolics were 4-(3-hydroxy-2-methoxyphenyl)-butan-2-one (10.37%, **2**), 1-(4-hydroxy-3-methoxyphenyl) oct-4-en-3-one (3-Shagaol) (10.20%, **3**), and 1-(4-Hydroxy-3-methoxyphenyl) decane-3,5-dione (7.13%, **4**). The GC chromatogram of GP oil and the mass spectrum of these major compounds are provided in **Appendix 16**. Zingerone and shogaols have also been identified as major bioactive compounds in $scCO_2$ - ethanol extracts of dried ginger and spent ginger.[74,122] However, unlike those extracts, our GP oil did not contain zingiberene, gingerols, or α-curcumene, which are typically reported as key bioactive constituents.

GC-MS analysis of the scCR and scThB extracts support the ^{1}H-NMR and IR findings, confirming that fatty acids and long-chain hydrocarbons are the major components. The primary fatty acids identified were palmitic acid (22.46 % in scCR; 44.43 % in scThB) and oleic acid (11.37 % in scCR; 5.81 % in scThB), along with other compounds such as oleamide, heneicosane ($C_{21}H_{44}$), pentacosane ($C_{25}H_{52}$), and heptacosane ($C_{27}H_{56}$) (**Table 3.26**). The GC chromatogram and the mass spectra of the three major compounds in scCR and scThB extracts are provided in **Appendix 17** and **18**, respectively. These results are consistent with literature reports indicating that palmitic and oleic acids are among the most abundant fatty acids in coriander and basil. [175,320]

However, characteristic essential oil constituents of coriander and basil, such as linalool, geranial, and estragole,[175,176,178] were not detected as major compounds under the $scCO_2$ extraction conditions with 10% ethanol. Instead, this extraction method selectively recovered fatty acids and long-chain hydrocarbons, which accounted for 37.06% of the total composition in scCR and 66.25% in scThB (based on GC peak areas). In contrast, the same extraction conditions were more suitable for ginger, where only 4.58% of the extract consisted of fatty acids, while essential oil compounds represented 51.29% of the total detected components.

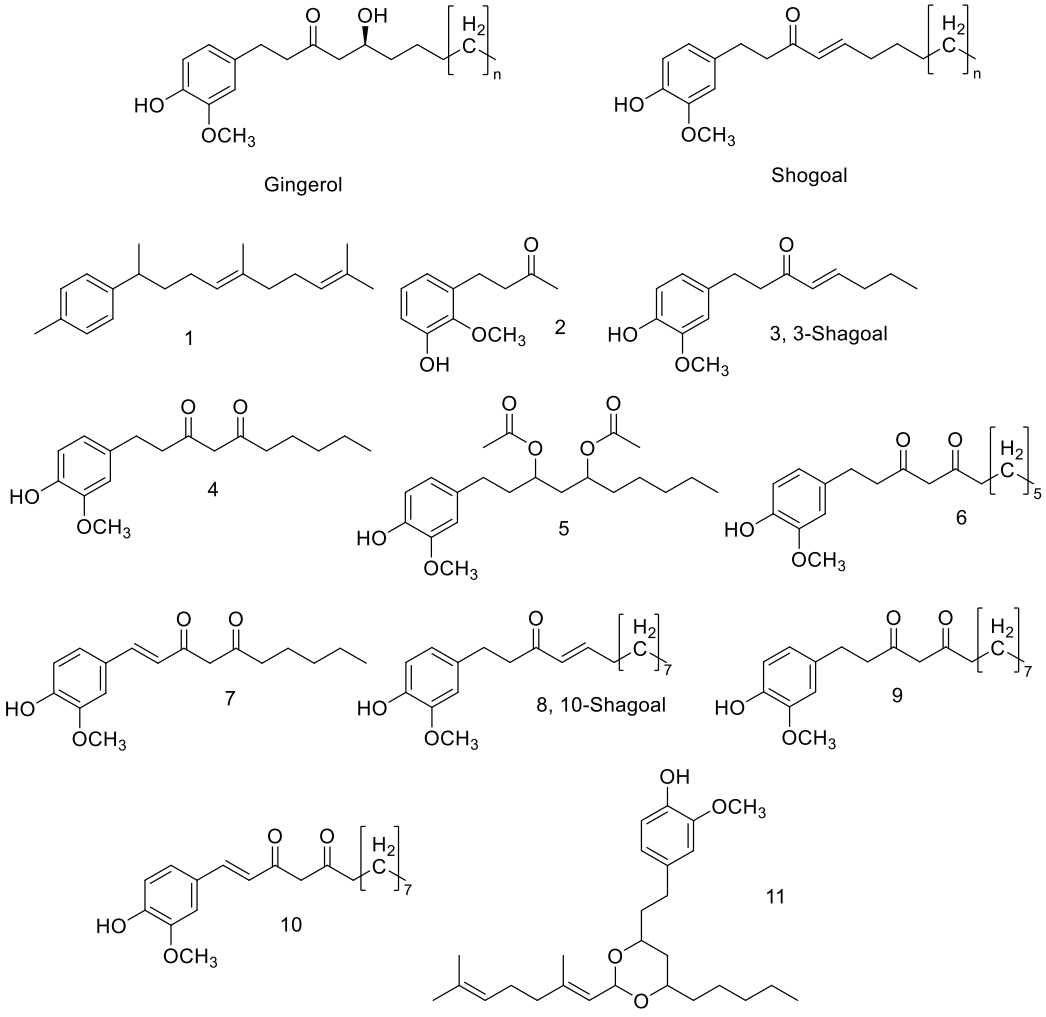

Figure 3.40. Phenolic compounds found in GP oil identified based on GC-MS result.

Table 3.26. Major identified compounds by GC-MS in GP oil, scCR and scThB extracts.

Compound	Aromatic compound no.	Retention time (t_R, min)	Area (%)		
			GP oil	scCR	scThB
Palmitic acid		5.59	1.61	22.46	40.43
(*E*)-1-(6, 10-dimethylundeca-5, 9-dien-2-yl)-4-methylBenzene	**1**	5.62	1.53		
Oleic acid		6.00		11.37	5.81
Linoleic acid		6.01	2.97		
4-(3-hydroxy-2-methoxyphenyl)-butan-2-one	**2**	6.31	10.37		
Heneicosane		6.33			6.47
1-(4-hydroxy-3-methoxyphenyl) oct-4-en-3-one (3-Shagaol)	**3**	6.47	10.20		
Oleamide		6.57		3.24	5.01
1-(4-Hydroxy-3-methoxyphenyl) decane-3,5-dione	**4**	6.60	7.13		
Pentacosane		6.86			6.49
1-(4-Hydroxy-3-methoxyphenyl) decane-3,5-diyl diacetate	**5**	7.07	5.51		
1-(4-Hydroxy-3-methoxyphenyl) dodecane-3,5-dione	**6**	7.22	1.49		
1-(4-hydroxy-3-methoxyphenyl) dec-1-ene-3,5-dione	**7**	7.41	3.87		
Heptacosane		7.51			2.04
1-(4-Hydroxy-3-methoxyphenyl) tetradec-4-en-3-one (10-Shagaol)	**8**	7.84	4.66		
1-(4-Hydroxy-3-methoxyphenyl) tetradecane-3,5-dione	**9**	8.06	4.32		
1-(4-hydroxy-3-methoxyphenyl) tetradec-1-ene-3,5-dione	**10**	9.52	1.09		
4-(2-(2-(2,6-Dimethylhepta-1,5-dien-1-yl)-6-pentyl-1,3-dioxan-4-yl) ethyl)-2-methoxyphenol	**11**	9.84	1.12		

3.2.3. Isolation and characterisation of protein isolated from acid-free microwave-assisted hydrolysates obtained from GP, CR and ThB (Objective A2 (iii) and A3 (iii))

This section presents the preliminary results of protein recovery from the GP, CR, and ThB hydrolysates (by-products of defibrillated cellulose production; **section 3.2.4**) obtained from acid-free conventional water (50 °C, 2h) or microwave-assisted treatment at low to moderate temperatures. For microwave-assisted extraction (MAE), oil-free GP was processed across a temperature range of 60 – 120 °C. Oil-free CR was treated at 60 and 80 °C, based on the results obtained for GP, while ThB was evaluated at 80 °C following the outcomes from both GP and CR.

Table 3.27 summarises the isolated protein yield and protein content of crude GP, CR, and ThB extracts. Protein recovered from water extraction of oil-free GP (GPP-W) yielded 0.82 wt.%, whereas microwave-assisted extraction produced up to 3.56 wt.% as the temperature increased from 60 to 100 °C. At 120 °C, however, no protein could be recovered. In contrast, the protein content, estimated by nitrogen analysis and the Bradford assay, decreased with increasing microwave temperature. This reduction at higher temperatures is likely due to thermal denaturation, consistent with literature that microwave temperatures between 46 and 65°C are optimal for extracting proteins from soybean and herbal roots.[145] Denaturation alters protein structure and can lead to aggregation, thereby reducing the availability of dye-binding sites for Coomassie Brilliant Blue G-250. Additionally, partial hydrolysis at elevated temperatures may produce smaller peptides that bind the dye less effectively, resulting in lower protein content values determined using the Bradford assay. However, protein denaturation itself should not affect nitrogen-based measurements. The observed decrease in nitrogen-derived protein content may instead be due to the loss of nitrogen, for example through the leaching of soluble nitrogen-containing compounds into the liquid fraction or through thermal degradation processes.

Table 3.27. Yield and protein content of isolated protein from oil-free GP, CR, and ThB.

Sample	Yield (wt.%)	Protein content	
		Based on N content* (%)	Bradford assay (%)
GPP-W	0.82 ± 0.04^{d}	61.13 ± 0.18^{e}	0.020 ± 0.002^{d}
GPP-MW60	0.82 ± 0.37^{d}	51.19 ± 1.06^{c}	0.021 ± 0.001^{d}
GPP-MW80	2.13 ± 0.20^{g}	33.16 ± 0.04^{b}	0.011 ± 0.003^{b}
GPP-MW100	3.56 ± 0.31^{h}	14.88 ± 0.44^{a}	0.006 ± 0.002^{a}
GPP-MW120	-	-	-
CRP-W	0.35 ± 0.01^{b}	59.88 ± 0.35^{d}	0.011 ± 0.001^{b}
CRP-MW60	0.88 ± 0.09^{e}	65.28 ± 0.31^{f}	0.018 ± 0.001^{c}
CRP-MW80	0.91 ± 0.09^{f}	60.84 ± 0.49^{e}	0.022 ± 0.001^{d}
ThBP-W	0.21 ± 0.07^{a}	72.56 ± 0.62^{h}	0.006 ± 0.002^{a}
ThBP-MW80	0.54 ± 0.08^{c}	68.72 ± 0.57^{g}	0.007 ± 0.002^{a}

* Protein content is estimated from N × 6.25 conversion factor. Values are presented as mean ± SD (n = 3). Letters indicate the significant differences ($p < 0.05$).

IR spectra of isolated protein from oil-free GP (GPP; **Figure 3.41A**) reveals characteristic protein absorption peaks at 3282, 1635, 1515, and 1235 cm^{-1}, corresponding to N-H stretching of amide bonds (Amide A), C=O stretching (Amide I), N-H bending (Amide II), and N-H bending combined with C-N stretching (Amide III), respectively.[323] At a MW extraction temperature of 100 °C (GPP-MW100), the intensities of these protein-associated peaks decreased, while the carbohydrate-related peak at 1019 cm^{-1} (-C-O stretching of glycosidic bond) became more pronounced.[161,321] These changes indicate that protein denaturation likely occurred at 100 °C under MAE, and the increased isolated yield may be attributed to a higher proportion of carbohydrates. Therefore, microwave temperatures below 100 °C are preferable for protein extraction.

Based on the results obtained from GP, MAE temperatures below 100 °C (60 and 80 °C) were performed on CR, with water included as a control. Water extraction yielded 0.35 wt.% crude protein (CRP-W), while MAE at 80 °C produced up to 0.91 wt.% (CRP-MW80) (**Table 3.27**). As MW temperature increased, the protein content calculated from nitrogen (N) content decreased from approximately 65% (CRP-MW60) to 61% (CRP-MW80). In contrast, protein content estimated from Bradford assay increased, ranging from about 0.018% (CRP-MW60) to

0.022% (CRP-MW80). The large discrepancy between these two methods could be explained by the limitations of N-based protein estimation, which may overestimate protein content because nitrogen measurements include all nitrogen-containing compounds, not just proteins. For example, residual nitrate, which normally present in ginger as a natural occurring compound and in aeroponically grown plants as a nutrient can contribute significantly to the total nitrogen detected. In contrast, Bradford assay provides greater specificity for protein determination, in which acidic cationic Coomassie Blue G-250 (brownish green; absorption at 470 nm) binds to proteins through hydrophobic interaction, providing a stable protein-bound anionic Coomassie Blue G-250 form (blue; absorption at 595 nm; see **Figure 3.42**).[327]

Based on the Bradford assay, MAE at 80 °C yielded the highest protein content in the isolated CR crude protein (CRP-MW80; 21.54 mg/100 g). Therefore, MAE at 80 °C was subsequently applied to ThB, producing 0.54 wt.% of isolated ThBP-MW80 protein with a protein content of 7.08 mg/100 g. In comparison, the control water extraction of ThB yielded a lower protein content (ThBP-W; 0.21 wt.%).

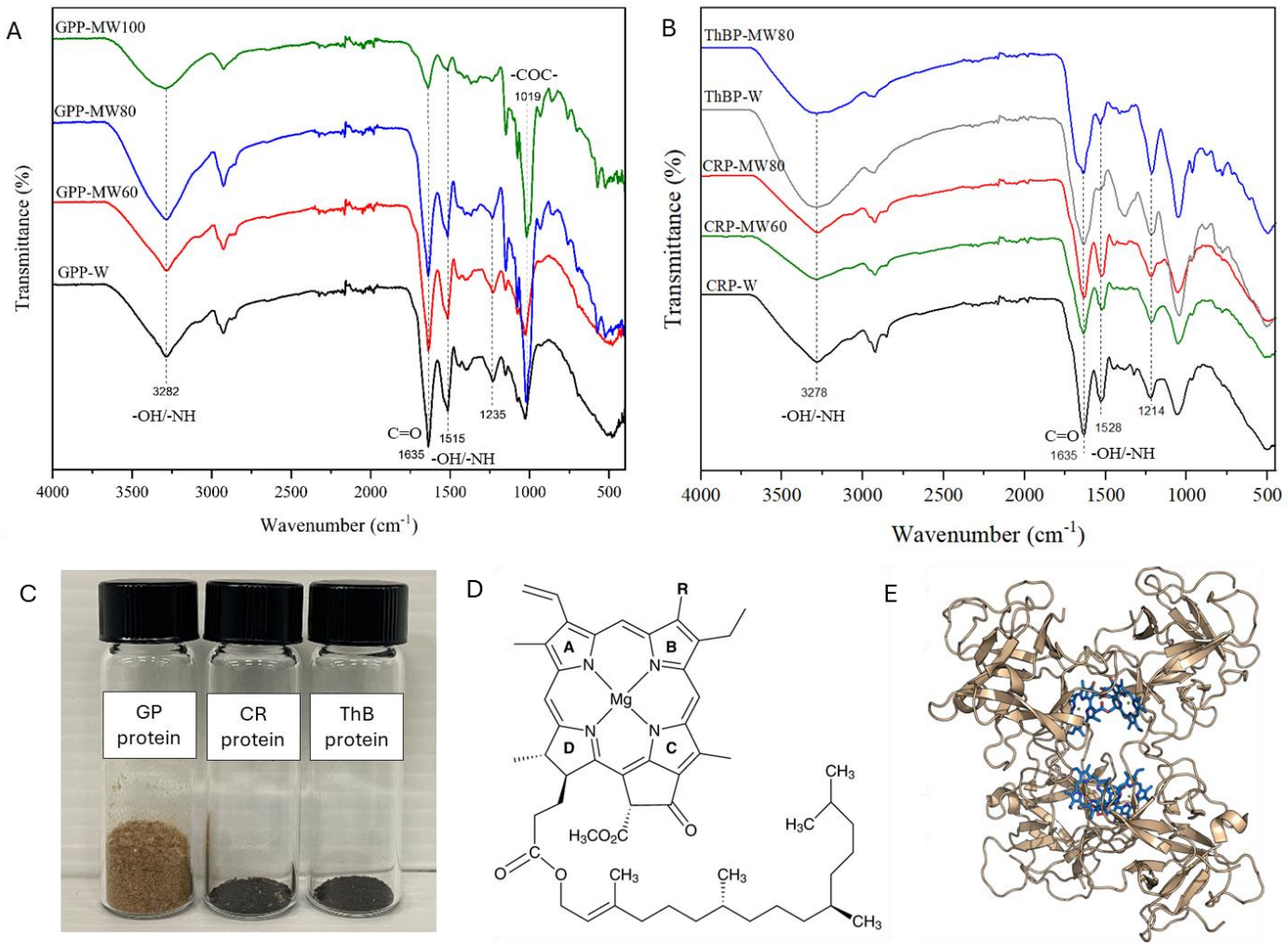

Figure 3.41. IR spectra of isolated protein from GP (A), and CR/ThB (B), appearance of isolated protein (C), structure of chlorophyll (D), crystallographic example of water-soluble chlorophyll protein with polypeptide (beige) and chlorophyll (blue) (E).[328]

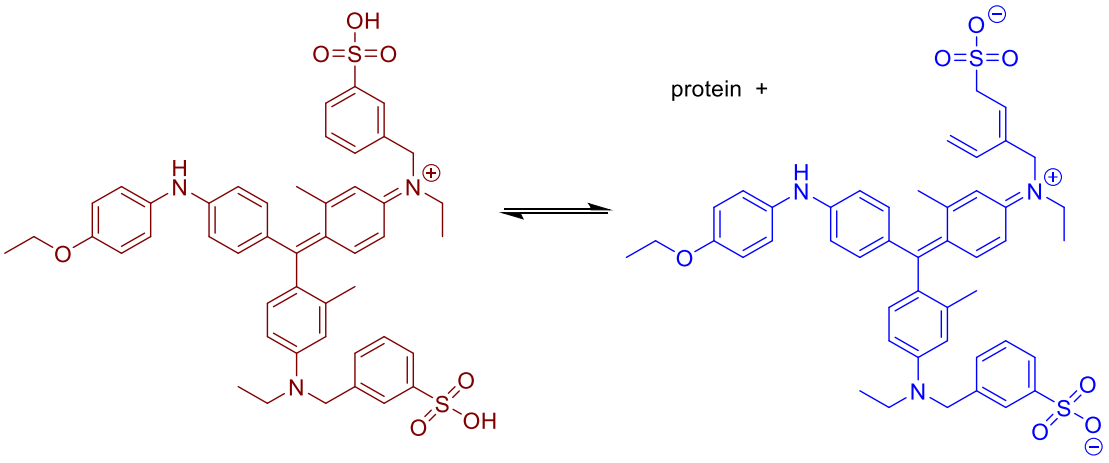

Figure 3.42. Chemical scheme of Coomassie Blue G-250 used in the Bradford assay for protein determination.[327]

IR spectra of isolated proteins from oil-free CR and ThB (CRP and ThBP; **Figure 3.41B**), further confirmed the presence of protein, indicated by strong characteristic peaks corresponding to Amide A (N-H stretching; 3278 cm^{-1}), Amide I (C=O stretching; 1635 cm^{-1}), Amide II (N-H bending; 1528 cm^{-1}), and Amide III (N-H bending combined with C-N stretching; 1214 cm^{-1}).[323] However, the ThBP spectrum exhibited less pronounced peaks at 3278 and 1528 cm^{-1}, associated with N-H functional groups, suggesting a lower protein content. This observation is consistent with the protein content determined by the Bradford assay (**Table 3.27**).

In addition, the presence of Chlorophyll binding protein is assumed to be in the isolated CR and ThB protein, as indicated by their dark green colouration (see **Figure 3.41C**). This observation also helps explain the overestimation of protein content when calculated from nitrogen (N) measurements. Because chlorophyll contains nitrogen atoms within its porphyrin ring, its presence contributes additional non-protein nitrogen, leading to inflated protein values when using N-based conversion factors.

An example of a water-soluble Chlorophyll-protein (WSCP) complex is shown in **Figure 3.41D** and **3.41E**, where the magnesium cation of Chlorophyll preferably binds with carbonyl groups of amide or amide side chains, depending on types of Chlorophyll.[328] WSCPs were first reported by Liang *et al*. as highly efficient photosensitisers for photodynamic therapy (PDT), a technique typically used for cancer therapy and have been shown to remain stable in air and at temperatures up to 100 °C.[329] These proteins can also be isolated from cauliflower, Brussel sprouts, Japanese radish, and Virginia pepper weed.[328]

3.2.4. Acid-free microwave-assisted production of defibrillated celluloses from GP, CR and ThB (Objective A2 (iv) and A3 (iv))

This section presents the production and characterisation of defibrillated cellulose (DFC) derived from the GP, CR, and ThB residues obtained through acid-free microwave-assisted protein extraction (MAE), followed by microwave-hydrothermal reprocessing (MHT) at 160 °C. Based on the optimal protein yields and protein contents determined by the Bradford assay (**Table 3.26**), the optimal MAE conditions were identified as 60 °C for GP and 80 °C for both CR and ThB. Accordingly, the residues generated under these optimal conditions (GPR-MW60, CRR-MW80, and ThBR-MW80) were subjected to MHT at 160 °C to produce defibrillated cellulose (DFC-GP60, DFC-CR80, and DFC-ThB80). In addition, structural changes in GP, CR, and ThB following protein extraction by water or MAE (denoted as GPR, CRR, and ThBR) were evaluated, along with DFC samples.

3.2.4.1. Yield and microstructure analysis

Yield of the extruded ginger residues (GPR), CR residues (CRR), and ThB residues (ThBR) obtained from acid-free conventional water or MAE, as well as the isolated DFC fractions produced by MHT reprocessing at 160 °C, are summarised in **Table 3.28**. Under conventional water extraction (50 °C, 2h), the residue yields were 39.30 wt.% for GPR-W, 81.29 wt.% for CRR-W, and 66.25 wt.% for ThBR-W, which are reported as the controls. As microwave temperature increased, the yield of GPRs declined markedly from 45.18 to 22.22 wt.%, likely due to the enhanced release of starch (see **Section 3.2.5.1**). In contrast, the residue yields of the CRRs remained relatively stable at around 74 wt.%.

The yield of DFC-GP60 (34.58 wt.%) was substantially lower than those of DFC-CR80 (74.53 wt.%) and DFC-ThB80 (77.50 wt.%). This trend corresponds to the compositional differences among the raw materials, where GP is predominantly starch-based, whereas CR and ThB contain mainly lignocellulosic components, which are less extractable under the applied conditions.

The ash content of all samples decreased by approximately half following acid-free water treatment, whether by conventional extraction or MAE. Specifically, ash contents were reduced from the raw material values of GP (3.26 wt.%) to 1.40 - 1.75 wt.% in GPRs and 1.52 wt.% in DFC-GP60; from CR (9.44 wt.%) to 6.56 - 6.69 wt.% in CRRs and 5.69 wt.% in DFC-

CR80; and from ThB (10.16 wt.%) to 5.68 - 6.93 wt.% in ThBRs and 5.49 wt.% in DFC-ThB80. The reduction of ash content could be due to the decrease in soluble inorganic matters during the acid-free water treatments.

Table 3.28. Yield of residues and DFC derived from oil-free GP, CR, and ThB.

Sample	Yield (wt.%)	Ash content (wt.%)
Residue sample		
GPR-W	39.30 ± 5.53^{bc}	1.57 ± 0.03^{c}
GPR-MW60	45.18 ± 3.71^{c}	1.70 ± 0.11^{d}
GPR-MW80	37.85 ± 6.45^{bc}	1.29 ± 0.01^{a}
GPR-MW100	30.82 ± 6.58^{ab}	1.40 ± 0.03^{b}
GPR-MW120	22.22 ± 3.72^{a}	1.75 ± 0.24^{d}
CRR-W	81.29 ± 0.78^{h}	6.63 ± 0.19^{f}
CRR-MW60	74.66 ± 0.25^{f}	6.69 ± 0.24^{f}
CRR-MW80	74.57 ± 0.52^{f}	6.56 ± 0.15^{f}
ThBR-W	66.25 ± 0.21^{e}	5.68 ± 0.25^{e}
ThBR-MW80	61.97 ± 0.58^{d}	6.93 ± 0.21^{g}
DFC sample		
DFC-GP60	34.58 ± 0.23^{b}	1.52 ± 0.03^{c}
DFC-CR80	74.53 ± 0.73^{f}	5.69 ± 0.35^{e}
DFC-ThB80	77.50 ± 0.75^{g}	5.49 ± 0.01^{e}

Values are presented as mean ± SD (n = 3). Letters indicate the significant differences ($p < 0.05$).

SEM analysis was conducted to evaluate the effect of acid-free extraction on the morphology of the extruded ginger pomace (GP) (**Figure 3.43**), extruded aeroponically grown coriander roots (CR) and Thai basil roots (ThB) (**Figure 3.44**). The native GP displayed clusters of starch granules (highlighted in the red circles) along with other components, whereas the GPR samples and the DFC-GP60 exhibited more ruptured surfaces. As the microwave hydrothermal treatment (MHT) temperature increased from 60–120 °C, the SEM images showed progressively more ruptured surfaces, greater exposure of fibres (yellow circles), and fewer visible starch granules. Unlike GP, SEM images of CR and ThB not did not show any starch

granules; instead, only surface ruptures were observed, consistent with their lignocellulosic nature.

In addition, the starch granules underwent noticeable surface changes, in which the initially round and smooth granules observed in GP, GPR-W, and GPR-MW60 became increasingly cracked and rough with higher MW temperatures, eventually disappearing entirely at 120 °C. This observation supports that the reduced yields of GPR and DFC-GP60 are associated with starch loss. Furthermore, the DFC-GP60 sample revealed more distinct fibre bundles, indicating that MHT reprocessing of GPR-MW60 at 160 °C not only enhanced starch removal but also promoted cellulose defibrillation.

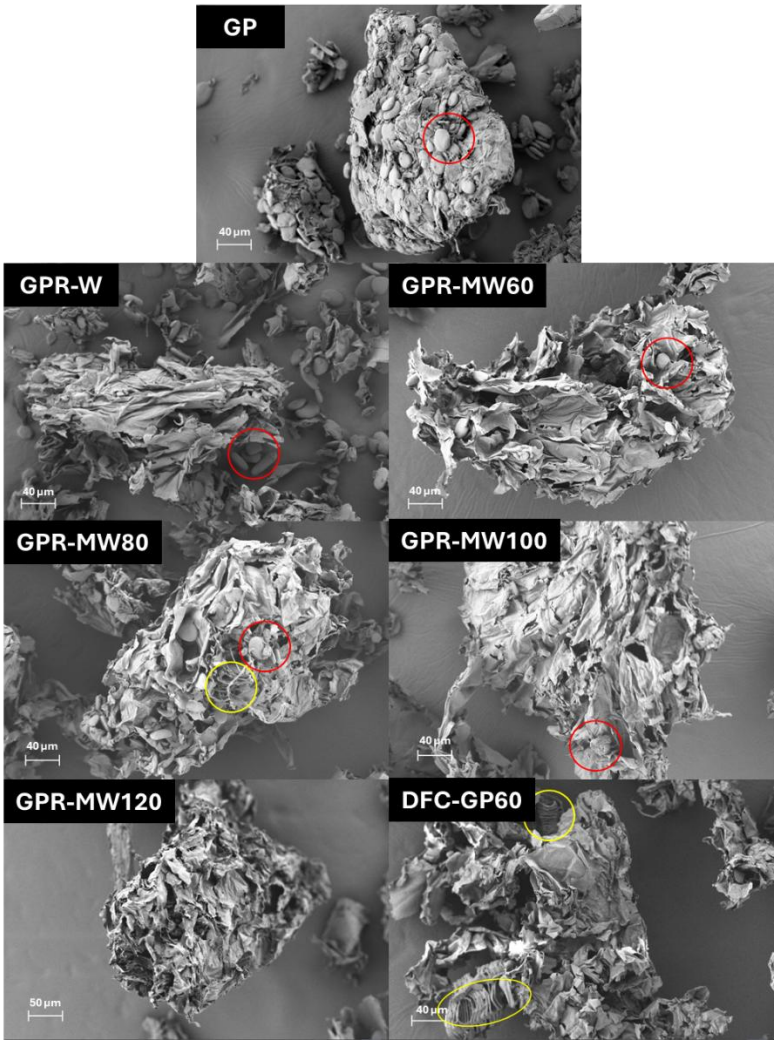

Figure 3.43. SEM images of GPR samples and DFC-GP60 sample at 250× magnification; red circle shows starch granules; yellow circle refers cellulose fibrils.

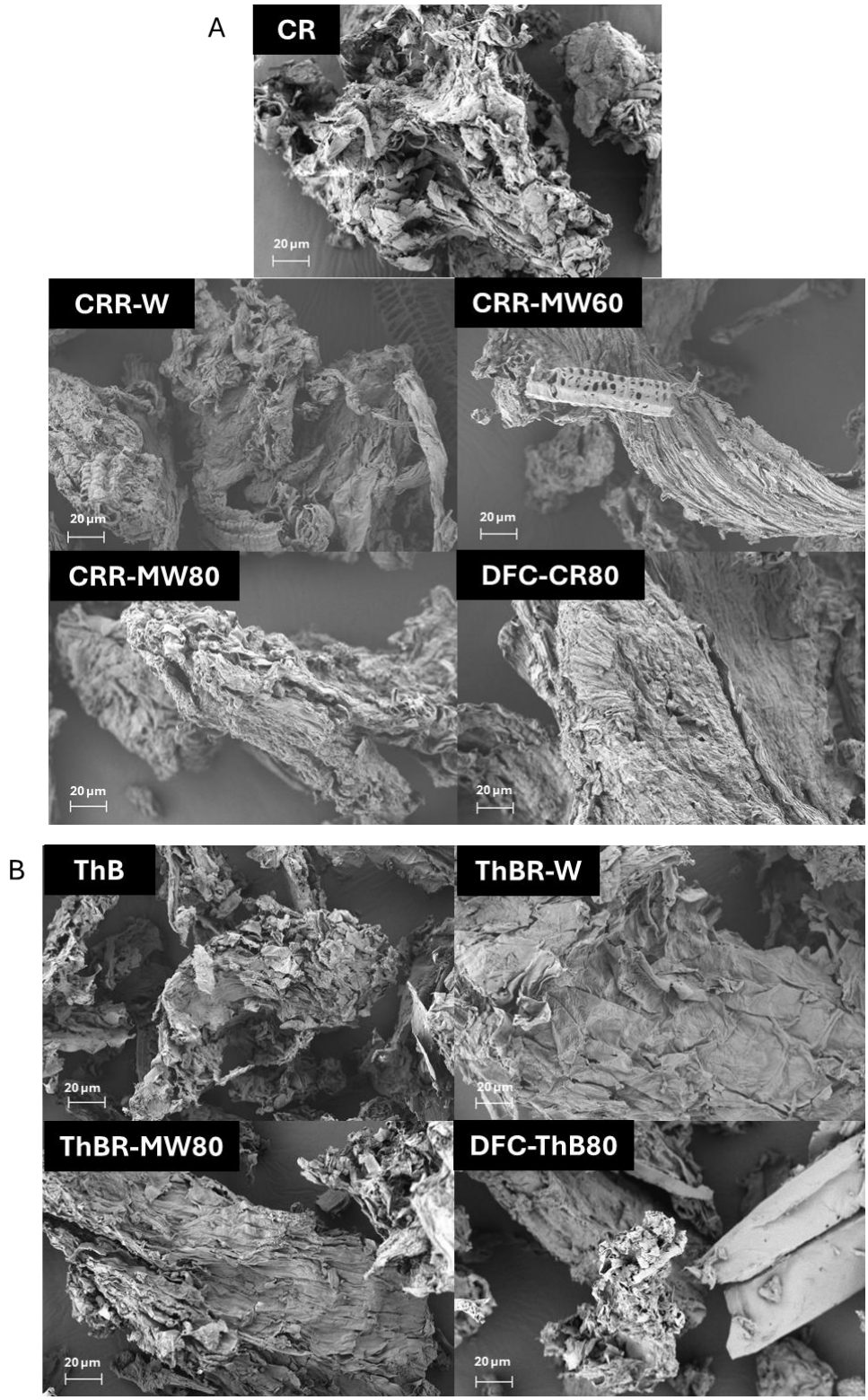

Figure 3.44. SEM images of CR, CRR samples and DFC-CR80 sample (A), and of ThB, ThBR samples and DFC-ThB80 (B) at 500× magnification.

3.2.4.2. ATR-IR spectroscopy analysis

The ATR-IR spectra of native GP, the GPR residues, and the defibrillated cellulose (DFC-GP60) are stacked and presented in **Figure 3.45A**, along with CR-derived and ThB-derived samples (**Figure 3.45B** and **3.45C**). All samples exhibit IR transmittance peaks characteristic of polysaccharides, which are the main carbohydrate constituents in these materials, and particularly cellulose and starch in GP samples. The broad band at approximately 3200 – 3400 cm^{-1} corresponds to the stretching vibration of -OH groups. The bands at 2920 cm^{-1} and 1640 cm^{-1} are attributed to the -CH stretching and -OH bending or C=O stretching vibration, respectively. The stretching vibration of C-O-C glycosidic bonds is also evident in the region of 990 – 1030 cm^{-1}.[161,321]

In addition, with increasing MW temperature, a shift in the C-O-C related vibration from 998 to 1024 cm^{-1} was observed in GP samples (**Figure 3.45A**), along with an increase in the intensity of the band at 1602 cm^{-1}. The vibration near 998 cm^{-1} may be associated with the C-O-C glycosidic bonds of amylopectin, while those at around 1020 cm^{-1} may be correlated to amylose or cellulose (see **Appendix 17**; ATR-IR spectrum of commercial polysaccharides). Thus, the shift from 998 to 1024 cm^{-1} suggests structural changes within the starch components or the loss of starch, resulting in a more prominent cellulose-related peak.

In the IR spectra of the CR and ThB samples, a reduction in the peak at 1538 cm^{-1}, assigned to N-H bending of Amide II was observed, indicating the partial loss of protein during acid-free water extraction or MAE. However, other protein-related peaks, including the N-H stretching vibration near 3300 cm^{-1} (Amide A) and the C=O stretching vibration around 1630 cm^{-1} (Amide I),[323] overlapped with polysaccharide-associated peaks in the same spectral region, making it difficult to resolve these protein signals clearly. In addition, strong absorption peak at around 1630 cm^{-1} may also attributed to C=O stretching, related to the presence of calcium oxalate dihydrate (supported by pXRD result; see **Figure 3.46**).[330]

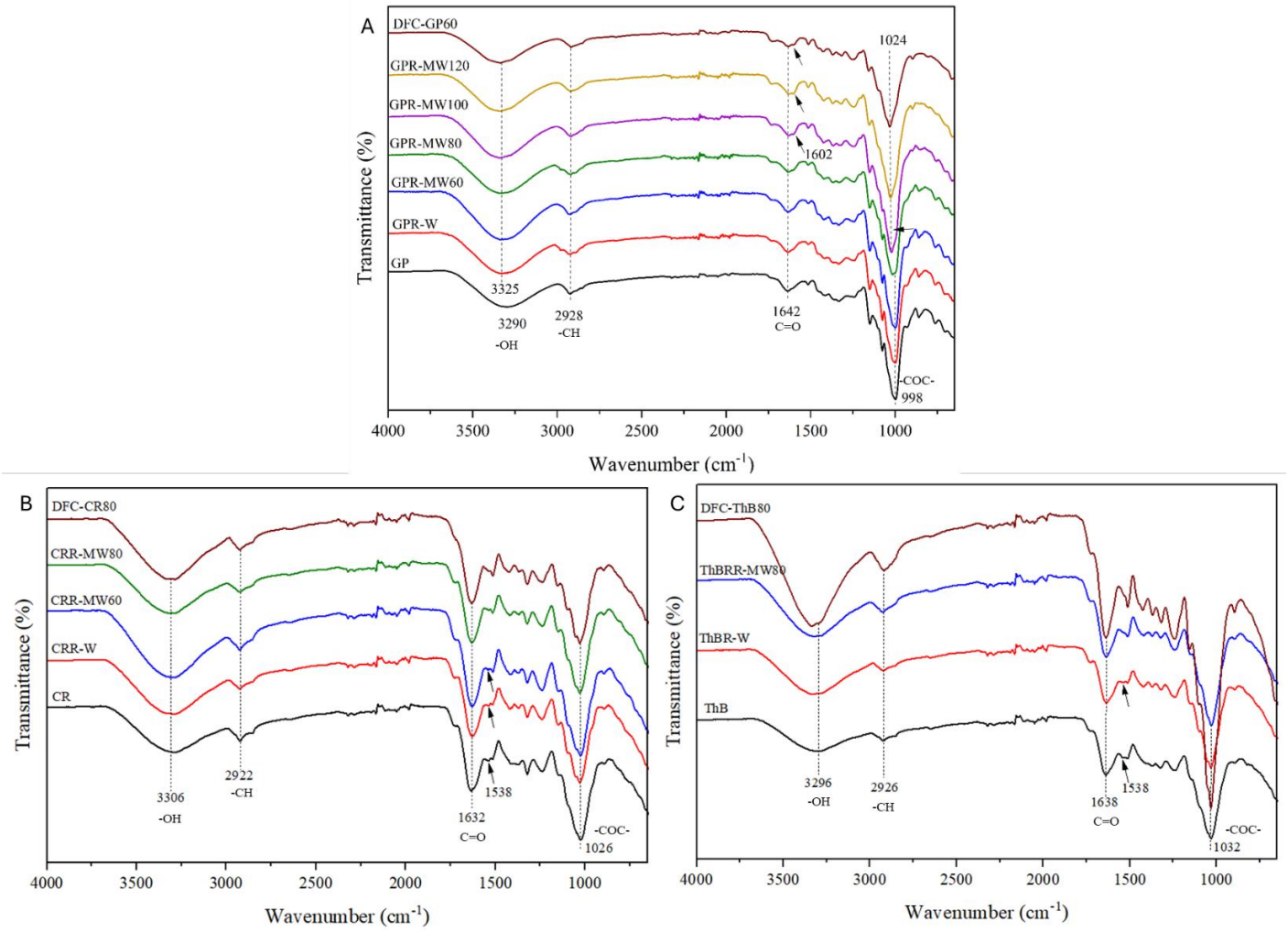

Figure 3.45. ATR-IR spectrum of native GP, GPR samples and DFC-GP60 (A), of native CR, CRR samples and DFC-CR80 (B), and native ThB, ThBR samples and DFC-ThB80 (C).

3.2.4.3. Powder X-ray diffraction (pXRD) analysis

The determination of cellulose's crystalline structure is particularly important because the balance between its crystalline and amorphous regions dictates many of its functional properties. Higher crystallinity typically enhances rigidity and thermal stability, while lower crystallinity increases chemical reactivity and water accessibility. Changes in the crystalline structure of the GP-derived, CR-derived, and ThB-derived samples, along with their corresponding DFCs, were examined using pXRD. The stacked pXRD diffractograms are presented in **Figure 3.46**.

Native GP (**Figure 3.46A**) displayed crystalline peaks at 15.0°, 17.1°, 17.8°, 19.9°, and 22.7°, along with weaker diffraction peaks at 11.3° and 26.4°, which likely attributed to the characteristic peaks of A-type starch.[23,321] Conventional water treatment (GPR-W) resulted in a slight reduction in the intensity of these starch peaks. With increasing MW temperature up to 80 °C, the starch-related peaks gradually diminished and ultimately disappeared at 100 °C. No starch crystallinity was detected in GPR-MW100, GPR-MW120, or DFC-GP60, indicating that the crystalline structure of starch was destroyed or that starch was completely removed at MHT temperatures of 100 °C and above.

In contrast, characteristic cellulose peaks at 15.9°, 22.0°, and 34.5° emerged in GPR-MW100, GPR-MW120, and DFC-GP60.[253] The intensities of the 15.9° and 22.0° reflections increased with higher temperatures up to 120 °C, and the DFC-GP60 sample, obtained by MHT reprocessing GPR-MW60 at 160 °C, exhibited the highest intensities. A similar trend was observed in the cellulose crystallinity index (CrI), which increased from 18.3% in GPR-MW100 to 27.7% in GPR-MW120 and reached 39.8% in DFC-GP60. This suggests that amorphous components were increasingly hydrolysed and removed during MHT, leading to higher cellulose crystallinity.

For both CR and ThB samples, characteristic cellulose crystalline peaks at 15.6°, 22.1°, and 34.6° were observed (**Figure 3.46B** and **3.46C**), along with strong calcium oxalate dihydrate peaks at 14.3°, 20.1°, and 32.2°, which are commonly found in many plant materials.[330–332] Compared with the native samples, CR (CrI = 15.7%) and ThB (17.6%), water extraction slightly increased cellulose crystallinity in CRR-W (CrI = 18.3%) and ThBR-W (20.4%). MAE at 60 or 80 °C further enhanced the CrI values of CRR-MW60 (18.7%), CRR-MW80 (19.1%), and ThBR-

MW80 (28.7%). Subsequent MHT reprocessing at 160 °C again improved the crystalline structure of the DFC materials, with CrI values of 28.4% for DFC-CR80 and 32.8% for DFC-ThB80.

With respect to calcium oxalate dihydrate, the peak intensities at 14.3°, 20.1°, and 32.2° slightly decreased in DFC-CR80 and DFC-ThB80 samples compared with the native CR and ThB samples; however, the peaks remained prominent, suggesting that MHT up to 160 °C does not alter the crystalline structure of calcium oxalate dihydrate. The presence of calcium oxalate was further supported by thermogravimetric analysis and solid state ^{13}C CP/MAS NMR spectroscopy (see **section 3.2.4.4** and **3.2.4.5.**).

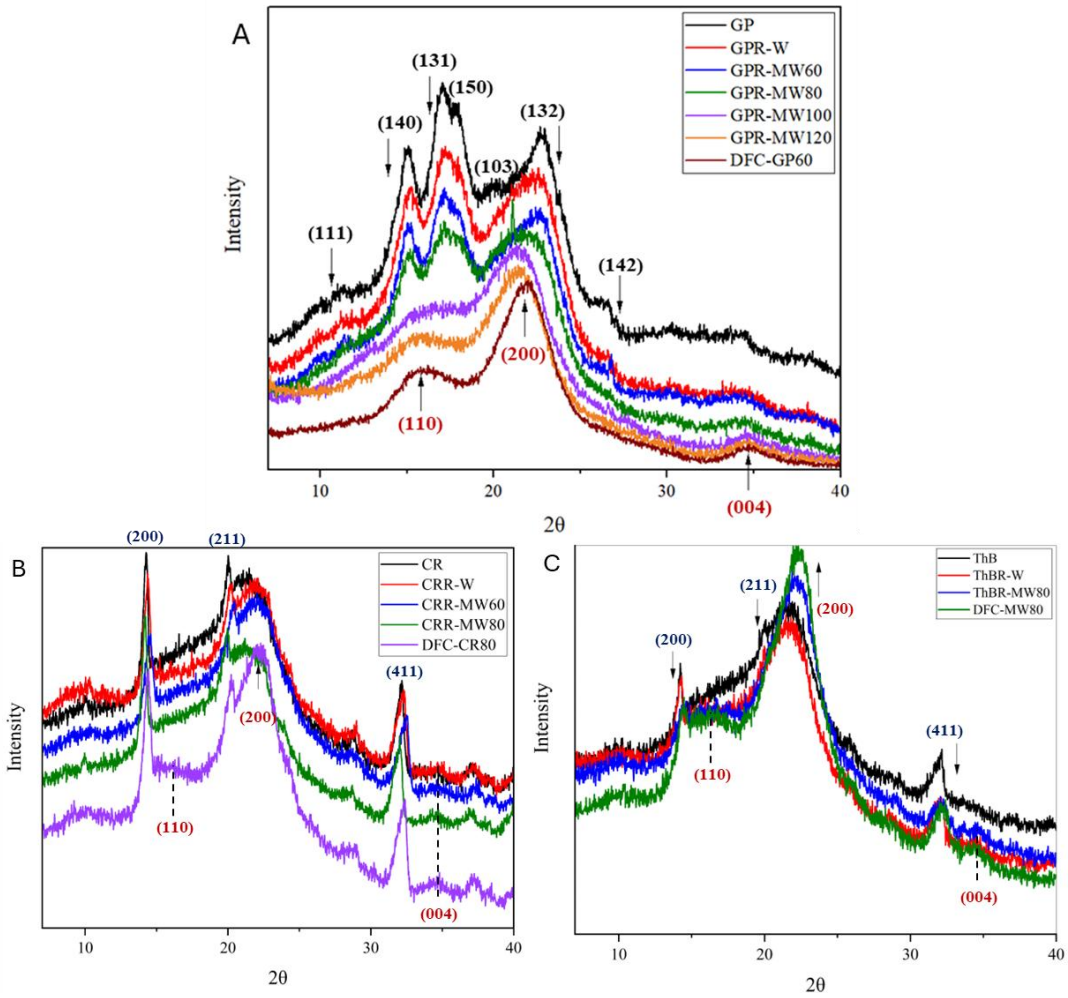

Figure 3.46. pXRD diffractograms of native GP, GPR samples and DFC-GP60 (A), of native CR, CRR samples and DFC-CR80 (B), and native ThB, ThBR samples and DFC-ThB80 (C); crystalline plane of cellulose (red), starch (black), and calcium oxalate dihydrate (blue).

3.2.4.4. Solid state ^{13}C CP/MAS NMR analysis

Changes in native GP, GPR after treatment, and defibrillated cellulose (DFC-GP60) were also evaluated using solid state ^{13}C CP/MAS NMR spectroscopy, and the NMR spectrum were plotted in **Figure 3.47**. Native GP showed resonances characteristic of both cellulose and starch, with starch signals appearing more intense. The resonances of starch in the GP resembled of A-type native corn starch and debranched cassava starch, showing peaks at around δ102 (C1), 83 (C4), 73 – 76 (C2, C3, and C5), and 63 ppm (C6).[333,334] Cellulose resonances appeared at δ105 (C1), 89 (crystalline C4), 83 (amorphous C4), 73 – 76 (C2, C3, and C5), 65 (crystalline C6) and 63 ppm (amorphous C6), identified based on commercial microcrystalline cellulose (CMC) (see **Figure 3.13** and **Table 3.9**).

As the MW temperature increased, the starch-related resonances at δ102, 73, and 63 ppm decreased, while the cellulose-related peaks at δ105, 89, 76, and 65 ppm became more pronounced, especially in the DFC-GP60 sample. In addition, the enhanced signals at δ89 and 65 ppm, associated with crystalline cellulose,[264] further indicate an increase in cellulose crystallinity. These results are consistent with the pXRD findings, indicating that amorphous regions were gradually hydrolysed and eliminated during MHT, resulting in increased cellulose crystallinity.

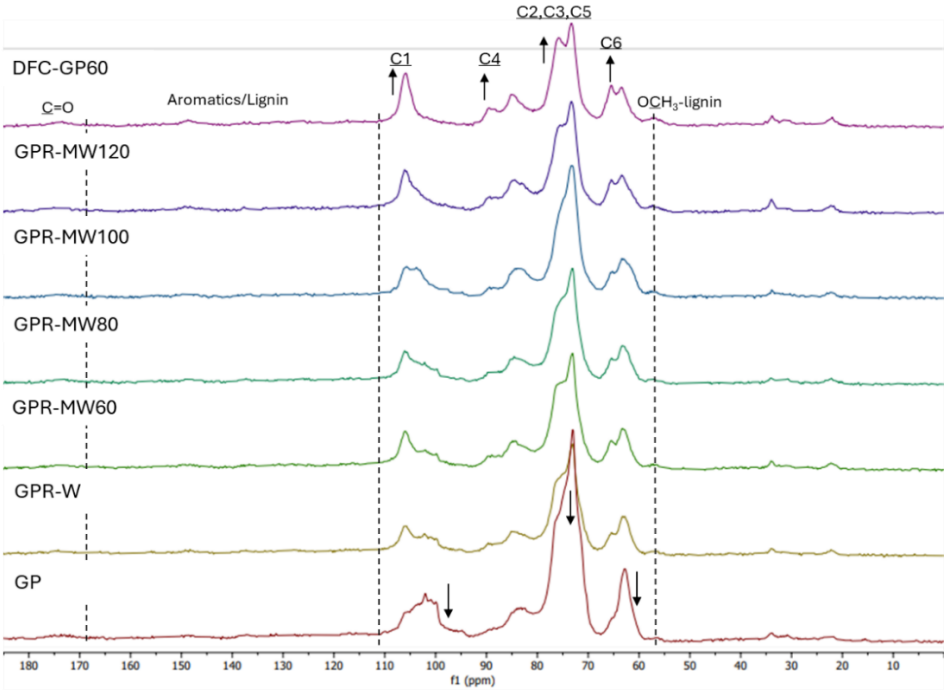

Figure 3.47. Solid state ^{13}C CP/MAS NMR spectra of GP, GPRs, and DFC-GP60.

Solid state ^{13}C CP/MAS NMR spectra of native CR, ThB, and their residues and DFC samples were dominated by lignocellulosic materials. Characteristic cellulose resonances re observed between δ60 and 110 ppm, while lignin-related aromatics and carbonyl signals appeared in the range of δ110 - 180 ppm (**Figure 3.48**). Similar resonance patterns were detected in native BC pomace, and its DFC samples (**Figure 3.13**) and detailed assignments of each peak were summarised in **Table 3.9**.

With respect to acid-free conventional water extraction or MAE, comparable trends were observed for GP, CR and ThB. Extraction at temperatures below 100 °C slightly enhanced the purity of cellulosic materials, as evidenced by more pronounced cellulose resonances, without altering their crystalline structure. This indicates that these extraction conditions are suitable for recovering thermally sensitive compounds such as proteins.

In contrast, DFC-CR80 and DFC-ThB80 obtained from MHT reprocessing at 160 °C exhibited more intense cellulose resonances at δ105, 89, 76, and 65 ppm. Especially, the increased intensity of peaks at δ89 and 65 ppm, which are associated with crystalline cellulose, suggests an increase in cellulose crystallinity. These findings are in good agreement with the pXRD results discussed in **section 3.2.4.3**.

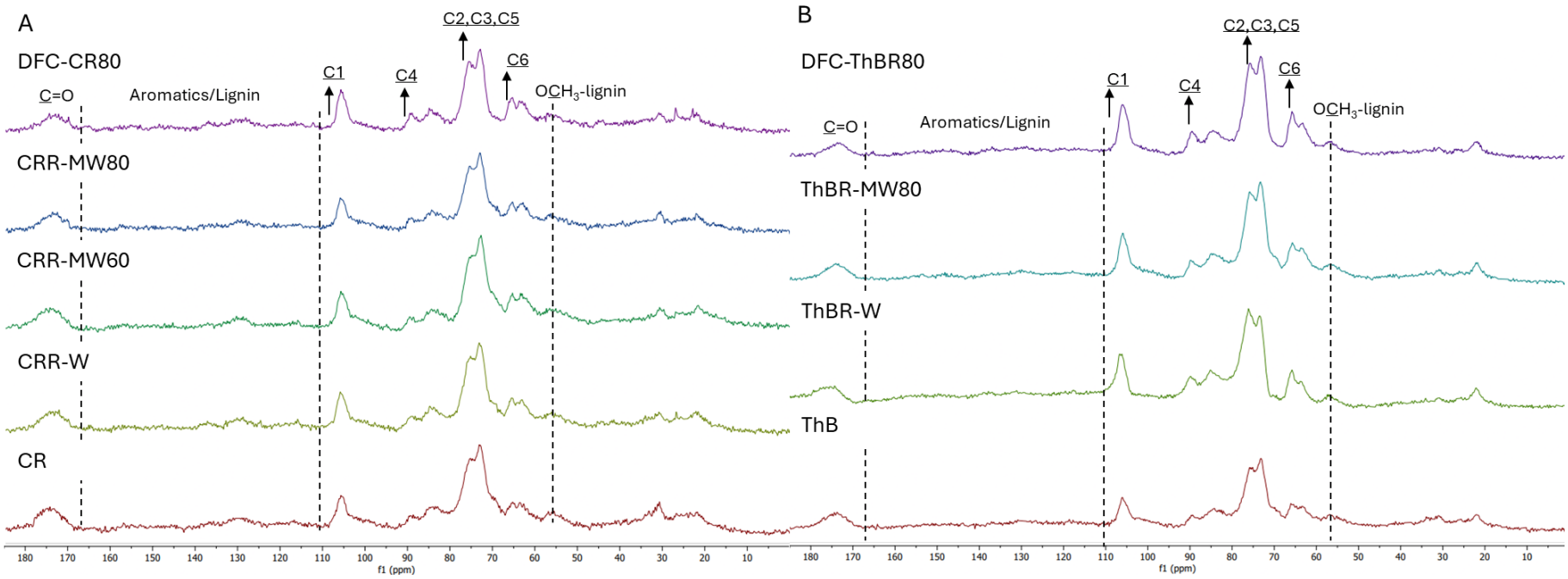

Figure 3.48. Solid state ^{13}C CP/MAS NMR spectra of CR, CRRs, and DFC-CR80 (A), and of ThB, ThBRs, and DFC-ThB80 (B).

3.2.4.5. Thermogravimetric analysis

Thermogravimetric analysis (TGA) and its derivative (dTG) for GP, CR, and ThB samples are presented in **Figure 3.49**. All samples exhibited two major mass loss between 25 – 150 °C, and 150 – 400 °C, corresponding to the loss of moisture or volatile compounds, and the decomposition of carbohydrates, respectively. For comparison, commercial amylose, amylopectin, and cellulose showed characteristic thermal degradation ranges of 245 – 345 °C (T_d = 296 °C), 290 – 335 °C (T_d = 309 °C), and 295 – 360 °C (T_d = 340 °C), respectively (see **Appendix 18**).

For GP-derived samples (**Figure 3.49A** and **3.49B**), GPR samples displayed the main mass loss within the carbohydrate degradation region between 250 – 400 °C (T_d = 314 °C), indicating starch (including amylose and amylopectin) as the main component. As the MW treatment temperature increased, this T_d value decreased, and a cellulose-related peak at T_d = 343 °C appeared in GPR-MW120, suggesting progressive starch loss at higher MW temperatures.

For CR-derived and ThB-derived samples (**Figure 3.49C** and **3.49D**), the carbohydrate degradation region exhibited a cellulose-related peak at T_d = 339 °C and 347 °C, respectively. Apart from mass loss associated with moisture evaporation and carbohydrate decomposition, a further mass loss observed between 400 and 500 °C was attributed to the presence of lignin, indicating that lignocellulosic materials constitute the major components of these samples. Furthermore, additional minor mass losses were detected in the CR-derived samples at approximately 130 - 160 °C and 460 - 500 °C (**Figure 3.49C**; yellow regions), which may be associated with the thermal degradation of calcium oxalate. The first transition, occurring between 130 and 160 °C, corresponds to the release of tightly bound water (Equation 3.1), while the following mass loss from 460 to 500 °C is attributed to the decarbonisation of calcium oxalate (Equation 3.2).[335,336] However, literature reports indicate that CO was detected along with CO_2, which may result from the disproportionation of CO (Equation 3.3).[335]

$$CaC_2O_4 \cdot nH_2O \rightarrow CaC_2O_4 + nH_2O \quad (\textit{Equation 3.1})$$

$$CaC_2O_4 \rightarrow CaCO_3 + CO \quad (\textit{Equation 3.2})$$

$$2CO \rightarrow C + CO_2 \quad (\textit{Equation 3.3})$$

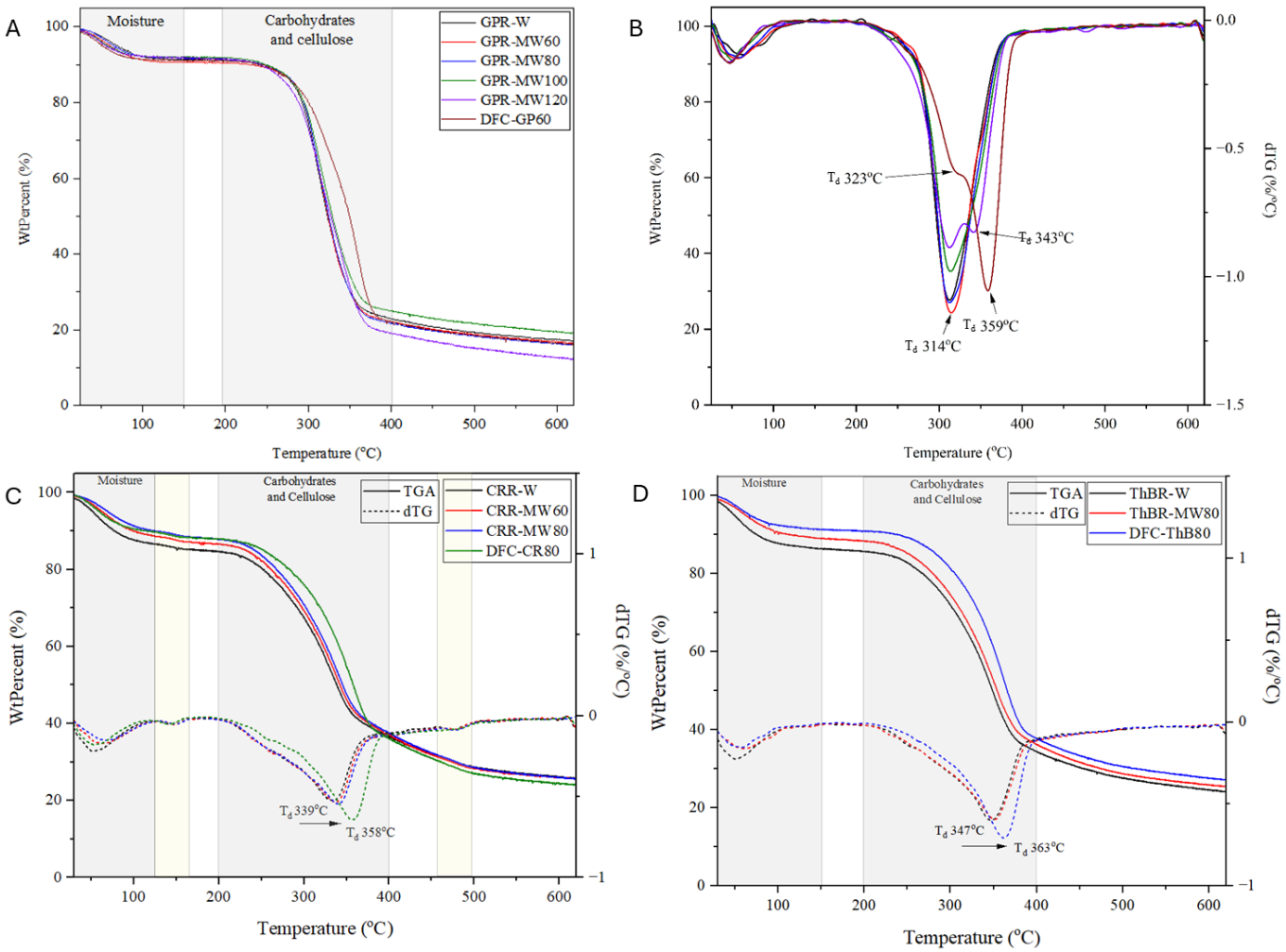

Figure 3.49. TGA thermogram (A) and dTG curve (B) of GPRs and DFC-GP60 samples, TGA thermogram and dTG curve of CRRs and DFC-CR80 samples (C); calcium oxalate degradation (yellow region), and ThBRs and DFC-ThB80 samples (D).

Interestingly, DFC-GP60 exhibited a main T_d at 359 °C, accompanied by a shoulder peak at 323 °C (**Figure 3.49A**), while DFC-CR80 and DFC-ThB80 showed the main T_d at 358 and 363 °C, respectively (**Figure 3.49C** and **3.49D**). The higher T_d is attributed to crystalline cellulose, whereas the shoulder likely reflects the presence of residual carbohydrates, specifically starch in DFC-GP60, or amorphous cellulose. This observation agrees with the literature that amorphous hemicellulose, starch, and cellulose could not be completely remove under the MHT conditions below 200 °C,[74] although this work applied double MW treatment to produce DFC-GP60. In addition, the DFC-GP60, DFC-CR80 and DFC-ThB80 samples exhibited improved thermal stability compared to commercial CMC (T_d = 340 °C). This enhanced stability corresponds well with the increased crystallinity index (CrI) reported in **section 3.2.3.4**.

3.2.4.6. Water-holding capacity (WHC) and hydrogel formation

Water-holding capacity (WHC) values of GP-derived, CR-derived, and ThB-derived samples are summarised in **Table 3.29**. Native GP (3.90 g/g), CR (5.02 g/g) and ThB (6.41 g/g) revealed the lowest WHC values within their groups. Conventional water extraction slightly increased the WHC values of GPR-W (8.80 g/g), CRR-W (6.23 g/g), and ThBR-W (7.82 g/g).

MAE (60 – 120 °C) facilitated the removal of tightly packed starch in GP-derived samples, as evidenced by SEM images (**Figure 3.43**), thereby increasing surface area and enhancing WHC, reaching up to 14.01 g/g. Subsequent MHT reprocessing at 160 °C for DFC production further promoted the removal of amorphous components and cellulose defibrillation (**Figure 3.43**), resulting in a further increase in surface area and WHC (DFC-GP60; 17.33 g/g).

In contrast, MAE and MHT reprocessing at 160 °C slightly improved the WHC of CR- and ThB-derived samples, with maximum ΔWHC values of 1.41 g/g and 1.79 g/g, respectively. This limited improvement can be attributed to the presence of lignin, a hydrophobic biopolymer tightly associated with cellulose fibres (as indicated by solid state ^{13}C NMR; **Figure 3.48**), as well as calcium oxalate salts, which are highly insoluble in water (as evidenced by pXRD; **Figure 3.46**). These components hinder hydrogen bonding between water molecules and cellulose fibrils, resulting in lower WHC values compared with GP-derived samples. However, further treatment, such as acid washing or chelation, could promote demineralisation of the CR- and ThB-derived samples, potentially improving their WHC and gel-forming ability.

Table 3.29. Water-holding capacity (WHC; g/g) of GP-derived, CR-derived and ThB-derived samples

Sample	WHC (g/g)
GP	3.90 ± 0.25[a]
GPR-W	8.80 ± 0.42[f]
GPR-MW60	10.84 ± 0.56[g]
GPR-MW80	11.26 ± 0.50[g]
GPR-MW100	13.65 ± 0.15[h]
GPR-MW120	14.01 ± 0.52[h]
DFC-GP60	17.33 ± 0.12[i]
CR	5.02 ± 0.12[b]
CRR-W	6.23 ± 0.23[d]
CRR-MW60	5.95 ± 0.32[c]
CRR-MW80	6.38 ± 0.20[d]
DFC-CR80	6.43 ± 0.26[d]
ThB	6.41 ± 0.43[d]
ThBR-W	7.82 ± 0.28[e]
ThBR-MW80	7.60 ± 0.48[e]
DFC-ThBR80	8.20 ± 0.37[ef]

Values are presented as mean ± SD (n = 3). Letters indicate the significant differences ($p < 0.05$).

Given the relatively high WHC of GP-derived, CR-derived, and ThB-derived samples, a hydrogel inversion test was conducted to evaluate hydrogel formation at concentrations of 2.5 wt.%, 5.0 wt.%, and 7.5 wt.%. GPR-W, GPR-MW60 and GPR-MW80 formed stable hydrogels at a concentration of 7.5 wt.%, while GPR-MW100, GPR-MW120 and DFC-GP60 achieved hydrogel formation at a lower concentration of 5.0 wt.% (**Figure 3.50**).

These results correlate well with the WHC results (**Table 3.29**), where higher WHC values enabled hydrogel formation at lower material concentrations. In addition, hydrogel formation of GPR samples is likely due to starch gelatinisation at 30 °C, the hydrogel formation temperature employed in this study. GPR-W, GPR-MW60 and GPR-MW80 required higher concentrations (7.5 wt.%) to form hydrogels, which is consistent with their

lower WHC values (8.80 – 11.26 g/g). This could be attributed to the presence of crystalline starch with strong internal hydrogen bonding, as evidenced by pXRD patterns (**Figure 3.46**) and the presence of intact starch granules observed in SEM images (**Figure 3.43**).

In contrast, higher MAE (100 – 120 °C) and MHT reprocessing at 160 °C reduced crystalline starch crystallinity (pXRD; **Figure 3.46**) and enhanced cellulose defibrillation (SEM images; **Figure 3.43**). These structural changes facilitated starch gelatinisation and promoted hydrogen bonding between defibrillated cellulose and water, enabling hydrogel formation at a lower concentration of 5.0 wt.% in GPR-MW100, GPR-MW120, and DFC-GP60. However, due to the presence of non-polar compounds and fatty acids in native GP, CR and ThB (**section 3.2.2**), as well as the presence of lignin and calcium oxalate salts in CR- and ThB-derived samples, inhibited effective hydrogel formation. As a result, these materials were unable to form stable hydrogels at concentrations ranging from 2.5 – 7.5 wt.%.

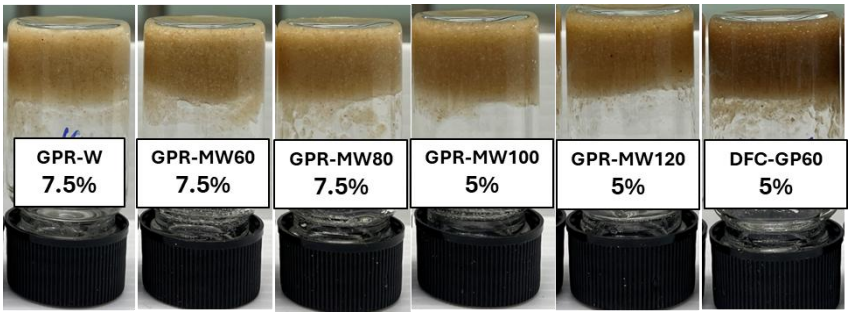

Figure 3.50. Hydrogel forming of GP-derived samples.

3.2.5. Recovery of ginger starch from acid-free microwave-assisted derived hydrolysates (Objective A2 (v))

Ginger is well known as one of the starchy plants. In this section, insoluble matter (GPI) and soluble starch (GPS) were recovered from extruded ginger pomace (GP) hydrolysates obtained from acid-free conventional water extraction (50 °C, 2 h) and microwave-assisted extraction (MAE; 60 - 120 °C). GPI was obtained by centrifugation of stainless steel-mesh (150 µm) filtered GP hydrolysates, while GPS was recovered from GPI- and protein-free hydrolysates by ethanol precipitation. The recovered fractions were subsequently dried, weighed, and characterised in terms of yield and physicochemical properties to evaluate the influence of extraction method and temperature on starch recovery. However, starch is not a major component of lignocellulosic plants such as coriander and Thai basil roots.

Therefore, this section does not address starch recovery from extruded coriander and Thai basil roots.

3.2.5.1. Starch yield

Starch yield, including both insoluble matter and soluble starch, is summarised in **Table 3.30**. Insoluble matter (GPI) obtained by water extraction as the control (GPI-W) accounted for 27.48 wt.%. With increasing microwave-assisted extraction (MAE) temperature (60 - 120 °C), GPI yield initially increased, reaching a maximum of 31.88 wt.% at 80 °C, and then decreased to 14.13 wt.% at 120 °C.

In contrast, soluble starch (GPS) was not recovered from either water extraction or MAE at 60 °C. GPS yield began to increase at an MAE temperature of 80 °C (GPR-MW80; 2.33 wt.%) and rose substantially to 37.09 wt.% at 120 °C (GPR-MW120). The inverse relationship observed between GPS and GPI yields at higher MAE temperatures may be attributed to the microwave-induced transformation of ginger starch granules from a semi-crystalline, water-insoluble form to a more soluble form. This structural transformation, evidenced by surface cracking and granule disruption in SEM images of GPR samples (**Figure 3.43**). The phenomena have been well explained by Hu *et al*., in which the polar molecules of starch directly absorb the MW radiation, resulting in rapid molecular rotation and frictional heating, which subsequently induces surface cracking of starch granules.[337] In addition, changes in crystalline structure associated with semi-crystalline starch granules were also observed and are further discussed in **Section 3.2.5.3**.

Table 3.30. Yield of GP insoluble matter (GPI) and soluble starch (GPS).

GPI sample	Yield (wt.%)	GPS sample	Yield (wt.%)
GPI-W	27.48 ± 3.87^{b}	GPS-W	-
GPI-MW60	28.06 ± 5.42^{b}	GPS-MW60	-
GPI-MW80	31.88 ± 6.09^{b}	GPS-MW80	2.33 ± 0.32^{A}
GPI-MW100	28.44 ± 4.00^{b}	GPS-MW100	9.32 ± 0.86^{B}
GPI-MW120	14.13 ± 2.63^{a}	GPS-MW120	37.09 ± 0.48^{C}

Values are presented as mean ± SD (n = 3). Letters indicate the significant differences ($p < 0.05$).

3.2.5.2. ATR-IR spectroscopy analysis

Figure 3.51 show the physical appearance and ATR-IR spectra of GPI and GPS. All samples exhibit characteristic IR absorption bands associated with carbohydrates, which are consistent with starch-related functional groups.[216,321] The broad band observed at approximately 3300 cm^{-1} corresponds to the stretching vibration of -OH groups. Peaks at 2920 cm^{-1} and 1640 cm^{-1} are attributed to the -CH stretching and -OH bending vibration, respectively. In addition, the stretching vibration of C-O-C glycosidic bonds is evident in the region of 990 – 1020 cm^{-1}, further confirming the starch-based nature of both GPI and GPS samples.[161,321]

With increasing microwave (MW) processing temperature, a noticeable shift in the C-O-C-related absorption peak from 994 to 1014 cm^{-1} was observed in GPI samples (**Figure 3.51A**). This shift is indicative of structural changes within the starch components, particularly in relation to double-helix ordering. The absorbance ratio at 995/1022 cm^{-1} is commonly employed to quantify the degree of double-helix structure in starch systems.[216] The calculated degrees of double-helix structure for GPI and GPS samples are summarised in **Table 3.31**. Increasing MW temperature resulted in a reduction in double-helix content for both fractions, with GPI consistently exhibiting a higher degree of double-helix structure than the corresponding GPS samples. The reduction in double-helix structure with increasing MW temperature indicates decreased molecular ordering, associated with the crystalline structures of starch granules. These findings are in good agreement with the pXRD results discussed in **Section 3.2.5.3**, further confirming the loss of starch crystalline structures at elevated MW temperatures.

Table 3.31. Structural constituents of GPI and GPS samples.

GPI sample	Degree of double helix[a]	GPS sample	Degree of double helix[a]
GPI-W	1.12	GPS-W	-
GPI-MW60	1.11	GPS-MW60	-
GPI-MW80	1.02	GPS-MW80	0.93
GPI-MW100	1.02	GPS-MW100	0.79
GPI-MW120	0.97	GPS-MW120	0.87

[a]Absorbance ratio of IR bands at 995 and 1022 cm^{-1} (995/1022). Values are presented as single measurements (n = 1); therefore, no statistical comparison among samples was performed.

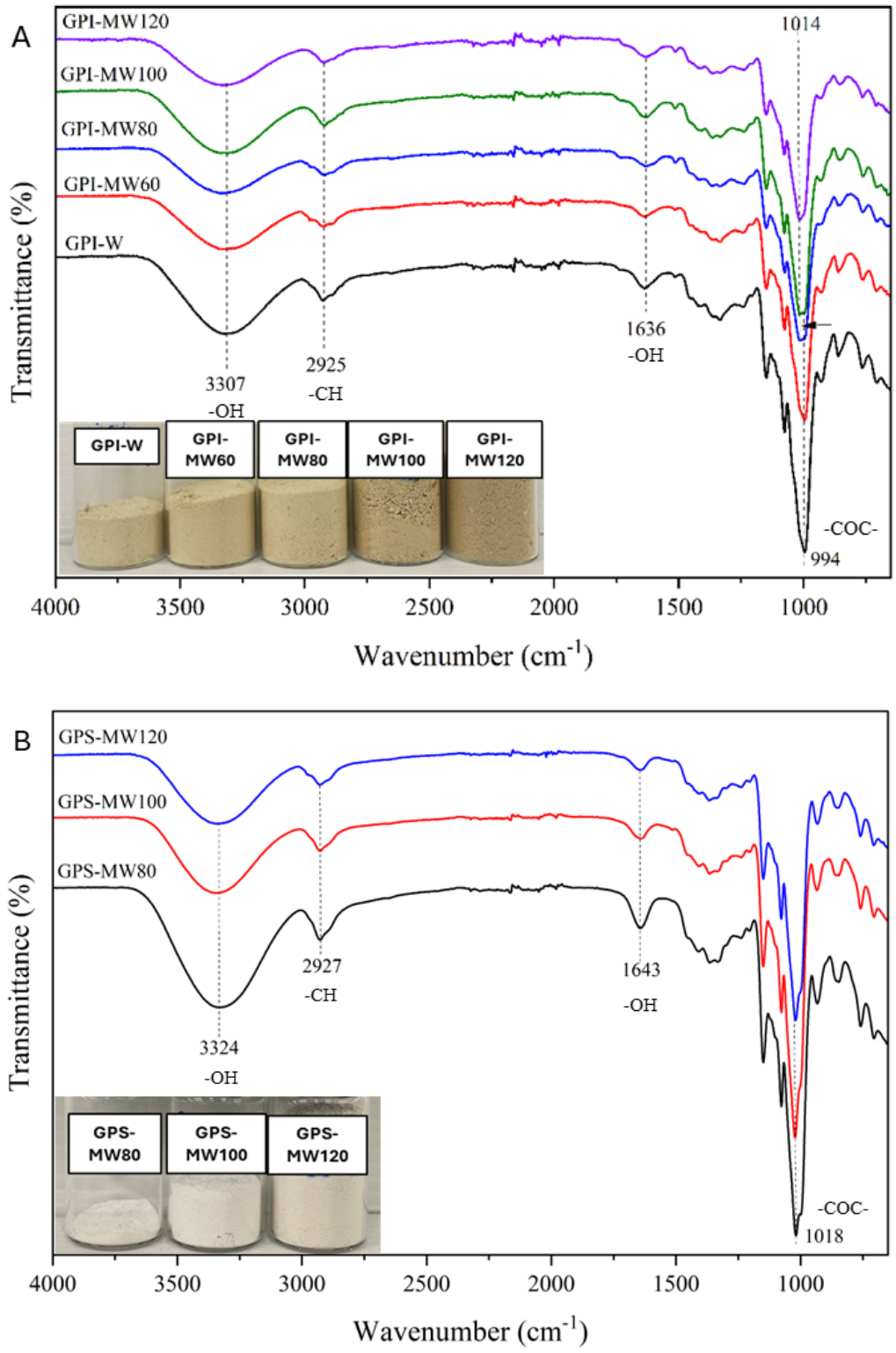

Figure 3.51. ATR-IR spectra of GPI (A) and GPS (B) samples; Inset pictures show the physical appearance of GPI and GPS.

3.2.5.3. Powder X-ray diffraction (pXRD) analysis

GPI samples displayed crystalline peaks at 11.3°, 15.0°, 17.1°, 17.8°, 19.9°, 22.7°, and 26.4° (**Figure 3.52A**), which can be attributed to the (111), (140), (131), (150), (103), (132), and (142) crystalline planes of A-type starch, respectively.[23,338] As the MW treatment temperature increased to 80 °C, the intensities of these starch-related diffraction peaks gradually decreased and completely disappeared at 100 °C. No detectable starch crystallinity was observed in GPI-MW120, indicating that the native crystalline structure of starch was fully disrupted at MW temperatures of 100 °C and above.

In contrast, GPS samples exhibited a markedly lower degree of starch crystallinity, characterized by weak diffraction peaks at 13.0° and 19.7° (**Figure 3.52B**). These peaks are indicative of V-type starch, which consists of single-helical amylose complexes formed through interactions with suitable ligands such as fatty acids, aroma compounds, or other small hydrophobic molecules.[339] V-type starch typically forms under ethanol-aqueous conditions, which promote amylose-ligand complexation.[340,341] Moreover, amylose-ligand complexes are widely applied as carriers for bioactive compounds, flavours, and lipophilic nutrients.[339,340] Consequently, the presence of V-type starch in GPS samples suggests potential applications in functional foods, encapsulation systems, and starch-based biodegradable materials.

3.2.5.4. Thermogravimetric analysis

Thermogravimetric analysis (TGA) and its derivative (dTG) for GPI and GPS samples are presented in **Figure 3.52C** and **3.52D**. All samples exhibited a major mass loss between 250 - 350 °C, corresponding to the thermal degradation of starch. For comparison, commercial amylose and amylopectin showed characteristic thermal degradation ranges of 245 - 345 °C (T_d = 296 °C) and 290 - 335 °C (T_d = 309 °C), respectively (see **Appendix 18**). Both GPI and GPS samples exhibited higher degradation temperatures ($T_d \approx 315$ °C), indicating greater thermal resistance compared with the commercial starches. With increasing MW treatment temperature, a slight decrease in T_d was observed, which may be associated with the loss of crystalline structure at elevated MW temperatures. These findings are consistent with the pXRD results discussed in **Section 3.2.5.3**.

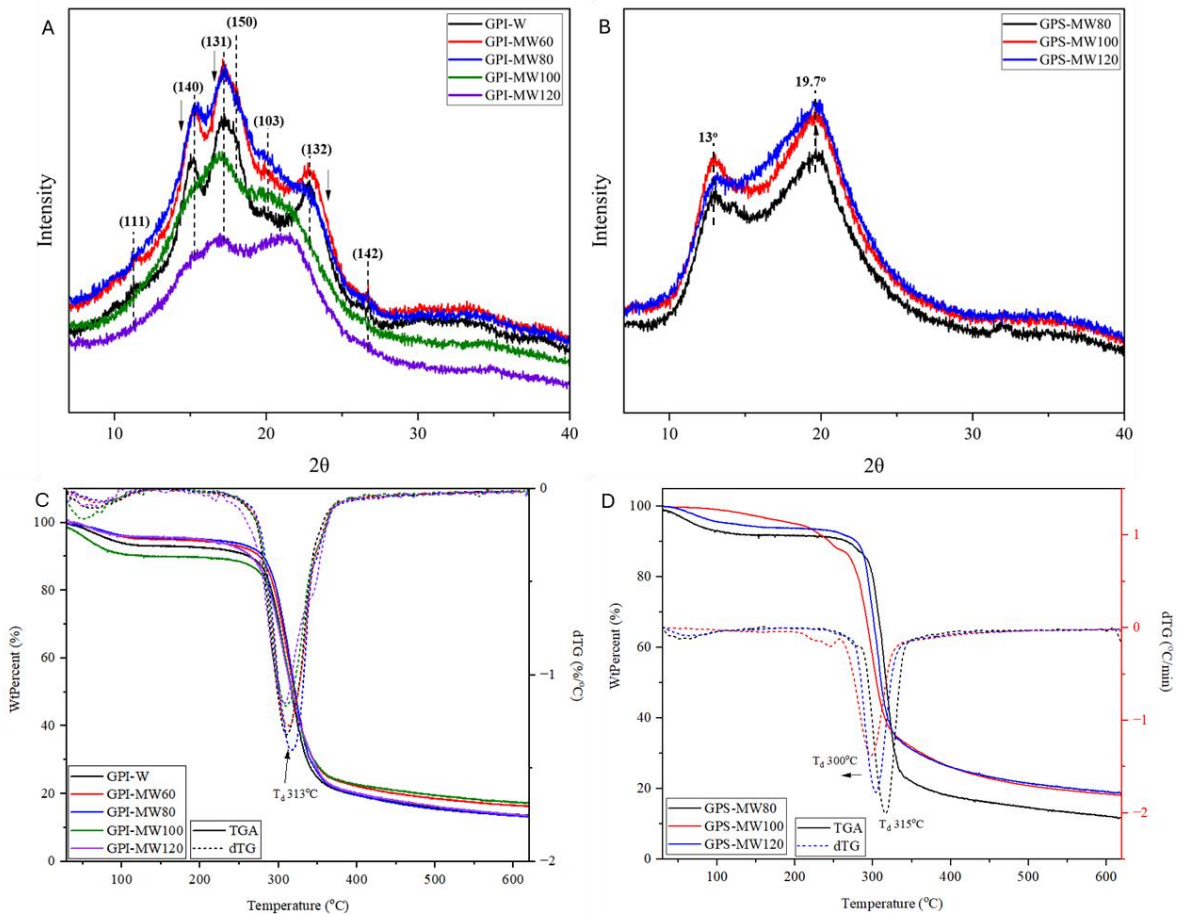

Figure 3.52. pXRD diffractograms of GPI (A) and GPS (B) samples, TGA and dTG thermograms of GPI (C) and GPS (D) samples.

3.2.5.5. Determination of amylose and amylopectin content.

Amylose content plays an important role in determining functional properties of starch such as gel strength and gelatinisation temperature.[342] Amylose and amylopectin contents in GPI and GPS samples were determined through the formation of iodine-starch complexes in an alkali medium.[216] The amylose-iodine complex produced a characteristic blue colour, whereas the amylopectin-iodine complex exhibited a purplish-red colour, which is attributed to the higher degree of branching and larger molecular weight of amylopectin.[216]

As shown in **Table 3.32**, conventional water extracted GPI (GPI-W) contained 48.85% of amylose and 52.89% of amylopectin. However, amylose content in GPI-W was significantly higher than 31.16% reported for isolated fresh ginger starch,[342] which may be attributed to differences in pretreatment and extraction methods.

Amylose content in GPI samples decreased from 39.12 to 23.66% (GPI-MW60 to GPI-MW120) with respect to the increasing MW temperature. This could be because MW

radiation facilitated surface cracking of starch granules, thereby releasing amylose, water-soluble starch, into aqueous phase. Therefore, the water-soluble starch (GPS) samples exhibited higher amylose contents, ranging from 41.85% to 46.70%, compared with the GPI samples at the same MW treatment temperatures. This elevated amylose content is consistent with the pXRD results, which revealed the presence of V-type starch, single-helical amylose complexes, in the GPS samples (**Section 3.2.5.3**).

Table 3.32. Starch content and its purity in GPI and GPS samples.

Sample	**Amylose content[a] (%)**	**Amylopectin content[a] (%)**
GPI-W	48.85 ± 0.99^{g}	52.89 ± 1.00^{a}
GPI-MW60	39.12 ± 0.25^{d}	61.29 ± 0.25^{c}
GPI-MW80	33.09 ± 0.46^{c}	68.19 ± 0.46^{d}
GPI-MW100	24.91 ± 0.33^{b}	75.25 ± 0.33^{e}
GPI-MW120	23.66 ± 0.13^{a}	76.71 ± 0.13^{f}
GPS-MW80	46.70 ± 0.22^{f}	53.43 ± 0.22^{a}
GPS-MW100	46.65 ± 0.66^{f}	53.69 ± 0.67^{a}
GPISMW120	41.85 ± 0.43^{e}	58.13 ± 0.44^{b}

[a] Estimated from colorimetric Iodine-complex assay.[216]Values are presented as mean ± SD (n = 3). Letters indicate the significant differences ($p < 0.05$).

Chapter 4: Conclusions and Future Work

4.1. Conclusions

Based on the results reported and discussed, this thesis successfully demonstrates the valorisation of renewable biomasses e.g. blackcurrant pomace (BC), extruded ginger pomace (GP) and extruded aeroponically grown coriander (CR) and Thai basil (ThB) roots into biobased chemicals and materials via green technologies. Significant new knowledge has been created and disseminated via the following peer-reviewed publications.

1. Inthalaeng, N.; Gao, Y.; Remón, J.; Dugmore, T. I. J.; Ozel, M. Z.; Sulaeman, A.; Matharu, A. S. Ginger Waste as a Potential Feedstock for a Zero-Waste Ginger Biorefinery: A Review. RSC Sustainability 2023, 1 (2), 213–223. https://doi.org/10.1039/d2su00099g. (**Impact factor, 4.9**).
2. Inthalaeng, N.; Barker, R. E.; Dugmore, T. I. J.; Matharu, A. S. Microwave-Assisted Production of Defibrillated Lignocelluloses from Blackcurrant Pomace via Citric Acid and Acid-Free Conditions. Molecules 2024, 29 (23). https://doi.org/10.3390/molecules29235665. (**Impact factor, 5.3**).
3. Inthalaeng, N.; Dugmore, T. I. J.; Matharu, A. S. Production of Hydrogels from Microwave-Assisted Hydrothermal Fractionation of Blackcurrant Pomace. Gels 2023, 9 (9). https://doi.org/10.3390/gels9090674. (**Impact factor, 4.6**).
4. Inthalaeng, N.; Dugmore, T. I. J.; Matharu, A. S. Repurposing of Blackcurrant Pomace via Microwave-Assisted Hydrothermal Fractionation into pH-Sensitive Films. ACS Sustain Chem Eng 2025, 13 (34), 13988–14002. https://doi.org/10.1021/acssuschemeng.5c05240. (**Impact factor, 7.3**).

4.1.1. Valorisation of blackcurrant pomace

This section explored the valorisation of blackcurrant pomace through three processing routes: (i) conventional solvent extraction to obtain lipids, phenolics, and anthocyanins; (ii) conventional acid extraction and microwave-assisted hydrothermal treatment (MHT) to produce pectin (BCP) and anthocyanin-containing hydrolysates (BCH) as by-products; and (iii) MHT of depectinated residues to generate defibrillated cellulose (DFC) and its bleached derivative (BDFC). The resulting fractions, including BCP, BCH, and bleached DFC, originating from blackcurrant pomace were subsequently combined with sodium alginate to demonstrate their potential application in pH-responsive films. The overall conclusion is summarised in **Figure 4.1**.

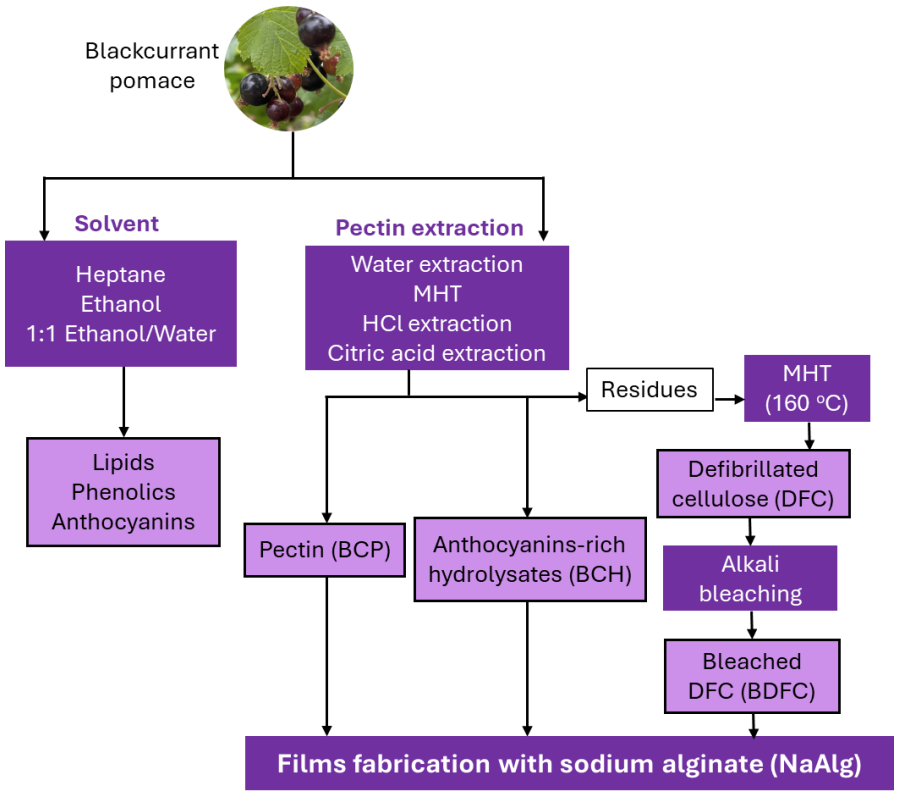

Figure 4.1. Diagram of the blackcurrant pomace valorisation process.

The findings show that blackcurrant pomace can be successfully separated into BCPs and DFCs through acid-free MHT and acid-assisted extraction. The resulting BCPs exhibited a low degree of esterification (16.6-21.4%) and retained antioxidant activity, as well as phenolics and anthocyanins. MHT at ≤ 140 °C found to be more suitable and selective for BCP extraction than acid extraction, as no detectable protein was present in the resulting pectin. Furthermore, BCPs produced via MHT contained higher galacturonic acid content compared with those derived from citric acid extraction.

The DFCs derived from acid-free microwave-assisted and/or acid processing yielded lignocellulosic materials with different physicochemical properties, in which acid-derived DFCs exhibited smaller size, lower crystallinity and lower thermal stability compared to MW-DFCs. Interestingly, crystalline xylans were detected in acid-derived DFC, identified by ^{13}C CP/MAS NMR, pXRD and residue xylose via carbohydrate analysis, which showed higher xylose content and signal intensity than MW-DFCs. This suggests that acid treatment promotes hydrolysis of xylan side chains, reducing their water solubility and driving self-assembly into ordered structures. These findings support the conclusion that MHT at moderate temperatures (100-160 °C) effectively prevents xylan self-assembly, offering an advantage for controlled carbohydrate polymer fractionation in biomass.

Both processing methods produced DFC materials with water-holding capacity but lacked the ability to form a hydrogel. Through further bleaching of the DFC using H_2O_2 under alkaline conditions, their water-holding capacity (WHC) was significantly enhanced. The bleached samples can hold water at a rate of up to 10.9 g H_2O/g sample, which is twice the capacity of the unbleached samples (up to 5.6 g H_2O/g sample). Additionally, the bleached samples display stable hydrogel formation at a concentration of 5% w/v for acid-free MHT derived samples, and at 7.5% w/v for acid-derived samples. The viscoelastic, shear-thinning and time-dependent behaviours observed in bleached DFC gels indicate their potential for applications in food, pharmaceuticals, and cosmetics.

Conventional solvent extractions, including heptane, ethanol, ethanol-water extraction, were evaluated to compared with BCH. Among all extractions, heptane showed the selectivity for non-polar compounds, yielding primarily palmitic acid, linoleic acid, and tetracosane. Ethanol extracted a broader range of components, including sugars, phenolics, anthocyanins, and fatty acids. Fatty acid ethyl esters were also detected, likely due to esterification between fatty acids and ethanol. Further purification of the ethanol extract with ethyl acetate improved the separation of lipid-rich and anthocyanin-rich fractions. Both ethanol-water extract (ETW) and BCH contained predominantly polar constituents, such as phenolics, anthocyanins, citric acid, and sugars.

Ethanol-water extraction demonstrated greater selectivity for anthocyanins than MHT and acid-assisted extraction, with ETW exhibiting a total anthocyanin content (TAC) twice that of BCH (15.32 mg C3G/g for ETW vs. 7.22 mg C3G/g for BCH-M1). In contrast, BCH displayed stronger antioxidant activity than the solvent extracts, and MHT showed increasing selectivity for phenolic extraction with temperature, reaching a total phenolic content of 195.54 mg GA/g at 140 °C (BCH-M3). Four major anthocyanins, which are delphinidin-3-glucoside (D3G), cyanidin-3-glucoside (C3G), delphinidin-3-rutinoside (D3R), and cyanidin-3-rutinoside (C3R), were identified in both solvent extracts and BCH by HPLC-DAD-MS/MS. The rutinoside forms dominated in solvent extracts and BCH obtained from MHT and citric acid extraction; however, D3G and C3G became dominant in BCH-H, likely due to HCl-driven hydrolysis of the rhamnose-glucose linkage in rutinosides.

Among all evaluated extraction conditions, BCH-M1 is recommended for anthocyanin recovery, as it yields high TAC without the need for mineral acids or organic solvents and responds well to both acidic and basic pH, comparable to the ETW control. Therefore, BCH-M1 is the most suitable MHT-derived hydrolysate for pH-responsive applications.

The integrated MHT at 100 °C successfully yielded anthocyanins (ACN), BCP, and DFC from blackcurrant pomace, with each component functionally involved in the final film products. The blending of ACN, BCP and DFC derived from blackcurrant pomace within a NaAlg matrix can produce pH-sensitive biobased films for potential food applications. These colorimetric films can detect NH_3 as a proxy for food freshness monitoring. Their antifogging properties, supported by high water vapour permeability (WVP), make them especially suitable for packaging highly perishable produce. Rheological studies revealed that NaAlg-BCP50 exhibited the most solid-like behaviour, highest recovery, and highest tensile strength among all NaAlg-BCP films, making it potential for applications requiring structural integrity under stress. However, for a wider range of commercial applications the tensile strength of the prepared films based on NaAlg needs to be improved and the oxygen permeability and barrier properties need to be explored. By leveraging blackcurrant pomace-derived components, the study highlights a sustainable approach to reducing food waste, enhancing food safety and committing to responsible production and consumption. Moreover, the feasibility of using blackcurrant pomace as a multifunctional raw material is demonstrated using microwave-assisted hydrothermal treatment, which consumes less time and energy than conventional extraction methods, offering a more environmentally friendly alternative.

4.1.2. Valorisation of extruded ginger pomace, extruded aeroponically grown coriander and Thai basil roots

This section examined the valorisation of extruded ginger pomace (GP), extruded aeroponic coriander (CR), and Thai basil (ThB) roots through green fractionation approaches. These included supercritical CO_2 extraction, microwave-assisted extraction (MAE) of proteins and starch, and microwave hydrothermal processing to produce defibrillated cellulose (DFC). **Figure 4.2** concludes the overall valorisation and fractionation pathways applied to GP, CR, and ThB, yielding lipids, essential oils, proteins, starch, and DFC.

Supercritical CO_2 using 10% ethanol as a co-solvent proved effective for selectively recovering essential oils from GP, characterised by a high content of zingerone and shogaol derivatives and a low proportion of fatty acids. In contrast, the same extraction conditions preferentially recovered fatty acids and long-chain hydrocarbons from CR and ThB, highlighting the feedstock-dependent selectivity of supercritical CO_2 extraction.

Subsequent MAE of the oil-/fatty-acid-free residues enabled further fractionation into protein and starch fractions, with starch recovered only from GP. MAE conducted at temperatures below 100 °C was suitable for protein extraction across all feedstocks. Based on extraction yield and protein content determined by the Bradford assay, 60 °C was optimal for protein extraction from GP, while 80 °C was more suitable for CR and ThB.

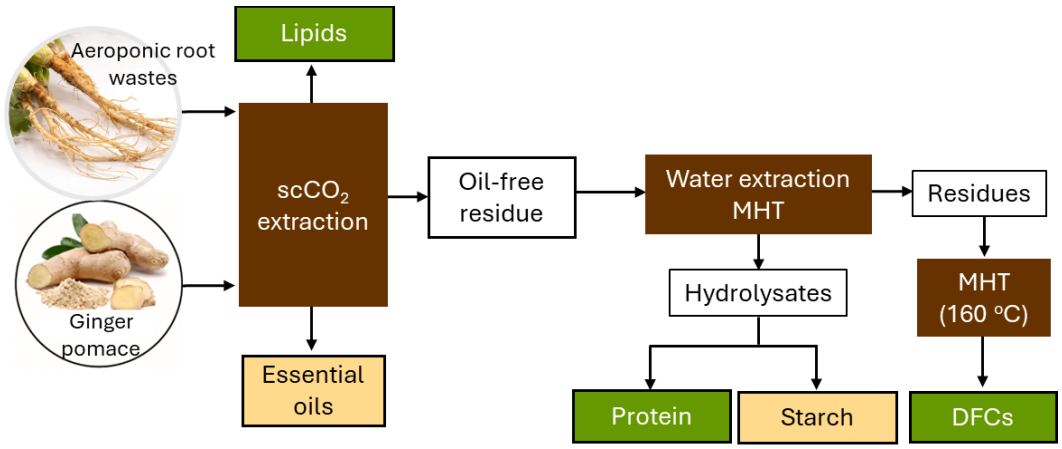

Figure 4.2. Diagram of the valorisation processes for ginger pomace and aeroponic root wastes. Products obtained from ginger pomace and aeroponic root wastes are shown in green boxes, while yellow boxes indicate products derived exclusively from ginger pomace.

Starch recovered from the GP MAE hydrolysate consisted of insoluble starch (GPI) and soluble starch (GPS) fractions. GPI was the only starch fraction obtained under MAE at 60 °C and under conventional water extraction conditions (50 °C), exhibiting a high amylose content of up to 48.85%. As MAE temperature increased (up to 120 °C), GPI yield and amylose content decreased, while GPS yield increased and exhibited high amylose content (up to 46.70%). This behaviour is attributed to microwave irradiation promoting surface cracking and disruption of the crystalline structure of starch granules, as evidenced by SEM and pXRD analyses, thereby facilitating the release of amylose and water-soluble starch into the aqueous phase.

pXRD analysis further revealed a crystallinity transformation from A-type starch in GPI to V-type starch in GPS, suggesting that MAE at temperatures ≥ 80 °C promoted the formation of amylose-ligand complexes. V-type starch is widely recognised for its applications as an encapsulation matrix for bioactive compounds, flavours, and lipophilic nutrients. Accordingly, the presence of V-type starch in GPS indicates strong potential for applications in functional foods, encapsulation systems, and starch-based biodegradable materials. In addition, both GPI and GPS exhibited higher thermal stability (T_d = 300-315 °C) compared to commercial potato starch (amylopectin T_d = 309 °C; amylose T_d = 298 °C;

Appendix 20), further supporting their suitability for advanced material and food applications at high temperature.

The DFCs produced via acid-free MAE followed by MHT reprocessing of GP, CR, and ThB yielded lignocellulosic materials with water-holding capacity (WHC). Among them, DFC-GP60 exhibited the highest WHC (17.33 g/g), substantially exceeding those of DFC-CR80 (6.43 g/g) and DFC-ThB80 (8.20 g/g). Consistent with this behaviour, DFC-GP60 demonstrated the ability to form a stable gel at 5%w/v, whereas DFC-CR80 and DFC-ThB80 did not exhibit gelation within the investigated concentration range (2.5 – 7.5%w/v). Solid-state ^{13}C CP/MAS NMR finding indicated higher lignin content in DFC-CR80 and DFC-ThB80, as evident in higher lignin signal intensities. In addition, pXRD analysis revealed pronounced crystalline calcium oxalate dihydrate in DFC-CR80 and DFC-ThB80, suggesting that the combined presence of lignin and inorganic crystalline phases may hinder hydrogel formation. All DFCs showed enhanced thermal stability and crystallinity relative to their native counterparts, with degradation temperatures ranging from 358 to 363 °C and crystallinity indices between 28.4 and 32.8%. Collectively, these findings highlight DFC-GP60 as the most promising candidate for hydrogel-based applications, while DFC-CR80 and DFC-ThB80 demonstrate potential for high-temperature and structurally robust material applications.

4.2. Future Work

Because of time limitations and availability of equipment, several ideas could not be fully explored to enhance the quality of this work. The following section discusses these ideas as potential future work.

4.2.1. Supercritical CO_2 extraction

In this study, supercritical CO_2 extraction was conducted under a single condition (10% ethanol co-solvent, 350 bar, 35 °C, 2h) to extract essential oils and fatty acids from the extruded ginger pomace (GP) and the extruded aeroponically grown coriander (CR) and Thai basil (ThB) roots. Preliminary results showed that within the same extraction condition, fatty acids and long-chain hydrocarbons was preferentially recovered from CR and ThB, while essential oil with high content of zingerone and shogaol was predominantly extracted from GP. Thus, exploring a wider range of extraction parameters such as pressure, temperature, CO_2 flow rate, and the use of co-solvents, could significantly improve extraction efficiency and selectivity. Future studies should investigate the effect of these variables to optimise yield, and composition of the extracted compounds.

In addition, the $scCO_2$ extracts may contain variations in phenolics, fatty acids, and pigments, which could exhibite antioxidant activity. Therefore, further evaluation of the antioxidant properties of these extracts is recommended to assess their potential applications as functional food ingredients or natural antioxidant agents.

4.2.2. Further characterisation of extracted protein

The characterisation of extracted proteins from GP, CR and ThB was limited in this study. Additional analyses, such as sodium dodecyl sulphate-polyacrylamide gel electrophoresis (SDS-PAGE) and protein composition analysis using a protein analyser, would allow for a better understanding of molecular weight distribution and amino acid profiles.

Furthermore, evaluation of functional properties, including antioxidant activity, solubility, emulsifying capacity, foaming ability, and thermal stability, would help assess the suitability of these proteins for industrial food and pharmaceutical applications, particularly in the growing demand for plant-based proteins. In addition, ginger proteins are known to exhibit enzymatic properties and bioactivities. Therefore, future work should include catalytic activity measurements and bioactivity assays to further investigate the functional potential of ginger proteins derived from microwave-assisted extraction.

4.2.3. Properties testing of extracted polysaccharides: blackcurrant pectin and ginger starch

The extracted polysaccharides in this study, namely blackcurrant pectin and ginger starch, were obtained using microwave-hydrothermal treatment (MHT) at different temperatures. Structural modifications were observed, including a reduced degree of esterification in blackcurrant pectin and a crystalline transformation of ginger starch from A-type to V-type. However, molecular weight distribution and comprehensive functional property evaluations were not conducted.

Given the structural alterations induced by MHT, the functional properties of blackcurrant pectin and ginger starch are likely to be affected. Therefore, future work should include detailed characterisation of their molecular weight distribution, rheological behaviour, gelling ability, emulsion stability, and digestive properties. Such investigations would provide valuable insights into their suitability and potential applications in food, pharmaceutical, and biopolymer-based industries.

4.2.4. Carbonisation of extracted polysaccharides; blackcurrant pectin and ginger starch, for production of Starbon-like materials

The extracted polysaccharides, specifically blackcurrant pectin and ginger starch, exhibited structural changes under MHT, which may influence their gelation behaviour. Future research could explore the potential of blackcurrant pectin and ginger starch gel as precursors to produce mesoporous carbonaceous materials (Starbon) through carbonisation by assessing the effects of carbonisation temperature and activation conditions on porosity, surface area, and adsorption performance. This approach could expand the valorisation potential of the extracted biopolymers for applications in catalysis, separation, and environmental remediation.

4.2.5. Effect of inorganic minerals on the characteristics and properties of defibrillated cellulose derived from aeroponically grown coriander and Thai basil roots

Aeroponically grown coriander and Thai basil roots were cultivated in a nutrient mist containing dissolved inorganic salts, typically including macronutrients such as nitrogen, phosphorus, and potassium, together with micronutrients and secondary nutrients including calcium, magnesium, and sulphur. As a result, residual inorganic minerals may remain associated with the root biomass even after cellulose isolation and defibrillation. In this study, highly crystalline calcium oxalate dihydrate was observed in the defibrillated cellulose derived from aeroponically grown coriander and Thai basil roots, which likely hindered the gel-forming ability of the resulting defibrillated cellulose. These inorganic constituents may also influence the physicochemical characteristics of the material during processing. In particular, mineral species can alter local heat transfer and may affect microwave-assisted treatment through interactions with bound water and ionic polarisation, although calcium oxalate dihydrate itself is not considered a highly efficient microwave absorber. Therefore, future work should investigate the effect of demineralisation pretreatments prior to defibrillation. Treatments such as dilute acid washing or chelation may help remove residual inorganic deposits, including crystalline calcium oxalate dihydrate, and could potentially improve fibrillation efficiency, water-holding capacity, and gel-forming ability of the resulting defibrillated cellulose.

4.2.6. Rheological properties of ginger pomace defibrillated cellulose hydrogels

The rheological behaviour of ginger defibrillated cellulose hydrogels was not investigated in this study. Future work should focus on characterising their viscoelastic properties, including storage and loss modulus, yield stress, and shear-thinning behaviour. Such analyses are essential for understanding the structural stability and flow behaviour of the hydrogels, which are critical for their potential applications in food, biomedical, and packaging materials.

4.2.7. Development of blackcurrant extracts pH-responsive film

Although blackcurrant extracts were incorporated into films, their practical application was limited by the short stability of anthocyanins within the film matrix. Future studies should investigate encapsulation strategies, such as microencapsulation or nanoencapsulation, to improve anthocyanin stability and prolong functional performance. Additionally, film formulations should be optimised to meet commercial standards, including mechanical strength, barrier properties, and shelf-life requirements. Validation using real food spoilage tests is also necessary to assess the effectiveness of the films as intelligent packaging materials.

4.2.8. Scale-up for industrial applications

All experiments in this study were conducted at a laboratory scale. Future work should focus on scaling up the extraction processes to pilot or industrial scale, while evaluating process efficiency, energy consumption, economic feasibility, and environmental impact, which would be essential for commercial implementation and could contribute to the reduction and valorisation of food and agricultural waste.

Appendices

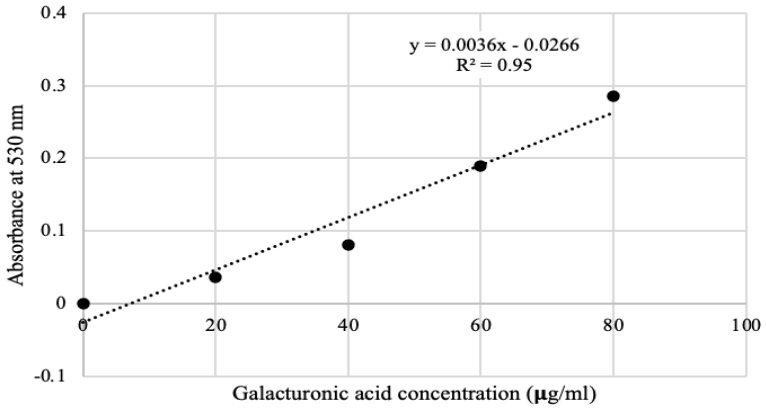

Appendix 1. Calibration curve of galacturonic acid (0-80 µg/mL) at 530 nm for uronic acid determination in BCP using MHDP method.

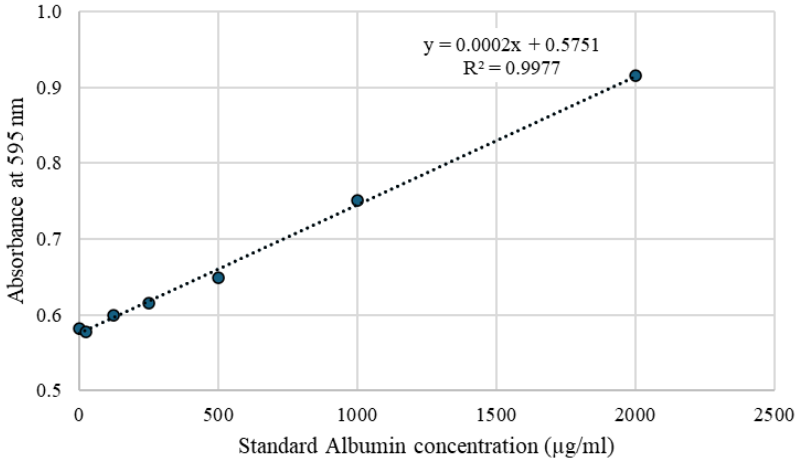

Appendix 2. Calibration curve of standard albumin (0-2000 µg/mL) at 595 nm for protein determination in GR, CR, and ThB protein extracts using Bradford assay.

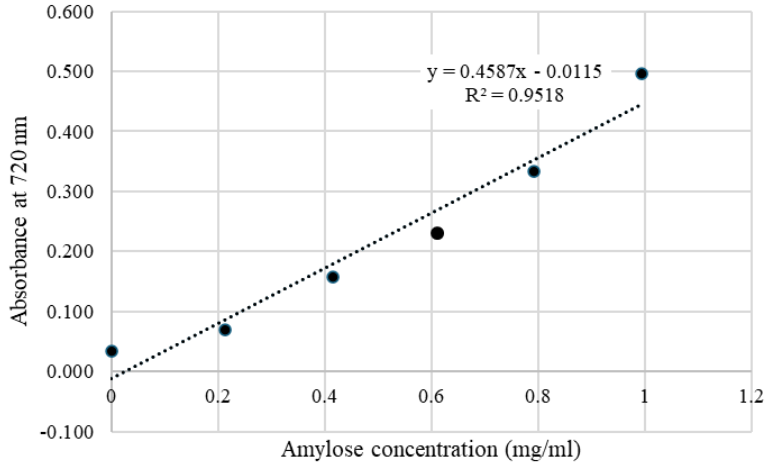

Appendix 3. Calibration curve of standard amylose (0-1 mg/mL) at 720 nm for determination of GR starch purity.

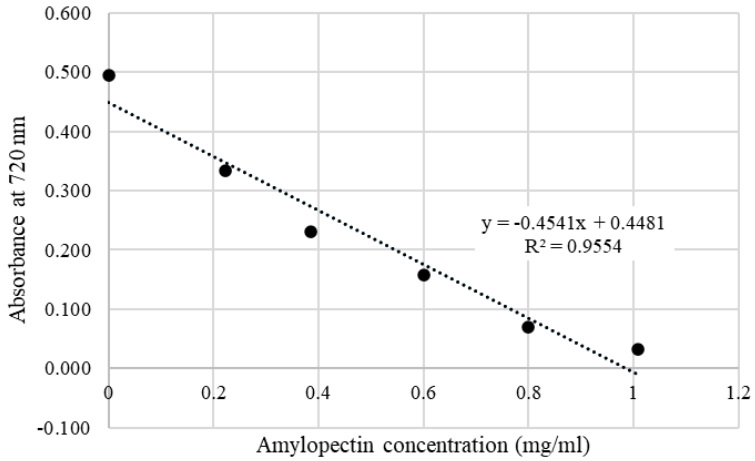

Appendix 4. Calibration curve of standard amylopectin (0-1 mg/mL) at 720 nm for GR determination of starch purity

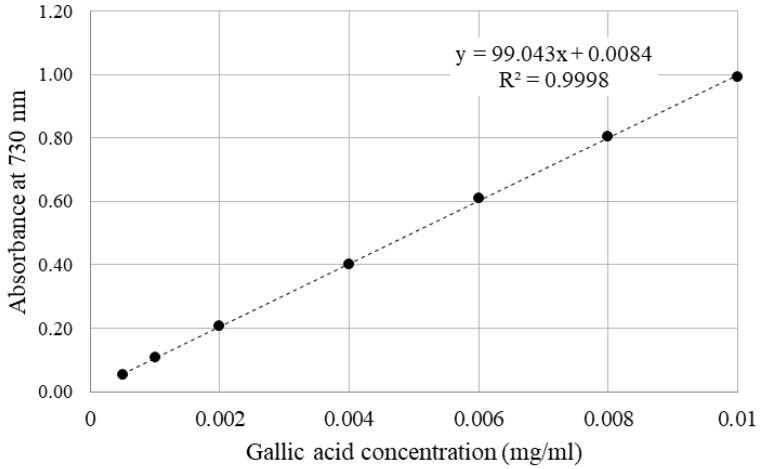

Appendix 5. Calibration curve of gallic acid (0-0.01 mg/mL) at 730 nm for determination of total phenolic content

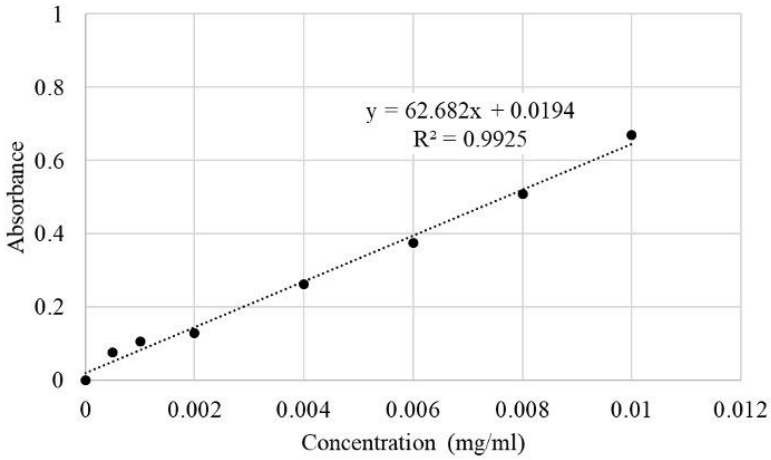

Appendix 6. Calibration curve of quercetin (0-0.01 mg/mL) at 420 nm for determination of total flavonoid content

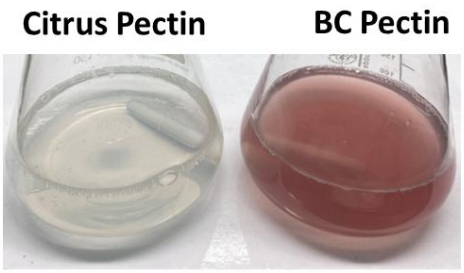

1. Phenolpthalein was used as indicator

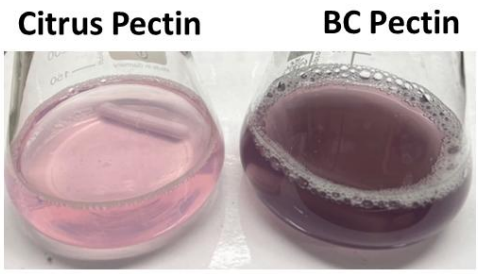

2. Titrate with 0.1M NaOH (V_1)

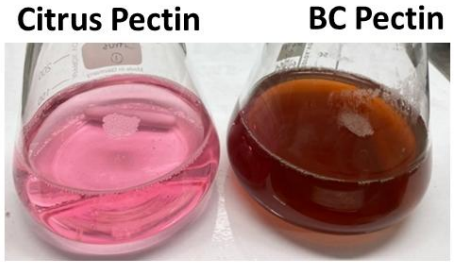

3. Sponification of pectin by adding 0.5M NaOH

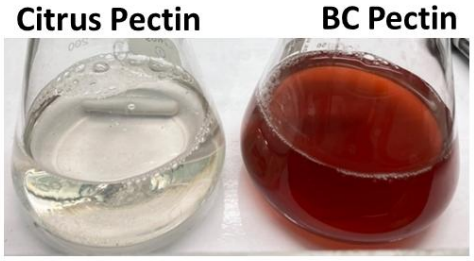

4. Neutrilisation by adding 0.5M HCl

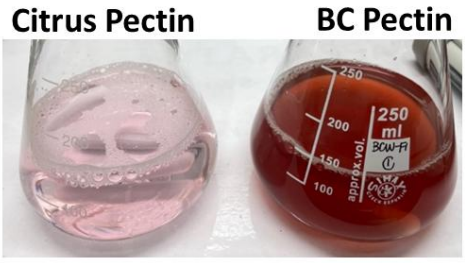

5. Titrate with 0.1M NaOH (V_2)

$$\text{Degree of Esterification (\%)} = \frac{V_2 \times 100}{V_1 + V_2}$$

V_1 = content of GalA without esterification
V_2 = content of esterified GalA in the pectin sample

Appendix 7. Appearance of citrus pectin and blackcurrant pomace pectin during determination of degree of esterification via the titration method.

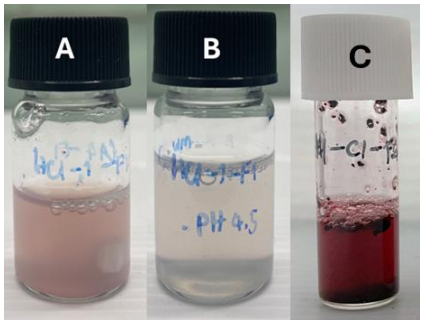

Appendix 8. BCP-H solution at pH 1 (A) and pH 4 (B), and BCH-H solution (C).

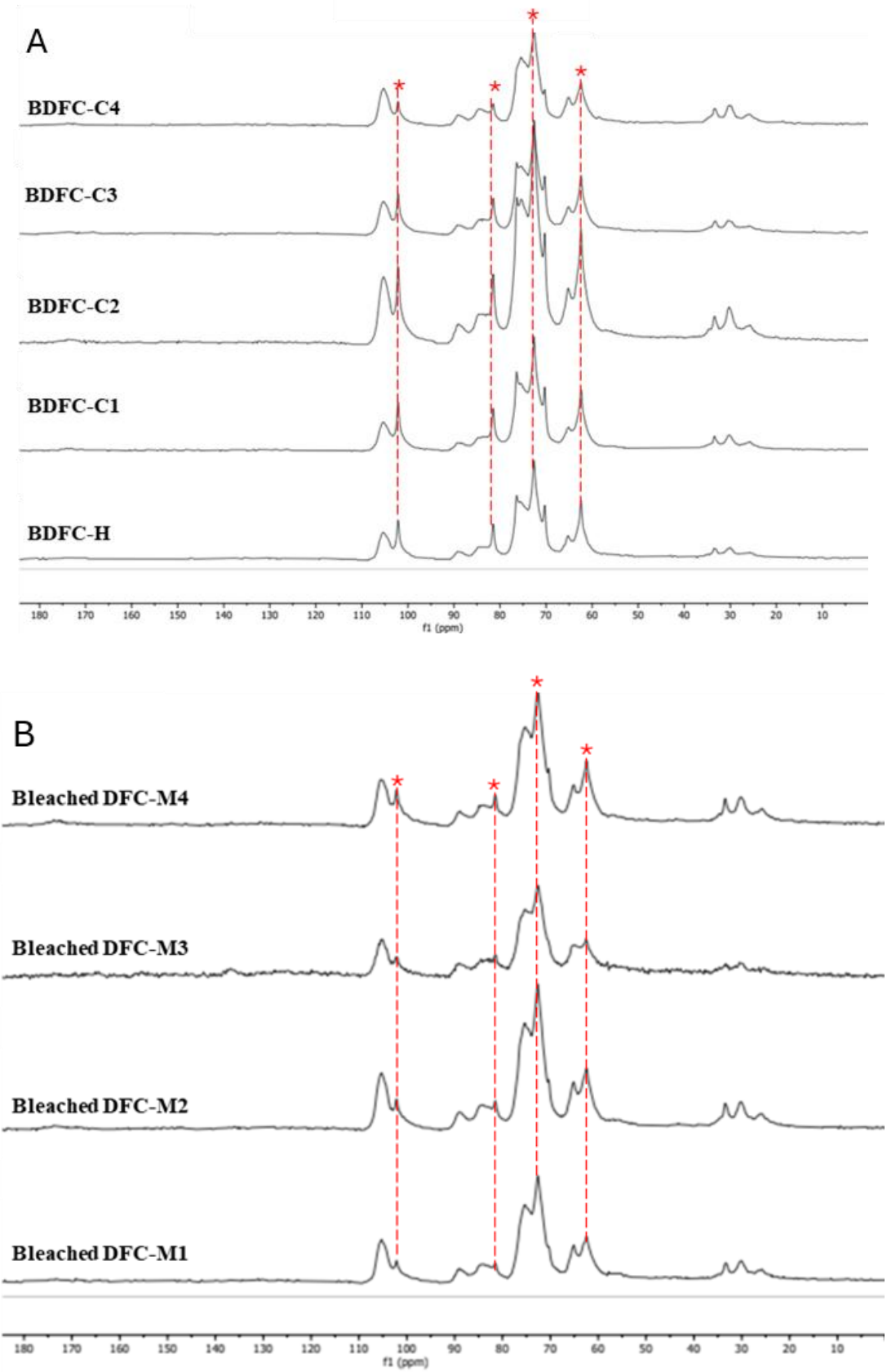

*Appendix 9. Solid state ^{13}C CP/MAS NMR spectra of bleached acid-derived DFC (A) and bleached acid-free derived DFC (B); * refers to crystalline Xylan signals.*

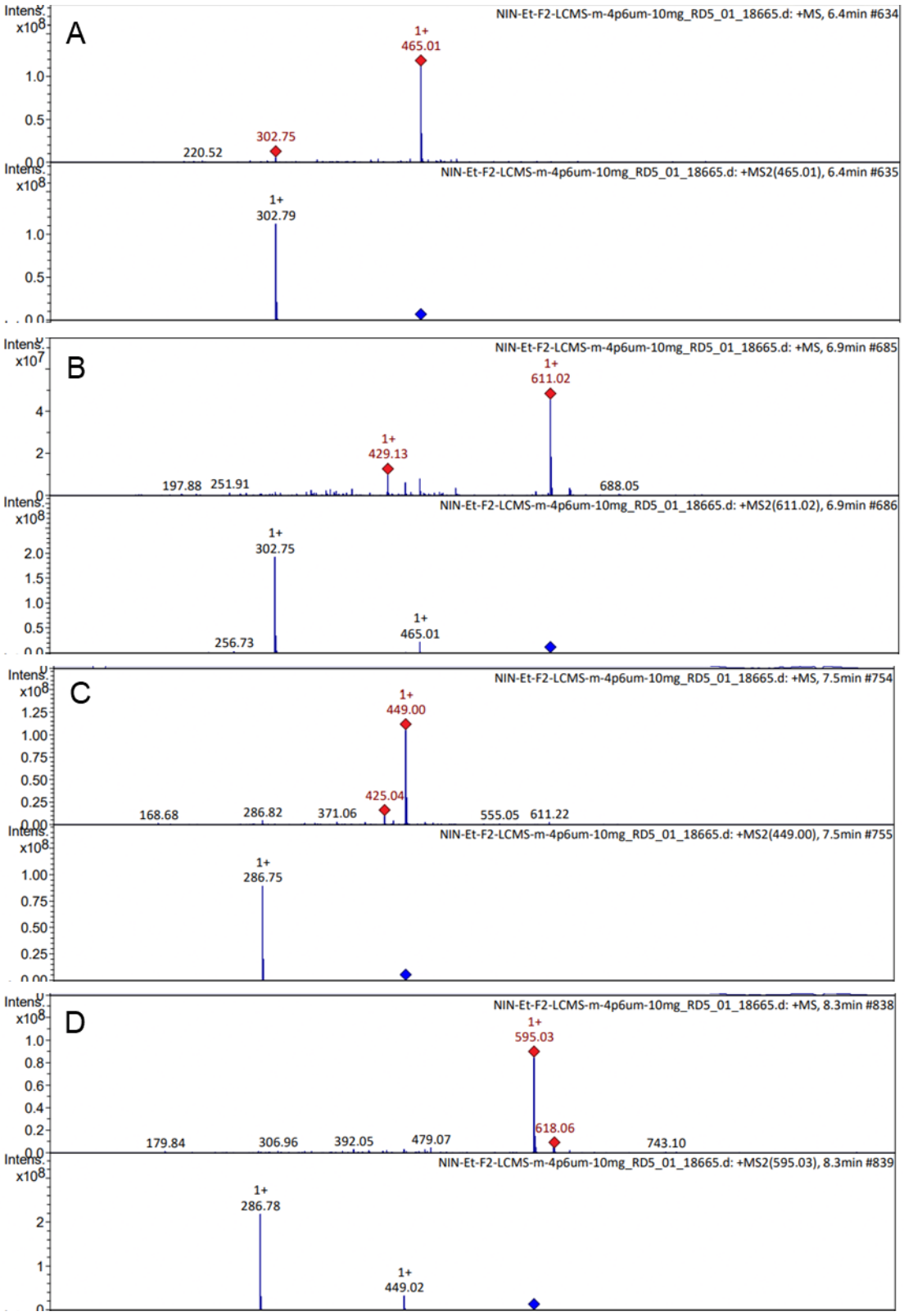

Appendix 10. Mass spectroscopy and fragmentations of delphinidin-3-glucoside (D3G, A), delphinidin-3-rutinoside (D3R, B), cyanidin-3-glucoside (C3G, C), cyanidin-3-rutinoside (C3R, D).

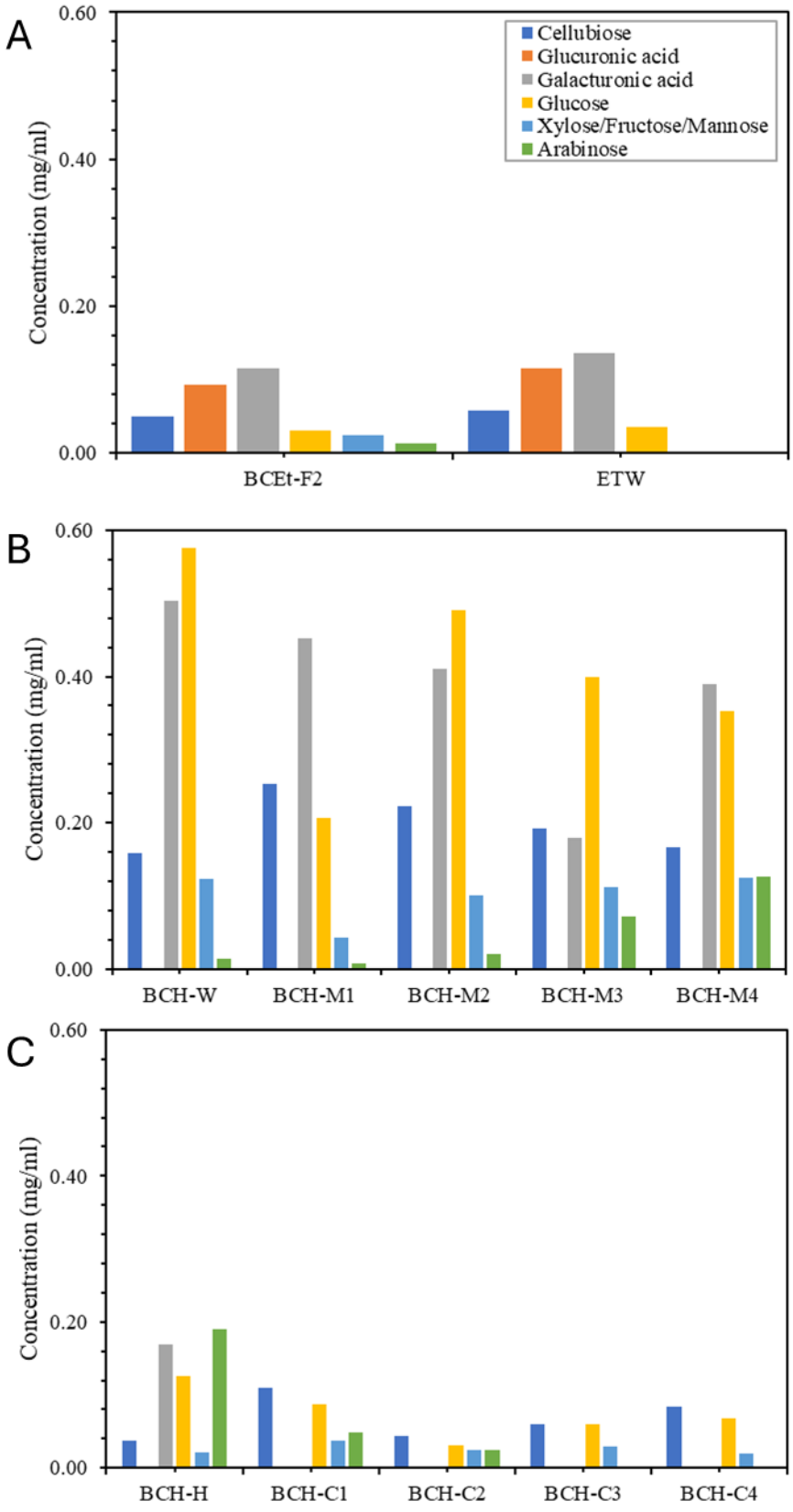

Appendix 11. Sugar analyses of ethanol-ethyl acetate-insoluble fraction (BCEt-F2), ethanol-water extract (ETW)(A), acid-free BCH (B), and acid-derived BCH (C).

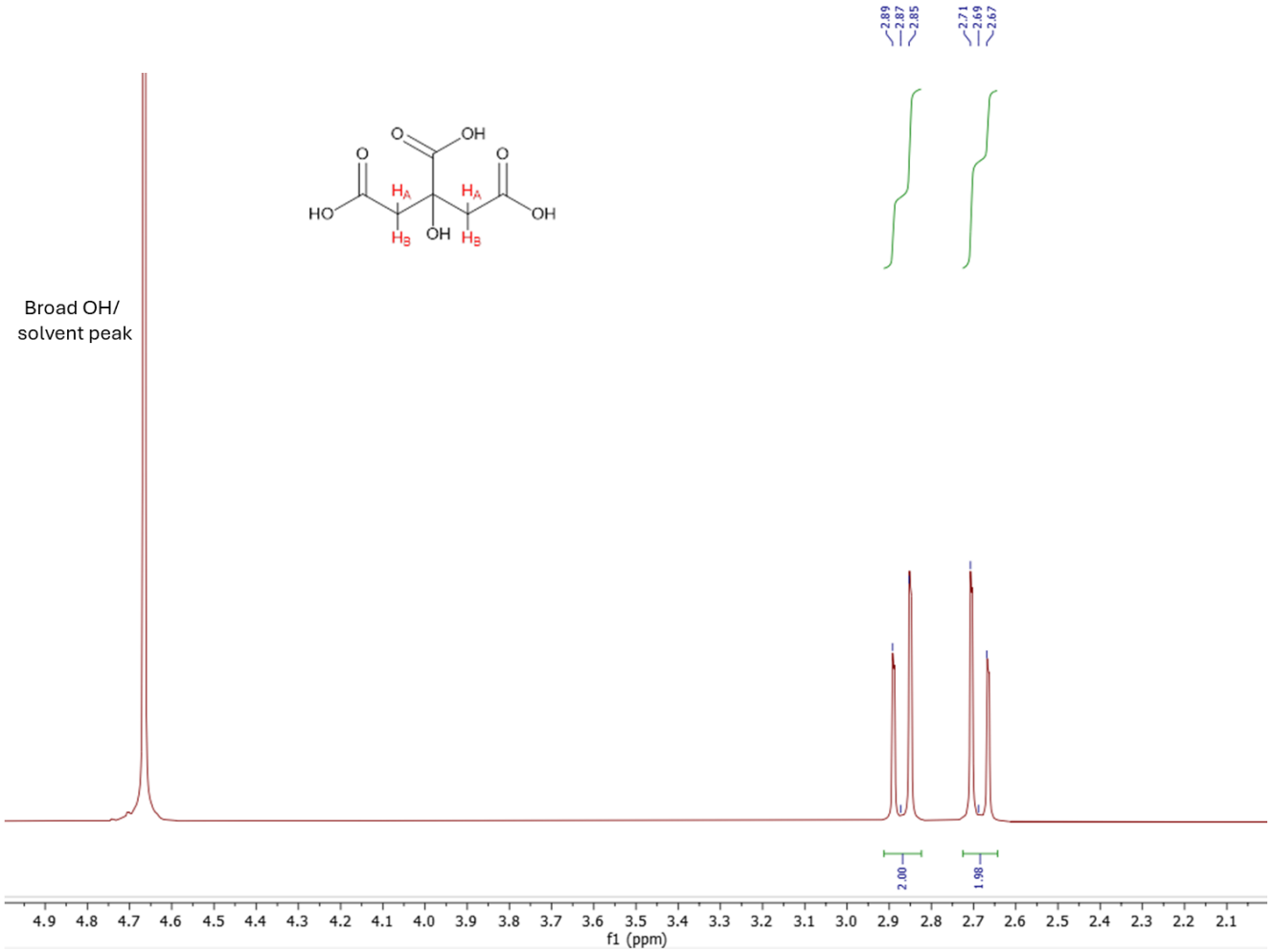

Appendix 12. ^{1}H-NMR spectra of citric acid in D_2O.

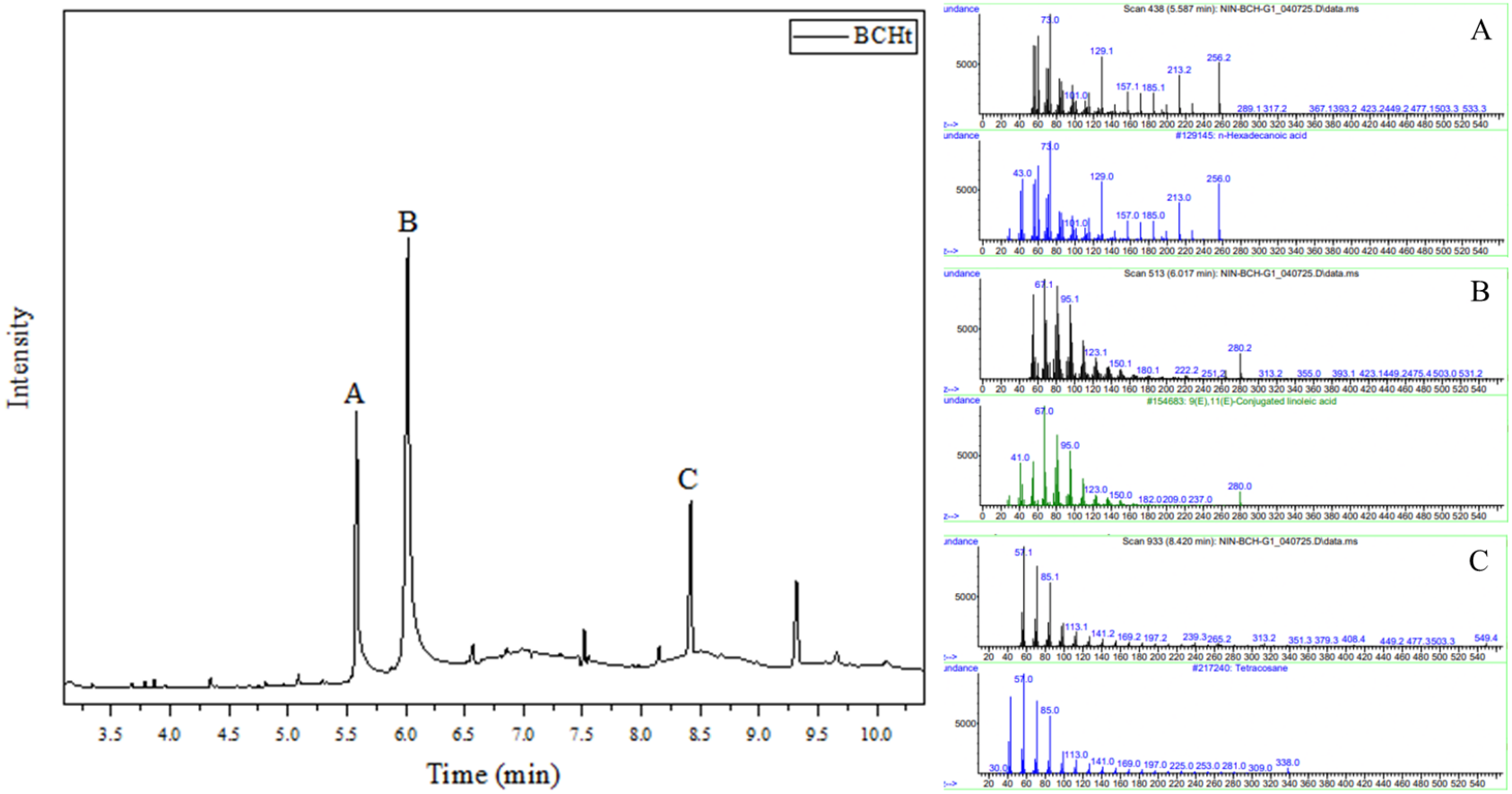

Appendix 13. GC chromatogram and MS spectra of three major compounds identified in BCHt: palmitic acid (A), linoleic acid (B), and tetracosane (C).

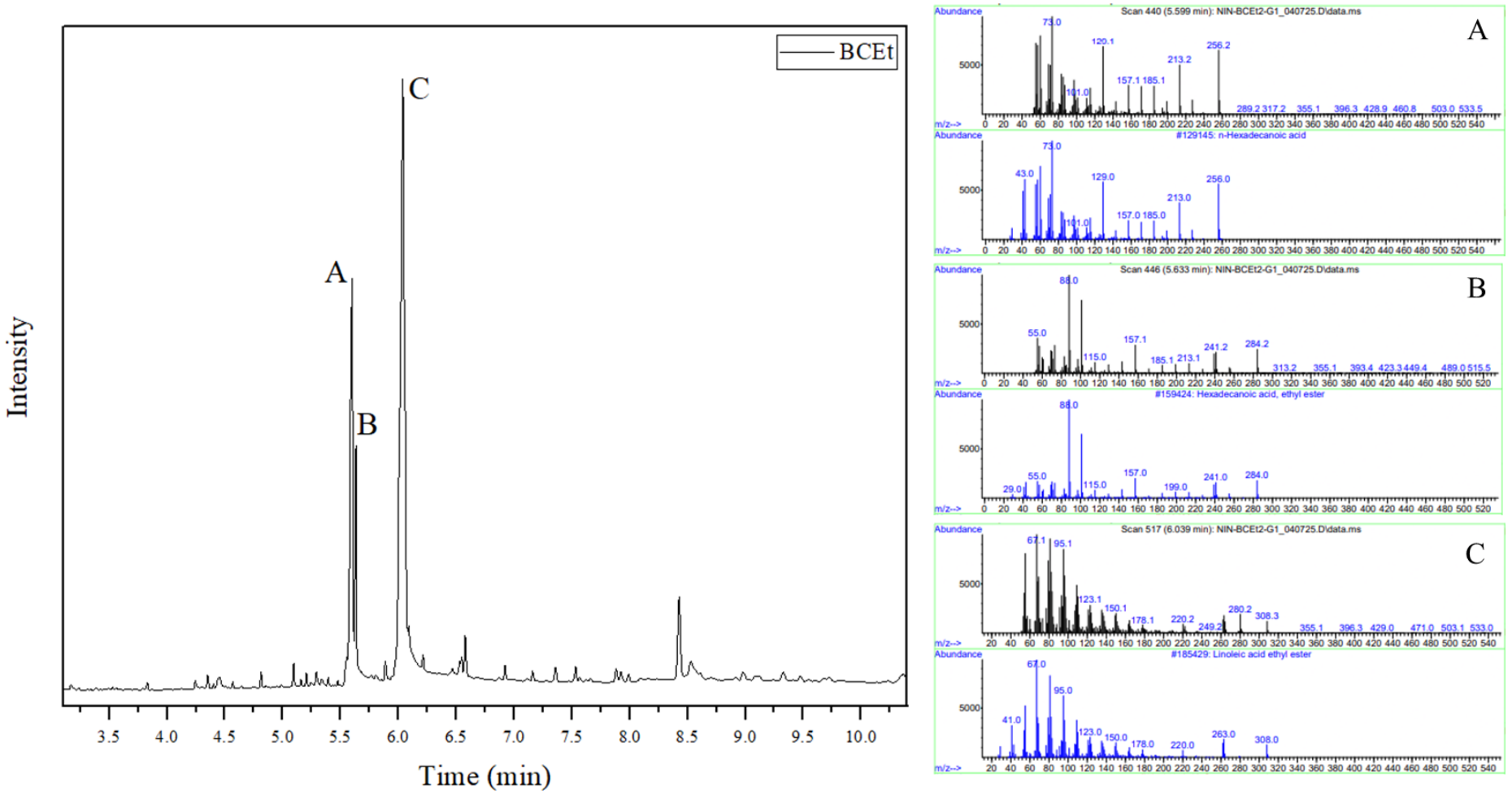

Appendix 14. GC chromatogram and MS spectra of three major compounds identified in BCEt: palmitic acid (A), palmitic acid ethyl ester (B), and mixtures of linoleic acid and its ethyl ester (C).

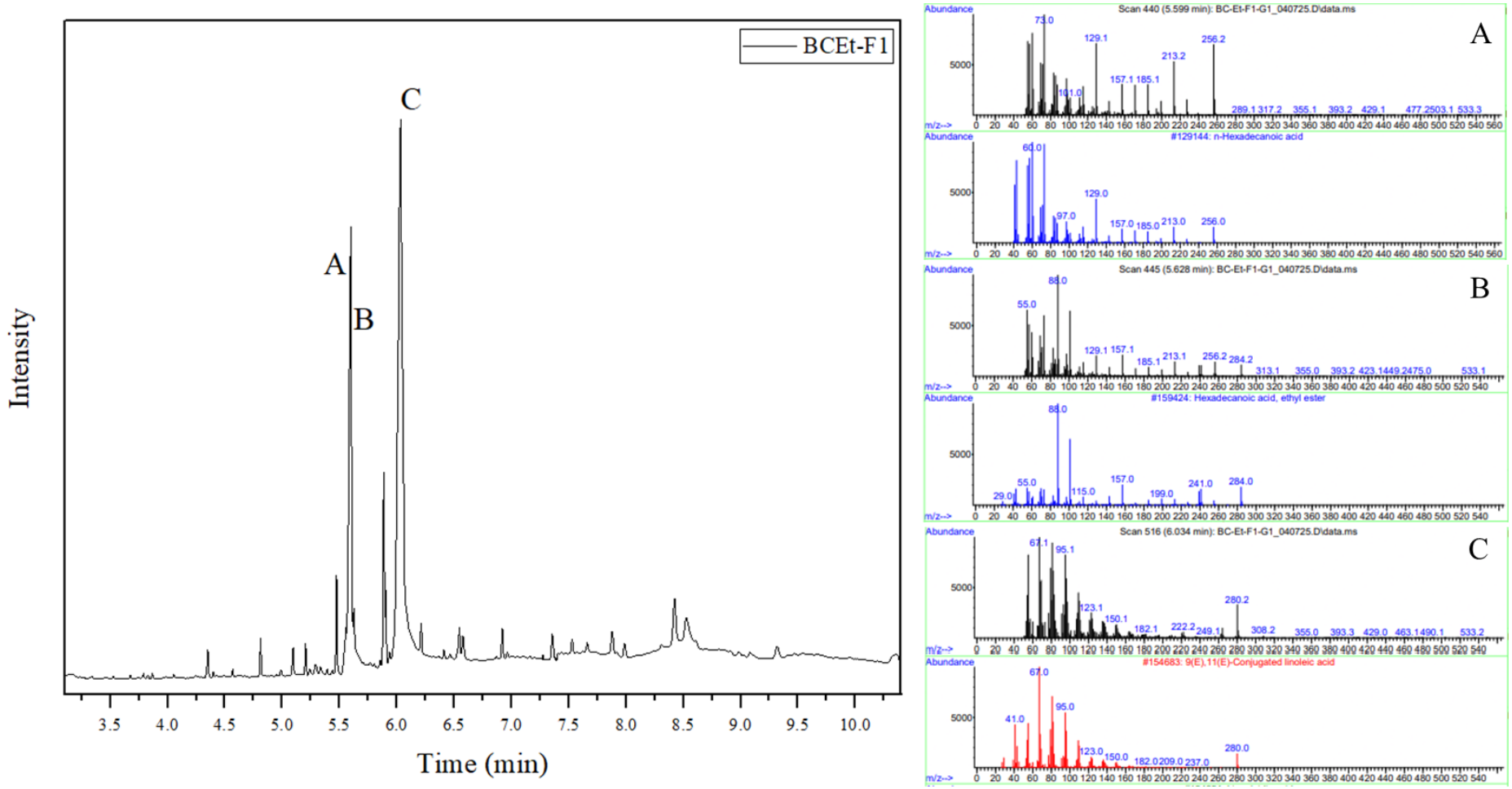

Appendix 15. GC chromatogram and MS spectra of three major compounds identified in BCEt-F1: palmitic acid (A), palmitic acid ethyl ester (B), and mixtures of linoleic acid and its ethyl ester (C).

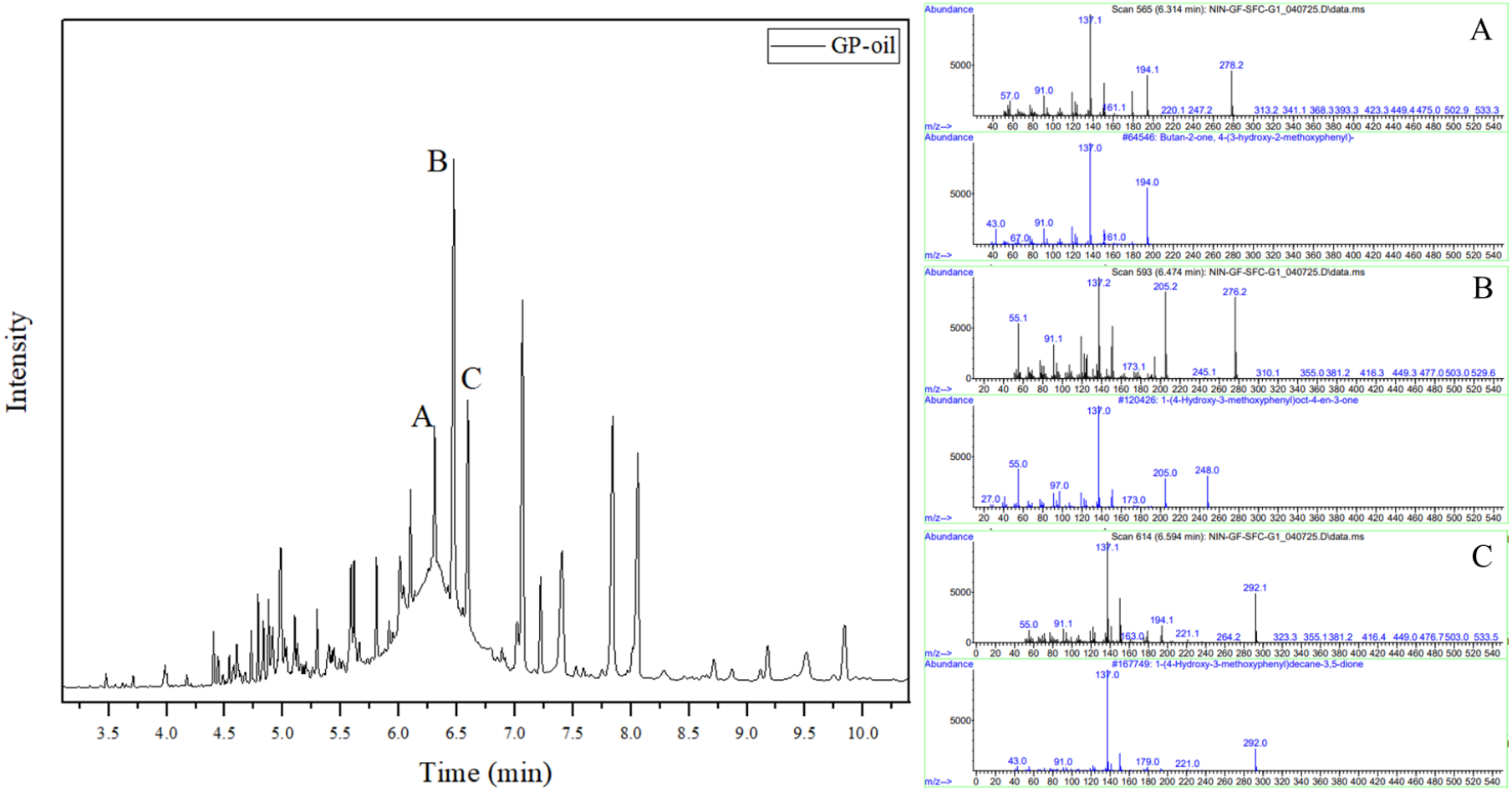

Appendix 16. GC chromatogram and MS spectra of three major compounds identified in GP-oil: 4-(3-hydroxy-2-methoxyphenyl)-Butan-2-one (A), 1-(4-hydroxy-3-methoxyphenyl)oct-4-en-3-one (B), and 1-(4-Hydroxy-3-methoxyphenyl) decane-3, 5-dione (C).

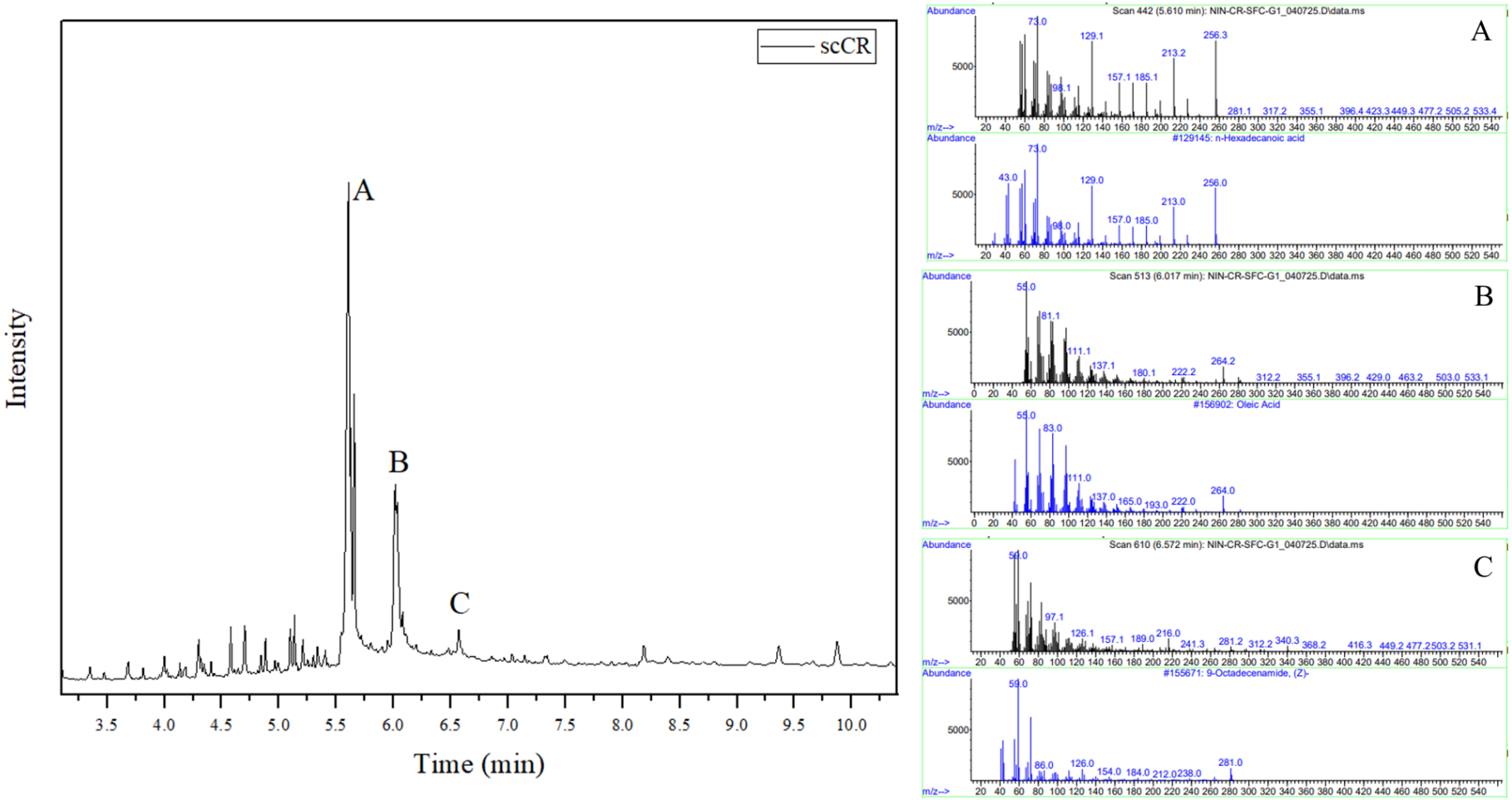

Appendix 17. GC chromatogram and MS spectra of three major compounds identified in scCR extract: palmitic acid (A), oleic acid (B), and oleamide (C).

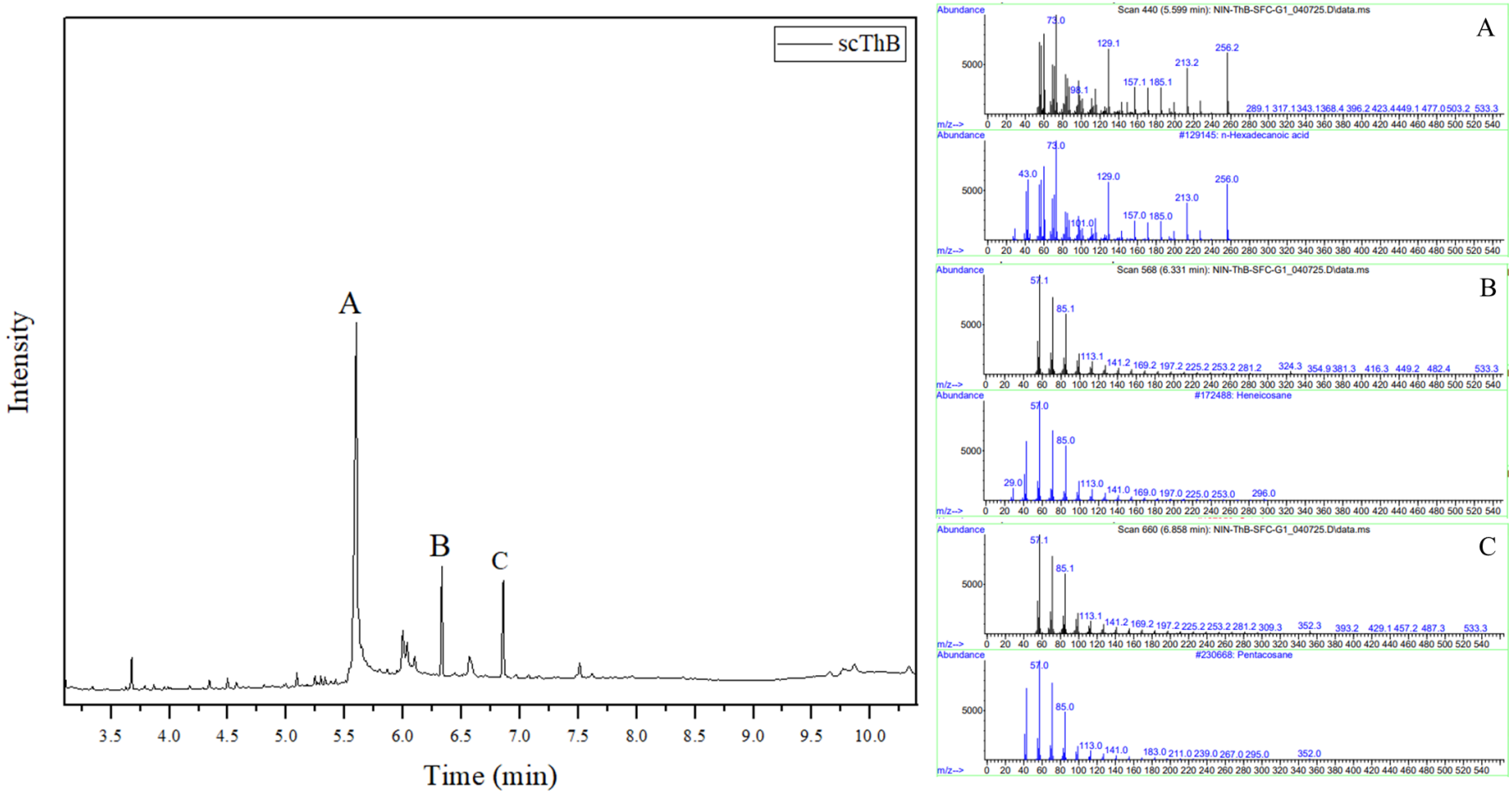

Appendix 18. GC chromatogram and MS spectra of three major compounds identified in scThB extract: palmitic acid (A), heneicosane (B), and pentacosane (C).

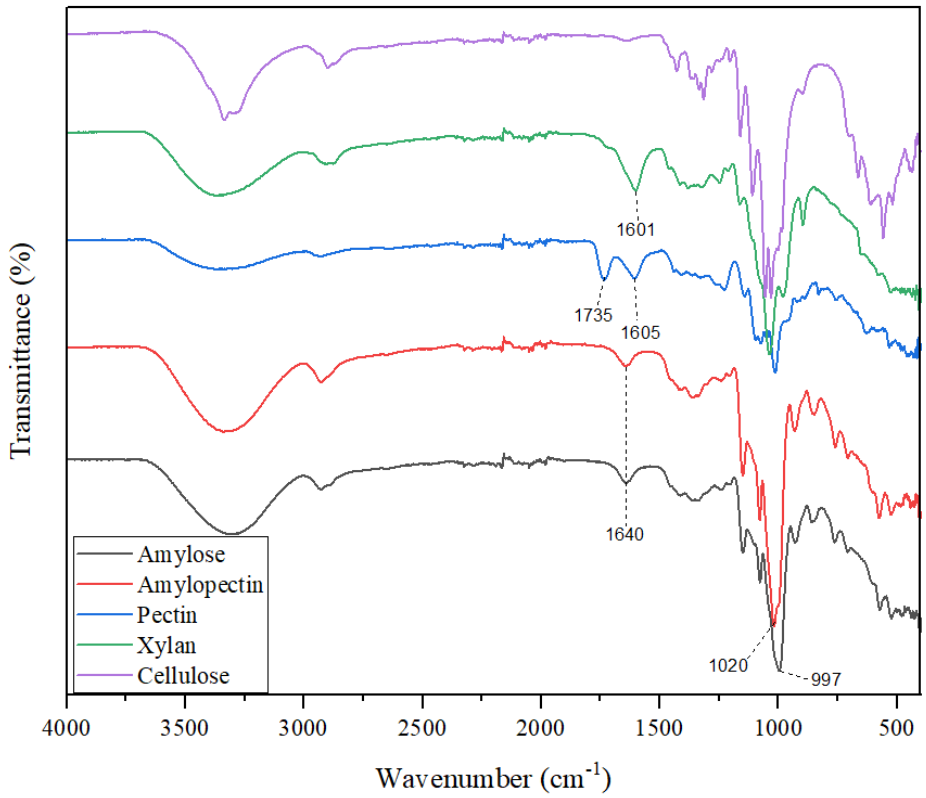

Appendix 19. ATR-IR spectrum of commercial polysaccharides.

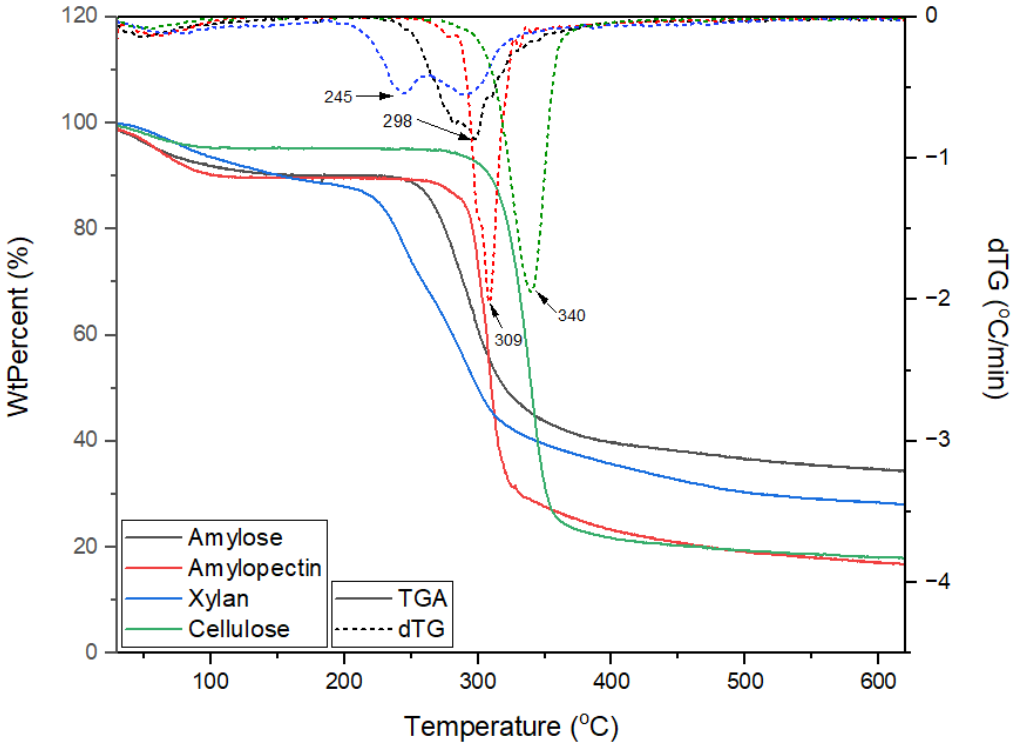

Appendix 20. TGA thermogram of commercial polysaccharides.

References

(1) Stockholm Resilience Centre. *Planetary boundaries*. https://www.stockholmresilience.org/research/planetary-boundaries.html (accessed 2025-10-27).

(2) Sakschewski, B.; Caesar, L.; Andersen, L. S.; Bechthold, M.; Bergfeld, L.; Beusen, A.; Billing, M.; Leon Bodirsky, B.; Botsyun, S.; Dennis, D. P.; Donges, J. F.; Dou, X.; Eriksson, A.; Fetzer, I.; Gerten, D.; Häyhä, T.; Hebden, S.; Heckmann, T.; Huiskamp, W.; Jahnke, A.; Kaiser, J.; Kitzmann, N. H.; Krönke, J.; Kühnel, D.; Laureanti, N. C.; Li, C.; Liu, Z.; Loriani, S.; Ludescher, J.; Mathesius, S.; Norström, A.; Otto, F.; Paolucci, A.; Pokhotelov, D.; Rafiezadeh Shahi, K.; Raju, E.; Rostami, M.; Schaphoff, S.; Schmidt, C.; Steinert, N. J.; Stenzel, F.; Virkki, V.; Wendt-Potthoff, K.; Wunderling, N.; Rockström, J. *A Scientific Assessment of the State of the Planet Executive Summary*; 2025. https://doi.org/10.48485/pik.2025.017.

(3) The Centre for Research on the Epidemiology of Disasters (CRED) and United Nations Office for Disaster Risk Reduction (UNISDR). *The Human Cost of Weather-Related Disasters 1995-2015*. https://www.unisdr.org/files/46796_cop21weatherdisastersreport2015.pdf (accessed 2025-09-19).

(4) Copernicus Climate Change Service (C3S) and World Meteorological Organization (WMO). *European State of the Climate 2024*; 2025. https://doi.org/doi.org/10.24381/14j9-s541.

(5) Lan, X.; Tans, P.; Thoning. K.W. *Trends in globally-averaged CO_2 determined from NOAA Global Monitoring Laboratory measurements*. https://doi.org/https://doi.org/10.15138/9N0H-ZH07.

(6) United Nations Framework Convention on Climate Change (UNFCCC). *The Paris Agreement*; 2015. https://unfccc.int/process-and-meetings/the-paris-agreement (accessed 2025-09-19).

(7) Stocker, T. *Climate Change 2013: The Physical Science Basis: Working Group I Contribution to the Fifth Assessment Report of the Intergovernmental Panel on Climate Change*; Cambridge University Press, 2014.

(8) Cherubini, F. The Biorefinery Concept: Using Biomass Instead of Oil for Producing Energy and Chemicals. *Energy Convers Manag* 2010, *51* (7), 1412–1421. https://doi.org/10.1016/j.enconman.2010.01.015.

(9) International Energy Agency (IEA). *Oil 2025: Analysis and Forecast to 2030*; Paris, 2025. https://www.iea.org/reports/oil-2025 (accessed 2025-09-19).

(10) Pandey, A.; Sharma, Y. C. Advancements in Biomass Valorization in Integrated Biorefinery Systems. *Biofuels, Bioproducts and Biorefining* 2024, *18* (6), 2078–2090. https://doi.org/10.1002/bbb.2670.

(11) Singh, V.; Tiwari, R.; Chaturvedi, V. K.; Singh, N.; Mishra, V. Microbiological Aspects of Bioenergy Production: Recent Update and Future Directions. In *Bioenergy Research: Revisiting Latest Development. Clean Energy Production Technologies*; Springer, Singapore, 2021; pp 29–52. https://doi.org/10.1007/978-981-33-4615-4_2.

References

(12) Alba, K.; Campbell, G. M.; Kontogiorgos, V. Dietary Fibre from Berry-Processing Waste and Its Impact on Bread Structure: A Review. *J Sci Food Agric* 2019, *99* (9), 4189–4199. https://doi.org/10.1002/jsfa.9633.

(13) Deshavath, N. N.; Veeranki, V. D.; Goud, V. V. Lignocellulosic Feedstocks for the Production of Bioethanol: Availability, Structure, and Composition. In *Sustainable Bioenergy: Advances and Impacts*; Elsevier, 2019; 1–19. https://doi.org/10.1016/B978-0-12-817654-2.00001-0.

(14) Flauzino Neto, W. P. Morphological Investigation of Cellulose Nanocrystals and Nanocomposite Applications. Ph. D. Thesis, Federal University of Uberlândia, 2017.

(15) Tokumasu, N.; Nakano, T.; Yoshida, S.; Kimura, Y.; Endo, T. Facile Preparation of Cellulose IVII Using Ionic Liquids. *CrystEngComm* 2024, *26* (40), 5777–5784. https://doi.org/10.1039/d4ce00761a.

(16) Hernández-Varela, J. D.; Chanona-Pérez, J. J.; Calderón Benavides, H. A.; Cervantes Sodi, F.; Vicente-Flores, M. Effect of Ball Milling on Cellulose Nanoparticles Structure Obtained from Garlic and Agave Waste. *Carbohydr Polym* 2021, *255*, 117347. https://doi.org/10.1016/j.carbpol.2020.117347.

(17) Flauzino Neto, W. P.; Putaux, J. L.; Mariano, M.; Ogawa, Y.; Otaguro, H.; Pasquini, D.; Dufresne, A. Comprehensive Morphological and Structural Investigation of Cellulose i and II Nanocrystals Prepared by Sulphuric Acid Hydrolysis. *RSC Adv* 2016, *6* (79), 76017–76027. https://doi.org/10.1039/c6ra16295a.

(18) Wu, Q.; Xu, J.; Zhu, S.; Kuang, Y.; Wang, B.; Gao, W. Crystalline Stability of Cellulose III Nanocrystals in the Hydrothermal Treatment and NaOH Solution. *Carbohydr Polym* 2020, *249*, 116827. https://doi.org/10.1016/j.carbpol.2020.116827.

(19) Wada, M.; Chanzy, H.; Nishiyama, Y.; Langan, P. Cellulose III I Crystal Structure and Hydrogen Bonding by Synchrotron X-Ray and Neutron Fiber Diffraction. *Macromolecules* 2004, *37* (23), 8548–8555. https://doi.org/10.1021/ma0485585.

(20) Cao, J.; Wei, W.; Gou, G.; Jiang, M.; Cui, Y.; Zhang, S.; Wang, Y.; Zhou, Z. Cellulose Films from the Aqueous DMSO/TBAH-System. *Cellulose* 2018, *25* (3), 1975–1986. https://doi.org/10.1007/s10570-017-1639-5.

(21) Gundekari, S.; Mitra, J.; Varkolu, M. Classification, Characterization, and Properties of Edible and Non-Edible Biomass Feedstocks. In *Advanced Functional Solid Catalysts for Biomass Valorization*; Elsevier, 2020; pp 89–120. https://doi.org/10.1016/B978-0-12-820236-4.00004-0.

(22) Gírio, F. M.; Fonseca, C.; Carvalheiro, F.; Duarte, L. C.; Marques, S.; Bogel-Łukasik, R. Hemicelluloses for Fuel Ethanol: A Review. *Bioresour Technol* 2010, *101* (13), 4775–4800. https://doi.org/10.1016/j.biortech.2010.01.088.

(23) Zhiguang, C.; Haixia, Z.; Min, C.; Fayong, G.; Jing, L. The Fine Structure of Starch: A Review. *NPJ Sci Food* 2025, *9* (1), 50. https://doi.org/10.1038/s41538-025-00414-x.

(24) Leclere, L.; Cutsem, P. Van; Michiels, C. Anti-Cancer Activities of PH- or Heat-Modified Pectin. *Front Pharmacol* 2013, *4*, 128. https://doi.org/10.3389/fphar.2013.00128.

(25) Amos, R. A.; Atmodjo, M. A.; Huang, C.; Gao, Z.; Venkat, A.; Taujale, R.; Kannan, N.; Moremen, K. W.; Mohnen, D. Polymerization of the Backbone of the Pectic Polysaccharide Rhamnogalacturonan I. *Nat Plants* 2022, *8* (11), 1289–1303. https://doi.org/10.1038/s41477-022-01270-3.

(26) Einhorn-Stoll, U. Pectin-Water Interactions in Foods – From Powder to Gel. *Food Hydrocoll* 2018, *78*, 109–119. https://doi.org/10.1016/j.foodhyd.2017.05.029.

(27) Rumpf, J.; Do, X. T.; Burger, R.; Monakhova, Y.; Schulze, M. Types of Lignin, Properties, and Structural Characterization Techniques. In *Lignin-Based Materials for Biomedical Applications*; Elsevier, 2021; pp 105–158. https://doi.org/10.1016/B978-0-12-820303-3.00001-1.

(28) Li, W.; Chen, H.; Xu, B.; Wang, Y.; Zhang, C.; Cao, Y.; Xing, X. Research Progress on Classification, Sources and Functions of Dietary Polyphenols for Prevention and Treatment of Chronic Diseases. *Journal of Future Foods* 2023, *3* (4), 289–305. https://doi.org/10.1016/j.jfutfo.2023.03.001.

(29) Shen, N.; Wang, T.; Gan, Q.; Liu, S.; Wang, L.; Jin, B. Plant Flavonoids: Classification, Distribution, Biosynthesis, and Antioxidant Activity. *Food Chem* 2022, *383*, 132531. https://doi.org/10.1016/j.foodchem.2022.132531.

(30) Hano, C.; Tungmunnithum, D. Plant Polyphenols, More than Just Simple Natural Antioxidants: Oxidative Stress, Aging and Age-Related Diseases. *Medicines* 2020, *7* (5), 26. https://doi.org/10.3390/medicines7050026.

(31) Zhang, B.; Biswal, B. K.; Zhang, J.; Balasubramanian, R. Hydrothermal Treatment of Biomass Feedstocks for Sustainable Production of Chemicals, Fuels, and Materials: Progress and Perspectives. *Chem Rev* 2023, *123* (11), 7193–7294. https://doi.org/10.1021/acs.chemrev.2c00673.

(32) Byrappa, K.; Yoshimura, M. *Handbook of Hydrothermal Technology*; Elsevier, 2013. https://doi.org/10.1016/C2009-0-20354-0.

(33) McCollom, T. M.; Seewald, J. S. Abiotic Synthesis of Organic Compounds in Deep-Sea Hydrothermal Environments. *Chem Rev* 2007, *107* (2), 382–401. https://doi.org/10.1021/cr0503660.

(34) Dong, X.; Greening, C.; Rattray, J. E.; Chakraborty, A.; Chuvochina, M.; Mayumi, D.; Dolfing, J.; Li, C.; Brooks, J. M.; Bernard, B. B.; Groves, R. A.; Lewis, I. A.; Hubert, C. R. J. Metabolic Potential of Uncultured Bacteria and Archaea Associated with Petroleum Seepage in Deep-Sea Sediments. *Nat Commun* 2019, *10* (1), 1816. https://doi.org/10.1038/s41467-019-09747-0.

(35) *Application of Hydrothermal Reactions to Biomass Conversion*; Jin, F., Ed.; Springer Berlin Heidelberg: Berlin, Heidelberg, 2014. https://doi.org/10.1007/978-3-642-54458-3.

(36) Gao, Y.; Remón, J.; Matharu, A. S. Microwave-Assisted Hydrothermal Treatments for Biomass Valorisation: A Critical Review. *Green Chemistry* 2021, *23* (10), 3502–3525. https://doi.org/10.1039/d1gc00623a.

(37) Tsubaki, S.; Azuma, J. ichi; Fujii, S.; Singh, R.; Thallada, B.; Wada, Y. Microwave-Driven Biorefinery for Utilization of Food and Agricultural Waste Biomass. In *Waste Biorefinery: Potential and Perspectives*; Elsevier, 2018; pp 393–408. https://doi.org/10.1016/B978-0-444-63992-9.00013-6.

(38) United Nations Environment Programme (UNEP). *Food Waste Index Report 2024. Think Eat Save: Tracking Progress to Halve Global Food Waste*; 2024. https://wedocs.unep.org/20.500.11822/45230 (accessed 2025-09-19).

(39) Kierońska, E.; Skoczylas, J.; Dziadek, K.; Pomietło, U.; Piątkowska, E.; Kopeć, A. Basic Chemical Composition, Selected Polyphenolic Profile and Antioxidant Activity in

Various Types of Currant (Ribes Spp.) Fruits. *Applied Sciences* 2024, *14* (19), 8882. https://doi.org/10.3390/app14198882.

(40) Food and Agriculture Organization Statistical Database (FAOSTAT). *Crops and livestock products*. https://www.fao.org/faostat/en/#data/QCL/visualize (accessed 2025-09-19).

(41) International Blackcurrant Association (IBA). *Global Blackcurrant Production Statistics 2020 - 2024*. https://www.blackcurrant-iba.com/agronomy/blackcurrant-statistics/ (accessed 2025-09-19).

(42) Cortez, R. E.; Gonzalez de Mejia, E. Blackcurrants (Ribes Nigrum): A Review on Chemistry, Processing, and Health Benefits. *J Food Sci* 2019, *84* (9), 2387–2401. https://doi.org/10.1111/1750-3841.14781.

(43) Wądrzyk, M.; Plata, M.; Korzeniowski, Ł.; Janus, R.; Lewandowski, M. Towards Sustainable Valorization of Blackcurrant Pomace: Investigation of Hot-Water Extraction Combined with Hydrothermal Liquefaction. *Renew Energy* 2025, *240*, 122117. https://doi.org/10.1016/j.renene.2024.122117.

(44) Laaksonen, O. A.; Mäkilä, L.; Sandell, M. A.; Salminen, J. P.; Liu, P.; Kallio, H. P.; Yang, B. Chemical-Sensory Characteristics and Consumer Responses of Blackcurrant Juices Produced by Different Industrial Processes. *Food Bioproc Tech* 2014, *7* (10), 2877–2888. https://doi.org/10.1007/s11947-014-1316-8.

(45) Vorobyova, V.; Skiba, M.; Vasyliev, G.; Chygyrynets, O. Component Composition and Antioxidant Activity of the Blackcurrant (Ribesnigrum L.) and Apricot Pomace (Prunusarmeniaca L.) Extracts. *Journal of Chemical Technology and Metallurgy* 2021, *56* (4), 710–719.

(46) Cîrstea, N.; Nour, V.; Corbu, A. R.; Codină, G. G. Blackcurrant Pomace Extract as a Natural Antioxidant in Vienna Sausages Reformulated by Replacement of Pork Backfat with Emulsion Gels Based on High Oleic Sunflower and Flaxseed Oils. *Gels* 2024, *10* (8), 534. https://doi.org/10.3390/gels10080534.

(47) Maryam Adilah, Z. A.; Nur Hanani, Z. A.; Ezzat, M. A.; Nor Asma, A. R.; Noranizan, M. A. Impact of Ultrasound-Assisted Extraction on Physical Properties, Antioxidant Activity, and Colorimetric PH-Response of Blackcurrant Pomace Extract. *ACS Food Science and Technology* 2024, *4* (11), 2645–2654. https://doi.org/10.1021/acsfoodscitech.4c00486.

(48) Pocevičienė, I.; Jūrienė, L.; Pukalskienė, M.; Baranauskienė, R.; Venskutonis, P. R. Supercritical CO2 Separation of Lipids from Mechanically Pre-Fractionated Black Currant Pomace: Chemical Composition, Bioactivities and Application Perspectives. *Sep Purif Technol* 2025, *373*, 133641. https://doi.org/10.1016/j.seppur.2025.133641.

(49) Déniel, M.; Haarlemmer, G.; Roubaud, A.; Weiss-Hortala, E.; Fages, J. Bio-Oil Production from Food Processing Residues: Improving the Bio-Oil Yield and Quality by Aqueous Phase Recycle in Hydrothermal Liquefaction of Blackcurrant (Ribes Nigrum L.) Pomace. *Energy and Fuels* 2016, *30* (6), 4895–4904. https://doi.org/10.1021/acs.energyfuels.6b00441.

(50) Wądrzyk, M.; Plata, M.; Zaborowska, K.; Janus, R.; Lewandowski, M. Py-GC-MS Study on Catalytic Pyrolysis of Biocrude Obtained via HTL of Fruit Pomace. *Energies (Basel)* 2021, *14* (21), 7288. https://doi.org/10.3390/en14217288.

(51) Wądrzyk, M.; Korzeniowski, Ł.; Plata, M.; Janus, R.; Lewandowski, M.; Borówka, G.; Maziarka, P. Solvothermal Liquefaction of Blackcurrant Pomace in the Water-Monohydroxy Alcohol Solvent System. *Energies (Basel)* 2023, *16* (3), 1127. https://doi.org/10.3390/en16031127.

(52) Wądrzyk, M.; Korzeniowski, Ł.; Plata, M.; Janus, R.; Lewandowski, M.; Michalik, M.; Magdziarz, A. Pyrolysis of Hydrochars Obtained from Blackcurrant Pomace in Single and Binary Solvent Systems. *Renew Energy* 2023, *214*, 383–394. https://doi.org/https://doi.org/10.1016/j.renene.2023.06.018.

(53) Alba, K.; MacNaughtan, W.; Laws, A. P.; Foster, T. J.; Campbell, G. M.; Kontogiorgos, V. Fractionation and Characterisation of Dietary Fibre from Blackcurrant Pomace. *Food Hydrocoll* 2018, *81*, 398–408. https://doi.org/10.1016/j.foodhyd.2018.03.023.

(54) Ćorović, M.; Petrov Ivanković, A.; Milivojević, A.; Veljković, M.; Simović, M.; López-Revenga, P.; Montilla, A.; Moreno, F. J.; Bezbradica, D. Valorisation of Blackcurrant Pomace by Extraction of Pectin-Rich Fractions: Structural Characterization and Evaluation as Multifunctional Cosmetic Ingredient. *Polymers (Basel)* 2024, *16* (19), 2779. https://doi.org/10.3390/polym16192779.

(55) Gomes, M. G.; Paranhos, A. G. de O.; Camargos, A. B.; Baêta, B. E. L.; Baffi, M. A.; Gurgel, L. V. A.; Pasquini, D. Pretreatment of Sugarcane Bagasse with Dilute Citric Acid and Enzymatic Hydrolysis: Use of Black Liquor and Solid Fraction for Biogas Production. *Renew Energy* 2022, *191*, 428–438. https://doi.org/https://doi.org/10.1016/j.renene.2022.04.057.

(56) Bittencourt, G. A.; de Souza Vandenberghe, L. P.; Valladares-Diestra, K. K.; Soccol, C. R. Soybean Hull Valorization for Sugar Production through the Optimization of Citric Acid Pretreatment and Enzymatic Hydrolysis. *Ind Crops Prod* 2022, *186*, 115178. https://doi.org/https://doi.org/10.1016/j.indcrop.2022.115178.

(57) Song, S.; Su, D.; Xu, X.; Yang, X.; Wei, L.; Li, K.; Shao, G.; An, Q.; Zhai, S.; Liu, N. Using Citric Acid to Suppress Lignin Repolymerization in the Organosolv Pretreatment of Corn Stalk. *Ind Crops Prod* 2023, *200*, 116881. https://doi.org/https://doi.org/10.1016/j.indcrop.2023.116881.

(58) Rodríguez-Machín, L.; Arteaga-Pérez, L. E.; Pérez-Bermúdez, R. A.; Casas-Ledón, Y.; Prins, W.; Ronsse, F. Effect of Citric Acid Leaching on the Demineralization and Thermal Degradation Behavior of Sugarcane Trash and Bagasse. *Biomass Bioenergy* 2018, *108*, 371–380. https://doi.org/10.1016/j.biombioe.2017.11.001.

(59) De Melo, E. M.; Clark, J. H.; Matharu, A. S. The Hy-MASS Concept: Hydrothermal Microwave Assisted Selective Scissoring of Cellulose for: In Situ Production of (Meso)Porous Nanocellulose Fibrils and Crystals. *Green Chemistry* 2017, *19* (14), 3408–3417. https://doi.org/10.1039/c7gc01378g.

(60) Gao, Y.; Xia, H.; Sulaeman, A. P.; De Melo, E. M.; Dugmore, T. I. J.; Matharu, A. S. Defibrillated Celluloses via Dual Twin-Screw Extrusion and Microwave Hydrothermal Treatment of Spent Pea Biomass. *ACS Sustain Chem Eng* 2019, *7* (13), 11861–11871. https://doi.org/10.1021/acssuschemeng.9b02440.

(61) Xia, H.; Houghton, J. A.; Clark, J. H.; Matharu, A. S. Potential Utilization of Unavoidable Food Supply Chain Wastes-Valorization of Pea Vine Wastes. *ACS Sustain Chem Eng* 2016, *4* (11), 6002–6009. https://doi.org/10.1021/acssuschemeng.6b01297.

(62) Sulaeman, A. P.; Gao, Y.; Dugmore, T.; Remón, J.; Matharu, A. S. From Unavoidable Food Waste to Advanced Biomaterials: Microfibrilated Lignocellulose Production by Microwave-Assisted Hydrothermal Treatment of Cassava Peel and Almond Hull. *Cellulose* 2021, *28* (12), 7687–7705. https://doi.org/10.1007/s10570-021-03986-5.

(63) Sójka, M.; Król, B. Composition of Industrial Seedless Black Currant Pomace. *European Food Research and Technology* 2009, *228* (4), 597–605. https://doi.org/10.1007/s00217-008-0968-x.

(64) Nawirska, A.; Kwaśniewska, M. Dietary Fibre Fractions from Fruit and Vegetable Processing Waste. *Food Chem* 2005, *91* (2), 221–225. https://doi.org/10.1016/j.foodchem.2003.10.005.

(65) Sankowski, L. V.; Morales-Medina, R.; Fula Arguello, C.; Reißner, A. M.; Struck, S.; Rohm, H.; Drusch, S.; Brückner-Gühmann, M. Thermal-Mechanical Treatment of Blackcurrant Pomace for Enrichment in Yoghurt. *Food Hydrocoll* 2024, *146*, 109296. https://doi.org/10.1016/j.foodhyd.2023.109296.

(66) Jakobsdottir, G.; Nilsson, U.; Blanco, N.; Sterner, O.; Nyman, M. Effects of Soluble and Insoluble Fractions from Bilberries, Black Currants, and Raspberries on Short-Chain Fatty Acid Formation, Anthocyanin Excretion, and Cholesterol in Rats. *J Agric Food Chem* 2014, *62* (19), 4359–4368. https://doi.org/10.1021/jf5007566.

(67) Roman-Benn, A.; Contador, C. A.; Li, M. W.; Lam, H. M.; Ah-Hen, K.; Ulloa, P. E.; Ravanal, M. C. Pectin: An Overview of Sources, Extraction and Applications in Food Products, Biomedical, Pharmaceutical and Environmental Issues. *Food Chemistry Advances* 2023, *2*, 100192. https://doi.org/10.1016/j.focha.2023.100192.

(68) Salleh, N.; Goh, K. K. T.; Sims, I. M.; Bell, T. J.; Huffman, L. M.; Weeks, M.; Matia-Merino, L. Characterization of Anthocyanin-Bound Pectin-Rich Fraction Extracted from New Zealand Blackcurrant (Ribes Nigrum) Juice. *ACS Food Science and Technology* 2021, *1* (6), 1130–1142. https://doi.org/10.1021/acsfoodscitech.0c00128.

(69) Pancerz, M.; Kruk, J.; Witek, M.; Ptaszek, A. The Effect of Biopolymer-Water Interaction on Relaxation Phenomena in Blackcurrant Pectin Solutions. *Food Chem* 2022, *383*, 132600. https://doi.org/10.1016/j.foodchem.2022.132600.

(70) Romruen, O.; Kaewprachu, P.; Karbowiak, T.; Rawdkuen, S. Isolation and Characterization Cellulose Nanosphere from Different Agricultural By-Products. *Polymers (Basel)* 2022, *14* (13), 2534. https://doi.org/10.3390/polym14132534.

(71) Dai, H.; Ou, S.; Huang, Y.; Huang, H. Utilization of Pineapple Peel for Production of Nanocellulose and Film Application. *Cellulose* 2018, *25* (3), 1743–1756. https://doi.org/10.1007/s10570-018-1671-0.

(72) Tanpichai, S.; Witayakran, S.; Boonmahitthisud, A. Study on Structural and Thermal Properties of Cellulose Microfibers Isolated from Pineapple Leaves Using Steam Explosion. *J Environ Chem Eng* 2019, *7* (1), 102836. https://doi.org/https://doi.org/10.1016/j.jece.2018.102836.

(73) Jilani, S. B.; Olson, D. G. Mechanism of Furfural Toxicity and Metabolic Strategies to Engineer Tolerance in Microbial Strains. *Microb Cell Fact* 2023, *22* (1), 221. https://doi.org/10.1186/s12934-023-02223-x.

(74) Gao, Y.; Ozel, M. Z.; Dugmore, T.; Sulaeman, A.; Matharu, A. S. A Biorefinery Strategy for Spent Industrial Ginger Waste. *J Hazard Mater* 2021, *401*, 123400. https://doi.org/10.1016/j.jhazmat.2020.123400.

(75) Cao, L.; Park, Y.; Lee, S.; Kim, D. O. Extraction, Identification, and Health Benefits of Anthocyanins in Blackcurrants (Ribes Nigrum l.). *Applied Sciences* 2021, *11* (4), 1863. https://doi.org/10.3390/app11041863.

(76) Kruszewski, B.; Boselli, E. Blackcurrant Pomace as a Rich Source of Anthocyanins: Ultrasound-Assisted Extraction under Different Parameters. *Applied Sciences* 2024, *14* (2), 821. https://doi.org/10.3390/app14020821.

(77) Ejaz, A.; Waliat, S.; Afzaal, M.; Saeed, F.; Ahmad, A.; Din, A.; Ateeq, H.; Asghar, A.; Shah, Y. A.; Rafi, A.; Khan, M. R. Biological Activities, Therapeutic Potential, and Pharmacological Aspects of Blackcurrants (Ribes Nigrum L): A Comprehensive Review. *Food Sci Nutr* 2023, *11* (10), 5799–5817. https://doi.org/10.1002/fsn3.3592.

(78) Nour, V.; Stampar, F.; Veberic, R.; Jakopic, J. Anthocyanins Profile, Total Phenolics and Antioxidant Activity of Black Currant Ethanolic Extracts as Influenced by Genotype and Ethanol Concentration. *Food Chem* 2013, *141* (2), 961–966. https://doi.org/10.1016/j.foodchem.2013.03.105.

(79) Azman, E. M.; Charalampopoulos, D.; Chatzifragkou, A. Acetic Acid Buffer as Extraction Medium for Free and Bound Phenolics from Dried Blackcurrant (Ribes Nigrum L.) Skins. *J Food Sci* 2020, *85* (11), 3745–3755. https://doi.org/10.1111/1750-3841.15466.

(80) Azman, E. M.; Nor, N. D. M.; Charalampopoulos, D.; Chatzifragkou, A. Effect of Acidified Water on Phenolic Profile and Antioxidant Activity of Dried Blackcurrant (Ribes Nigrum L.) Pomace Extracts. *LWT* 2022, *154*, 112733. https://doi.org/10.1016/j.lwt.2021.112733.

(81) Oancea, S.; Ghincevici, D.; Ketney, O. The Effect of Ultrasonic Pretreatment and Sample Preparation on the Extraction Yield of Antioxidant Compounds and Activity of Black Currant Fruits. *Acta Chim Slov* 2015, *62* (1), 242–248. https://doi.org/10.17344/acsi.2014.895.

(82) Khalaf, D.; Pradal, D.; Dimitrov, K. Multi-Criteria Optimization Including Environmental Impacts of Ultrasound-Assisted Extraction of Phenolic Antioxidants from Blackcurrant Pomace by-Product. *Chemical Engineering and Processing - Process Intensification* 2024, *204*, 109935. https://doi.org/10.1016/j.cep.2024.109935.

(83) Piasecka, I.; Brzezińska, R.; Kalisz, S.; Wiktor, A.; Górska, A. Recovery of Antioxidants and Oils from Blackcurrant and Redcurrant Wastes by Ultrasound-Assisted Extraction. *Food Biosci* 2024, *57*, 103511. https://doi.org/10.1016/j.fbio.2023.103511.

(84) Pap, N.; Beszédes, S.; Pongrácz, E.; Myllykoski, L.; Gábor, M.; Gyimes, E.; Hodúr, C.; Keiski, R. L. Microwave-Assisted Extraction of Anthocyanins from Black Currant Marc. *Food Bioproc Tech* 2013, *6* (10), 2666–2674. https://doi.org/10.1007/s11947-012-0964-9.

(85) Landbo, A. K.; Meyer, A. S. Enzyme-Assisted Extraction of Antioxidative Phenols from Black Currant Juice Press Residues (Ribes Nigrum). *J Agric Food Chem* 2001, *49* (7), 3169–3177. https://doi.org/10.1021/jf001443p.

(86) Landbo, A. K.; Meyer, A. S. Effects of Different Enzymatic Maceration Treatments on Enhancement of Anthocyanins and Other Phenolics in Black Currant Juice. *Innovative Food Science and Emerging Technologies* 2004, *5* (4), 503–513. https://doi.org/10.1016/j.ifset.2004.08.003.

(87) Gagneten, M.; Leiva, G.; Salvatori, D.; Schebor, C.; Olaiz, N. Optimization of Pulsed Electric Field Treatment for the Extraction of Bioactive Compounds from Blackcurrant. *Food Bioproc Tech* 2019, *12* (7), 1102–1109. https://doi.org/10.1007/s11947-019-02283-1.

(88) Li, X.; Chen, F.; Li, S.; Jia, J.; Gu, H.; Yang, L. An Efficient Homogenate-Microwave-Assisted Extraction of Flavonols and Anthocyanins from Blackcurrant Marc: Optimization Using Combination of Plackett-Burman Design and Box-Behnken Design. *Ind Crops Prod* 2016, *94*, 834–847. https://doi.org/10.1016/j.indcrop.2016.09.063.

(89) Gong, Z.; Su, L. Y. F.; Zhang, J. S.; Chen, T.; Wang, Y. C. Understanding the Association between Date Labels and Consumer-Level Food Waste. *Food Qual Prefer* 2022, *96*, 104373. https://doi.org/10.1016/j.foodqual.2021.104373.

(90) U.S. Food and Drug Administration (FDA). *How to Cut Food Waste and Maintain Food Safety*; 2019. https://www.fda.gov/media/101389/download (accessed 2025-12-19).

(91) Meng, Y.; Luo, H.; Dong, C.; Zhang, C.; He, Z.; Long, Z.; Cha, R. Hydroxypropyl Guar/Cellulose Nanocrystal Film with Ionic Liquid and Anthocyanin for Real-Time and Visual Detection of NH3. *ACS Sustain Chem Eng* 2020, *8* (26), 9731–9741. https://doi.org/10.1021/acssuschemeng.0c01833.

(92) Komitopoulou, E. Microbial and chemical Markers of meat Spoilage. *International Meat Topics* 2012, *3* (3), 23–25.

(93) Her, J. Y.; Cho, H.; Kim, M. K.; Lee, K. G. Organic Acids as a Freshness Indicator for Tofu (Soybean Curd). *J Food Sci Technol* 2017, *54* (11), 3443–3450. https://doi.org/10.1007/s13197-017-2799-x.

(94) Teigiserova, D. A.; Hamelin, L.; Thomsen, M. Review of High-Value Food Waste and Food Residues Biorefineries with Focus on Unavoidable Wastes from Processing. *Resour Conserv Recycl* 2019, *149*, 413–426. https://doi.org/10.1016/j.resconrec.2019.05.003.

(95) You, P.; Wang, L.; Zhou, N.; Yang, Y.; Pang, J. A PH-Intelligent Response Fish Packaging Film: Konjac Glucomannan/Carboxymethyl Cellulose/Blackcurrant Anthocyanin Antibacterial Composite Film. *Int J Biol Macromol* 2022, *204*, 386–396. https://doi.org/10.1016/j.ijbiomac.2022.02.027.

(96) Yar, M. S.; Ibeogu, I. H.; Bako, H. K.; Alnadari, F.; Bilal, M.; Rehman, F.; Zhu, J.; Zhou, T.; Zhao, Z.; Li, C. A Novel Carboxymethyl Cellulose/Gum Xanthan and Citric Acid-Based Film That Enhances the Precision of Blackcurrant Anthocyanin-Induced Color Detection for Beef Spoilage Tracking. *Food Chem* 2024, *461*, 140905. https://doi.org/10.1016/j.foodchem.2024.140905.

(97) En, C. L.; Nawawi, N. I. M.; Ijod, G.; Hasanah, N. N.; Zainal Abedin, N. H.; Rahman, Q.; Mohammad Rashedi, I. F.; Mohamad Azman, E. Potato Starch/Agar-Based Intelligent Films Infused with Dried Blackcurrant Pomace Anthocyanins for Freshness Monitoring of Freshwater Prawns. *Int Food Res J* 2025, *32* (3), 762–775. https://doi.org/10.47836/ifrj.32.3.11.

(98) Kurek, M.; Benbettaieb, N.; Ščetar, M.; Chaudy, E.; Repajić, M.; Klepac, D.; Valić, S.; Debeaufort, F.; Galić, K. Characterization of Food Packaging Films with Blackcurrant Fruit Waste as a Source of Antioxidant and Color Sensing Intelligent Material. *Molecules* 2021, *26* (9), 2569. https://doi.org/10.3390/molecules26092569.

(99) Pakulska, A.; Bartosiewicz, E.; Galus, S. The Potential of Apple and Blackcurrant Pomace Powders as the Components of Pectin Packaging Films. *Coatings* 2023, *13* (8), 1409. https://doi.org/10.3390/coatings13081409.

(100) Matharu, A. S.; Houghton, J. A.; Lucas-Torres, C.; Moreno, A. Acid-Free Microwave-Assisted Hydrothermal Extraction of Pectin and Porous Cellulose from Mango Peel Waste-towards a Zero Waste Mango Biorefinery. *Green Chemistry* 2016, *18* (19), 5280–5287. https://doi.org/10.1039/c6gc01178k.

(101) Alchera, F.; Ginepro, M.; Giacalone, G. Microwave-Assisted Extraction of Polyphenols from Blackcurrant By-Products and Possible Uses of the Extracts in Active Packaging. *Foods* 2022, *11* (18), 2727. https://doi.org/10.3390/foods11182727.

(102) Wang, Q.; Jiang, Y.; Chen, W.; Julian McClements, D.; Ma, C.; Liu, X.; Liu, F. Development of PH-Responsive Active Film Materials Based on Purple Corncob and Its Application in Meat Freshness Monitoring. *Food Research International* 2022, *161*, 111832. https://doi.org/10.1016/j.foodres.2022.111832.

(103) Nešić, A.; Onjia, A.; Davidović, S.; Dimitrijević, S.; Errico, M. E.; Santagata, G.; Malinconico, M. Design of Pectin-Sodium Alginate Based Films for Potential Healthcare Application: Study of Chemico-Physical Interactions between the Components of Films and Assessment of Their Antimicrobial Activity. *Carbohydr Polym* 2017, *157*, 981–990. https://doi.org/10.1016/j.carbpol.2016.10.054.

(104) Janik, W.; Nowotarski, M.; Ledniowska, K.; Shyntum, D. Y.; Krukiewicz, K.; Turczyn, R.; Sabura, E.; Furgoł, S.; Kudła, S.; Dudek, G. Modulation of Physicochemical Properties and Antimicrobial Activity of Sodium Alginate Films through the Use of Chestnut Extract and Plasticizers. *Sci Rep* 2023, *13* (1), 11530. https://doi.org/10.1038/s41598-023-38794-3.

(105) Khalil, H. P. S. A.; Tye, Y. Y.; Chow, S. T.; Saurabh, C. K.; Tahir, P. M.; Dungani, R.; Syakir, M. I. Cellulosic Pulp Fiber as Reinforcement Materials In-Based Film. *Bioresources* 2017, *12* (1), 29–42.

(106) Gohil, R. M. Synergistic Blends of Natural Polymers, Pectin and Sodium Alginate. *J Appl Polym Sci* 2011, *120* (4), 2324–2336. https://doi.org/10.1002/app.33422.

(107) Rezvanian, M.; Ahmad, N.; Mohd Amin, M. C. I.; Ng, S. F. Optimization, Characterization, and in Vitro Assessment of Alginate-Pectin Ionic Cross-Linked Hydrogel Film for Wound Dressing Applications. *Int J Biol Macromol* 2017, *97*, 131–140. https://doi.org/10.1016/j.ijbiomac.2016.12.079.

(108) Lei, Y.; Yao, Q.; Jin, Z.; Wang, Y. C. Intelligent Films Based on Pectin, Sodium Alginate, Cellulose Nanocrystals, and Anthocyanins for Monitoring Food Freshness. *Food Chem* 2023, *404*, 134528. https://doi.org/10.1016/j.foodchem.2022.134528.

(109) Procopio, F. R.; Ferraz, M. C.; Paulino, B. N.; do Amaral Sobral, P. J.; Hubinger, M. D. Spice Oleoresins as Value-Added Ingredient for Food Industry: Recent Advances and Perspectives. *Trends Food Sci Technol* 2022, *122*, 123–139. https://doi.org/10.1016/j.tifs.2022.02.010.

(110) Shukla, A.; Naik, S. N.; Goud, V. V.; Das, C. Supercritical CO2 Extraction and Online Fractionation of Dry Ginger for Production of High-Quality Volatile Oil and Gingerols Enriched Oleoresin. *Ind Crops Prod* 2019, *130*, 352–362. https://doi.org/10.1016/j.indcrop.2019.01.005.

(111) Das, S.; Das, A. K.; Manda, S. C. Evaluation of Antimicrobial Activities of Various Solvent Extracts of Ginger Rhizome Peels and Whole Ginger Rhizome without Peels. *World J Pharm Res* 2017, *6*, 1450–1468. https://doi.org/10.20959/wjpr201716-10322.

(112) The Centre for the Promotion of Imports (CBI). *The European market potential for ginger*. https://www.cbi.eu/market-information/fresh-fruit-vegetables/ginger/market-potential#which-trends-offer-opportunities-or-pose-threats-in-the-european-ginger-market (accessed 2025-10-29).

(113) Konar, E. M.; Harde, S. M.; Kagliwal, L. D.; Singhal, R. S. Value-Added Bioethanol from Spent Ginger Obtained after Oleoresin Extraction. *Ind Crops Prod* 2013, *42* (1), 299–307. https://doi.org/10.1016/j.indcrop.2012.05.040.

(114) Yu, H.; Cao, Y.; Li, H.; Zhao, G.; Zhang, X.; Cheng, S.; Wei, W. An Efficient Heterogeneous Acid Catalyst Derived from Waste Ginger Straw for Biodiesel Production. *Renew Energy* 2021, *176*, 533–542. https://doi.org/10.1016/j.renene.2021.05.098.

(115) Chen, X.; Chen, G.; Wang, Z.; Kan, J. A Comparison of a Polysaccharide Extracted from Ginger (Zingiber Officinale) Stems and Leaves Using Different Methods: Preparation, Structure Characteristics, and Biological Activities. *Int J Biol Macromol* 2020, *151*, 635–649. https://doi.org/10.1016/j.ijbiomac.2020.02.222.

(116) Chen, X.; Wang, Z.; Kan, J. Polysaccharides from Ginger Stems and Leaves: Effects of Dual and Triple Frequency Ultrasound Assisted Extraction on Structural Characteristics and Biological Activities. *Food Biosci* 2021, *42*, 101166. https://doi.org/10.1016/j.fbio.2021.101166.

(117) Zendrato, H. M.; Devi, Y. S.; Masruchin, N.; Wistara, N. J. Soda Pulping of Torch Ginger Stem: Promising Source of Nonwood-Based Cellulose. *Journal of the Korean Wood Science and Technology* 2021, *49* (4), 287–298. https://doi.org/10.5658/WOOD.2021.49.4.287.

(118) Zabot, G. L. Decaffeination Using Supercritical Carbon Dioxide. In *Green Sustainable Process for Chemical and Environmental Engineering and Science: Supercritical Carbon Dioxide as Green Solvent*; Elsevier, 2019; pp 255–278. https://doi.org/10.1016/B978-0-12-817388-6.00011-8.

(119) Nozari, B.; Kander, R. Supercritical CO2 Technology for Biomass Extraction: Review. *Ind Crops Prod* 2025, *233*, 121348. https://doi.org/10.1016/j.indcrop.2025.121348.

(120) Duba, K. S.; Fiori, L. Supercritical CO2 Extraction of Grape Seed Oil: Effect of Process Parameters on the Extraction Kinetics. *Journal of Supercritical Fluids* 2015, *98*, 33–43. https://doi.org/10.1016/j.supflu.2014.12.021.

(121) Li, J. huan; Huang, Z.; Wei, J. lin; Xu, L. A New Optimization Method for Parameter Determination in Modeling Solid Solubility in Supercritical CO2. *Fluid Phase Equilib* 2013, *344*, 117–124. https://doi.org/10.1016/j.fluid.2013.01.028.

(122) Spyrou, A.; Batista, M. G. F.; Corazza, M. L.; Papadaki, M.; Antonopoulou, M. Extraction of High Value Products from Zingiber Officinale Roscoe (Ginger) and Utilization of Residual Biomass. *Molecules* 2024, *29* (4), 871. https://doi.org/10.3390/molecules29040871.

(123) Ko, M. J.; Nam, H. H.; Chung, M. S. Conversion of 6-Gingerol to 6-Shogaol in Ginger (Zingiber Officinale) Pulp and Peel during Subcritical Water Extraction. *Food Chem* 2019, *270*, 149–155. https://doi.org/10.1016/j.foodchem.2018.07.078.

(124) Yingngam, B.; Brantner, A. Boosting the Essential Oil Yield from the Rhizomes of Cassumunar Ginger by an Eco-Friendly Solvent-Free Microwave Extraction Combined with Central Composite Design. *Journal of Essential Oil Research* 2018, *30* (6), 409–420. https://doi.org/10.1080/10412905.2018.1503099.

(125) Argo, B. D.; Hermanto, M. B.; Andriani, D. W.; Rosadhani, J. S. The Effect of Ginger Oil Extraction Using Microwave Assisted Hydro-Distillation (MAHD) Method on Zingiberene Content. In *IOP Conference Series: Earth and Environmental Science*; Institute of Physics Publishing, 2020; Vol. 542. https://doi.org/10.1088/1755-1315/542/1/012002.

(126) Guo, J. B.; Fan, Y.; Zhang, W. J.; Wu, H.; Du, L. M.; Chang, Y. X. Extraction of Gingerols and Shogaols from Ginger (Zingiber Officinale Roscoe) through Microwave Technique Using Ionic Liquids. *Journal of Food Composition and Analysis* 2017, *62*, 35–42. https://doi.org/10.1016/j.jfca.2017.04.014.

(127) Gonzalez-Gonzalez, M.; Yerena-Prieto, B. J.; Carrera, C.; Vázquez-Espinosa, M.; González-de-Peredo, A. V.; García-Alvarado, M. Á.; Palma, M.; Rodríguez-Jimenes, G. del C.; Barbero, G. F. Optimization of an Ultrasound-Assisted Extraction Method for the Extraction of Gingerols and Shogaols from Ginger (Zingiber Officinale). *Agronomy* 2023, *13* (7), 1787. https://doi.org/10.3390/agronomy13071787.

(128) Alqahtani, N. K.; Salih, Z. A.; Asiri, S. A.; Siddeeg, A.; Elssiddiq, S. A. D.; Alnemr, T. M.; Habib, H. M. Optimizing Physicochemical Properties, Antioxidant Potential, and Antibacterial Activity of Dry Ginger Extract Using Sonication Treatment. *Heliyon* 2024, *10* (16), e36473. https://doi.org/10.1016/j.heliyon.2024.e36473.

(129) Žitek, T.; Kučuk, N.; Postružnik, V.; Leitgeb, M.; Knez, Ž.; Primožič, M.; Marevci, M. K. Synergistic Effect of Supercritical and Ultrasound-Assisted Ginger (Zingiber Officinale Roscoe) Extracts. *Plants* 2022, *11* (21), 2872. https://doi.org/10.3390/plants11212872.

(130) Nurul, I.; Maulana Alif, G.; Rohmatul, F.; Andesra, Z. Optimization of Emprit Ginger Oil Yield through Operating Temperature with Microwave Ultrasonic Steam Diffusion Method. *Journal of Applied Sciences, Management and Engineering Technology* 2021, *2* (2), 83–89.

(131) Drinić, Z.; Jovanović, M.; Pljevljakušić, D.; Čujić-Nikolić, N.; Bigović, D.; Šavikin, K. Microwave-Assisted Extraction of Essential Oil from Ginger (Zingiber Officinale Rosc.). *Lekovite sirovine* 2021, *41* (1), 22–27. https://doi.org/10.5937/leksir2141022d.

(132) Chen, P.; Yang, Q.; Zhang, L.; Zhong, R.; Cao, Y.; Miao, J. Ginger Essential Oil Extracted by Low-Temperature Continuous Phase Transition and Its Preservation Effect on Prepared Duck Meat. *Food Bioproc Tech* 2025, *18* (3), 2806–2819. https://doi.org/10.1007/s11947-024-03643-2.

(133) Handayani, D.; Amalia, R.; Endy Yulianto, M.; Hartati, I.; Murni. Determination of Influential Factors during Enzymatic Extraction of Ginger Oil Using Immobile Isolated Cow Rumen Enzymes. *International Journal of Technology* 2018, *9* (3), 455–463. https://doi.org/10.14716/ijtech.v9i3.489.

(134) Kumar, M.; Tomar, M.; Potkule, J.; Verma, R.; Punia, S.; Mahapatra, A.; Belwal, T.; Dahuja, A.; Joshi, S.; Berwal, M. K.; Satankar, V.; Bhoite, A. G.; Amarowicz, R.; Kaur, C.; Kennedy, J. F. Advances in the Plant Protein Extraction: Mechanism and

Recommendations. *Food Hydrocoll* 2021, *115*, 106595. https://doi.org/10.1016/j.foodhyd.2021.106595.

(135) Thompson, E. H.; Wolf, I. D.; Allen, C. E. Ginger Rhizome: A New Source of Proteolytic Enzyme. *J Food Sci* 1973, *38* (4), 652–655. https://doi.org/10.1111/j.1365-2621.1973.tb02836.x.

(136) Su, H. P.; Huang, M. J.; Wang, H. T. Characterization of Ginger Proteases and Their Potential as a Rennin Replacement. *J Sci Food Agric* 2009, *89* (7), 1178–1185. https://doi.org/10.1002/jsfa.3572.

(137) Huang, X. W.; Chen, L. J.; Luo, Y. B.; Guo, H. Y.; Ren, F. Z. Purification, Characterization, and Milk Coagulating Properties of Ginger Proteases. *J Dairy Sci* 2011, *94* (5), 2259–2269. https://doi.org/10.3168/jds.2010-4024.

(138) Hashim, M. M.; Mingsheng, D.; Iqbal, M. F.; Xiaohong, C. Ginger Rhizome as a Potential Source of Milk Coagulating Cysteine Protease. *Phytochemistry* 2011, *72* (6), 458–464. https://doi.org/10.1016/j.phytochem.2010.12.002.

(139) Zhang, S.; Zhang, L.; Wang, S.; Zhou, Y. Comparison of Plant-Origin Proteases and Ginger Extract on Quality Properties of Beef Rump Steaks. *Food Sci Technol Res* 2019, *25* (4), 529–538. https://doi.org/10.3136/fstr.25.529.

(140) Wang, H.; Ng, T. B. An Antifungal Protein from Ginger Rhizomes. *Biochem Biophys Res Commun* 2005, *336* (1), 100–104. https://doi.org/10.1016/j.bbrc.2005.08.058.

(141) Sultan, A.; Aziz, T.; Islam, Z.; Uzair, M. S.; Alhindary, I. A.; Khan, R. U.; Tiwari, R. Effect of Ginger-Based Zingibain Enzyme on Growth and Intestinal Health in Japanese Quails. *Arch Anim Breed* 2024, *67* (4), 571–581. https://doi.org/10.5194/aab-67-571-2024.

(142) Khan, A.; Sultan, A.; Islam, Z.; Uzair, M. S.; Alhidary, I. A.; Khan, R. U.; Naz, S.; Momand, N. K.; Tiwari, R. Optimising Growth Performance, Nutrients Digestibility, Immunity and Gut Health in Broilers through Ginger-Derived Phyto-Protease Enzyme (Zingibain) Supplementation. *Ital J Anim Sci* 2024, *23* (1), 1695–1703. https://doi.org/10.1080/1828051X.2024.2416586.

(143) Uzair, M. S.; Sultan, A.; Islam, Z.; Shah, M.; Tahir, M.; Naz, S.; Alrefaei, A. F.; Adil, S.; Momand, N. K.; Khan, R. U. Efficacy of Zingibain Phyto-Protease on Growth Performance, Litter Quality and Gut Microbiota in Broilers Fed High Animal Protein Concentrates. *Ital J Anim Sci* 2025, *24* (1), 336–346. https://doi.org/10.1080/1828051X.2025.2452244.

(144) Chandran, A. S.; Suri, S.; Choudhary, P. Sustainable Plant Protein: An up-to-Date Overview of Sources, Extraction Techniques and Utilization. *Sustainable Food Technology* 2023, *1* (4), 466–483. https://doi.org/10.1039/d3fb00003f.

(145) Barrios, C.; Fernández-Delgado, M.; López-Linares, J. C.; García-Cubero, M. T.; Coca, M.; Lucas, S. A Techno-Economic Perspective on a Microwave Extraction Process for Efficient Protein Recovery from Agri-Food Wastes. *Ind Crops Prod* 2022, *186*, 115166. https://doi.org/10.1016/j.indcrop.2022.115166.

(146) Cherian, R. M.; Tharayil, A.; Varghese, R. T.; Antony, T.; Kargarzadeh, H.; Chirayil, C. J.; Thomas, S. A Review on the Emerging Applications of Nano-Cellulose as Advanced Coatings. *Carbohydr Polym* 2022, *282*, 119123. https://doi.org/10.1016/j.carbpol.2022.119123.

(147) Noremylia, M. B.; Hassan, M. Z.; Ismail, Z. Recent Advancement in Isolation, Processing, Characterization and Applications of Emerging Nanocellulose: A

Review. *Int J Biol Macromol* 2022, *206*, 954–976. https://doi.org/10.1016/j.ijbiomac.2022.03.064.

(148) Pradhan, D.; Jaiswal, A. K.; Jaiswal, S. Emerging Technologies for the Production of Nanocellulose from Lignocellulosic Biomass. *Carbohydr Polym* 2022, *285*, 119258. https://doi.org/10.1016/j.carbpol.2022.119258.

(149) Abral, H.; Ariksa, J.; Mahardika, M.; Handayani, D.; Aminah, I.; Sandrawati, N.; Pratama, A. B.; Fajri, N.; Sapuan, S. M.; Ilyas, R. A. Transparent and Antimicrobial Cellulose Film from Ginger Nanofiber. *Food Hydrocoll* 2020, *98*, 105266. https://doi.org/10.1016/j.foodhyd.2019.105266.

(150) Squinca, P.; Berglund, L.; Hanna, K.; Rakar, J.; Junker, J.; Khalaf, H.; Farinas, C. S.; Oksman, K. Multifunctional Ginger Nanofiber Hydrogels with Tunable Absorption: The Potential for Advanced Wound Dressing Applications. *Biomacromolecules* 2021, *22* (8), 3202–3215. https://doi.org/10.1021/acs.biomac.1c00215.

(151) Saedi, S.; Kim, J. T.; Lee, E. H.; Kumar, A.; Shin, G. H. Fully Transparent and Flexible Antibacterial Packaging Films Based on Regenerated Cellulose Extracted from Ginger Pulp. *Ind Crops Prod* 2023, *197*, 116554. https://doi.org/10.1016/j.indcrop.2023.116554.

(152) Tavana, S.; Riyahi, A.; Nikjoo, S.; Shafi-Moghaddam, S.; Taheri, R.; Akhavannezhad, Z.; Mokaberi, P.; Chamani, J. Synthesis and Characterization of Cellulose Nanocrystals Derived from Ginger Stick for Berberine Delivery: Exploring Interactions with Human Holo-Transferrin. *Colloid Polym Sci* 2024, *302* (10), 1617–1633. https://doi.org/10.1007/s00396-024-05297-0.

(153) Zhang, H.; Zou, P.; Yuan, F.; Yu, Z.; Huang, S.; Lu, L. Ginger Residue-Derived Nanocellulose as a Sustainable Reinforcing Agent for Composite Films. *Int J Biol Macromol* 2025, *308*, 142754. https://doi.org/10.1016/j.ijbiomac.2025.142754.

(154) Mahardika, M.; Firmanda, A.; Pratama, A. W.; Amelia, D.; Abral, H.; Fahma, F.; Ilyas, R. A.; Asyraf, M. R. M. Antimicrobial and Antioxidant of Biocomposite Food Packaging Based on Ginger Tubers (Zingiber Officinale). In *Plant Tuber and Root-Based Biocomposites: Development, Characterization, and Applications*; Elsevier, 2024; pp 39–59. https://doi.org/10.1016/B978-0-443-14126-3.00003-5.

(155) Jacob, J.; Haponiuk, J. T.; Thomas, S.; Peter, G.; Gopi, S. Use of Ginger Nanofibers for the Preparation of Cellulose Nanocomposites and Their Antimicrobial Activities. *Fibers* 2018, *6* (4), 79. https://doi.org/10.3390/fib6040079.

(156) Zhou, C.; Song, X.; Wang, S.; Chen, F. Characterization and Comparison of Cellulose Extraction from Ginger Stalk by Two Different Chemical Treatments. *PBM·Cellulose Extraction* 2017, *2* (2), 1–7.

(157) Zendrato, H. M.; Masruchin, N.; Nikmatin, S.; Wistara, N. J. Effective Cellulose Isolation from Torch Ginger Stem by Alkaline Hydrogen Peroxide – Peracetic Acid System. *Journal of Industrial and Engineering Chemistry* 2024, *131*, 376–387. https://doi.org/10.1016/j.jiec.2023.10.040.

(158) Rashwan, A. K.; Younis, H. A.; Abdelshafy, A. M.; Osman, A. I.; Eletmany, M. R.; Hafouda, M. A.; Chen, W. Plant Starch Extraction, Modification, and Green Applications: A Review. *Environ Chem Lett* 2024, *22* (5), 2483–2530. https://doi.org/10.1007/s10311-024-01753-z.

(159) Braga, M. E. M.; Moreschi, S. R. M.; Meireles, M. A. A. Effects of Supercritical Fluid Extraction on Curcuma Longa L. and Zingiber Officinale R. Starches. *Carbohydr Polym* 2006, *63* (3), 340–346. https://doi.org/10.1016/j.carbpol.2005.08.055.

(160) Madeneni, M. N.; Faiza, S.; Ramaswamy, R.; Guha, M.; Pullabhatla, S. Physico-Chemical and Functional Properties of Starch Isolated from Ginger Spent. *Starch/Staerke* 2011, *63* (9), 570–578. https://doi.org/10.1002/star.201100011.

(161) Singh, A.; Kumar, V.; Kumar, R.; Mahant, H. Valorization and Characterization of Starch from Ginger (Zingiber Officinale). *International Journal of Innovative Research in Engineering and Management* 2025, *12* (1), 66–68. https://doi.org/10.55524/ijirem.2025.12.1.10.

(162) Godiyal, S.; Nakkala, K.; Laddha, K. S. Separation of Starch from Zingiber Officinale (Ginger) and Study It's Characterization. *Int J Pharm Sci Res* 2021, *12* (1), 459. https://doi.org/10.13040/IJPSR.0975-8232.12(1).459-64.

(163) Afolayan, M. O.; Adama, K. K.; Oberafo, A.; Omojola, M.; Thomas, S. Isolation and Characterization Studies of Ginger (Zingiber Officinale) Root Starch as a Potential Industrial Biomaterial. *American Journal of Materials Science* 2014, *2014* (2), 97–102. https://doi.org/10.5923/j.materials.20140402.06.

(164) Oluba, O. M.; Obi, C. F.; Akpor, O. B.; Ojeaburu, S. I.; Ogunrotimi, F. D.; Adediran, A. A.; Oki, M. Fabrication and Characterization of Keratin Starch Biocomposite Film from Chicken Feather Waste and Ginger Starch. *Sci Rep* 2021, *11* (1), 8768. https://doi.org/10.1038/s41598-021-88002-3.

(165) Oluba, O. M.; Owoso, T. O.; Bayo-Olorunmeke, A. O.; Erifeta, G. O.; Josiah, S. J.; Ojeaburu, S. I.; Subbiah, N.; Palanisamy, T. Probing the Role of Ginger Starch on Physicochemical and Thermal Properties of Gum Arabic Hybrid Biocomposite for Food Packaging Applications. *Carbohydrate Polymer Technologies and Applications* 2025, *9*, 100650. https://doi.org/10.1016/j.carpta.2024.100650.

(166) Rahmasari, Y.; Yemiş, G. P. Characterization of Ginger Starch-Based Edible Films Incorporated with Coconut Shell Liquid Smoke by Ultrasound Treatment and Application for Ground Beef. *Meat Sci* 2022, *188*, 108799. https://doi.org/10.1016/j.meatsci.2022.108799.

(167) Ahmed, M.; Djebli, N.; Hammoudi, S.; Aissat, S.; Akila, B.; Hemida, H. Additive Potential of Ginger Starch on Antifungal Potency of Honey against Candida Albicans. *Asian Pac J Trop Biomed* 2012, *2* (4), 253–255. https://doi.org/10.1016/S2221-1691(12)60018-5.

(168) Zhang, R. Y.; Chen, P. X.; Liu, A. B.; Zhu, W. X.; Jiang, M. M.; Wang, X. De; Liu, H. M. Effects of Different Isolation Methods on the Structure and Functional Properties of Starch from Tiger Nut (Cyperus Esculentus L.) Meal. *LWT* 2024, *196*. https://doi.org/10.1016/j.lwt.2024.115853.

(169) Zhang, X.; Cheng, Y.; Jia, X.; Geng, D.; Bian, X.; Tang, N. Effects of Extraction Methods on Physicochemical and Structural Properties of Common Vetch Starch. *Foods* 2022, *11* (18), 2920. https://doi.org/10.3390/foods11182920.

(170) Li, M.; Tian, Y.; Dhital, S. Starch Extraction. In *Starch and Starchy Food Products*; CRC Press, 2022; pp 17–40. https://doi.org/10.1201/9781003088929-2.

(171) Nawaz, H.; Shad, M. A.; Saleem, S.; Khan, M. U. A.; Nishan, U.; Rasheed, T.; Bilal, M.; Iqbal, H. M. N. Characteristics of Starch Isolated from Microwave Heat Treated Lotus

(Nelumbo Nucifera) Seed Flour. *Int J Biol Macromol* 2018, *113*, 219–226. https://doi.org/10.1016/j.ijbiomac.2018.02.125.

(172) Xie, Y.; Yan, M.; Yuan, S.; Sun, S.; Huo, Q. Effect of Microwave Treatment on the Physicochemical Properties of Potato Starch Granules. *Chem Cent J* 2013, *7* (1), 113. https://doi.org/10.1186/1752-153X-7-113.

(173) Araújo, R. G.; Rodríguez-Jasso, R. M.; Ruiz, H. A.; Govea-Salas, M.; Rosas-Flores, W.; Aguilar-González, M. A.; Pintado, M. E.; Lopez-Badillo, C.; Luevanos, C.; Aguilar, C. N. Hydrothermal-Microwave Processing for Starch Extraction from Mexican Avocado Seeds: Operational Conditions and Characterization. *Processes* 2020, *8* (7), 759. https://doi.org/10.3390/pr8070759.

(174) Mieles-Gómez, L.; Quintana, S. E.; García-Zapateiro, L. A. Comparison of Ultrasound- and Microwave-Assisted Extraction Techniques on Chemical, Technological, Rheological, and Microstructural Properties of Starch from Mango Kernel. *Gels* 2025, *11* (5), 330. https://doi.org/10.3390/gels11050330.

(175) Ramadan, M. F. *Handbook of Coriander (Coriandrum Sativum)*, 1st Edition.; CRC Press: Boca Raton, 2023. https://doi.org/10.1201/9781003204626.

(176) Łyczko, J.; Masztalerz, K.; Lipan, L.; Lech, K.; Carbonell-Barrachina, Á. A.; Szumny, A. Chemical Determinants of Dried Thai Basil (O. Basilicum Var. Thyrsiflora) Aroma Quality. *Ind Crops Prod* 2020, *155*, 112769. https://doi.org/10.1016/j.indcrop.2020.112769.

(177) Nazir, S.; Jan, H.; Tungmunnithum, D.; Drouet, S.; Zia, M.; Hano, C.; Abbasi, B. H. Callus Culture of Thai Basil Is an Effective Biological System for the Production of Antioxidants. *Molecules* 2020, *25* (20), 4859. https://doi.org/10.3390/molecules25204859.

(178) Tangpao, T.; Chung, H. H.; Sommano, S. R. Aromatic Profiles of Essential Oils from Five Commonly Used Thai Basils. *Foods* 2018, *7* (11), 175. https://doi.org/10.3390/foods7110175.

(179) Thongtip, A.; Mosaleeyanon, K.; Janta, S.; Wanichananan, P.; Chutimanukul, P.; Thepsilvisut, O.; Chutimanukul, P. Assessing Light Spectrum Impact on Growth and Antioxidant Properties of Basil Family Microgreens. *Sci Rep* 2024, *14* (1), 27875. https://doi.org/10.1038/s41598-024-79529-2.

(180) Nguyen, D. T. P.; Lu, N.; Kagawa, N.; Kitayama, M.; Takagaki, M. Short-Term Root-Zone Temperature Treatment Enhanced the Accumulation of Secondary Metabolites of Hydroponic Coriander (Coriandrum Sativum L.) Grown in a Plant Factory. *Agronomy* 2020, *10* (3), 413. https://doi.org/10.3390/agronomy10030413.

(181) Yang, X.; Xiao, F.; Jiang, P.; Luo, Y. Calculation and Prediction of Water Requirements for Aeroponic Cultivation of Crops in Greenhouses. *Horticulturae* 2025, *11* (9), 1034. https://doi.org/10.3390/horticulturae11091034.

(182) Lawrance, A.; Ram, K. V.; Harish, R. CFD Analysis of Aeroponic Nutrient Spray Characteristics for Enhanced Plant Nourishment in Sustainable Agriculture. *Smart Agricultural Technology* 2025, *10*, 100733. https://doi.org/10.1016/j.atech.2024.100733.

(183) Khater, E. S.; Bahnasawy, A.; Abass, W.; Morsy, O.; El-Ghobashy, H.; Shaban, Y.; Egela, M. Production of Basil (Ocimum Basilicum L.) under Different Soilless Cultures. *Sci Rep* 2021, *11* (1), 12754. https://doi.org/10.1038/s41598-021-91986-7.

(184) Chandra, S.; Khan, S.; Avula, B.; Lata, H.; Yang, M. H.; Elsohly, M. A.; Khan, I. A. Assessment of Total Phenolic and Flavonoid Content, Antioxidant Properties, and Yield of Aeroponically and Conventionally Grown Leafy Vegetables and Fruit Crops: A Comparative Study. *Evidence-based Complementary and Alternative Medicine* 2014, *2014*, 1–9. https://doi.org/10.1155/2014/253875.

(185) Mandal, S.; Mandal, M. Coriander (Coriandrum Sativum L.) Essential Oil: Chemistry and Biological Activity. *Asian Pac J Trop Biomed* 2015, *5* (6), 421–428. https://doi.org/10.1016/j.apjtb.2015.04.001.

(186) Neffati, M.; Marzouk, B. Roots Volatiles and Fatty Acids of Coriander (Coriandrum Sativum L.) Grown in Saline Medium. *Acta Physiol Plant* 2009, *31* (3), 455–461. https://doi.org/10.1007/s11738-008-0253-4.

(187) Al-Khayri, J. M.; Banadka, A.; Nandhini, M.; Nagella, P.; Al-Mssallem, M. Q.; Alessa, F. M. Essential Oil from Coriandrum Sativum: A Review on Its Phytochemistry and Biological Activity. *Molecules* 2023, *28* (2), 696. https://doi.org/10.3390/molecules28020696.

(188) Zeković, Z.; Pavlić, B.; Cvetanović, A.; Đurović, S. Supercritical Fluid Extraction of Coriander Seeds: Process Optimization, Chemical Profile and Antioxidant Activity of Lipid Extracts. *Ind Crops Prod* 2016, *94*, 353–362. https://doi.org/10.1016/j.indcrop.2016.09.008.

(189) Kamel, M.; Mouna, B. T.; Karim, H.; Salem, N.; Sonia, T.; Iness, B.; Mohamed, H.; Férid, L.; Brahim, M. Comparison of Different Extraction Methods for the Determination of Essential Oils and Related Compounds from Coriander (Coriandrum Sativum L.). *Acta Chim. Slov.* 2012, *59*, 803–813.

(190) Coelho, J.; Veiga, J.; Karmali, A.; Nicolai, M.; Reis, C. P.; Nobre, B.; Palavra, A. Supercritical CO2 Extracts and Volatile Oil of Basil (Ocimum Basilicum L.) Comparison with Conventional Methods. *Separations* 2018, *5* (2), 21. https://doi.org/10.3390/separations5020021.

(191) Illés, V.; Daood, H. G.; Perneczki, S.; Szokonya, L.; Then, M. Extraction of Coriander Seed Oil by CO2 and Propane at Super-and Subcritical Conditions. *Journal of Supercritical Fluids* 2000, *17*, 177–186.

(192) Neffati, M.; Marzouk, B. Changes in Essential Oil and Fatty Acid Composition in Coriander (Coriandrum Sativum L.) Leaves under Saline Conditions. *Ind Crops Prod* 2008, *28* (2), 137–142. https://doi.org/10.1016/j.indcrop.2008.02.005.

(193) An, Q.; Ren, J. N.; Li, X.; Fan, G.; Qu, S. S.; Song, Y.; Li, Y.; Pan, S. Y. Recent Updates on Bioactive Properties of Linalool. *Food Funct* 2021, *12*, 10370–10389. https://doi.org/10.1039/d1fo02120f.

(194) Arsenijević, J.; Jovanović, A.; Kovačević, N.; Drobac, M. Basil Essential Oil: Estragole Content and Chemical Profiles. *Acta Aliment* 2025, *54* (1), 133–144. https://doi.org/10.1556/066.2024.00244.

(195) Milenković, L.; Stanojević, J.; Cvetković, D.; Stanojević, L.; Lalević, D.; Šunić, L.; Fallik, E.; Ilić, Z. S. New Technology in Basil Production with High Essential Oil Yield and Quality. *Ind Crops Prod* 2019, *140*, 111718. https://doi.org/10.1016/j.indcrop.2019.111718.

(196) Bhat, S.; Kaushal, P.; Kaur, M.; Sharma, H. K. Coriander (Coriandrum Sativum L.): Processing, Nutritional and Functional Aspects. *African Journal of Plant Science* 2014, *8* (1), 25–33. https://doi.org/10.5897/ajps2013.1118.

(197) Nazir, S.; Wani, I. A.; Masoodi, F. A. Extraction Optimization of Mucilage from Basil (Ocimum Basilicum L.) Seeds Using Response Surface Methodology. *J Adv Res* 2017, *8* (3), 235–244. https://doi.org/10.1016/j.jare.2017.01.003.

(198) Nazir, S.; Wani, I. A. Protein Isolate from Basil Seeds (Ocimum Basilicum L.): Physicochemical and Functional Characterisation. *Food Chemistry Advances* 2023, *3*, 100424. https://doi.org/10.1016/j.focha.2023.100424.

(199) Rohr, K.; Engling, F. P.; Lebzien, P.; Oslage, H. J. Analysis and evaluation of coriander oilmeal for ruminant diets. *Landbauforschung Völkenrode* 1990, *40* (2), 133–137.

(200) Aluko, R. E.; Mcintosh, T.; Reaney, M. Comparative Study of the Emulsifying and Foaming Properties of Defatted Coriander (Coriandrum Sativum) Seed Flour and Protein Concentrate. *Food Research International* 2001, *34*, 733–738. https://doi.org/https://doi.org/10.1016/S0963-9969(01)00095-3.

(201) Hojilla-Evangelista, M. P.; Evangelista, R. L. Effects of Steam Distillation and Screw-Pressing on Extraction, Composition and Functional Properties of Protein in Dehulled Coriander (Coriandrum Sativum L.). *JAOCS, Journal of the American Oil Chemists' Society* 2017, *94* (2), 315–324. https://doi.org/10.1007/s11746-017-2948-4.

(202) Peñas, E.; Hernandez-Ledesma, B.; Martinez-Villaluenga, C. Microwave-Assisted Extraction of Plant Proteins. In *Green Protein Processing Technologies from Plants*; Springer International Publishing: Cham, 2023; pp 211–236. https://doi.org/10.1007/978-3-031-16968-7_9.

(203) Contreras, M. del M.; Lama-Muñoz, A.; Manuel Gutiérrez-Pérez, J.; Espínola, F.; Moya, M.; Castro, E. Protein Extraction from Agri-Food Residues for Integration in Biorefinery: Potential Techniques and Current Status. *Bioresour Technol* 2019, *280*, 459–477. https://doi.org/10.1016/j.biortech.2019.02.040.

(204) Sluiter, A.; Hames, B.; Hyman, D.; Payne, C.; Ruiz, R.; Scarlata, C.; Sluiter, J.; Templeton, D.; Wolfe, J. *Determination of Total Solids in Biomass and Total Dissolved Solids in Liquid Process Samples Laboratory Analytical Procedure (LAP)*; 2008. www.nrel.gov (accessed 2025-10-20).

(205) Sluiter, A.; Hames, B.; Ruiz, R.; Scarlata, C.; Sluiter, J.; Templeton, D. *Determination of Ash in Biomass: Laboratory Analytical Procedure (LAP)*; 2008. www.nrel.gov (accessed 2025-10-20).

(206) Sluiter, A.; Hames, B.; Ruiz, R.; Scarlata, C.; Sluiter, J.; Templeton, D.; Crocker, D. *Determination of Structural Carbohydrates and Lignin in Biomass: Laboratory Analytical Procedure (LAP)*; 2008. http://www.nrel.gov/biomass/analytical_procedures.html (accessed 2025-10-20).

(207) Guandalini, B. B. V.; Rodrigues, N. P.; Marczak, L. D. F. Sequential Extraction of Phenolics and Pectin from Mango Peel Assisted by Ultrasound. *Food Research International* 2019, *119*, 455–461. https://doi.org/10.1016/j.foodres.2018.12.011.

(208) Demir, D.; Ceylan, S.; Göktürk, D.; Bölgen, N. Extraction of Pectin from Albedo of Lemon Peels for Preparation of Tissue Engineering Scaffolds. *Polymer Bulletin* 2021, *78* (4), 2211–2226. https://doi.org/10.1007/s00289-020-03208-1.

(209) Hames, B.; Scarlata, C.; Sluiter, A. *Determination of Protein Content in Biomass: Laboratory Analytical Procedure (LAP)*; 2008. www.nrel.gov (accessed 2025-10-20).

(210) Šimerdová, B.; Bobríková, M.; Lhotská, I.; Kaplan, J.; Křenová, A.; Šatínský, D. Evaluation of Anthocyanin Profiles in Various Blackcurrant Cultivars over a Three-

Year Period Using a Fast HPLC-DAD Method. *Foods* 2021, *10* (8), 1745. https://doi.org/10.3390/foods10081745.

(211) Bae, J.-Y.; Lim, S. S.; Choi, J.-S.; Kang, Y.-H. Protective Actions of Rubus Coreanus Ethanol Extract on Collagenous Extracellular Matrix in Ultraviolet-B Irradiation-Induced Human Dermal Fibroblasts. *Nutr Res Pract* 2007, *1* (4), 279–284.

(212) Vergara, C.; Von Baer, D.; Hermosín, I.; Ruiz, A.; Hitschfeld, M. A.; Castillo, N.; Mardones, C. Anthocyanins That Confer Characteristic Color to Red Copihue Flowers (Lapageria Rosea). *J. Chil. Chem. Soc* 2009, *54* (2), 194–197.

(213) Skaar, I.; Adaku, C.; Jordheim, M.; Byamukama, R.; Kiremire, B.; Andersen, Ø. M. Purple Anthocyanin Colouration on Lower (Abaxial) Leaf Surface of Hemigraphis Colorata (Acanthaceae). *Phytochemistry* 2014, *105*, 141–146. https://doi.org/10.1016/j.phytochem.2014.05.016.

(214) Kim, H. W.; Kim, S. R.; Lee, Y. M.; Jang, H. H.; Kim, J. B. Analysis of Variation in Anthocyanin Composition in Korean Coloured Potato Cultivars by LC-DAD-ESI-MS and PLS-DA. *Potato Res* 2018, *61* (1), 1–17. https://doi.org/10.1007/s11540-017-9348-x.

(215) Jong, S. H.; Abdullah, N.; Muhammad, N. Effect of Acid Type and Concentration on the Yield, Purity, and Esterification Degree of Pectin Extracted from Durian Rinds. *Results in Engineering* 2023, *17*, 100974. https://doi.org/https://doi.org/10.1016/j.rineng.2023.100974.

(216) Wu, Z. W.; Xu, S.; Cheng, W. J.; Cai, X. S.; Liu, H. M.; Ma, Y. X.; Wang, X. De. Physicochemical Properties and in Vitro Digestive Properties of Amylose and Amylopectin Isolated from Tigernut (Cyperus Esculentus L.) Starch. *Journal of Food Measurement and Characterization* 2024, *18* (5), 3960–3973. https://doi.org/10.1007/s11694-024-02468-z.

(217) Alara, O. R.; Abdurahman, N. H.; Olalere, O. A. Ethanolic Extraction of Flavonoids, Phenolics and Antioxidants from Vernonia Amygdalina Leaf Using Two-Level Factorial Design. *J King Saud Univ Sci* 2020, *32* (1), 7–16. https://doi.org/https://doi.org/10.1016/j.jksus.2017.08.001.

(218) Inácio, M. R. C.; de Lima, K. M. G.; Lopes, V. G.; Pessoa, J. D. C.; de Almeida Teixeira, G. H. Total Anthocyanin Content Determination in Intact Açaí (Euterpe Oleracea Mart.) and Palmitero-Juçara (Euterpe Edulis Mart.) Fruit Using near Infrared Spectroscopy (NIR) and Multivariate Calibration. *Food Chem* 2013, *136* (3), 1160–1164. https://doi.org/https://doi.org/10.1016/j.foodchem.2012.09.046.

(219) Lee, J.; Durst, R. W.; Wrolstad, R. E. Determination of Total Monomeric Anthocyanin Pigment Content of Fruit Juices, Beverages, Natural Colorants, and Wines by the PH Differential Method: Collaborative Study. *J AOAC Int* 2005, *88* (5), 1269–1278. https://doi.org/10.1093/jaoac/88.5.1269.

(220) Do, Q. D.; Angkawijaya, A. E.; Tran-Nguyen, P. L.; Huynh, L. H.; Soetaredjo, F. E.; Ismadji, S.; Ju, Y. H. Effect of Extraction Solvent on Total Phenol Content, Total Flavonoid Content, and Antioxidant Activity of Limnophila Aromatica. *J Food Drug Anal* 2014, *22* (3), 296–302. https://doi.org/10.1016/j.jfda.2013.11.001.

(221) Ferri, M.; Papchenko, K.; Degli Esposti, M.; Tondi, G.; De Angelis, M. G.; Morselli, D.; Fabbri, P. Fully Biobased Polyhydroxyalkanoate/Tannin Films as Multifunctional Materials for Smart Food Packaging Applications. *ACS Appl Mater Interfaces* 2023, *15* (23), 28594–28605. https://doi.org/10.1021/acsami.3c04611.

(222) Segal, L.; Creely, J. J.; Martin, A. E.; Conrad, C. M. An Empirical Method for Estimating the Degree of Crystallinity of Native Cellulose Using the X-Ray Diffractometer. *Textile Research Journal* 1959, *29* (10), 786–794. https://doi.org/10.1177/004051755902901003.

(223) Kadan, R. S.; Bryant, R. J.; Miller, J. A. Effects of Milling on Functional Properties of Rice Flour. *J Food Sci* 2008, *73* (4), E151–E154. https://doi.org/10.1111/j.1750-3841.2008.00720.x.

(224) Zain, N. F. M.; Yusop, S. M.; Ahmad, I. Preparation and Characterization of Cellulose and Nanocellulose from Pomelo (Citrus Grandis) Albedo. *J Nutr Food Sci* 2014, *05* (01), 1000334. https://doi.org/10.4172/2155-9600.1000334.

(225) Azmi, N. S.; Basha, R. K.; Othman, S. H.; Mohammed, M. A. P.; Wakisaka, M.; Ariffin, S. H.; Salim, N. H. Development of Fish Gelatin Film for Anti-Fogging Mushroom Packaging. *J Food Eng* 2025, *387*, 112306. https://doi.org/10.1016/j.jfoodeng.2024.112306.

(226) Wexler, A. Vapor Pressure Formulation for Water in Range 0 to 100 Degrees C. A Revision. *Journal of Research of the National Bureau of Standards- A. Physics and Chemistry* 1976, *80A* (5), 775–785.

(227) Kanovsky, N.; Margel, S. Fabrication of Transparent Silica/PEG Smooth Thin Coatings on Polymeric Films for Antifogging Applications. *ACS Omega* 2022, *7* (24), 20505–20514. https://doi.org/10.1021/acsomega.1c07293.

(228) Wu, J.; Zhu, K.; Li, J.; Ye, X.; Chen, S. An Optimize Adaptable Method for Determining the Monosaccharide Composition of Pectic Polysaccharides. *Int J Biol Macromol* 2024, *277*, 133591. https://doi.org/10.1016/j.ijbiomac.2024.133591.

(229) *Fluidized Bed Reactors: Principles and Applications*; Beike, K., Ed.; Nova Science, 2020.

(230) Węgrzyk, G.; Grzęda, D.; Leszczyńska, M.; Nędza, B.; Bulanda, K.; Oleksy, M.; Ryszkowska, J.; Cabulis, U. Viscoelastic Polyurethane Foam Biocomposites with Enhanced Flame Retardancy. *Polymers (Basel)* 2024, *16* (22), 3189. https://doi.org/10.3390/polym16223189.

(231) Silvestre, W. P.; Galafassi, P. L.; Ferreira, S. D.; Godinho, M.; Pauletti, G. F.; Baldasso, C. Fodder Radish Seed Cake Biochar for Soil Amendment. *Environmental Science and Pollution Research* 2018, *25* (25), 25143–25154. https://doi.org/10.1007/s11356-018-2571-4.

(232) Nosal, H.; Moser, K.; Warzała, M.; Holzer, A.; Stańczyk, D.; Sabura, E. Selected Fatty Acids Esters as Potential PHB-V Bioplasticizers: Effect on Mechanical Properties of the Polymer. *J Polym Environ* 2020, *29*, 38–53. https://doi.org/10.1007/s10924-020-01841-5.

(233) Kamboh, M. A.; Chang, A. S.; Wan Ibrahim, W. A.; Sanagi, M. M.; Mahesar, S. A.; Sirajuddin; Hussain Sherazi, S. T. A Green Method for the Quantitative Assessment of Neutral Oil in Palm Fatty Acid Distillates by Single Bounce Attenuated Total Reflectance Fourier-Transform Infrared Spectroscopy. *RSC Adv* 2015, *5* (62), 50591–50596. https://doi.org/10.1039/c5ra06987d.

(234) Salim, R. M.; Asik, J.; Sarjadi, M. S. Chemical Functional Groups of Extractives, Cellulose and Lignin Extracted from Native Leucaena Leucocephala Bark. *Wood Sci Technol* 2021, *55* (2), 295–313. https://doi.org/10.1007/s00226-020-01258-2.

(235) Liang, T.; Wang, L. Thermal Treatment of Poplar Hemicelluloses at 180 to 220 °C under Nitrogen Atmosphere. *Bioresources* 2017, *12* (1), 1128–1135.

(236) Kalapathy, U.; Proctor, A. Effect of Acid Extraction and Alcohol Precipitation Conditions on the Yield and Purity of Soy Hull Pectin. *Food Chem* 2001, *73*, 393–396.

(237) Manas, E.; Saura-Calixto, F. Ethanolic Precipitation: A Source of Error in Dietary Fibre Determination. *Food Chem* 1993, *47*, 351–355.

(238) Meng, X. Valorisation of Citrus Fruit Peel Wastes and Blackcurrant Pomace via Acid-Free Microwave Hydrothermal Processes. Ph. D. Thesis, University of York, York, 2022.

(239) Slavu, M.; Aprodu, I.; Milea, Ștefania A.; Enachi, E.; Râpeanu, G.; Bahrim, G. E.; Stănciuc, N. Thermal Degradation Kinetics of Anthocyanins Extracted from Purple Maize Flour Extract and the Effect of Heating on Selected Biological Functionality. *Foods* 2020, *9* (11), 1593. https://doi.org/10.3390/foods9111593.

(240) Yu, Y.; Wang, Y.; Liu, X.; Liu, Y.; Ji, L.; Zhou, Y.; Sun, L. Comparison of Analytical Methods for Determining Methylesterification and Acetylation of Pectin. *Applied Sciences* 2021, *11* (10), 4461. https://doi.org/10.3390/app11104461.

(241) Kintner III, P. K.; Buren, J. P. Van. Carbohydrate Interference and Its Correction in Pectin Analysis Using the M-Hydroxydiphenyl Method. *J Food Sci* 1982, *47* (3), 756–759. https://doi.org/https://doi.org/10.1111/j.1365-2621.1982.tb12708.x.

(242) Blumenkrantz, N.; Asboe-Hansen, G. New Method for Quantitative Determination of Uronic Acids. *Anal Biochem* 1973, *54* (2), 484–489. https://doi.org/https://doi.org/10.1016/0003-2697(73)90377-1.

(243) López-Lorente, Á. I.; Mizaikoff, B. Mid-Infrared Spectroscopy for Protein Analysis: Potential and Challenges. *Anal Bioanal Chem* 2016, *408* (11), 2875–2889. https://doi.org/10.1007/s00216-016-9375-5.

(244) Alhazmi, H. A.; Bratty, M. Al; Meraya, A. M.; Najmi, A.; Alam, M. S.; Javed, S. A.; Ahsan, W. Spectroscopic Characterization of the Interactions of Bovine Serum Albumin with Medicinally Important Metal Ions: Platinum (IV), Iridium (III) and Iron (II). *Acta Biochim Pol* 2021, *68* (1), 99–107. https://doi.org/10.18388/abp.2020_5462.

(245) Monsoor, M. A. Effect of Drying Methods on the Functional Properties of Soy Hull Pectin. *Carbohydr Polym* 2005, *61* (3), 362–367. https://doi.org/10.1016/j.carbpol.2005.06.009.

(246) Spinei, M.; Oroian, M. The Influence of Extraction Conditions on the Yield and Physico-Chemical Parameters of Pectin from Grape Pomace. *Polymers (Basel)* 2022, *14* (7), 1378. https://doi.org/10.3390/polym14071378.

(247) Yu, Y.; Cui, L.; Liu, X.; Wang, Y.; Song, C.; Pak, U. H.; Mayo, K. H.; Sun, L.; Zhou, Y. Determining Methyl-Esterification Patterns in Plant-Derived Homogalacturonan Pectins. *Front Nutr* 2022, *9*, 925050. https://doi.org/10.3389/fnut.2022.925050.

(248) Zhang, T.; Wang, H.; Qi, D.; Xia, L.; Li, L.; Li, X.; Jiang, S. Multifunctional Colorimetric Cellulose Acetate Membrane Incorporated with Perilla Frutescens (L.) Britt. Anthocyanins and Chamomile Essential Oil. *Carbohydr Polym* 2022, *278*, 118914. https://doi.org/https://doi.org/10.1016/j.carbpol.2021.118914.

(249) Bondancia, T. J.; De Aguiar, J.; Batista, G.; Cruz, A. J. G.; Marconcini, J. M.; Mattoso, L. H. C.; Farinas, C. S. Production of Nanocellulose Using Citric Acid in a Biorefinery Concept: Effect of the Hydrolysis Reaction Time and Techno-Economic Analysis. *Ind*

Eng Chem Res 2020, *59* (25), 11505–11516. https://doi.org/10.1021/acs.iecr.0c01359.

(250) Fouad, H.; Kian, L. K.; Jawaid, M.; Alotaibi, M. D.; Alothman, O. Y.; Hashem, M. Characterization of Microcrystalline Cellulose Isolated from Conocarpus Fiber. *Polymers (Basel)* 2020, *12* (12), 1–11. https://doi.org/10.3390/polym12122926.

(251) Trache, D.; Khimeche, K.; Mezroua, A.; Benziane, M. Physicochemical Properties of Microcrystalline Nitrocellulose from Alfa Grass Fibres and Its Thermal Stability. *J Therm Anal Calorim* 2016, *124* (3), 1485–1496. https://doi.org/10.1007/s10973-016-5293-1.

(252) Burhenne, L.; Messmer, J.; Aicher, T.; Laborie, M.-P. The Effect of the Biomass Components Lignin, Cellulose and Hemicellulose on TGA and Fixed Bed Pyrolysis. *J Anal Appl Pyrolysis* 2013, *101*, 177–184. https://doi.org/https://doi.org/10.1016/j.jaap.2013.01.012.

(253) Nanda, S.; Mohanty, P.; Pant, K. K.; Naik, S.; Kozinski, J. A.; Dalai, A. K. Characterization of North American Lignocellulosic Biomass and Biochars in Terms of Their Candidacy for Alternate Renewable Fuels. *Bioenergy Res* 2013, *6* (2), 663–677. https://doi.org/10.1007/s12155-012-9281-4.

(254) Shah, M. A.; Hayder, G.; Kumar, R.; Kumar, V.; Ahamad, T.; Kalam, M. A.; Soudagar, M. E. M.; Mohamed Shamshuddin, S. Z.; Mubarak, N. M. Development of Sustainable Biomass Residues for Biofuels Applications. *Sci Rep* 2023, *13* (1), 14248. https://doi.org/10.1038/s41598-023-41446-1.

(255) French, A. D. Idealized Powder Diffraction Patterns for Cellulose Polymorphs. *Cellulose* 2014, *21* (2), 885–896. https://doi.org/10.1007/s10570-013-0030-4.

(256) Nam, S.; French, A. D.; Condon, B. D.; Concha, M. Segal Crystallinity Index Revisited by the Simulation of X-Ray Diffraction Patterns of Cotton Cellulose Iβ and Cellulose II. *Carbohydr Polym* 2016, *135*, 1–9. https://doi.org/https://doi.org/10.1016/j.carbpol.2015.08.035.

(257) SriBala, G.; Chennuru, R.; Mahapatra, S.; Vinu, R. Effect of Alkaline Ultrasonic Pretreatment on Crystalline Morphology and Enzymatic Hydrolysis of Cellulose. *Cellulose* 2016, *23* (3), 1725–1740. https://doi.org/10.1007/s10570-016-0893-2.

(258) Gil Giraldo, G. A.; Mantovan, J.; Marim, B. M.; Kishima, J. O. F.; Mali, S. Surface Modification of Cellulose from Oat Hull with Citric Acid Using Ultrasonication and Reactive Extrusion Assisted Processes. *Polysaccharides* 2021, *2* (2), 218–233. https://doi.org/10.3390/polysaccharides2020015.

(259) Pereira, J. F.; Marim, B. M.; Mali, S. Chemical Modification of Cellulose Using a Green Route by Reactive Extrusion with Citric and Succinic Acids. *Polysaccharides* 2022, *3* (1), 292–305. https://doi.org/10.3390/polysaccharides3010017.

(260) Johnson, A. M.; Mottiar, Y.; Ogawa, Y.; Karaaslan, M. A.; Zhang, H.; Hua, Q.; Mansfield, S. D.; Renneckar, S. The Formation of Xylan Hydrate Crystals Is Affected by Sidechain Uronic Acids but Not by Lignin. *Cellulose* 2023, *30* (13), 8475–8494. https://doi.org/10.1007/s10570-023-05422-2.

(261) Akhtar, N.; Goyal, D.; Goyal, A. Physico-Chemical Characteristics of Leaf Litter Biomass to Delineate the Chemistries Involved in Biofuel Production. *J Taiwan Inst Chem Eng* 2016, *62*, 239–246. https://doi.org/https://doi.org/10.1016/j.jtice.2016.02.011.

(262) Kohn, B.; Davis, M.; Maciel, G. E. In Situ Study of Dilute H2SO4 Pretreatment of 13C-Enriched Poplar Wood, Using 13C NMR. *Energy and Fuels* 2011, *25* (5), 2301–2313. https://doi.org/10.1021/ef2000213.

(263) Gao, A. H.; Bule, M. V.; Laskar, D. D.; Chen, S. Structural and Thermal Characterization of Wheat Straw Pretreated with Aqueous Ammonia Soaking. *J Agric Food Chem* 2012, *60* (35), 8632–8639. https://doi.org/10.1021/jf301244m.

(264) Mittal, A.; Katahira, R.; Himmel, M. E.; Johnson, D. K. Effects of Alkaline or Liquid-Ammonia Treatment on Crystalline Cellulose: Changes in Crystalline Structure and Effects on Enzymatic Digestibility. *Biotechnol Biofuels* 2011, *4*, 41. https://doi.org/10.1186/1754-6834-4-41.

(265) Kono, H.; Yunoki, S.; Shikano, T.; Fujiwara, M.; Erata, T.; Takai, M. CP/MAS 13C NMR Study of Cellulose and Cellulose Derivatives. 1. Complete Assignment of the CP/MAS 13C NMR Spectrum of the Native Cellulose. *J. Am. Chem. Soc.* 2002, *124* (25), 7506.

(266) Lahaye, M.; Rondeau-Mouro, C.; Deniaud, E.; Buléon, A. Solid-State 13C NMR Spectroscopy Studies of Xylans in the Cell Wall of Palmaria Palmata (L. Kuntze, Rhodophyta). *Carbohydr Res* 2003, *338* (15), 1559–1569. https://doi.org/10.1016/S0008-6215(03)00241-6.

(267) Duan, P.; Kaser, S. J.; Lyczakowski, J. J.; Phyo, P.; Tryfona, T.; Dupree, P.; Hong, M. Xylan Structure and Dynamics in Native Brachypodium Grass Cell Walls Investigated by Solid-State NMR Spectroscopy. *ACS Omega* 2021, *6* (23), 15460–15471. https://doi.org/10.1021/acsomega.1c01978.

(268) Kim, S. H.; Lee, C. M.; Kafle, K. Characterization of Crystalline Cellulose in Biomass: Basic Principles, Applications, and Limitations of XRD, NMR, IR, Raman, and SFG. *Korean Journal of Chemical Engineering* 2013, *30* (12), 2127–2141. https://doi.org/10.1007/s11814-013-0162-0.

(269) Lee, C. M.; Mittal, A.; Barnette, A. L.; Kafle, K.; Park, Y. B.; Shin, H.; Johnson, D. K.; Park, S.; Kim, S. H. Cellulose Polymorphism Study with Sum-Frequency-Generation (SFG) Vibration Spectroscopy: Identification of Exocyclic CH2OH Conformation and Chain Orientation. *Cellulose* 2013, *20* (3), 991–1000. https://doi.org/10.1007/s10570-013-9917-3.

(270) Idström, A.; Schantz, S.; Sundberg, J.; Chmelka, B. F.; Gatenholm, P.; Nordstierna, L. 13C NMR Assignments of Regenerated Cellulose from Solid-State 2D NMR Spectroscopy. *Carbohydr Polym* 2016, *151*, 480–487. https://doi.org/https://doi.org/10.1016/j.carbpol.2016.05.107.

(271) Simmons, T. J.; Mortimer, J. C.; Bernardinelli, O. D.; Pöppler, A. C.; Brown, S. P.; DeAzevedo, E. R.; Dupree, R.; Dupree, P. Folding of Xylan onto Cellulose Fibrils in Plant Cell Walls Revealed by Solid-State NMR. *Nat Commun* 2016, *7*, 13902. https://doi.org/10.1038/ncomms13902.

(272) Mendoza, L.; Batchelor, W.; Tabor, R. F.; Garnier, G. Gelation Mechanism of Cellulose Nanofibre Gels: A Colloids and Interfacial Perspective. *J Colloid Interface Sci* 2018, *509*, 39–46. https://doi.org/https://doi.org/10.1016/j.jcis.2017.08.101.

(273) Albornoz-Palma, G.; Betancourt, F.; Mendonça, R. T.; Chinga-Carrasco, G.; Pereira, M. Relationship between Rheological and Morphological Characteristics of Cellulose Nanofibrils in Dilute Dispersions. *Carbohydr Polym* 2020, *230*, 115588. https://doi.org/10.1016/j.carbpol.2019.115588.

(274) Taheri, H.; Samyn, P. Effect of Homogenization (Microfluidization) Process Parameters in Mechanical Production of Micro- and Nanofibrillated Cellulose on Its Rheological and Morphological Properties. *Cellulose* 2016, *23* (2), 1221–1238. https://doi.org/10.1007/s10570-016-0866-5.

(275) Jaiswal, A. K.; Kumar, V.; Khakalo, A.; Lahtinen, P.; Solin, K.; Pere, J.; Toivakka, M. Rheological Behavior of High Consistency Enzymatically Fibrillated Cellulose Suspensions. *Cellulose* 2021, *28* (4), 2087–2104. https://doi.org/10.1007/s10570-021-03688-y.

(276) Saarikoski, E.; Saarinen, T.; Salmela, J.; Seppälä, J. Flocculated Flow of Microfibrillated Cellulose Water Suspensions: An Imaging Approach for Characterisation of Rheological Behaviour. *Cellulose* 2012, *19* (3), 647–659. https://doi.org/10.1007/s10570-012-9661-0.

(277) Morales-Medina, R.; Dong, D.; Schalow, S.; Drusch, S. Impact of Microfluidization on the Microstructure and Functional Properties of Pea Hull Fibre. *Food Hydrocoll* 2020, *103*, 105660. https://doi.org/10.1016/j.foodhyd.2020.105660.

(278) Zhao, M.; Bai, J.; Bu, X.; Tang, Y.; Han, W.; Li, D.; Wang, L.; Yang, Y.; Xu, Y. Microwave-Assisted Aqueous Two-Phase Extraction of Phenolic Compounds from Ribes Nigrum L. and Its Antibacterial Effect on Foodborne Pathogens. *Food Control* 2021, *119*, 107449. https://doi.org/https://doi.org/10.1016/j.foodcont.2020.107449.

(279) Jiang, X.; Sun, J.; Bai, W. Anthocyanins in Food. In *Handbook of Dietary Phytochemicals*; Springer Singapore: Singapore, 2021; pp 371–421. https://doi.org/10.1007/978-981-15-4148-3_13.

(280) Oancea, S. A Review of the Current Knowledge of Thermal Stability of Anthocyanins and Approaches to Their Stabilization to Heat. *Antioxidants* 2021, *10* (9), 1337. https://doi.org/10.3390/antiox10091337.

(281) Wang, T.; Zhai, Y.; Zhu, Y.; Li, C.; Zeng, G. A Review of the Hydrothermal Carbonization of Biomass Waste for Hydrochar Formation: Process Conditions, Fundamentals, and Physicochemical Properties. *Renewable and Sustainable Energy Reviews* 2018, *90*, 223–247. https://doi.org/10.1016/j.rser.2018.03.071.

(282) Steinbach, D.; Kruse, A.; Sauer, J. Pretreatment Technologies of Lignocellulosic Biomass in Water in View of Furfural and 5-Hydroxymethylfurfural Production- A Review. *Biomass Convers Biorefin* 2017, *7* (2), 247–274. https://doi.org/10.1007/s13399-017-0243-0.

(283) Hobuss, C. B.; Da Silva, F. A.; Dos Santos, M. A. Z.; De Pereira, C. M. P.; Schulz, G. A. S.; Bianchini, D. Synthesis and Characterization of Monoacylglycerols through Glycerolysis of Ethyl Esters Derived from Linseed Oil by Green Processes. *RSC Adv* 2020, *10* (4), 2327–2336. https://doi.org/10.1039/c9ra07834g.

(284) Wang, X. Y.; Yang, D.; Gan, L. J.; Zhang, H.; Shin, J. A.; Lee, Y. H.; Jang, Y. S.; Lee, K. T. Effect of Positional Distribution of Linoleic Acid on Oxidative Stability of Triacylglycerol Molecules Determined by 1H NMR. *JAOCS, Journal of the American Oil Chemists' Society* 2015, *92* (2), 157–165. https://doi.org/10.1007/s11746-015-2590-y.

(285) Dona, A. C.; Kyriakides, M.; Scott, F.; Shephard, E. A.; Varshavi, D.; Veselkov, K.; Everett, J. R. A Guide to the Identification of Metabolites in NMR-Based Metabonomics/Metabolomics Experiments. *Comput Struct Biotechnol J* 2016, *14*, 135–153. https://doi.org/10.1016/j.csbj.2016.02.005.

(286) Del Campo, G.; Berregi, I.; Caracena, R.; Santos, J. I. Quantitative Analysis of Malic and Citric Acids in Fruit Juices Using Proton Nuclear Magnetic Resonance Spectroscopy. *Anal Chim Acta* 2006, *556* (2), 462–468. https://doi.org/10.1016/j.aca.2005.09.039.

(287) Milić, A.; Daničić, T.; Horecki, A. T.; Šumić, Z.; Teslić, N.; Kovačević, D. B.; Putnik, P.; Pavlić, B. Sustainable Extractions for Maximizing Content of Antioxidant Phytochemicals from Black and Red Currants. *Foods* 2022, *11* (3), 325. https://doi.org/10.3390/foods11030325.

(288) Rose, P. M.; Cantrill, V.; Benohoud, M.; Tidder, A.; Rayner, C. M.; Blackburn, R. S. Application of Anthocyanins from Blackcurrant (Ribes Nigrum L.) Fruit Waste as Renewable Hair Dyes. *J Agric Food Chem* 2018, *66* (26), 6790–6798. https://doi.org/10.1021/acs.jafc.8b01044.

(289) Makaremi, M.; Yousefi, H.; Cavallaro, G.; Lazzara, G.; Goh, C. B. S.; Lee, S. M.; Solouk, A.; Pasbakhsh, P. Safely Dissolvable and Healable Active Packaging Films Based on Alginate and Pectin. *Polymers (Basel)* 2019, *11* (10), 1594. https://doi.org/10.3390/polym11101594.

(290) Kang, S.; Xiao, Y.; Guo, X.; Huang, A.; Xu, H. Development of Gum Arabic-Based Nanocomposite Films Reinforced with Cellulose Nanocrystals for Strawberry Preservation. *Food Chem* 2021, *350*, 129199. https://doi.org/https://doi.org/10.1016/j.foodchem.2021.129199.

(291) Wu, C.; Li, Y.; Sun, J.; Lu, Y.; Tong, C.; Wang, L.; Yan, Z.; Pang, J. Novel Konjac Glucomannan Films with Oxidized Chitin Nanocrystals Immobilized Red Cabbage Anthocyanins for Intelligent Food Packaging. *Food Hydrocoll* 2020, *98*, 105245. https://doi.org/https://doi.org/10.1016/j.foodhyd.2019.105245.

(292) Cao, L.; Lu, W.; Mata, A.; Nishinari, K.; Fang, Y. Egg-Box Model-Based Gelation of Alginate and Pectin: A Review. *Carbohydr Polym* 2020, *242*, 116389. https://doi.org/https://doi.org/10.1016/j.carbpol.2020.116389.

(293) Vityazev, F. V; Khramova, D. S.; Saveliev, N. Y.; Ipatova, E. A.; Burkov, A. A.; Beloserov, V. S.; Belyi, V. A.; Kononov, L. O.; Martinson, E. A.; Litvinets, S. G.; Markov, P. A.; Popov, S. V. Pectin–Glycerol Gel Beads: Preparation, Characterization and Swelling Behaviour. *Carbohydr Polym* 2020, *238*, 116166. https://doi.org/https://doi.org/10.1016/j.carbpol.2020.116166.

(294) Prietto, L.; Mirapalhete, T. C.; Pinto, V. Z.; Hoffmann, J. F.; Vanier, N. L.; Lim, L. T.; Guerra Dias, A. R.; da Rosa Zavareze, E. PH-Sensitive Films Containing Anthocyanins Extracted from Black Bean Seed Coat and Red Cabbage. *LWT* 2017, *80*, 492–500. https://doi.org/10.1016/j.lwt.2017.03.006.

(295) Liu, Y.; Qin, Y.; Bai, R.; Zhang, X.; Yuan, L.; Liu, J. Preparation of PH-Sensitive and Antioxidant Packaging Films Based on κ-Carrageenan and Mulberry Polyphenolic Extract. *Int J Biol Macromol* 2019, *134*, 993–1001. https://doi.org/https://doi.org/10.1016/j.ijbiomac.2019.05.175.

(296) Yan, P.; Lan, W.; Xie, J. Modification on Sodium Alginate for Food Preservation: A Review. *Trends Food Sci Technol* 2024, *143*, 104217. https://doi.org/10.1016/j.tifs.2023.104217.

(297) Solberg, A.; Draget, K. I.; Schatz, C.; Christensen, B. E. Alginate Blocks and Block Polysaccharides: A Review. *Macromol Symp* 2023, *408* (1), 2200072. https://doi.org/10.1002/masy.202200072.

(298) Singh, P.; Baisthakur, P.; Yemul, O. S. Synthesis, Characterization and Application of Crosslinked Alginate as Green Packaging Material. *Heliyon* 2020, *6* (1), e03026. https://doi.org/10.1016/j.heliyon.2019.e03026.

(299) Sun, Y.; Liu, Z.; Zhang, L.; Wang, X.; Li, L. Effects of Plasticizer Type and Concentration on Rheological, Physico-Mechanical and Structural Properties of Chitosan/Zein Film. *Int J Biol Macromol* 2020, *143*, 334–340. https://doi.org/10.1016/j.ijbiomac.2019.12.035.

(300) Basak, S.; Annapure, U. S. Rheological Performance of Film-Forming Solutions and Barrier Properties of Films Fabricated from Cold Plasma-Treated High Methoxyl Apple Pectin and Crosslinked by Ca2+: Impact of Plasma Treatment Voltage. *Int J Biol Macromol* 2023, *227*, 938–951. https://doi.org/10.1016/j.ijbiomac.2022.12.161.

(301) Bélafi-Bakó, K.; Cserjési, P.; Beszédes, S.; Csanádi, Z.; Hodúr, C. Berry Pectins: Microwave-Assisted Extraction and Rheological Properties. *Food Bioproc Tech* 2012, *5* (3), 1100–1105. https://doi.org/10.1007/s11947-011-0592-9.

(302) Ma, J.; Lin, Y.; Chen, X.; Zhao, B.; Zhang, J. Flow Behavior, Thixotropy and Dynamical Viscoelasticity of Sodium Alginate Aqueous Solutions. *Food Hydrocoll* 2014, *38*, 119–128. https://doi.org/10.1016/j.foodhyd.2013.11.016.

(303) Luchese, C. L.; Sperotto, N.; Spada, J. C.; Tessaro, I. C. Effect of Blueberry Agro-Industrial Waste Addition to Corn Starch-Based Films for the Production of a PH-Indicator Film. *Int J Biol Macromol* 2017, *104*, 11–18. https://doi.org/10.1016/j.ijbiomac.2017.05.149.

(304) Chen, L.; Tian, Y.; Bai, Y.; Wang, J.; Jiao, A.; Jin, Z. Effect of Frying on the Pasting and Rheological Properties of Normal Maize Starch. *Food Hydrocoll* 2018, *77*, 85–95. https://doi.org/10.1016/j.foodhyd.2017.09.024.

(305) Franck, A. Creep Recovery Measurements of Polymers. In *Creep Recovery Measurements of Polymers*; the 77th Annual Meeting of the American Society of Rheology in Vancouver, 2005; p AAN022.

(306) Hosseini, S. F.; Rezaei, M.; Zandi, M.; Ghavi, F. F. Preparation and Functional Properties of Fish Gelatin–Chitosan Blend Edible Films. *Food Chem* 2013, *136* (3), 1490–1495. https://doi.org/https://doi.org/10.1016/j.foodchem.2012.09.081.

(307) Ibrahim, S. F. B.; Mohd Azam, N. A. N.; Amin, K. A. M. Sodium Alginate Film: The Effect of Crosslinker on Physical and Mechanical Properties. In *IOP Conference Series: Materials Science and Engineering*; Institute of Physics Publishing, 2019; Vol. 509, p 012063. https://doi.org/10.1088/1757-899X/509/1/012063.

(308) Colinart, T.; Glouannec, P. Accuracy of Water Vapor Permeability of Building Materials Reassessed by Measuring Cup's Inner Relative Humidity. *Build Environ* 2022, *217*, 109038. https://doi.org/https://doi.org/10.1016/j.buildenv.2022.109038.

(309) Zhang, J.; Youngblood, J. P. Cellulose Nanofibril-Based Hybrid Coatings with Enhanced Moisture Barrier Properties. *Mater Adv* 2025, *6* (9), 2833–2844. https://doi.org/10.1039/d4ma01276c.

(310) Zhao, J.; Song, L.; Ming, W. Antifogging and Frost-Resisting Polymeric Surfaces. In *Contamination Mitigating Polymeric Coatings for Extreme Environments*; Wohl, C. J., Berry, D. H., Eds.; Springer International Publishing: Cham, 2019; pp 185–214. https://doi.org/10.1007/12_2017_42.

(311) Jiang, H.; Zhang, W.; Khan, M. R.; Ahmad, N.; Rhim, J. W.; Jiang, W.; Roy, S. Film Properties of Pectin Obtained from Various Fruits' (Lemon, Pomelo, Pitaya) Peels. *Journal of Composites Science* 2023, *7* (9), 366. https://doi.org/10.3390/jcs7090366.

(312) Domínguez-Robles, J.; Larrañeta, E.; Fong, M. L.; Martin, N. K.; Irwin, N. J.; Mutjé, P.; Tarrés, Q.; Delgado-Aguilar, M. Lignin/Poly(Butylene Succinate) Composites with Antioxidant and Antibacterial Properties for Potential Biomedical Applications. *Int J Biol Macromol* 2020, *145*, 92–99. https://doi.org/https://doi.org/10.1016/j.ijbiomac.2019.12.146.

(313) Priyadarshi, R.; Ezati, P.; Rhim, J. W. Recent Advances in Intelligent Food Packaging Applications Using Natural Food Colorants. *ACS Food Science and Technology* 2021, *1* (2), 124–138. https://doi.org/10.1021/acsfoodscitech.0c00039.

(314) Xue, H.; Zhao, J.; Wang, Y.; Shi, Z.; Xie, K.; Liao, X.; Tan, J. Factors Affecting the Stability of Anthocyanins and Strategies for Improving Their Stability: A Review. *Food Chem X* 2024, *24*, 101883. https://doi.org/10.1016/j.fochx.2024.101883.

(315) Liu, Y.; Tong, Y.; Tong, Q.; Xu, W.; Wang, Z. Effects of Sunflower Pectin on Thermal Stability of Purple Sweet Potato Anthocyanins at Different PH. *Int J Biol Macromol* 2023, *253*, 126663. https://doi.org/https://doi.org/10.1016/j.ijbiomac.2023.126663.

(316) Stintzing, F. C.; Carle, R. Functional Properties of Anthocyanins and Betalains in Plants, Food, and in Human Nutrition. *Trends Food Sci Technol* 2004, *15* (1), 19–38. https://doi.org/https://doi.org/10.1016/j.tifs.2003.07.004.

(317) Patras, A.; Brunton, Nigel. P.; O'Donnell, C.; Tiwari, B. K. Effect of Thermal Processing on Anthocyanin Stability in Foods; Mechanisms and Kinetics of Degradation. *Trends Food Sci Technol* 2010, *21* (1), 3–11. https://doi.org/https://doi.org/10.1016/j.tifs.2009.07.004.

(318) Soares, J. P.; Santos, J. E.; Chierice, G. O.; G Cavalheiro, E. T. Thermal Behavior of Alginic Acid and Its Sodium Salt. *Ecl. Quím.* 2004, *29* (2), 53–56.

(319) Thomas, L. C.; Schmidt, S. J. *"Apparent Melting": A New Approach to Characterizing Crystalline Structure in Pharmaceutical Materials*. https://www.tainstruments.com/applications-notes/apparent-melting-a-new-approach-to-characterizing-crystalline-structure-in-pharmaceutical-materials/ (accessed 2025-10-20).

(320) Nazir, S.; Wani, I. A. Physicochemical Characterization of Basil (Ocimum Basilicum L.) Seeds. *J Appl Res Med Aromat Plants* 2021, *22*, 100295. https://doi.org/10.1016/j.jarmap.2021.100295.

(321) Pozo, C.; Rodríguez-Llamazares, S.; Bouza, R.; Barral, L.; Castaño, J.; Müller, N.; Restrepo, I. Study of the Structural Order of Native Starch Granules Using Combined FTIR and XRD Analysis. *Journal of Polymer Research* 2018, *25* (12), 266. https://doi.org/10.1007/s10965-018-1651-y.

(322) Wang, Y. C.; Liang, Y. C.; Huang, F. L.; Chang, W. C. Effect of Freeze–Thaw Cycles on Physicochemical and Functional Properties of Ginger Starch. *Processes* 2023, *11* (6), 1828. https://doi.org/10.3390/pr11061828.

(323) Foggia, M. Di; Taddei, P.; Torreggiani, A.; Dettin, M.; Tinti, A. Self-Assembling Peptides for Biomedical Applications: IR and Raman Spectroscopies for the Study of Secondary Structure. *Proteomics Research Journal* 2011, *2* (3), 231–272.

(324) Dima, C.; Ifrim, G. A.; Coman, G.; Alexe, P.; Dima, Ş. Supercritical CO2 Extraction and Characterization of Coriandrum Sativum L. Essential Oil. *J Food Process Eng* 2016, *39* (2), 204–211. https://doi.org/10.1111/jfpe.12218.

(325) Minaei, S.; Saebi, A.; Mostasharshahidi, S. M.; Mahdavian, A.; Ebadi, M. T.; Markom, M. Thermodynamic Optimization of a Staged Supercritical CO2 System for High-Purity bioactive Separation from Coriander Seeds. *Journal of Supercritical Fluids* 2026, *227*, 106756. https://doi.org/10.1016/j.supflu.2025.106756.

(326) Bose, S.; Banerjee, D.; Vu, A. A. Ginger and Garlic Extracts Enhance Osteogenesis in 3D Printed Calcium Phosphate Bone Scaffolds with Bimodal Pore Distribution. *ACS Appl Mater Interfaces* 2022, *14* (11), 12964–12975. https://doi.org/10.1021/acsami.1c19617.

(327) Gee, C. T.; Kehoe, E.; Pomerantz, W. C. K.; Penn, R. L. Quantifying Protein Concentrations Using Smartphone Colorimetry: A New Method for an Established Test. *J Chem Educ* 2017, *94* (7), 941–945. https://doi.org/10.1021/acs.jchemed.6b00676.

(328) Palm, D. M.; Agostini, A.; Averesch, V.; Girr, P.; Werwie, M.; Takahashi, S.; Satoh, H.; Jaenicke, E.; Paulsen, H. Chlorophyll a/b Binding-Specificity in Water-Soluble Chlorophyll Protein. *Nat Plants* 2018, *4* (11), 920–929. https://doi.org/10.1038/s41477-018-0273-z.

(329) Liang, L.; Wang, W.; Li, M.; Xu, Y.; Lu, Z.; Wei, J.; Tang, B. Z.; Sun, F.; Tong, R. Cancer Photodynamic Therapy Enabled by Water-Soluble Chlorophyll Protein. *ACS Appl Mater Interfaces* 2025, *17* (11), 16668–16680. https://doi.org/10.1021/acsami.5c01280.

(330) López-Macías, B. M.; Morales-Martínez, S. E.; Loza-Cornejo, S.; Reyes, C. F.; Terrazas, T.; Patakfalvi, R. J.; Ortiz-Morales, M.; Miranda-Beltrán, M. de la L. Variability and Composition of Calcium Oxalate Crystals in Embryos-Seedlings-Adult Plants of the Globose Cacti Mammillaria Uncinata. *Micron* 2019, *125*, 102731. https://doi.org/10.1016/j.micron.2019.102731.

(331) Wang, Z.; Du, L.; Wang, Q.; Xie, J.; Fu, Z.; Zou, Z. Local Concentration Controls the Hydrate Phase of Calcium Oxalate. *CrystEngComm* 2024, *26* (18), 2394–2403. https://doi.org/10.1039/d3ce01286g.

(332) Hartl, W. P.; Klapper, H.; Barbier, B.; Ensikat, H. J.; Dronskowski, R.; Müller, P.; Ostendorp, G.; Tye, A.; Bauer, R.; Barthlott, W. Diversity of Calcium Oxalate Crystals in Cactaceae. *Canadian Journal of Botany* 2007, *85* (5), 501–517. https://doi.org/10.1139/B07-046.

(333) Šoltýs, A.; Hronský, V.; Šmídová, N.; Olčák, D.; Ivanič, F.; Chodák, I. Solid-State 1H and 13C NMR of Corn Starch Plasticized with Glycerol and Urea. *Eur Polym J* 2019, *117*, 19–27. https://doi.org/10.1016/j.eurpolymj.2019.04.042.

(334) Mutungi, C.; Passauer, L.; Onyango, C.; Jaros, D.; Rohm, H. Debranched Cassava Starch Crystallinity Determination by Raman Spectroscopy: Correlation of Features in Raman Spectra with X-Ray Diffraction and 13C CP/MAS NMR Spectroscopy. *Carbohydr Polym* 2012, *87* (1), 598–606. https://doi.org/10.1016/j.carbpol.2011.08.032.

(335) Curetti, N.; Pastero, L.; Bernasconi, D.; Cotellucci, A.; Corazzari, I.; Archetti, M.; Pavese, A. Thermal Stability of Calcium Oxalates from CO2 Sequestration for Storage

Purposes: An In-situ HT-XRPD and TGA Combined Study. *Minerals* 2022, *12* (1), 53. https://doi.org/10.3390/min12010053.

(336) Trouvé, G.; Michelin, L.; Kehrli, D.; Josien, L.; Rigolet, S.; Lebeau, B.; Gieré, R. The Multi-Analytical Characterization of Calcium Oxalate Phytolith Crystals from Grapevine after Treatment with Calcination. *Crystals (Basel)* 2023, *13* (6), 967. https://doi.org/10.3390/cryst13060967.

(337) Hu, Q.; He, Y.; Wang, F.; Wu, J.; Ci, Z.; Chen, L.; Xu, R.; Yang, M.; Lin, J.; Han, L.; Zhang, D. Microwave Technology: A Novel Approach to the Transformation of Natural Metabolites. *Chin Med* 2021, *16* (1), 87. https://doi.org/10.1186/s13020-021-00500-8.

(338) Singh, V.; Ali, S. Z.; Somashekar, R.; Mukherjee, P. S. Nature of Crystallinity in Native and Acid Modified Starches. *Int J Food Prop* 2006, *9* (4), 845–854. https://doi.org/10.1080/10942910600698922.

(339) Liang, Y.; Wang, F.; Ma, R.; Tian, Y. Structural Properties of the Intra- and Interhelical Cavities of V6-Type Crystalline Starches. *Carbohydr Polym* 2024, *330*, 121835. https://doi.org/10.1016/j.carbpol.2024.121835.

(340) Li, J.; Capuano, E.; Tong, L. T. Transformation of Native Starch into V-Type Granular Starch through Ethanol-Aqueous Heat Treatment and Its Swelling Behavior in Cold Water. *Carbohydr Polym* 2025, *354*, 123313. https://doi.org/10.1016/j.carbpol.2025.123313.

(341) Dries, D. M.; Gomand, S. V.; Delcour, J. A.; Goderis, B. V-Type Crystal Formation in Starch by Aqueous Ethanol Treatment: The Effect of Amylose Degree of Polymerization. *Food Hydrocoll* 2016, *61*, 649–661. https://doi.org/10.1016/j.foodhyd.2016.06.026.

(342) Pan, Y.; Wang, C.; Geng, S.; Liu, B. Ginger as a Novel Starch Resource: Preparation, Structural Characterization and Physicochemical Properties. *Food Chem* 2025, *497*, 146832. https://doi.org/10.1016/j.foodchem.2025.146832.